The Dissertation Committee for Jeffrey Robert Gohean
certifies that this is the approved version of the following dissertation:

Hierarchical Control of a Two-Piston Toroidal Blood Pump

Committee:

Raul Longoria, Supervisor

Dongmei "Maggie" Chen

Joseph Beaman

Manuel Rausch

Hierarchical Control of a Two-Piston Toroidal Blood Pump

by

Jeffrey Robert Gohean

DISSERTATION

Presented to the Faculty of the Graduate School of

The University of Texas at Austin

in Partial Fulfillment

of the Requirements

for the Degree of

DOCTOR OF PHILOSOPHY

THE UNIVERSITY OF TEXAS AT AUSTIN

May 2019

Hierarchical Control of a Two-Piston Toroidal Blood Pump

Publication No. _____

Jeffrey Robert Gohean, Ph.D.
The University of Texas at Austin, 2019

Supervisor: Raul Longoria

The two-piston toroidal pump (2PTP) is a new pulsatile pumping paradigm with potential physiological advantages compared to existing continuous flow blood pump technologies. The purpose of this research was to develop hierarchical control methods for this new pumping modality, including high-level physiological control and low-level piston control. First, geometric constraints were identified for this pump architecture and piston path-planning methods were developed to define pulsatile ejections. To develop high-level control, an open-loop lumped parameter model of the cardiovascular system was improved with a modified end-diastolic pressure-volume elastance curve and then used to study ventricular function curves with different types of blood pump support. It was determined that synchronous counterpulse support with the 2PTP provides a more physiological response to preload compared to continuous flow, which could prevent overpumping and ventricular suction at low preloads. To develop low-level piston control, a variable structure model of the 2PTP was developed and then used to test improved control techniques. An algorithmic approach to switched bond graph structures was developed for hydraulic networks to derive state equations for the variable structure model. Linear control and Kalman-filter-based estimation methods were developed with a reduced-order model of the pump. Improved control and estimation methods were tested and confirmed in preliminary experiments in mock circulatory loops. Estimation of pump flow and differential pump pressure were verified, which could be useful feedback to physiological control or as diagnostic tools for doctors.

Table of Contents

Abstract iv

List of Tables xi

List of Figures xii

Chapter 1. Introduction 1

1.1 Ventricular Assist Devices . . . 1

1.1.1 First-Generation Pulsatile VADs . . . 2

1.1.2 Continuous Flow VADs . . . 2

1.1.3 Rotary Piston VADs . . . 4

1.2 Hierarchical VAD Control . . . 6

1.2.1 High-Level VAD Control . . . 7

1.2.2 Low-Level VAD Control . . . 8

1.3 2PTP Hierarchical Control - Research Aims . . . 11

Part I Cardiovascular System Modeling 14

Chapter 2. Cardiac Output Autoregulation 15

2.1 Why is Cardiac Output Regulated? . . . 15

2.2 How is Cardiac Output Regulated? . . . 16

2.3 Pressure-Volume Loops . . . 18

2.4 Physiological Feedback for Cardiac Output Variation . . . 20

2.5 Ventricular Function Curves . . . 21

2.5.1 Ventricular Function Curves in Heart Failure . . . 25

2.6 Autoregulation with VADs . . . 25

Chapter 3. Cardiovascular System Modeling 27

3.1 Lumped Parameter Modeling of the Cardiovascular System . . . 27

3.1.1 Open-Loop Cardiovascular Model . . . 28

3.1.2 Closed-Loop Cardiovascular Model . . . 30

3.2 Lumped Parameter Model Equations . . . 30

3.2.1 Systemic Arteries . . . 30
3.2.1.1 Left Ventricular and Atrial Volume . . . 31
3.2.1.2 Ventricular and Atrial Pressure . . . 31
3.2.1.3 Time-Varying Elastance . . . 32
3.2.1.4 Aortic and Mitral Valve Flow . . . 33
3.2.2 Pulmonary Circulation . . . 35
3.2.3 Parameterization . . . 36
3.3 Lumped Parameter Model Simulation . . . 36

Chapter 4. Ventricular Elastance and Ventricular Function Curves 38
4.1 EDPVR Models . . . 38
4.1.1 Existing EDPVR Models - Exponential and Logarithmic . . . 39
4.1.1.1 Exponential EDPVR . . . 39
4.1.1.2 Logarithmic EDPVR . . . 40
4.1.2 Modified EDPVR Models - Exponential and Logarithmic . . . 41
4.1.2.1 Modified Exponential EDPVR Model . . . 41
4.1.2.2 Modified Logarithmic EDPVR Model . . . 42
4.2 Parameterization of EDPVR Model Coefficients . . . 43
4.2.1 Exponential EDPVR Coefficients . . . 43
4.2.2 Logarithmic EDPVR Coefficients . . . 44
4.2.3 Modified Exponential EDPVR Coefficients . . . 44
4.2.4 Modified Logarithmic EDPVR Coefficients . . . 44
4.2.5 Parameterization - Healthy and HF Operating Point . . . 45
4.2.6 Ventricular Function Curves . . . 45
4.3 Summary and Conclusion . . . 49

Part II High-level Control 50

Chapter 5. High-Level 2PTP Control - Pump Function 51
5.1 Rotary Piston Pump Introduction . . . 51
5.1.1 Two-Piston Toroidal Pump (2PTP) . . . 52
5.2 Pressure-Flow Curves . . . 56
5.3 2PTP Pumping Criteria . . . 58
5.4 2PTP Piston and Torus Geometry . . . 59
5.4.1 Angular Parameters and Constraints . . . 59
5.4.2 Geometric Parameters and Constraints . . . 63

5.4.3 Summary of Parameters 65
5.5 2PTP Dynamic Flow Characteristics 66
5.6 Reference Tracking Curves 75
5.6.1 Angular Velocity 75
5.6.2 Angular Position 75
5.6.3 Angular Acceleration 76

Chapter 6. High-Level 2PTP Control - Physiological Control 78
6.1 Physiological Control 78
6.2 2PTP Physiological Control 80
6.3 Passive Preload Sensitivity - CF vs 2PTP Counterpulse 83
6.3.1 Preload Sensitivity Simulation Methods 83
6.3.2 Preload Sensitivity Simulation Results 85
6.3.3 Preload Sensitivity Simulation Discussion 94
6.4 Summary and Conclusion 96

Part III 2PTP Model 97

Chapter 7. 2PTP Variable Structure Model 98
7.1 Motor and Piston Model 98
7.1.1 Motor Model 99
7.1.2 Piston Model 100
7.1.3 Magnetic Coupling Model 101
7.1.4 Motor and Piston State Equations 103
7.2 Pump Flow and Pressure Model 104
7.2.1 Pumping Modes 105
7.3 Building the Pump Flow and Pressure Model 107
7.3.1 A Simple Positive Displacement Model 107
7.3.2 Incorporate Piston Leakage 108
7.3.3 Fluid Inertance and Resistance 112
7.3.4 Inflow and Outflow Resistance 116
7.3.5 Transition 118
7.3.6 Occlusion Leakage 122
7.3.7 Special Case - Shunt 124
7.3.8 Inflow and Outflow Effects 126
7.4 Variable Structure Model 128

7.5 State Equations . . . 134
7.6 Structure Switching . . . 138
7.6.1 Event Detection . . . 138
7.6.2 Re-initialization . . . 138
7.7 Pump Parameters . . . 141
7.8 Simulation Results . . . 142

Chapter 8. Reduced-Order Model 146
8.1 Reduced-Order Model for Pumping . . . 147
8.1.1 Linearization . . . 150
8.1.2 State Equations . . . 150
8.1.3 State Space Representation . . . 152
8.1.4 Controllability and Observability . . . 154
8.2 Linear Model of Transition . . . 156
8.2.1 State Equations . . . 156
8.2.2 State Space . . . 157
8.2.3 Controllability and Observability . . . 158
8.3 Reduced-Order Model Zones . . . 158
8.4 Coupling . . . 161

Part IV Low-Level Control and Estimation 164

Chapter 9. Low-Level Control 165
9.1 Linear Quadratic Regulator . . . 166
9.1.1 LQR Weights . . . 167
9.2 Disturbance / Exogenous Variable Rejection . . . 169
9.3 Feedforward . . . 171
9.3.1 Fluid and Piston Feedforward . . . 172
9.3.2 Electrical back emf and Motor Dynamics . . . 173
9.3.3 Combining the Fluid, Piston, and Motor Feedforward . . . 173
9.4 Simulation Results . . . 174

Chapter 10. State Estimation 179
10.1 Kalman Filter . . . 179
10.2 2PTP Kalman Filter Setup . . . 181
10.3 Process and Measurement Noise . . . 182
10.4 Switching . . . 182
10.5 Practical Application - Suboptimal Kalman Filter . . . 186

Chapter 11. Stability and Robustness **189**
11.1 Switched Variable Structure Model Stability 189
11.2 Open-Loop Stability of the Reduced-Order Model 194
11.2.1 Open-Loop Stability of the Reduced-Order Model of Pumping 195
11.2.2 Open-Loop Stability of the Reduced-Order Model of Transition 195
11.2.3 Discussion on the Open-Loop Stability of the Reduced-Order Model . 196
11.3 Closed-Loop Stability of the Reduced-Order Model 196
11.3.1 Separation Principle 196
11.3.2 Poles Plots 197
11.3.2.1 Pumping and Transition Pole Plots 197
11.3.2.2 Switched Pole Plots Stability 201
11.3.3 Robustness 203
11.3.3.1 Mu Analysis 203
11.4 Stability Summary and Discussion 207

Chapter 12. Experiments **208**
12.1 Step Response 210
12.2 PID vs LQR Control 212
12.3 Pressure and Flow Estimation 218

Chapter 13. Discussion and Conclusions **221**
13.1 Limitations 223

Appendices **224**

Appendix A. High-Level 2PTP Control - Vibration Concerns **225**
A.1 2PTP and Tissue Model of Motion and Vibration 225
A.1.1 Eccentric Masses 225
A.1.2 Tissue Model 226
A.1.3 Fluid Momentum and Pressure Forces 226
A.1.4 Model 230
A.2 Future Direction 239

Appendix B. General Solution for Lagrange Subsystem With Conservative Exogenous Efforts **240**

Appendix C. Hybrid Model State Equations **245**

Appendix D. Coupled Fluid Inertia in Flow Junctions **278**
D.1 Generalized Model for Inertial Coupling at a Flow Junction 278
D.1.1 Case 1: Decoupled Inertance ($I_3 \ll I_1 \& I_2$) 282
D.1.2 Case 2: Strongly Coupled ($I_3 \gg I_1 \& I_2$) 283
D.1.3 Case 3: Coupled ($I_1 = I_2 = I_3$) 284

Bibliography **285**

List of Tables

3.1 Cardiovascular model parameters 37

5.1 Pump dimensions and operation parameters. 65

6.1 Baseline hemodynamic parameters for four simulation conditions 84
6.2 Preload sensitivity and cardiac output from the open-loop model simulation 86

7.1 States for 30 model structures 135
7.2 Pump parameters. 141

10.1 Number of multiplications for the real-time implementation of a tenth order model Kalman filer with 2 outputs 186

12.1 Asynchronous flow rates and pressures 216

List of Figures

1.1 Continuous flow VADs . . . 3
1.2 Schematic of the 2PTP . . . 5
1.3 The TORVAD system . . . 5
1.4 Sample position and error data of 2PTP collision event . . . 10

2.1 Double circulation of the cardiovascular system . . . 17
2.2 Left ventricular pressure-volume loop . . . 19
2.3 Left ventricular pressure-volume loop response to physiological feedback . . . 21
2.4 Starling's excised canine heart experiment and ventricular function curve . . . 22
2.5 Ventricular function curves and physiological feedback . . . 23
2.6 Ventricular function curves . . . 24
2.7 Ventricular function curves for healthy and heart failure conditions . . . 25

3.1 Schematic representation of the open-loop and closed-loop lumped parameter cardiovascular system models . . . 29
3.2 Normalized elastance curves for a HR of 80 bpm . . . 34
3.3 Time varying elastance . . . 34

4.1 Two models for EDPVR - linear and logarithmic . . . 39
4.2 Four models of EDPVR . . . 47
4.3 Simulated ventricular function curves . . . 48

5.1 R.E. Newcomb's Fluid Pump . . . 53
5.2 Popular Science cover: Rivals to the Wankel . . . 54
5.3 Ulert's Circular Artificial Heart . . . 54
5.4 Schematics representations of two-piston toroidal pumping . . . 55
5.5 Pressure-flow curves for continuous and positive displacement flow pumps . . . 57
5.6 Schematics representations of collision and shunt . . . 58
5.7 Piston and torus angles. . . . 61
5.8 Torus cross section heights and aspect ratios . . . 64
5.9 2PTP flow profiles . . . 67
5.10 2PTP sinusoidal flow profile . . . 69
5.11 Piston velocities during transition . . . 72

5.12 Example of piston position, velocity, and acceleration reference curves 77

6.1 Hemodynamic plots demonstrating synchronous support 81
6.2 Cardiac output vs phase delay with 2PTP vs CF support 82
6.3 Simulated ventricular function curves from the open-loop model 89
6.4 Aortic valve and VAD flow vs ventricular preload 90
6.5 Hemodynamics with PVR, SVR, HR, inotropic state, and blood volume changes. 91
6.6 Hemodynamic response of a PVR step-change with CF 92
6.7 Hemodynamic response of a PVR step-change with 2PTP 93

7.1 Bond graph model of a brushless DC motor 99
7.2 Bond graph model of the piston dynamics 101
7.3 Magnetic coupling between the motors and pistons 102
7.4 Magnetic coupling torque vs angular displacement 102
7.5 Bond graph model of the motor-piston subsystem 103
7.6 2PTP pump schematic 104
7.7 Schematics representations of the three pumping modes 106
7.8 A simple positive displacement pump model 107
7.9 Bond graph model of leakage flow around the piston 110
7.10 Bond graph of a positive displacement pump with leakage 111
7.11 Partitioning of the torus volume 113
7.12 Partitioning of the torus volume during transition 114
7.13 Bond graph of the 2PTP with four distinct volumes and flows 115
7.14 Bond graph model of the 2PTP with inflow and outflow port resistance . . . 117
7.15 Bond graph incorporating the resistances for both inflow and outflow into a single model 119
7.16 Three pumping models of variable structure 120
7.17 Quasistatic pressure across the piston during transition 121
7.18 2PTP flow pathways 123
7.19 Shunt condition 125
7.20 Coupling the inflow and outflow to the system 127
7.21 The complete bond graph model of the 2PTP pump 129
7.22 Schematic representations of 64 possible model structures 131
7.23 Bond graphs of 64 possible model structures 132
7.24 Piston trajectory map 133
7.25 Flow boundaries overlayed with model schematics 140
7.26 Simulated quasistatic pressure across the piston during transition 143

7.27 Ideal 2PTP pressure and flow at 5 L/min 144
7.28 2PTP pressure and flow with ideal motor control at 5 L/min and 100 mmHg 145

8.1 Simplified model of the 2PTP 147
8.2 Simplified model of the 2PTP with motor subsystems 149
8.3 Simplified linear model of the 2PTP transition 159
8.4 Piston trajectory map 160
8.5 Effective coupled mass moment of inertias 163

9.1 Simulated PID control at 5 L/min against 100 mmHg differential pump pressure176
9.2 Simulated LQR control at 5 L/min against 100 mmHg differential pump pressure. 177
9.3 Piston trajectory error, piston separation, and input voltage for PID and LQR control at 5 L/min against 100 mmHg differential pump pressure. 178

10.1 Normalized covariance at switch events 184
10.2 Normalized Kalman gains at switch events 185
10.3 Kalman gains vs time during a transition 188

11.1 Open and closed-loop poles for pumping and transition. 200
11.2 Compensator pole locations for the pumping/transition switched system . . 202
11.3 Compensator poles with parameter uncertainty. 206

12.1 Schematics of the mock loops used for experimental testing. 209
12.2 Hybrid mock loop experimental setup. 209
12.3 Simulation vs experimental results for a 10° reference trajectory step input . 211
12.4 Simulated model compared to experimental results at 5 L/min with PID control213
12.5 Simulated model compared to experimental results at 5 L/min with LQR control215
12.6 Motor position error from ideal trajectory for PID vs LQR 217
12.7 Pump estimated pressure at various flow (1-6 L/min) and pressures (50 and 100 mmHg) 219
12.8 Measured vs KF estimated dynamic differential pump pressure and flow . . . 220

A.1 Schematic of pump with eccentric masses in tissue 226
A.2 Commoon tissue models 227
A.3 2PTP control volume 227
A.4 Vectorized bond graph of a Lagrange subsystem 230
A.5 Bond graph of the multibody Lagrange subsystem with exogenous hydraulic efforts and coupled inertia 231
A.6 Pump motion in and forces on surrounding tissue at 5 L/min pump flow rate 236

A.7 Pump motion in and forces on surrounding tissue at 0 L/min pump flow rate with simulated beating heart pressure 237
A.8 Pump motion in and forces on surrounding tissue at 2.7 L/min counterpulse support 238

B.1 Vectorized bond graph of a Lagrange subsystem 240

D.1 Schematic of an inertially coupled flow junction 278
D.2 Causal bond graph of a flow junction 279
D.3 Coupled flow through T-junction with small system inertance ($I_3 \ll I_1 \& I_2$). In this case, the flows 1 and 2 become inertially decoupled. 282
D.4 Coupled flow at a junction with large system inertance ($I_3 \gg I_1 \& I_2$). In this case, the flows 1 and 2 become strongly coupled. 283
D.5 Coupled flow at a junction with large system inertance ($I_3 \gg I_1 \& I_2$). In this case, the flows 1 and 2 become strongly coupled. 284

Chapter 1

Introduction

This chapter provides a brief background on implantable blood pumps, introduces a new blood pump (the two-piston toroidal pump), and explains some of the unique challenges associated with modeling and controlling this kind of device. Research aims are listed and the dissertation is outlined at the end of the chapter.

1.1 Ventricular Assist Devices

Heart failure (HF) is a disease that affects over 5 million people in the United States [1], half of whom die within 5 years of the diagnosis. Heart failure is one of the leading and most expensive Medicare hospitalization diagnoses, costing approximately $32B in 2011 [2]. About 250,000 patients in the US suffer from severe HF, the end-stage of the disease. Heart transplantation is currently the best treatment option, but only 2,500 donor hearts become available in the US each year [3, 4]. Mechanical implantable blood pumps called ventricular assist devices (VADs) have emerged in recent years as a viable treatment option for patients with end-stage HF [5, 6]. They are most commonly used as a bridge-to-transplant for patients who would otherwise die while waiting for a heart transplant. They are also now being increasingly used as so-called 'destination therapy' for patients who aren't eligible for transplantation due to factors like age or other diseases such as cancer or diabetes. A small number of patients have also been able to utilize VADs as a bridge-to-recovery. In these patients, the VAD provides sufficient unloading to the heart to allow it to recover, at which point the device can be removed.

Ventricular assist devices are implantable blood pumps that provide additional blood flow to patients with end-stage heart failure [7]. They do not replace the patient's heart but are implanted intracorporeally (inside the body) and reside just below the heart. An inflow cannula is inserted into the left ventricle and an outflow graft is sewn to the aorta such that

the pump provides flow to the systemic circulation that is in parallel with the aortic valve.

The pumps are connected to a controller and battery by a driveline that protrudes through the skin (see Figure 1.1). The controller receives signals from the pump (e.g. motor back emf, motor position, or ventricular electrocardiogram, depending on pump capabilities) and provides power to the driving mechanism(s) of the device.

1.1.1 First-Generation Pulsatile VADs

The first VADs were pneumatic or mechanical positive displacement sac pumps that mimicked the ventricles by using artificial valves to separate filling and ejecting phases. These devices had stroke volumes of 60-70 ml and provided pulsatile flow that was similar to the normal healthy flow provided by the heart. These pumps were usually operated at a fixed rate or in a fill-to-empty mode. They were very large which limited the number of patients that could be served with this technology, were plagued by durability issues, and are therefore no longer used.

1.1.2 Continuous Flow VADs

Pulsatile VADs have since been replaced clinically by continuous flow (CF) VADs, which use centrifugal or axial turbomachinery principles to pump blood (see Figure 1.1). These devices are smaller than pulsatile VADs and have much better durability and reliability [8]. They are the current clinical standard of care for end-stage heart failure. But pumping continuously using high rotational speeds has disadvantages including reduced pulsatility and high shear. High shear can damage important blood components, for example damage to von Willebrand factor can lead to increased risk of bleeding, damage to platelets can lead to pump thrombosis, and damage to white blood cells can increase the risk of infection. The reduced pulsatility that results from continuous flow pumps can lead to gastrointestinal bleeding, poor end-organ perfusion, and increased arterial stiffness [9].

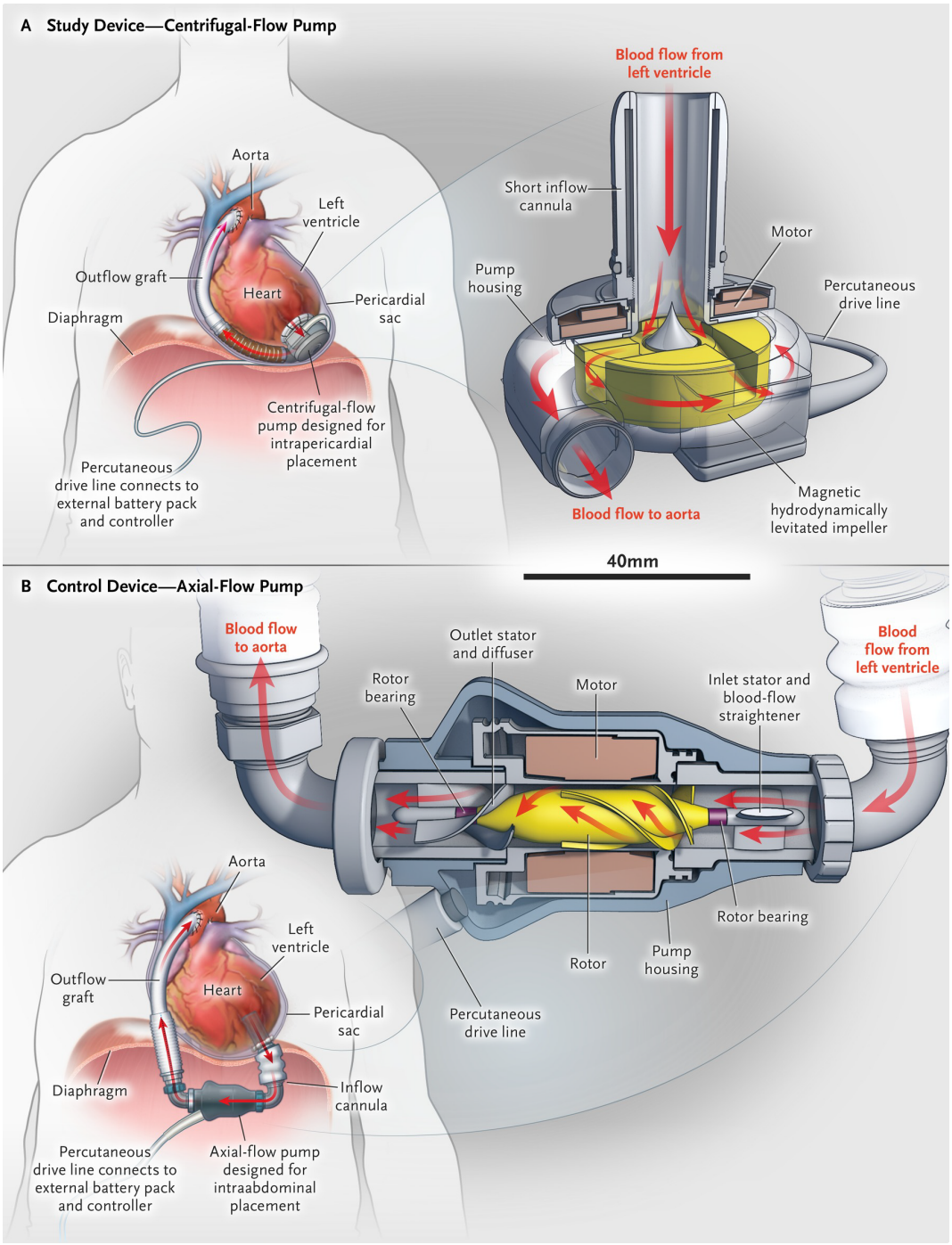

Figure 1.1: Continuous flow VADs (from [10]). Both centrifugal flow (top) and axial flow (bottom) are used clinically.

.

1.1.3 Rotary Piston VADs

This research focuses on a new pumping modality, the rotary piston pump. Most rotary piston pumps that have been developed use a single rotating piston [11]. The most common example of this principle is the Wankel engine. Early prototypes of these rotary piston pumps experienced thrombus issues in the axial gap between the rotor and pump housing and had seals which limited durability, caused blood clots to form, or required irrigation.

An alternative design, the two-piston toroidal pump (2PTP), has been developed. This concept was originally patented by Dr. Alan Ulert [12] and original prototypes of the design were developed as part of a Master's thesis in the Mechanical Engineering department at the University of Texas at Austin in 2005 [13]. The technology was transferred to Windmill Cardiovascular Systems (Austin, TX) for continued development, where the pump has been refined for clinical use and called the TORVAD (TORoidal Ventricular Assist Device). An image of the assembled device with controller is shown in Figure 1.3. Preliminary feasibility testing for the TORVAD has been completed including 60-day animal experiments that have established this device as a potential improvement over existing CF technology. But significant challenges remain, particularity as it relates to the control of this new pumping modality.

Two-Piston Toroidal Pump (2PTP)

The 2PTP uses two independently controlled pistons to produce pulsatile ejections [14] (see Figure 1.2). Each piston is magnetically coupled to a position-controlled brushless DC motor that resides within the inner diameter of the toroidal pumping chamber. The pistons are suspended in the middle of the torus lumen with small ceramic microhydrodynamics bearings that serve to reduce wear and to control the gap between the piston and torus walls to minimize shear stress to the blood. The current version embodied in the TORVAD has a 30 ml stroke volume, but the device stroke volume could be scaled to adapt to different patient sizes and needs. The pump can synchronize to the cardiac cycle or can be run at a fixed flow rate up to 8 L/min.

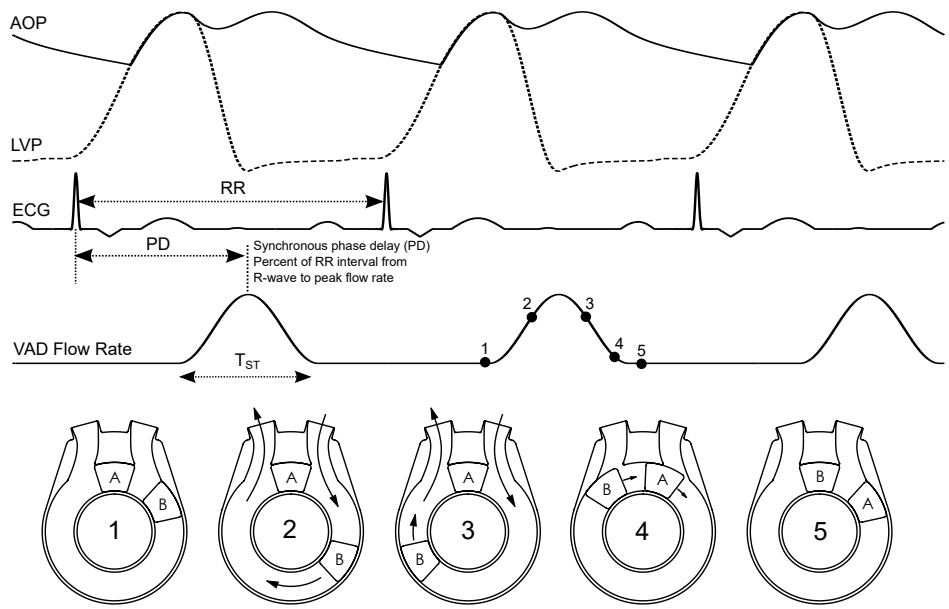

Figure 1.2: Schematic of the 2PTP (bottom), demonstrating how pumping is achieved by independently controlling two pistons (A/B) within a toroidal pumping chamber. From rest (1), one piston (A) is temporarily held stationary between the inflow and outflow ports, while the other piston (B) rotates around the torus (2/3) simultaneously aspirating blood from the left ventricle and ejecting blood into the arterial system. At the end of each pump stroke, the pistons move together (4), exchange roles, and are ready for the next ejection (5). The resultant pulsatile VAD flow rate is shown (middle), and the effect on aortic blood pressure (AOP) are demonstrated (top), when the pump is synchronized to the left ventricular pressure (LVP) contraction using the epicardial ECG and a pump phase delay.

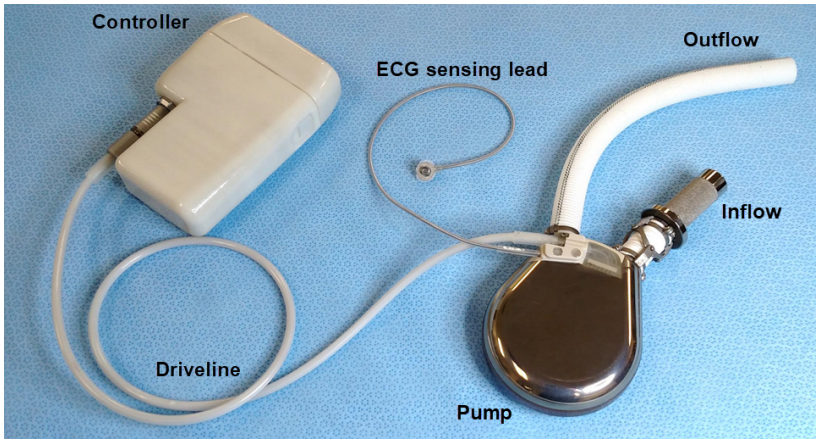

Figure 1.3: The TORVAD system showing the pump and controller connected by the driveline. The ECG sensing lead attaches to the heart surface to detect ventricular depolarization for pump synchronization. The inflow in inserted into the left ventricle and the outflow graft is anastamosed to the aorta.

1.2 Hierarchical VAD Control

Control of VADs is hierarchical. High-level control is used to make decisions on operating parameters such as ejection rate for positive displacement devices or rotational speeds for continuous flow devices. Low-level control is then responsible for controlling the driving mechanism of the device to achieve the specified high-level goals. Hierarchical control could also include event response to things like ventricular suction or arrhythmias.

At the risk of understating the problem, hierarchical control is meant to answer a single question: How should the VAD pump? The division between high- and low-level control could be drawn based on where the emphasis to the question is placed.

How *should* the VAD pump? This is high-level control. How much flow should a VAD deliver? Take the CF pump as an example. In clinical practice, high-level control of CF pumps consists of nothing more than the doctor simply setting a fixed rotational speed (impeller rpm). The doctor makes a judgment call on the optimal speed based on physiological feedback such as blood pressure, pump flow estimates, and aortic valve opening frequency. Exceptions to this rule and recent developments in field are discussed in the following sections and include more advanced automatic methods sometimes called 'physiological control' that seeks to automatically adjust the pump flow to deliver physiological flow, that is flow that is healthy and beneficial to the patients heart and health. The challenge here is in sufficiently understanding cardiovascular hemodynamics and working within the limitations of the VAD and available feedback to design control algorithms for physiologically beneficial, safe, and robust support.

***How* should the VAD pump?** This is low-level control. How does the driving mechanism of the pump need to be controlled in order to achieve the desired flow output determined by the high-level control? Again taking the CF as an example, low-level control is nothing more than three-phase brushless DC speed control by back emf sensing to maintain the constant rpm that is set by the doctor's high-level control decision. The 2PTP operates very differently than previous devices, so more complex low-level control methods are needed to precisely control the position and speed of the pistons to produce the desired pump ejections. This is discussed in more detail below.

1.2.1 High-Level VAD Control

With few exceptions, the high-level control setting of VADs is determined and manually set by the doctor, with periodic adjustments made at follow up appointments. First-generation sac-type pulsatile devices were set at a fixed open-loop rate and CF pumps are set at a fixed rotational speed. Academic research, little of which has found its way to the bedside, has explored numerous types of high-level control for VADs. The progress in the field is briefly summarized below.

Very few high-level control methods were studied for the first-generation sac-type pulsatile VADs. A few controls were designed to minimize power, and a few studies were performed to assess the effect of synchronous pumping (matching one pump ejection per heart beat), but these methods were never widely implemented [15, 16].

High-level physiological control of continuous flow VADs is an active research topic. The current clinical practice for CF devices is to set the pump at a fixed rpm. In this mode, the pump does not automatically respond to physiologic changes like exercise and rest, heart rate variation, arrhythmias, or blood pressure changes like a healthy heart would. This deficiency affects quality of life, limits device capabilities, and can cause adverse events such as ventricular suction, right heart failure, pump thrombosis, and over- or under-pumping the circulation. Control theory has been applied academically, though not yet clinically, to CF devices to propose modulation of rotational pump speed based on various pump-estimated or sensor-measured feedback parameters. Recent developments of control algorithms for CF VADs aim to achieve a target rotational speed to provide the correct amount of flow [17]. Control schemes have included PID [18, 19, 20, 21], fuzzy logic [22, 23, 24], optimal control [25], sliding mode control [26], and adaptive control [27].

High-level control of a synchronous positive displacement pump like the 2PTP poses unique problems because there are many more variables that can be adjusted. Instead of a single setting (like pulsatile pump rate or CF rpm), the 2PTP has multiple pump variations including asynchronous or synchronous pumping (how much to pump), synchronous phasing within the the cardiac cycle (when to pump), and pump ejection time (how quickly to pump).

High-Level 2PTP Control

The 2PTP produces sinusoidal flow ejections by controlling the piston to follow reference trajectories. Pump aspiration and ejection occur simultaneously (flow into the pump equals flow out of the pump, there is no internal pump compliance). In it's current embodiment, the TORVAD has a stroke volume of 30 ml. The pump has an epicardial ECG lead to detect ventricular depolarization so that the pump ejections can be synchronized to the cardiac cycle. ECG feedback is used to assess heart rate and rhythm, which can be used to set the pump flow rate. The default mode, if the heart rate is within normal ranges and has a regular rhythm, is synchronous counterpulse support where the pump ejects in early diastole, just after the ventricular contraction. If the heart rate falls outside of normal ranges (for example, < 40 or > 140 bpm), if the rhythm is irregular or in ventricular fibrillation then the pump can operate in asynchronous mode at 5 L/min. These are the current settings of the TORVAD, but infinite variation is possible, and these settings could be manually adjusted by doctors, nurses, caregivers, or patients.

1.2.2 Low-Level VAD Control

Continuous flow VADs are three-phase brushless DC motors. Permanent magnets are sealed into the impellers (which are the motor rotors) and stator coils are embedded in the pump housing. Speed control is accomplished with standard back emf techniques. An 'artificial pulse' mode has been introduced, but this consists of periodically cycling the rpm at low frequency to help wash out prosthetic or biologic surfaces such as the aortic valve that may be prone to thrombosis. Higher frequency (heart ejection-like) pulsing has been studied, but it is not yet known how the large gradients in impeller speed affect blood shear levels and pump motion and studies have indicated large increases in power level requirements. One such application has implemented PI control using a reference pulsating flow rate compared to a measured flow rate [28, 29]. Another formulated optimal control based on a mathematical model of the cardiovascular system with the goal of maximizing aortic valve flow and minimizing left stroke work [30]. This capability is restricted by motor rotor inertia, requiring very high power to cycle rotational speeds throughout the duration of a single cardiac cycle. These methods do not apply to the 2PTP, which operates very differently.

Low-Level 2PTP Control

The motion and position of the pistons in the 2PTP are controlled by two independent brushless DC motors via a magnetic coupling. Magnetic position angle sensors with 12-bit resolution (0.088°) are used for feedback of motor position [31]. Currently, the motors are driven to follow piece-wise sinusoidal reference curves using simple proportional-integral (PI) control on the error signal ($e = \theta_{ref} - \theta_m$, where the error ($e$) is calculated from the desired angular position (θ_{ref}) minus the actual position of the motor (θ_m) obtained from the angular magnetic sensor). This method works reasonably well, but is not robust and experiences problems when blood pressure is high or when the pump tries to pump at high flow rates. Problems especially arise when the pistons are moving close together during the transition period. During this time when the pistons transverse the inflow and outflow ports, large impulses can occur as the blood pressure switches from one side of the piston to the other. This poor transition control can lead to the pistons colliding. An example of collision in shown in experimental data displayed in Figure 1.4.

Improving 2PTP control is critical for:

1. Providing precisely timed pulsatile ejections that are important for maximizing the benefits of synchronous flow
2. Preventing collision if the pistons are too close together during transition that could result in damage to the pistons, pump failure, and possibly patient death
3. Preventing shunting and back flow if the pistons are too far apart during transition.
4. Minimizing vibration that could cause patient discomfort.
5. Reducing power, which may be unecessarily high due to poor control.

To improve the low-level control of the pistons, a model of the pump is needed that can be used to estimate and predict the forces on the pistons and motors so that a controller can be designed to minimize the error of the the specified reference curves.

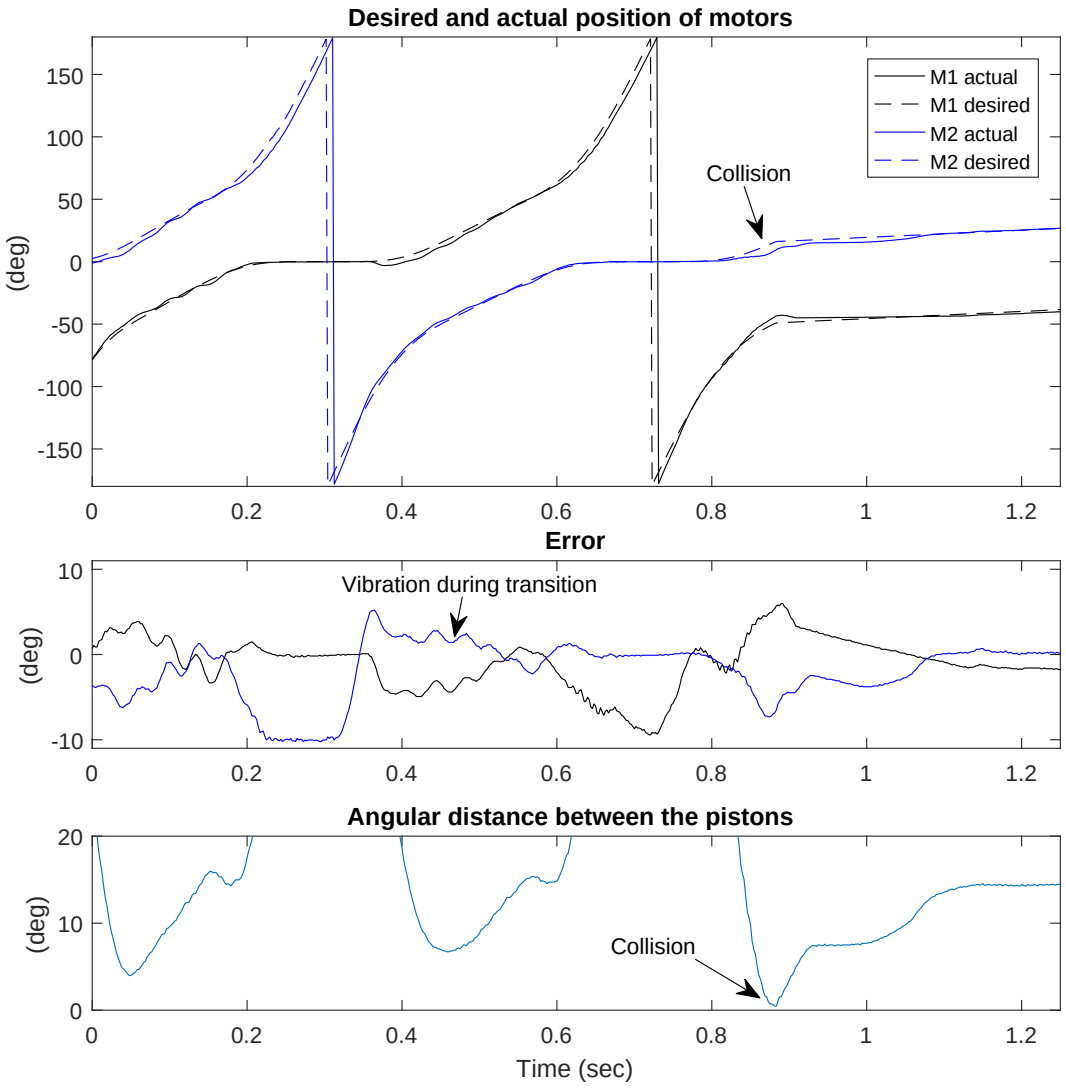

Figure 1.4: Sample position and error data of a 2PTP collision event in a chronic animal experiment. Zero degrees on the position plot (top) corresponds to the 'holding' position (where the A piston is located in Figure 1.2). The pistons rotate from 0 to 180 degrees clockwise, then through an angular convention change, returns to from -180 to 0 degrees clockwise. The collision occurs when the motor at rest (Motor 2) begins to accelerate while the other motor (Motor 1) is decelerating. Also of note is the vibration present during the transition, when both pistons are moving together, which could cause patient discomfort.

1.3 2PTP Hierarchical Control - Research Aims

There is a clinical need for a 2PTP VAD, which has potential advantages over existing CF technologies. But for this pumping modality to be a plausible option, physiologic control must be implemented to provide the proper level of support and the dynamic control of the pistons must be improved to ensure safe and robust operation. Therefore, the proposed research attempts to answer the following questions:

- How does a 2PTP affect cardiovascular hemodynamics, and how should high-level physiological control be designed for safe and beneficial hemodynamic support?
- How should a 2PTP be modeled to understand the pressures and flows with this pump structure, and what is the best way to deal with models of variable structure (when the pistons exchange functional roles during transition)?
- How can the two pistons be controlled to provide desired pump characteristics while minimizing the risk of collision, shunting, and vibration?

To address these questions, four research aims are proposed:

Aim 1 - Develop a cardiovascular system model that captures the Frank-Starling response

A lumped parameter model of the cardiovascular system is developed. This model is used to simulate hemodynamics (blood flow and pressure) for heart failure with support from a CF or 2PTP VAD. Existing lumped parameter models do not appear to capture the Frank-Starling response well, which is sensitivity of cardiac output to changes in ventricular preload (inflow pressure), afterload (outflow pressure or impedance), and heart rate. This response is important to model when designing high-level physiological control. The passive ventricular elastance (the relationship between pressure and volume of the ventricle when filling) contributes significantly to the Frank-Starling response. Different models for passive elastance are studied and a new model is proposed.

This Aim is developed in Part I of this dissertation. Chapter 2 (Cardiac Output Autoregulation) reviews the concepts of blood flow autoregulation by the cardiovascular system. Chapter 3 (Cardiovascular System Modeling) reviews cardiovascular modeling and describes a lumped

parameter model of the cardiovascular system. Chapter 4 (Ventricular Elastance and Ventricular Function Curves) explores how left ventricular elastance affects the relationship between cardiac output and left ventricular preload and proposes a new elastance model for capturing a physiological response.

Aim 2 - Design high-level physiological control for a two-piston toroidal VAD

Positive displacement support with the 2PTP provides unique challenges compared to existing CF technologies. The hemodynamics that result from positive displacement in cooperation with native ventricular contraction must be studied and understood, after which physiologic control algorithms can be designed.

Aim 2 is developed in Part II of this dissertation. Chapter 5 (High-Level 2PTP Control - Pump Function) provides an overview of two-piston toroidal pumping, defines geometric constraints and requirements of the pistons and torus, and defines ideal piston trajectories (velocities and positions) to produce the desired pump ejections. Chapter 6 (High-Level 2PTP Control - Physiological Control) studies physiological control with the synchronous positive displacement pumping modality of the 2PTP and proposes high-level control algorithms. Though not a primary focus of this research, the vibration and forces put on the body from the pump due to 2PTP eccentric pump masses and fluid momentum are explored in Appendix and are modeled using a general solution for a Lagrange subsystem with conservative exogenous efforts that is developed in Appendix .

Aim 3 - Develop a model of a two-piston toroidal pump

This is the first pump of its kind, so a model of a 2PTP is needed to design low-level control. Bond-graph methods are used to develop state equations. The particularly challenging problem is in dealing with the transition period of the pumping stroke, when the pistons exchange roles and the inflow and outflow ports are first partially and then totally occluded.

Aim 3 is developed in Part III of this dissertation. Chapter 7 (2PTP Variable Structure Model) uses lumped parameter and bond graph methods to develop a hybrid 2PTP model that can be used to account for the variable structure of the pump. Chapter 8 (Reduced-

Order Model) linearizes the model so that a simplified form can be used to develop control and estimation.

Aim 4 - Design low-level control to achieve high-level control aims

Low-level control of the pistons is developed. The existing technology uses simple PI control that can result in piston collision, shunts, and vibration. Instead, optimal control (LQR) is developed to improve control. An estimator or observer is designed to estimate unmeasurable pump states and disturbances, particularly the differential pressure across the pump.

Aim 4 is developed in Part IV of this dissertation. Chapter 9 (Low-Level Control) uses the linear model to develop control methods and assess the results using the variable structure hybrid model. Chapter 10 (State Estimation) develops estimation methods for unmeasurable states and disturbances (particularly the differential pressure across the pump). Chapter 11 (Stability and Robustness) studies the stability and robustness of the 2PTP system. Finally, Chapter 12 (Experiments) provides preliminary experimental evidence to support the computational results.

Part I

Cardiovascular System Modeling

Chapter 2. Cardiac Output Autoregulation

This chapter reviews the mechanisms by which the cardiovascular system autoregulates blood flow and introduces the concept of ventricular function curves, which are used to quantify the relationship between cardiac output and preload.

Chapter 3. Cardiovascular System Modeling

This chapter reviews cardiovascular system modeling by lumped parameter methods and develops open- and closed-loop models of the cardiovascular system for assessing hemodynamics with ventricular assist device support.

Chapter 4. Ventricular Elastance and Ventricular Function Curves

This chapter studies the relationship between left ventricular elastance and ventricular function curves and proposes new elastance definitions for generating a more physiologic response to preload.

Chapter 2

Cardiac Output Autoregulation

This chapter reviews the mechanisms by which the cardiovascular system autoregulates blood flow and introduces the concept of ventricular function curves, which are used to quantify the relationship between cardiac output and preload.

For this research, cardiovascular models are used to study and develop high-level physiological control for VADs. Before getting into the details of modeling, the requirements and characteristics of the model should be understood within this research context. Of particular importance as it relates to physiological control is the concept of cardiac output autoregulation. Ventricular assist devices are implanted in an attempt to restore the cardiac output deficit in patients with end-stage congestive heart failure, but VADs should also ideally restore a physiological response to metabolic demand which can vary throughout the day depending on the patient's activity level or physiological status.

2.1 Why is Cardiac Output Regulated?

Blood flow provides the motive force by which nutrients and waste are delivered throughout the body. The degree to which these nutrient and waste transport rates are affected by the rate of blood flow can be quantified by a 'safety factor', which is the delivery rate of the nutrient or waste in the blood divided by the utilization rate of the nutrient or waste [32]. Approximate safety factors for principle nutrients: oxygen (3x), fatty acids (28x), glucose (30x), and amino acids (36x). Approximate safety factors for principle wastes: carbon dioxide (25x) and nitrogenous waste (480x). The oxygen delivery rate is clearly the most sensitive, by an order of magnitude. If blood flow drops to less a third of normal, then cells stop receiving enough oxygen and begin to die. If oxygen demand increases three fold (for example, in light exercise) but blood flow does not increase in turn, then the muscles will quickly fatigue. If oxygen supply is sufficient, then the required transport rate of all of

other nutrients and wastes will be met. Therefore, it follows by reason that cardiac output is primarily regulated by oxygen demand.

Cardiac output varies through the day. For example, during peak exercise when the muscles consume oxygen at rates several times a normal resting level, cardiac output can increase six fold, from 5 to 30 L/min. Then, during deep REM-cycle sleep cardiac output could drop from 5 to 3.5 L/min. Stress and anxiety throughout the day can also alter cardiac output. Even things like body temperature and posture changes can affect cardiac output. Besides normal daily activity, cardiac output is also affected by pathological states like pulmonary disease, hyperthyroidism, pregnancy, or valvular disease.

2.2 How is Cardiac Output Regulated?

Blood is pumped through the body by the heart. The heart is really two different pumps configured in series, also referred to as double circulation (see Figure 2.1). The left ventricle pumps blood to the organs and tissue throughout the body (brain, kidney, liver, skin, and muscles). From the body, blood is returned by veins to the right ventricle, which pumps blood to the lungs. Once oxygenated by the lungs, blood is returned by the pulmonary veins to the left ventricle to begin the cycle again.

The left and right ventricles can be thought of as positive displacement diaphragm pumps. Valves provide unidirectional flow, and ventricular muscle contraction provides the force used to eject blood. The amount of blood ejected depends on four things: the rate of contraction (heart rate), the force of contraction (inotropic state), the amount of filling that occurs before contraction (preload), and the resistive load (afterload resistance or arterial pressure). How these four mechanisms affect cardiac output and how they are regulated by the body are be explored in the following sections. First, to understand the relationship between ventricle dynamics and cardiac output, it is be helpful to understand ventricular pressure-volume loops.

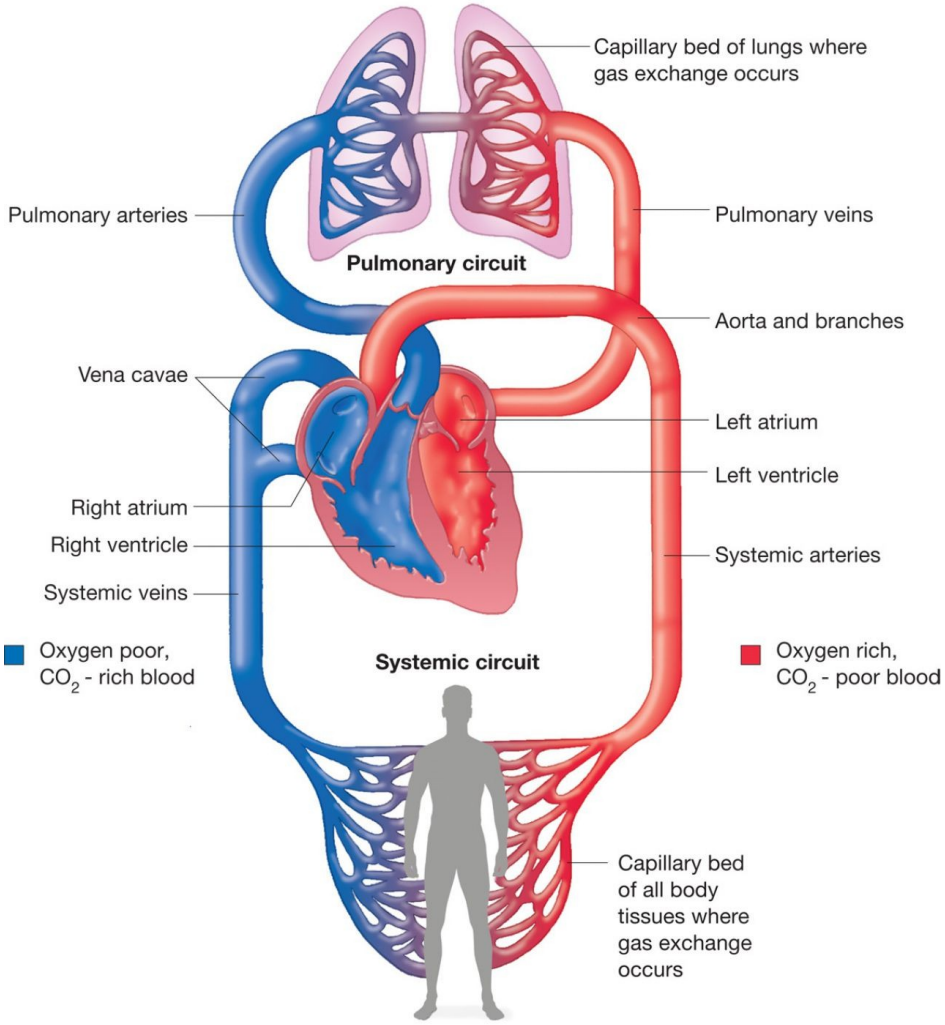

Figure 2.1: Double circulation of the cardiovascular system. The left and right ventricles are pumps in series. The left ventricle pumps blood to the body (the systemic circulation) and the right ventricle pumps blood to the lungs (the pulmonary circualtion).

2.3 Pressure-Volume Loops

Ventricular pressure-volume (PV) loops quantify the relationship between pressure and volume through the cardiac cycle (see Figure 2.2). PV loops have four phases:

a. **Filling**. The ventricle is relaxed in this case. Blood flows from the left atrium into the left ventricle through the inflow mitral valve. The amount of filling that occurs depends on the preload pressure and the passive compliance of the ventricle.
b. **Isovolumetric Contraction**. As the ventricle starts to contract in systole, pressure in the ventricle increases, which closes the inflow mitral valve. The outflow aortic valve also remains closed until the pressure in the ventricle exceeds that in the arteries. When both valves are closed volume is constant (isovolumetric).
c. **Ejection**. When the pressure in the ventricle exceeds that in the arteries, the outflow aortic valve opens and blood is ejected into the systemic circulation. The amount of blood ejected depends on the resistive load.
d. **Isovolumetric Relaxation**. When the ventricle relaxes and the pressure falls below the pressure in the arteries, the aortic valve closes and the pressure drops. During this phase both valves are closed and volume is constant. The inflow mitral valve opens and the filling phase starts when the pressure falls below the left atrial preload pressure.

Pressure-volume loops are constrained on the bottom (when the ventricle is relaxed) by the passive elastance curve, also known as the end-diastolic pressure-volume relationship (EDPVR). And PV loops are constrained on the top (at peak contraction) by the maximum elastance curve, also known as the end-systolic pressure-volume relationship (ESPVR). Ventricular elastance changes from EDPVR to ESPVR during cardiac contraction and then from ESPVR to EDPVR during relaxation. This variable elastance will be described in more detail in following chapters. The stroke volume (SV) of the ventricle can be calculated from the PV loop by the maximum volume (also known as the end-diastolic volume or EDV) minus the minimum volume (also known as the end-systolic volume or ESV). The cardiac output (CO) can be calculated using the stroke volume and heart rate ($\mathrm{CO} = \mathrm{SV} \cdot \mathrm{HR}$). The influence of preload, afterload, HR, and maximum force of contraction on cardiac output starts to become clear when PV loops are analyzed.

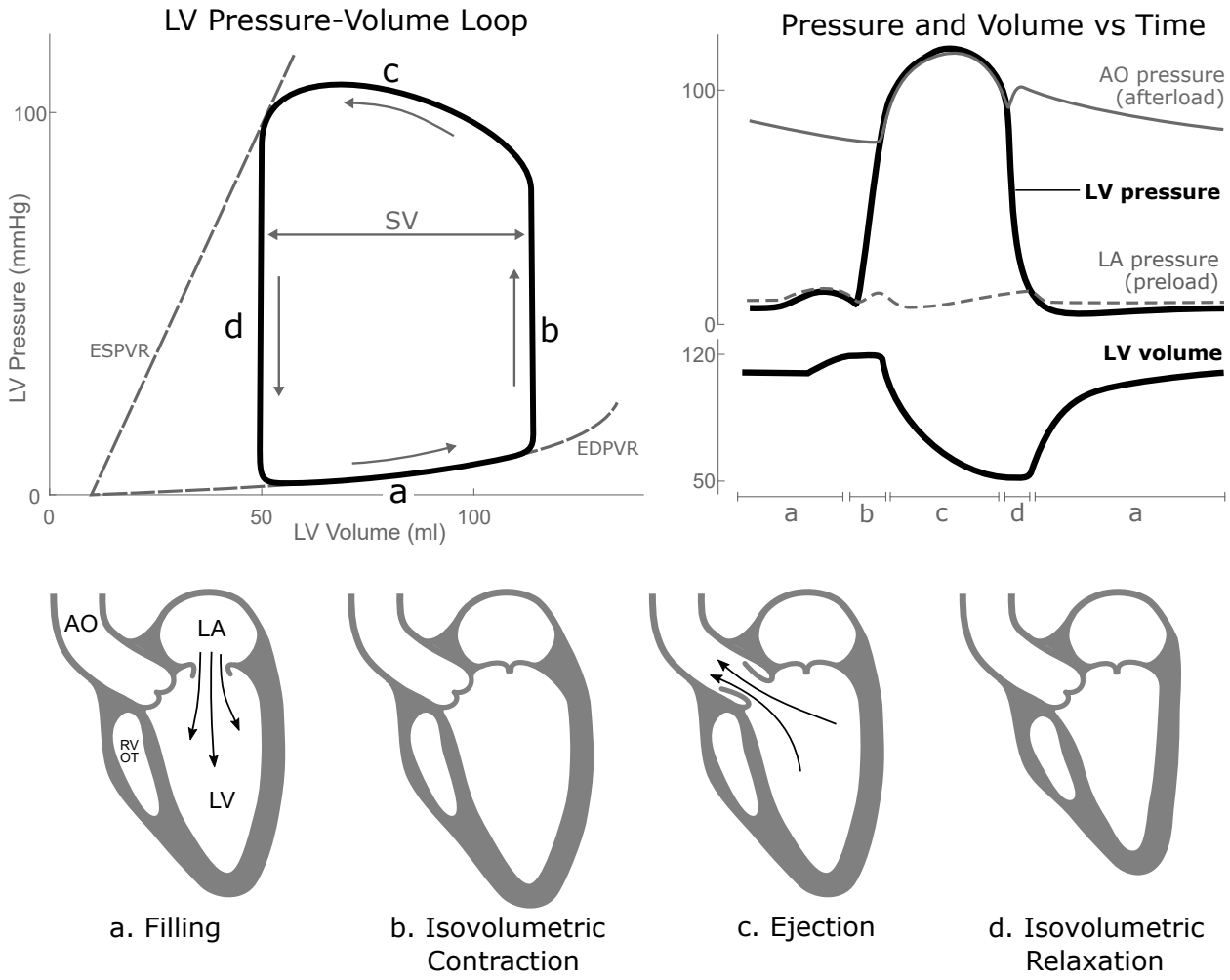

Figure 2.2: Left ventricular (LV) pressure-volume loops (top left) are displayed as well as the pressure and volume plotted as a function of time for a single cardiac cycle (top right). Schematic representations of the LV are also included (bottom) to illustrate the different pumping phases of the heart. During filling (a), blood flows from the left atrium(LA) to the LV through the mitral valve. When the ventricle starts to contract in systole, the mitral valve closes and pressure increases until the aortic valve opens; during this phase the volume is constant so it's called isovolumetric contraction (b). When the aortic valve opens, the ejection phase (c) begins, where blood is ejected from the LV into the aorta (AO) and the systemic circulation. Lastly, the ventricle begins to relax; when the pressure in the LV drops below the pressure in the AO, isovolumetric relaxation (d) occurs until LV pressure drops below LA pressure and the mitral valve opens, which begins the filling phase (a) again.

Legend: LV - left ventricle; LA - left atrium; AO - aorta; RVOT - right venticular outflow tract; ESPVR - end-systolic pressure-volume relationship; EDPVR - end-diastolic pressure-volume relationship; SV - stroke volume.

2.4 Physiological Feedback for Cardiac Output Variation

Cardiac output is regulated by four mechanisms of physiological feedback:

1. **Preload.** Preload is the ventricular inflow pressure from the left atrium. When the ventricle fills during diastole, the volume that the ventricle reaches by the end of diastole is a function of the inflow pressure, which is defined by to the passive elastance curve (EDPVR). This is a nonlinear relationship that increases exponentially at high volumes. The higher the preload, the higher the end-diastolic volume (EDV), which in turn increases the stroke volume of the ventricle. Conversely, if preload decreases, the stroke volume decreases.
2. **Afterload.** Afterload is the load on the ventricle from the arterial system. Afterload can refer to the resistive load or to a constant mean pressure load. Either way, increasing the afterload decreases the stroke volume of the ventricle, and vice versa.
3. **Heart rate.** The heart rate is the number of contractions (or beats) per minute (bpm). An increased heart rate typically leads to increased cardiac output, and vice versa (with the exception of extremely high heart rate or fibrillation, when cardiac output actually drops due to severely decreased filling time). The stroke volume is the amount of volume ejected for one cardiac cycle and can be calculated from the PV loop, then cardiac output can be found by $\mathrm{CO} = \mathrm{SV} \cdot \mathrm{HR}$.
4. **Force of contraction.** If the force of contraction increases, the slope of the maximum elastance curve (ESPVR) increases. If preload and afterload remain constant, then the stroke volume of the PV loop will increase, and vice versa.

These effects are illustrated in Figure 2.3. Numerous physiological stimuli contribute to variation of preload, afterload, heart rate, and the force of contraction, including sympathetic and parasympathetic activity by the autonomic nervous system, fluid volume status, and the local and systemic regulation of resistance from oxygen or shear mediated stimuli, to name only a few. The mechanisms behind such changes fills textbooks and is the subject of continued study, but it is outside the scope of interest for this research. For this research, it is important that the cardiovascular model adequately captures the cardiac output variation of these physiological feedback, not necessarily *why* these stimuli are changed.

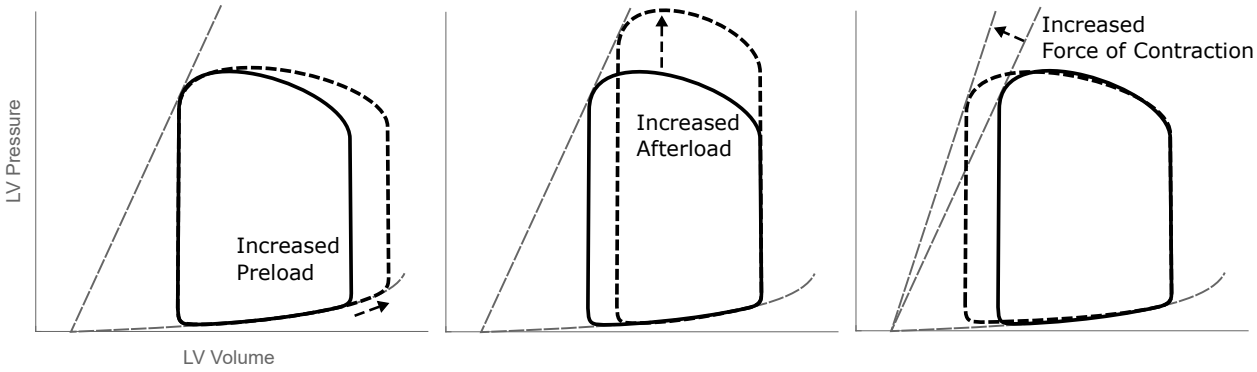

Figure 2.3: Left ventricular pressure-volume loops respond to physiological feedback of preload, afterload, and the force of contraction. These illustrative examples show how increasing the preload increases the stroke volume (left), increasing the afterload decreases the stroke volume (middle), and increases the force of contraction increases the stroke volume (right).

2.5 Ventricular Function Curves

Of the four physiological feedback mechanisms, the cardiac output response to preload is the most commonly understood and quantified in the clinical setting and medical literature. The relationship between cardiac output and preload is also referred to as the Frank-Starling law of the heart, or the Starling response [33]. In Starling's seminal work on ventricular autoregulation in intact hearts [34], he studied the relationship between cardiac output and ventricular preload using excised canine hearts (see Figure 2.4), and produced the first so-called Starling curves that demonstrated a highly nonlinear relationship between ventricular preload and cardiac output.

Starling curves quantify the cardiac output response to changes in *right* ventricular preload pressure, which accounts for the left and right ventricular function as well as the system and pulmonary circulations [32]. Others have isolated the left side from the right with ventricular function curves which express cardiac output as a function of left ventricular preload. For this research, the ventricular function curve approach will be favored, as it isolates the systemic circulation, which minimizes the degrees of freedom in the system and variables that must be defined. This approach also removes the wide variability in pulmonary vascular resistance and right ventricular function in patients with heart failure. It is important to note that these effects are not neglected, rather all possible right-side conditions can be incorporated by adjusting the boundary conditions of the systemic circulation.

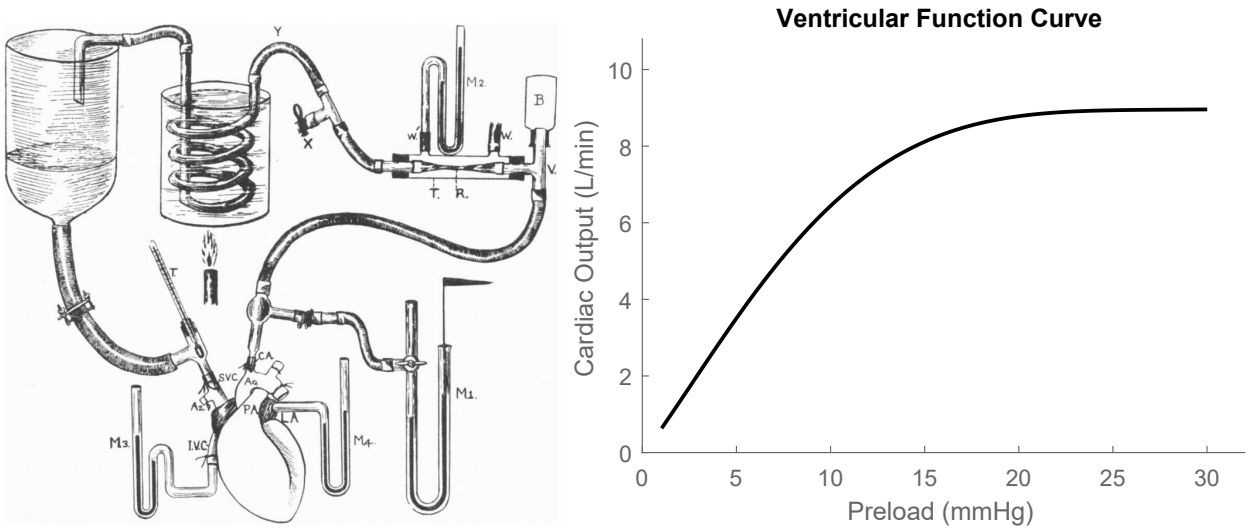

Figure 2.4: Experimental setup used by Starling [34] to study the relationship between cardiac output and preload with excised canine hearts (left). Ventricular function curves (right) illustrate the relationship between cardiac output and ventricular preload. At low preloads, the curve increases nearly linearly, but then becomes curvilinear and eventually plateaus at high preloads.

Ventricular function curves quantify the response of cardiac output to changes in ventricular preload while holding the other feedback mechanisms constant (heart rate, force of contraction, and afterload resistance). In this context, constant afterload can refer either to constant vascular resistance or constant mean arterial pressure. In this research, ventricular function curves are quantified for a constant vascular resistive afterload, following the approach taken by Guyton [32]. To quantify the effects of changing heart rate, force of contraction, and afterload, a family of ventricular functions curves can be generated at different conditions. Figure 2.5 provides examples of the effect of changing these other physiological feedback mechanisms on representative ventricular function curves.

To quantify the ventricular function curve, Salamonsen, et al [35] fit a sixth order polynomial to clinical cardiac output data at various left ventricular preloads [32].

$$Q_{\mathrm{CO}} = Q_{\mathrm{CO,max}} \left(C_1 p^5 + C_2 p^5 + C_3 p^4 + C_4 p^3 + C_5 p^2 + C_6 p + C_7 \right) \tag{2.1}$$

Cardiac output Q_{CO}, is a function of the ventricular preload p (mmHg). The equation is

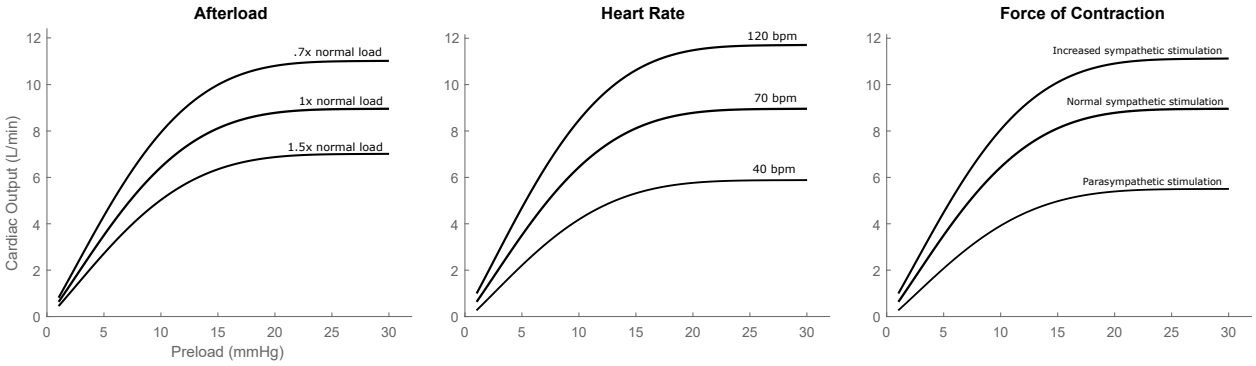

Figure 2.5: Ventricular function curves are plotted for constant afterload, heart rate, and myocardial force of contraction. To see how these autoregulatory feedback mechanisms affect ventricular function curves, a family of curves can be generated.

scaled for a given cardiac output maximum $Q_{\mathrm{CO,max}}$ [35].

$$C_1 = 8.210 \times 10^{-9} \qquad C_5 = 5.083 \times 10^{-3}$$
$$C_2 = -1.005 \times 10^{-6} \qquad C_6 = 8.260 \times 10^{-2}$$
$$C_3 = 4.642 \times 10^{-5} \qquad C_7 = 6.521 \times 10^{-1}$$
$$C_4 = -9.364 \times 10^{-4}$$

This polynomial formulation has excellent agreement with clinical data (r=0.99), but there are numerous coefficients that make it difficult to modify the shape of the curve for different disease states like congestive heart failure. Also, this formulation is invalid at high preloads because the polynomial does not reach an asymptotic value but starts to increase very quickly beyond the range in the plot. Therefore, it would be good to formulate a simpler model with fewer coefficients. To develop a new model, the asymptotic nature of the ventricular function curve can be utilized to formulate a linear-logarithmic function.

$$p = A\left[r\hat{Q}_{\mathrm{CO}} - (1-r)\ln\left(1-\hat{Q}_{\mathrm{CO}}\right)\right] \tag{2.2}$$

where $\hat{Q}_{\mathrm{CO}}$ is the normalized cardiac output, defined by

$$\hat{Q}_{\mathrm{CO}} = \frac{Q_{\mathrm{CO}} - Q_{\mathrm{CO},0}}{Q_{\mathrm{CO,max}} - Q_{\mathrm{CO},0}} \tag{2.3}$$

which is equal to zero at the zero pressure-flow rate $Q_{\mathrm{CO},0}$, and equal to one at the maximum flow $Q_{\mathrm{CO,max}}$. Like above, p is the preload pressure. There are four coefficients, the maximum cardiac output at which the curve asymptotes $\mathrm{CO}_{\mathrm{max}}$, the cardiac output at zero pressure

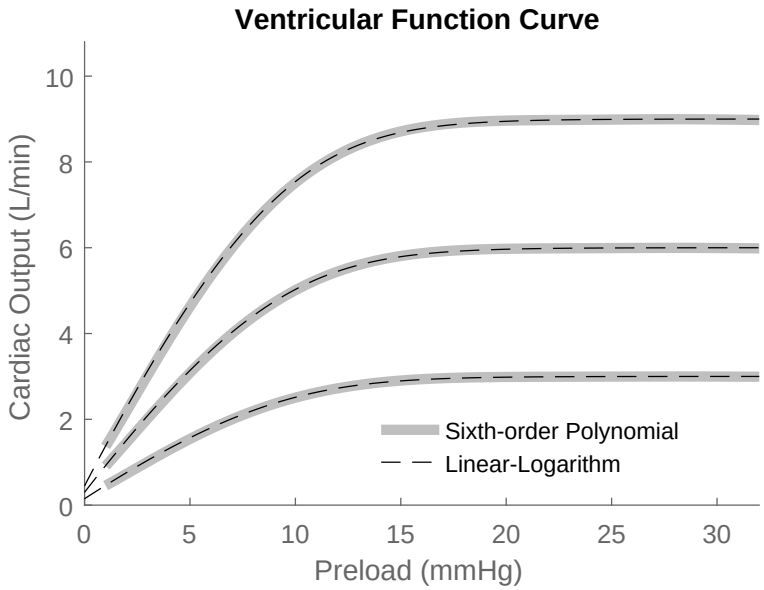

Figure 2.6: Ventricular function curves. Salamonsen, et al [35] fit a sixth order polynomial at three different afterload resistances (thick grey lines). Also shown is the newly proposed linear-logarithmic model (dashed line) that also fits clinical data but has fewer coefficients and asympototes at high preloads.

CO_0, the normalized slope at zero pressure A, and the ratio of the linear component to the logarithmic component r.

By setting $CO_0 = .05 \cdot CO_{max}$, $A = 9$, and $r = 0.7$, excellent agreement between the sixth-order polynomial and linear-logarithmic curves is obtained, as shown in Figure 2.6. To scale the curve for different mean arterial pressures (afterload), the only parameter that need be changed is CO_{max}, the other coefficients (A, r, and the relationship $CO_0 = 0.05 \cdot CO_{max}$) remain the same.

While this may be a representative ventricular function curve based on clinical data, it should go without saying that this curve will vary from patient to patient based on physiological variation (age, sex, weight, etc) and pathological condition (heart failure, valvular disease, pulmonary disease, etc). Instead, what's important to note from this curve is that the curve is nearly linear at low preloads, follows an exponential-like or logarithmic-like shape, and is asymptotic at high preloads.

2.5.1 Ventricular Function Curves in Heart Failure

In heart failure, the ventricle continues to autoregulate cardiac output, but the autoregulation is altered. In congestive heart failure, the ventricle weakens and dilates, which causes ventricular function curves to diminish in magnitude and the plateau inflection to shift toward higher preload pressures. This effect is shown in Figure 2.7.

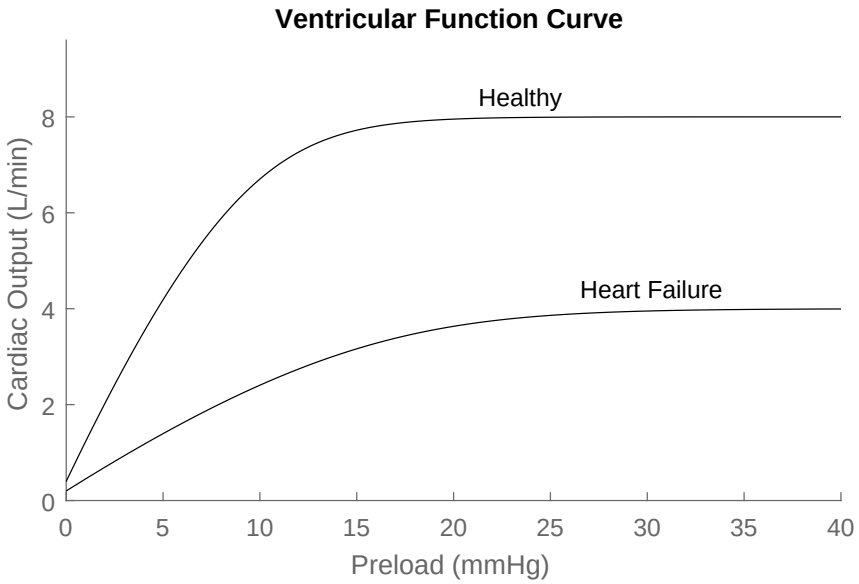

Figure 2.7: Ventricular function curves for healthy and heart failure conditions. In heart failure, the ventricle dilates and weakens, which causes cardiac output to decrease and preload to increase.

2.6 Autoregulation with VADs

Ventricular assist devices (VADs) are implanted in an attempt to recover the cardiac output deficit in patients with end-stage congestive heart failure when pharmaceutical approaches have been exhausted or when donor hearts for transplantation are not available. Currently, almost all implanted VADs are continuous flow (CF) devices, either axial flow pumps like the Abbott HeartMate II (HMII) or centricular flow pumps like the Medtronic HVAD and Abbott HeartMate 3. The flow produced by CF VADs are functions of the differential pressure drop across the pump ($\Delta P = P_{ao} - P_{LV}$) and the rotational speed setting of the device, usually expressed in revolutions per minute (rpm).

Response of CF device flow to changes in preload and afterload has been observed to drastically vary from the natural heart. Salamonsen et al, making a linear approximation within normal operation ranges, estimated that CF devices have half the sensitivity to preload and three times the sensitivity to afterload as compared to a natural heart [35].

It is unknown how a synchronous positive displacement pump like the 2PTP will affect cardiac output autoregulation and to what extent active physiological control might be needed. These questions are explored in this research and are address more directly in Chapter 6.

Chapter 3

Cardiovascular System Modeling

This chapter reviews cardiovascular system modeling by lumped parameter methods and develops open- and closed-loop models of the cardiovascular system for assessing hemodynamics with ventricular assist device support.

Computational modeling of the cardiovascular system is performed on several scales, from lumped parameter models to complex three-dimensional fluid structure interaction simulations. The selection of the model depends on the information one wishes to obtain. For system-wide hemodynamics, lumped parameter models are most commonly used. When spatial information is needed, for example to understand wave propagation in the arterial tree, or to obtain pressure and flow at multiple points in the cardiovascular system, one-dimensional arterial models may be more appropriate. Two dimensional models are sometimes employed to simple geometries such as the flow through a constricted artery or to model valve leaflet motion. Finally, three-dimensional simulations that incorporate fluid structure interaction can capture three dimensional flow effects, for example around the inflow cannula in the left ventricle or outflow graft at the aortic anastomosis.

The purpose of this research is in understanding how mechanical circulatory support alters hemodynamic parameters such as mean arterial and pulse pressure, cardiac output, and left ventricular preload. For this type of analysis, lumped parameter modeling is common [36], and is the approach taken for this research.

3.1 Lumped Parameter Modeling of the Cardiovascular System

Lumped parameter models of the cardiovascular system are routinely used to simulate the hemodynamics with VAD support. Lumped parameter modeling, also referred to as zero-dimensional (0-D) modeling, removes spatial parameters and assumes a constant flow and pressure within a selected volume of interest, for example the ventricles, systemic arteries,

and veins. These models have few terms, which makes parameterization relatively straightforward. Additionally, the models consist of simple ordinary differential equations, so they can be numerically integrated and solved quickly, which allows many different variations in physiological properties or levels of assist to be studied.

For this research, two lumped parameter models of the cardiovascular system are used: an open-loop and a closed-loop model. The open-loop simulations isolates the systemic circulation so that ventricular preload and afterload can be directly prescribed to obtain ventricular function curves. The closed-loop simulation includes the pulmonary circulation and can be used to study test cases, for example increased pulmonary vascular resistance or hypovolemia (low blood volume). Schematics of these models are shown in Figure 3.1.

The lumped parameter models that will be used for this research are not unique, they have been developed and utilized by many other research groups and validated against clinical data. The unique contributions of this research are the improvement of the model of passive left ventricular elastance to better reproduce physiological ventricular function curves and the use of an open-loop cardiovascular model for studying the preload response with different types of VAD support and developing physiological control for the 2PTP.

3.1.1 Open-Loop Cardiovascular Model

The open-loop model considers only the systemic circulation, which is defined to include the pulmonary veins, left atrium and ventricle and their associated valves (mitral and aortic), and the systemic arterial tree consisting of the larger elastic vessels and smaller resistive arterioles and capillaries. The pulmonary circulation is removed for this simulation, not because its function and response are unimportant, but rather to eliminate it as an additional variable so that the entire possible range of right-sided conditions (elevated pulmonary vascular resistance, right heart failure, pulmonary edema, etc.) can be studied by changing the boundary conditions to the open-loop left-sided model. The advantage of this open-loop model is that it enables ventricular function curves to be obtained by varying the prescribed preload pressure while maintaining a constant afterload resistance.

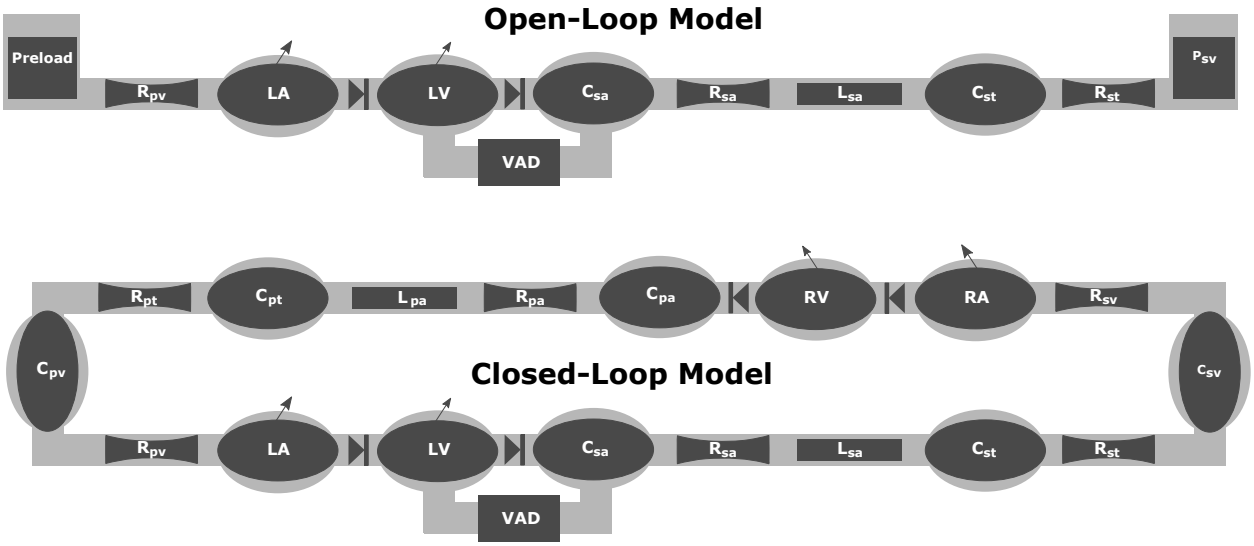

Figure 3.1: Schematic representations of the open-loop and closed-loop lumped parameter cardiovascular system models. The open-loop model directly prescribes the preload and afterload boundary conditions. The closed-loop model is used to study specific conditions such as high pulmonary vascular resistance. The systemic circulation includes left atrium (LA), left ventricular (LV), systemic arteries (sa), systemic arterial tree (st), and systemic veins (sv). The pulmonary circulation includes the right atrium (RA), right ventricle (RV), pulmonary arteries (pa), pulmonary artery tree (pt), and pulmonary vein (pv). The model consists of various compliant (C), resistive (R), and inertial (L) elements.

3.1.2 Closed-Loop Cardiovascular Model

For the closed-loop simulation, the pulmonary circulation is included so that specific conditions like elevated pulmonary vascular resistance (PVR) or hypovolemia can be studied to observe the Starling response with different modalities of VAD support. Elevated PVR is common in VAD patients [37] and can also occur during postural changes or the Valsalva maneuver [38, 39]. Step changes in PVR are commonly used in cardiovascular modeling to test the propensity of ventricular suction with VAD support [40, 41, 42].

3.2 Lumped Parameter Model Equations

To derive the differential equations and parameterize the cardiovascular system, a previously validated lumped parameter model is used as a framework [43, 14].

3.2.1 Systemic Arteries

The systemic arterial tree, which consists of the large arteries, arterioles, and capillaries, is represented with two Windkessel elements: an RLC for the larger systemic arteries (sa) and RC element for the systemic arterial tree (st).

The large systemic arteries have two states, pressure and flow, which are represented with the following ordinary differential equations:

$$\dot{P}_{sa} = \frac{Q_a + Q_{VAD} - Q_{sa}}{C_{sa}} \tag{3.1}$$

$$\dot{Q}_{sa} = \frac{P_{sa} - P_{st} - R_{sa}Q_{sa}}{L_{sa}} \tag{3.2}$$

where P_{sa} is the pressure in the systemic arteries, Q_a is the flow through the aortic valve, Q_{VAD} is the flow through the VAD, Q_{sa} is the flow in the systemic arteries, P_{st} is the pressure in the systemic arterial tree, C_{sa} is the compliance of the systemic arteries, R_{sa} is the viscous resistance to flow in the systemic arteries, and L_{sa} is the fluid inertance in the systemic arteries.

In the systemic arterial tree (st), which represents the flow through the arterioles and capillaries, the flow is not very dynamic, so no inertance term is needed, therefore there is only

one state, the pressure in the systemic arterial tree P_{st}:

$$\dot{P}_{st} = \frac{Q_{sa} - Q_{st}}{C_{st}} \tag{3.3}$$

where C_{st} is the compliance of the systemic arterial tree.

The flow through the systemic arterial tree is a function of the pressure states:

$$Q_{st} = \frac{P_{st} - P_{sv}}{R_{st}} \tag{3.4}$$

where P_{sv} is the pressure in the systemic vein, and R_{st} is the systemic arterial tree viscous resistance.

3.2.1.1 Left Ventricular and Atrial Volume

The volume in the left atrium (V_{la}) and left ventricule (V_{lv}) are modeled using the conservation of mass principle,

$$\dot{V}_{\mathrm{la}} = Q_{\mathrm{pv}} - Q_{\mathrm{m}} \tag{3.5}$$

$$\dot{V}_{\mathrm{lv}} = Q_{\mathrm{m}} - Q_{\mathrm{a}} - Q_{\mathrm{VAD}} \tag{3.6}$$

where Q_m is the flow through the mitral valve and the other flows were defined above.

3.2.1.2 Ventricular and Atrial Pressure

Ventricular contraction is a complex phenomenon. Several different models have been developed, including three-dimensional finite element with fluid-structure interaction [44] and models that incorporate chemical pathways and microscopic models of sarcomere contraction [45]. These models are often computationally intensive, such as the 3D FEM models, or require excessive parameterization, such as the chemical model that requires over 20 parameters such that it is difficult to fit from readily available data. The most common approach for modeling the ventricular contraction, especially when estimating systemic hemodynamics, is by using the lumped parameter approach and assuming the pressure in the ventricle is the same throughout, and by using a time-varying elastance to model the ventricular contraction.

3.2.1.3 Time-Varying Elastance

The most commonly used method of modeling ventricular contraction, first proposed by Suga and Sagawa [46], is the time-varying elastance model. The elastance (the inverse of the compliance) of the ventricle is used to describe the relationship between the lumped pressure and volume in the ventricle

$$E(t) = \frac{P(t)}{V(t) - V_0} \tag{3.7}$$

or written in terms of pressure as a function of volume:

$$P(t) = E(t)(V(t) - V_0) \tag{3.8}$$

where E is the elastance, P is the pressure in the chamber, V is the volume, and V_0 is the unstressed volume (the volume at zero pressure).

To incorporate contraction, the elastance E is defined as a function of time bounded by a minimum elastance during diastolic filling E_{ed} and a maximum at the end of systole E_{es} [47]. Pressure-volume curves defined by these minimum and maximum elastance are known as the end-diastolic pressure (P_{ed}) or end-diastolic pressure-volume relationship (EDPVR) and the end-systolic pressure (P_{es}) or end-systolic pressure-volume relationship (ESPVR). A normalized activation function $e(t)$ is used to describe the dynamic change in elastance during ventricular contraction through the cardiac cycle.

$$P = e(t)E_{es}(V - V_0) + [1 - e(t)]E_{ed}(V - V_0) \tag{3.9}$$

For the ventricles, this can be expressed in terms of the end-systolic and end-diastolic pressure

$$P = e(t)P_{es}(V) + [1 - e(t)]P_{ed}(V) \tag{3.10}$$

The left ventricular end-systolic and end-diastolic pressure-volume relationships (P_{es} and P_{ed}) require special attention because they strongly influence the ventricular function curves, so they are described in detail in the next chapter (Chapter 4).

The left atrial end-diastolic pressure is represented by the exponential function

$$P_{ed,la} = A_{\mathrm{la}} \left(e^{B_{\mathrm{la}}(V_{\mathrm{la}} - V_{\mathrm{la0}})} - 1 \right) \tag{3.11}$$

And the left atrial end-systolic pressure is a linear function of volume

$$P_{es,la} = E_{\mathrm{la}} \left(V_{\mathrm{la}} - V_{\mathrm{la0}} \right) \tag{3.12}$$

The normalized activation for the ventricles (e_v) and atria (e_a) can be described using piecewise sinusoidal functions. The ventricular normalized elastance $e_v(t)$ is defined by the following piecewise function:

$$e_v = \begin{cases} \frac{1}{2} - \frac{1}{2}\cos\left(\frac{3\pi t}{2T_{vc}}\right) & \text{for } 0 \leq t < \frac{2T_{vc}}{3} \\ \frac{1}{2} + \frac{1}{2}\cos\left(\frac{3\pi t}{T_{vc}} - 2\pi\right) & \text{for } \frac{2T_{vc}}{3} \leq t < T_{vc} \\ 0 & \text{for } t > T_{vc} \end{cases} \tag{3.13}$$

where the time (t) is normalized to the cardiac cycle, and where $t = 0$ corresponds to the start of ventricular contraction. The ventricular contraction time T_{vc} changes with heart rate.

$$T_{vc} = \frac{550 - 1.75\mathrm{HR}}{1000} \tag{3.14}$$

The atrium contracts just prior to the ventricle and is defined by the following normalized activation function.

$$e_a = \begin{cases} 0 & \text{for } 0 \leq t < RR - T_a \\ \frac{1}{2} - \frac{1}{2}\cos\left(2\pi\frac{t - RR + T_a}{T_a}\right) & \text{for } RR - T_a \leq t < RR \end{cases} \tag{3.15}$$

where RR is the R-wave-to-R-wave interval. The R-wave is the feature of the electrocardiogram (ECG) that represents the start of ventricular contraction. So RR and heart rate are related ($RR = 60/HR$), where HR is in beats per minute and RR is in seconds.

3.2.1.4 Aortic and Mitral Valve Flow

The mitral valve (m) and aortic valve (a) valves provide unidirectional flow between the left atrium and left ventricle and between the left ventricle and systemic arteries, respectively. A nonlinear diode orifice model is used to describe the flow rate,

$$Q_m = \begin{cases} \sqrt{P_{\mathrm{la}} - P_{\mathrm{lv}}}/R_{\mathrm{v}} & \text{for } P_{\mathrm{la}} \geq P_{\mathrm{lv}} \\ 0 & \text{for } P_{\mathrm{la}} < P_{\mathrm{lv}} \end{cases} \tag{3.16}$$

$$Q_a = \begin{cases} \sqrt{P_{\mathrm{lv}} - P_{\mathrm{sa}}}/R_{\mathrm{v}} & \text{for } P_{\mathrm{lv}} \geq P_{\mathrm{ao}} \\ 0 & \text{for } P_{\mathrm{lv}} < P_{\mathrm{ao}} \end{cases} \tag{3.17}$$

where the pressures have been defined in the previous sections, and R_v is the nonlinear valve orifice resistance.

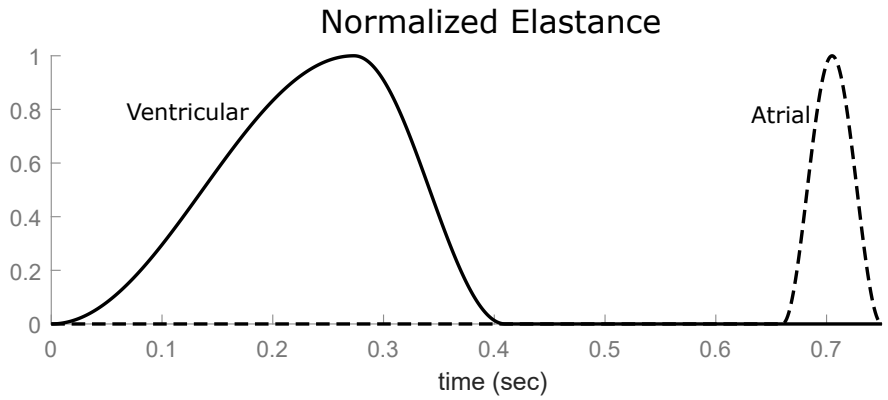

Figure 3.2: Normalized elastance curves for a HR of 80 bpm.

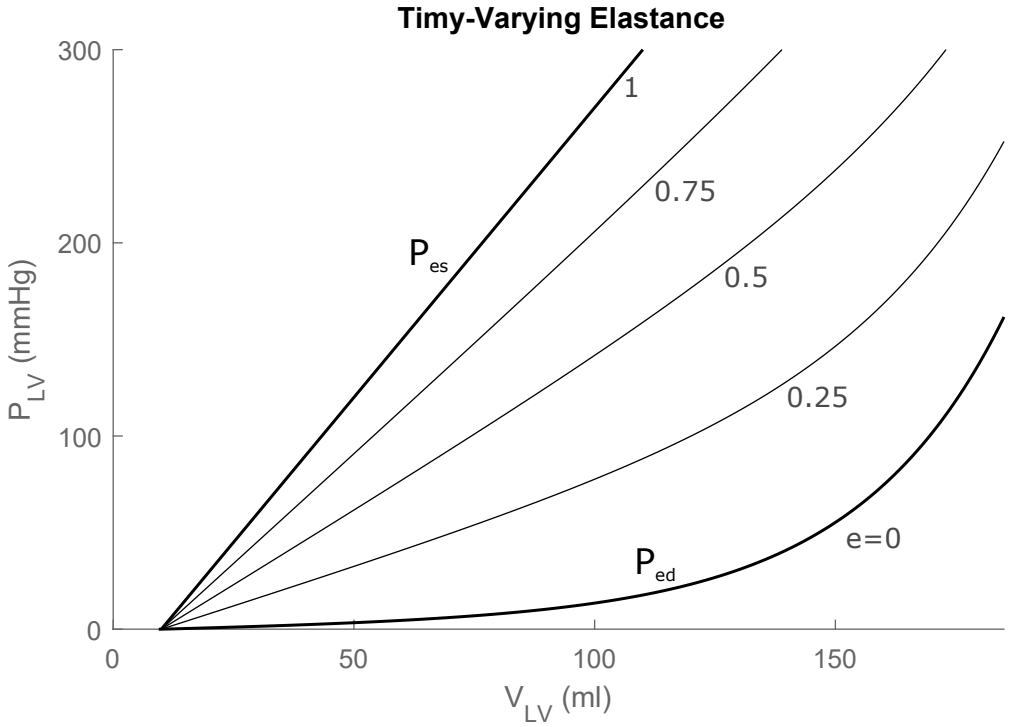

Figure 3.3: Pressure in the left ventricle P_{LV} is a function of the volume V_{LV} described by the end-systolic pressure (P_{es}), end-diastolic pressure (P_{ed}), and the normalized elastance function e. The normalized elastance is zero when the ventricle is relaxed and filling and one during peak contraction. As the ventricle contracts, the normalized index goes from 0 to 1 following the sinusoidal activation function. An exponential end-systolic pressure and linear end-systolic pressure are assumed for this illustration.

3.2.2 Pulmonary Circulation

The pulmonary circulation model is a mirror image of the systemic circulation model. The subscript definitions are: pulmonary arteries (pa), pulmonary artery tree (pt), right atrium (ra), right ventricle (rv), tricuspid valve (t), and pulmonary valve (p).

Flow and pressure in the pulmonary arteries and arterial tree:

$$\dot{P}_{pa} = \frac{Q_p - Q_{pa}}{C_{pa}} \tag{3.18}$$

$$\dot{Q}_{pa} = \frac{P_{pa} - P_{pt} - R_{pa}Q_{pa}}{L_{pa}} \tag{3.19}$$

$$\dot{P}_{pt} = \frac{Q_{pa} - Q_{pt}}{C_{pt}} \tag{3.20}$$

$$Q_{pt} = \frac{P_{pt} - P_{pv}}{R_{pt}} \tag{3.21}$$

Right atrial and ventricular volume:

$$\dot{V}_{\mathrm{ra}} = Q_{\mathrm{sv}} - Q_{\mathrm{t}} \tag{3.22}$$

$$\dot{V}_{\mathrm{rv}} = Q_{\mathrm{t}} - Q_{\mathrm{a}} \tag{3.23}$$

Right atrial and ventricular pressure are the same as the ventricles (though P_{es} and P_{ed} are different for each heart chamber)

$$P = e(t)P_{es}(V) + [1 - e(t)]P_{ed}(V) \tag{3.24}$$

Right atrial and ventricular pressure:

$$P_{ed,ra} = A_{\mathrm{ra}}\left(e^{B_{\mathrm{ra}}(V_{\mathrm{ra}} - V_{\mathrm{ra0}})} - 1\right) \tag{3.25}$$

$$P_{es,ra} = E_{\mathrm{ra}}\left(V_{\mathrm{ra}} - V_{\mathrm{ra0}}\right) \tag{3.26}$$

$$P_{ed,rv} = A_{\mathrm{rv}}\left(e^{B_{\mathrm{rv}}(V_{\mathrm{rv}} - V_{\mathrm{rv0}})} - 1\right) \tag{3.27}$$

$$P_{es,rv} = E_{\mathrm{rv}}\left(V_{\mathrm{rv}} - V_{\mathrm{rv0}}\right) \tag{3.28}$$

Tricuspid and pulmonary valve flow:

$$Q_{tv} = \begin{cases} \sqrt{P_{\mathrm{ra}} - P_{\mathrm{rv}}}/R_{\mathrm{v}} & \text{for } P_{\mathrm{ra}} \geq P_{\mathrm{rv}} \\ 0 & \text{for } P_{\mathrm{ra}} < P_{\mathrm{rv}} \end{cases} \tag{3.29}$$

$$Q_{pv} = \begin{cases} \sqrt{P_{\mathrm{rv}} - P_{\mathrm{pa}}}/R_{\mathrm{v}} & \text{for } P_{\mathrm{rv}} \geq P_{\mathrm{pa}} \\ 0 & \text{for } P_{\mathrm{rv}} < P_{\mathrm{pa}} \end{cases} \tag{3.30}$$

3.2.3 Parameterization

The left ventricular end-systolic and end-diastolic pressures $P_{es,lv}$ and $P_{ed,lv}$ require special treatment and are discussed in the detail in the following chapter (Chapter 4). The other parameters (resistances, compliances, etc) are provided in Table 3.1, and were taken from previously published valves [43].

3.3 Lumped Parameter Model Simulation

The ordinary differential equations (ODEs) that represent the time rate of change of the energy storage elements in the model can be numerically integrated with standard techniques. For this research, Matlab's ODE solvers were used (in this case, `ode23()`). The different simulation conditions that were run are detailed in Chapter 6.

	Parameter	Description	Value	Units
Valve	R_v	Valve resistance	.0025	mmHg/ml
Left atrium	E_{la}	Left atrium elastance	.25	mmHg/ml
	V_{la0}	Unstressed left atrium volume	10	ml
	A_{la}	Left atrium exponential constant	.45	mmHg
	B_{la}	Left atrium exponential constant	.05	1/ml
	T_a	Atrial ejection time	.09	sec
Right atrium	E_{ra}	Right atrium elastance	.25	mmHg/ml
	V_{ra0}	Unstressed right atrium volume	10	ml
	A_{ra}	Right atrium exponential constant	.45	mmHg
	B_{ra}	Right atrium exponential constant	.05	1/ml
	T_a	Atrial ejection time	.09	sec
Right ventricle	E_{rv}	Right ventricular elastance	.75(.45)	mmHg/ml
	V_{rv0}	Unstressed right atrium volume	5	ml
	A_{rv}	Right ventricle exponential constant	.04	mmHg
	B_{rv}	Right ventricle exponential constant	.05	1/ml
Systemic circulation	R_{sa}	Systemic artery resistance	.15	mmHg s/ml
	C_{sa}	Systemic artery compliance	1.25(.65)	ml/mmHg
	L_{sa}	Systemic artery inertance	.0022	mmHg s^2/ml
	R_{st}	Systemic arterial tree resistance	.8(.9)	mmHg s/ml
	C_{st}	Systemic arterial tree compliance	2.0(1.5)	ml/mmHg
	R_{sv}	Systemic venous resistance	.025	mmHg s/ml
	C_{sv}	Systemic venous compliance	20	ml/mmHg
Pulmonary circulation	R_{pa}	Pulmonary artery resistance	.07	mmHg s/ml
	C_{pa}	Pulmonary artery compliance	7.5	ml/mmHg
	L_{pa}	Pulmonary artery inertance	.0018	mmHg s^2/ml
	R_{pt}	Pulmonary arterial tree resistance	.04	mmHg s/ml
	C_{pt}	Pulmonary arterial tree compliance	.5	ml/mmHg
	R_{pv}	Pulmonary venous resistance	.003	mmHg s/ml
	C_{pv}	Pulmonary venous compliance	20	ml/mmHg

Table 3.1: Cardiovascular model parameters in a healthy state and in heart failure. Heart failure values are designated by parenthesis.

Chapter 4

Ventricular Elastance and Ventricular Function Curves

This chapter studies the relationship between left ventricular elastance and ventricular function curves and proposes new elastance definitions for generating a more physiologic response to preload.

The previous chapter described a lumped parameter model for the cardiovascular system, but provided limited details about left ventricular elastance. The first goal of this research is to develop a model of the cardiovascular system for studying the sensitivity of the left ventricular output to changes in preload and afterload in the presence of different types of ventricular assistance. Therefore, a model of left ventricular dynamics must be developed that captures the Starling response of the system to changes in preload and afterload. Of particular interest is assessing how the shape of the passive elastance curve (the end-diastolic pressure-volume relationship, or EDPVR) affects the cardiac output response over a wide range of preload and afterload conditions. Ventricular elastance and ventricular function curves are closely related, so in order to develop a cardiovascular system model that can be used to study physiological control, it's important that the system reproduced a physiological response to autoregulatory feedback.

4.1 EDPVR Models

The end-diastolic pressure-volume relationship (EDPVR) describes the passive filling phase of the ventricle when the muscle is not contracting. The relationship is highly nonlinear. At low volumes the ventricle is very compliant (high compliance / low elastance), but stiffens (low compliance / high elastance) as ventricular volume increases. This nonlinear relationship has been quantified using several curve fits including exponential, logarithmic, cubic, and power [48].

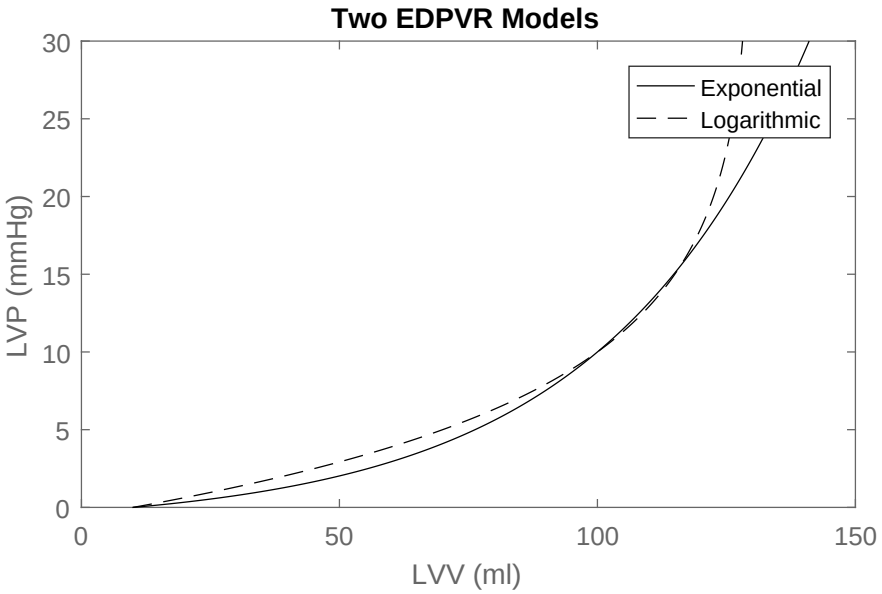

Figure 4.1: The end-diastolic pressure-volume relationship (EDPVR) is commonly modeled using an exponential curve fit or logarithmic curve fit.

4.1.1 Existing EDPVR Models - Exponential and Logarithmic

While several curve fits have been proposed, the exponential and logarithmic models of EDPVR are by far the most common approaches.

4.1.1.1 Exponential EDPVR

Most lumped parameter models of the cardiovascular system in the literature [49], including one by this author [43, 14], have used an exponential relationship to describe the filling of the passive ventricle.

$$P = \beta \left[e^{\alpha(V - V_0)} - 1 \right] \tag{4.1}$$

where β and α are exponential coefficients derived from end-diastolic pressure-volume curves from clinical or animal experiment data. This equation could also be written in the following form:

$$P = \frac{S_0}{\alpha} \left[e^{\alpha(V - V_0)} - 1 \right] \tag{4.2}$$

where S_0 is the stiffness at the unstressed volume V_0, which can be seen by evaluating the derivative at V_0

$$\left.\frac{\partial P}{\partial V}\right|_{V=V_0} = S_0 \tag{4.3}$$

These curves have been shown to represent the nonlinear aspect of filling relatively well, accounting for increased stiffness at higher filling volumes. These exponential relationships have often been determined using *ex vivo* hearts (hearts that have been explanted). This takes the heart out of its environment and removes the external constraints of the pericardium (a fiberous sac that encapsulates and protects the heart) as well as other surrounding muscle, tissue, bone, and organs. One downside of this model is the non-physiologic characteristic of increasing volume with increased pressure, when it has been shown that the ventricle reaches a practical working volume limit. Additionally, the model coefficients (β and α in the standard approach) are extremely sensitive to regression fitting analysis, so that coefficients with several orders of magnitude difference have been derived in the literature. Ideally, a model would use more intuitive and easily derived coefficients, as we shall see other models have tried to do.

4.1.1.2 Logarithmic EDPVR

Logarithmic models have also been proposed [50, 51, 52, 53, 54, 55], but have been rarely if ever used for VAD lumped parameter modeling research. The proposed model takes the following form:

$$P = -k \ln\left(\frac{V_m - V}{V_m - V_0}\right) \tag{4.4}$$

where k is a constant, V_0 is the unstressed volume, and V_m is the maximum volume of the ventricle, set by the pericardium and cardiac cytoskeleton [56, 57, 57]. In this form, the constant k doesn't directly relate to any property of the elastance. One potential way to modify the equation would be to solve for the initial stiffness (S_0) by taking the derivative of the logarithmic model at the unstressed volume V_0

$$S_0 = \left.\frac{\partial P}{\partial V}\right|_{V=V_0} = -\frac{k}{V_0 - V_m} \tag{4.5}$$

Therefore, the equation could also be rewritten in the form:

$$P = S_0 \left(V_0 - V_m\right) \ln\left(\frac{V_m - V}{V_m - V_0}\right) \tag{4.6}$$

This logarithmic function is asymptotic at the maximum volume V_m even if pressure continues to rise, which may be a better approximation than the exponential model which expands indefinitely.

4.1.2 Modified EDPVR Models - Exponential and Logarithmic

The existing models above each have two parameters that can be used to adjust the shape of the curve. We will see later that if we want to assign an operating point through which the curve must pass (V_n, P_c), then only one of the parameters can be adjusted. Either the initial stiffness S_0 or the exponential coefficient *alpha* in the case of the exponential model, and either the initial stiffness S_0 or the maximum volume V_m in the logarithmic model, but not both. It could be helpful to add one more degree of freedom, so that both terms can be directly adjusted. The following sections propose modified exponential and logarithmic models to add an extra degree of freedom by adding a linear term to the equation. This follows similar approaches taken by a few research groups [58, 59].

4.1.2.1 Modified Exponential EDPVR Model

The exponential model above typically has a very shallow slope at lower volumes and underestimates the elastance [60]. By recognizing the near-linear portion of the ventricular elastance curve at low preloads, a linear term could be added to control the stiffness at low volumes.

$$P = S_0 \left[r\left(V - V_0\right) + \left(1 - r\right) \frac{e^{\alpha(V - V_0)} - 1}{\alpha}\right] \tag{4.7}$$

where S_0 is the stiffness at the unstressed volume, which can be seen by by evaluating the derivative at V_0.

$$\left.\frac{\partial P_{ed}}{\partial V}\right|_{V=V_0} = S_0 \tag{4.8}$$

The is a proportional term r adjusts the proportion of the linear to exponential contributions. Notice that when $r = 0$ the model would be the same as the exponential model and when $r = 1$ the model would be a simple linear model.

4.1.2.2 Modified Logarithmic EDPVR Model

Besides serving as a source of comparison for the computational model against clinical data, the linear-logarithmic approximation of the ventricular function curve discussed in Chapter 2 suggests that the EDPVR curve may be best represented with a linear-logarithmic curve. This, in some ways, is working backwards. By taking the results of clinical derived ventricular function curves and working backward to infer the shape of the passive ventricular pressure relationship.

Here, a new model is proposed by making use of the linear-logarithmic relationship of the ventricular function curve. This model utilizes the physiological consideration of maximum ventricular volume that the logarithmic model provides with a linear term to modify the stiffness during filling.

It was shown above that a linear-logarithmic relationship can be used to represent preload as a function of cardiac output. Preload, which can be approximated as the end-diastolic pressure, determines the end-diastolic volume according to the P_{ed} relationship. This volumetric preload, in combination with a fixed afterload, would define the stroke volume of the ejection, and thus the cardiac output. Therefore, in a time-varying elastance model, the shape of the P_{ed} curve directly affects the cardiac output of the ventricle. Therefore, a linear-logarithmic relationship between preload and cardiac output would imply a linear-logarithmic relationship for the EDPVR curve, taking the same form as equation (2.2):

$$P = S_0 \left[r\left(V - V_0\right) + \left(1 - r\right)\left(V_0 - V_m\right) \ln\left(\frac{V_m - V}{V_m - V_0}\right) \right] \tag{4.9}$$

where S_0 is the initial stiffness, or slope at V_0, and r is a proportional term that adjusts the proportion of the linear to logarithmic contributions. Notice that when $r = 0$ the model would be the same as the logarithmic model and when $r = 1$ the model would be a simple linear model.

4.2 Parameterization of EDPVR Model Coefficients

The different models of EDPVR have various parameters that need to be defined. The exponential and logarithmic forms each have two model parameters, and the modified models have an extra degree of freedom.

Model	Equation	Parameters
Exponential	$\frac{S_0}{\alpha}\left[e^{\alpha(V-V_0)}-1\right]$	$S_0,\ \alpha$
Logarithmic	$S_0\left(V_0-V_m\right)\ln\left(\frac{V_m-V}{V_m-V_0}\right)$	$S_0,\ V_m$
Modified Exponential	$S_0\left[r\left(V-V_0\right)+\left(1-r\right)\frac{e^{\alpha(V-V_0)}-1}{\alpha}\right]$	$S_0,\ \alpha,\ r$
Modified Logarithmic	$S_0\left[r\left(V-V_0\right)+\left(1-r\right)\left(V_0-V_m\right)\ln\left(\frac{V_m-V}{V_m-V_0}\right)\right]$	$S_0,\ V_m,\ r$

Each model has coefficients that must be determined. To compare the models, a constraint can be added by defining a nominal operating point with ventricular pressure P_n and volume V_n through which each of the curves pass. This point should provide a common cardiac output for a given preload pressure P_n for all of the curves and allow a means of comparison. This nominal operating point would correspond to the end-diastolic pressure and end-diastolic volume which are two commonly assessed hemodynamic metrics.

4.2.1 Exponential EDPVR Coefficients

The exponential model has two parameters (S_0 and α). To determine the relationship between the them, the nominal operating point ($P_n,\ V_n$) is used:

$$P_n = \frac{S_0}{\alpha}\left[e^{\alpha(V_n-V_0)}-1\right] \tag{4.10}$$

Then, S_0 can be expressed in terms of α and the nominal operating point (P_n, V_n)

$$S_0 = \frac{P_n\alpha}{e^{\alpha(V_n-V_0)}-1} \tag{4.11}$$

There is one degree of freedom, α must be specified in addition to the operating point.

Alternatively, S_0 could be specified. In this case, there is no straightforward analytical solution to determine α, but it could be determined numerically.

4.2.2 Logarithmic EDPVR Coefficients

The logarithmic model also has two parameters (S and V_m), which can be related through with the operating point ($P_n,\ V_n$):

$$P_n = S_0 \left(V_0 - V_m\right) \ln\left(\frac{V_m - V_n}{V_m - V_0}\right) \tag{4.12}$$

Then, S_0 can be expressed in terms of V_m and the operating point ($P_n,\ V_n$)

$$S_0 = \frac{P_n}{\left(V_0 - V_m\right) \ln\left(\frac{V_m - V_n}{V_m - V_0}\right)} \tag{4.13}$$

Again, there is one degree of freedom, and the maximum volume V_m must be defined in addition to the operating point.

Alternatively, S_0 could be specified. In this case, there is no straightforward analytical solution to determine V_m, but it could be determined numerically.

4.2.3 Modified Exponential EDPVR Coefficients

The modified exponential model has three parameters (S_0, α, and r), which can be related through the operating point ($P_n,\ V_n$):

$$P_n = S_0 \left[r \left(V_n - V_0\right) + \left(1 - r\right) \frac{e^{\alpha(V_n - V_0)} - 1}{\alpha}\right] \tag{4.14}$$

In this case, there are two degrees of freedom, and two variables must be defined in addition to the nominal operating point. One possibility is to set α as was done in the exponential model above. But then, instead of the stiffness at the the unstressed volume S_0 begin determined, it could be set, and then r can be determined using the nominal operating point (P_n, V_n).

$$r = \frac{\frac{P_n \alpha}{S_0} - \left(e^{\alpha(V_n - V_0)} - 1\right)}{\alpha \left(V_n - V_0\right) - \left(e^{\alpha(V_n - V_0)} - 1\right)} \tag{4.15}$$

4.2.4 Modified Logarithmic EDPVR Coefficients

Like the modified exponential model, the modified logarithmic model has three parameters (S_0, V_m, and r), which can be related through with the operating point ($P_n,\ V_n$). This

allows for S_0 to be defined in addition to V_m. Then r can be determined using the nominal operating point.

$$P_n = S_0 \left[r\left(V_n - V_0\right) + \left(1 - r\right)\left(V_0 - V_m\right) \ln\left(\frac{V_m - V_n}{V_m - V_0}\right) \right] \tag{4.16}$$

Solving for r

$$r = \frac{\frac{P_n}{S_0} - \left(V_0 - V_m\right) \ln\left(\frac{V_m - V_n}{V_m - V_0}\right)}{\left(V_n - V_0\right) - \left(V_0 - V_m\right) \ln\left(\frac{V_m - V_n}{V_m - V_0}\right)} \tag{4.17}$$

4.2.5 Parameterization - Healthy and HF Operating Point

To continue to parameterize the curves, clinical values and values used in other computational models are used. Two general states will be assessed, normal healthy conditions, and end-stage heart failure. The parameters that must be chosen for the models as described are the operating or nominal end-diastolic volume and pressure, this is a common clinical measurement to assess ventricular status and will be used as the coincident operating point (V_n and P_n) for all four EDPVR models. For the healthy condition the operating point is chosen to be $V_n = 100$ ml at $P_n = 10$ mmHg. For heart failure, the operating point is chosen to be $V_n = 250$ ml at $P_n = 25$ mmHg. Both conditions use 10 ml as the unstressed volume V_0. Examples of different curves fOor the four models in the healthy condition are shown in Figure 4.2.

4.2.6 Ventricular Function Curves

The four different EDPVR models with parameters above, are used with the open-loop lumped parameter model cardiovascular model presented in Chapter 3. Preload is varied from 1 to 35 mmHg and systemic vascular resistance (SVR) is held constant. Ventricular function curves (cardiac output vs preload at constant afterload resistance) are obtained and compared to the clinical ventricular function curve defined in Chapter 2. Results are shown in Figure 4.3. The modified exponential and modified logarithmic EDPVR functions do a better job of recreating clinical ventricular function curves than the normal exponential and logarithmic functions. This is due to the inclusion of the extra degree of freedom that allows

the slope at the unstressed volume to be controlled (which effectively controls the slope of the ventricular function curve at low preloads).

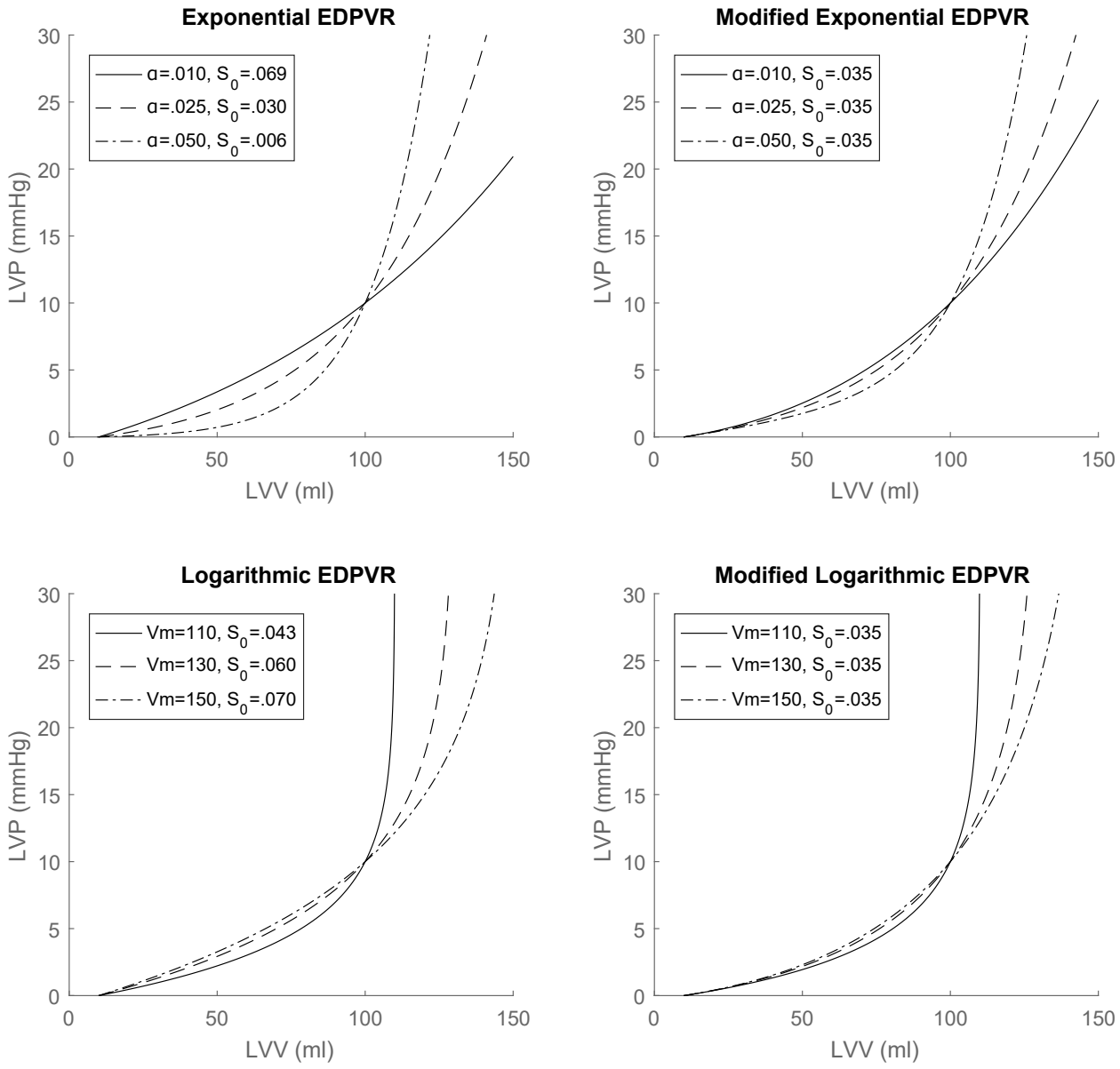

Figure 4.2: Four models of the end-diastolic pressure-volume relationship (EDPVR). LVP is left ventricular pressure and LVV is left ventricular volume. The exponential and logarithmic models on the left are represented and used often in the literature. The modified curves on the right allow for the stiffness at the unstressed volume (volume at zero pressure) to be controlled. All curves share a nominal operating point of 10 mmHg LVP and 100 ml. The exponential and modified exponential curves are plotted for three values of the exponential coefficient α (.010, .025, and .050 mmHg/ml). For the exponential model, the stiffness at the unstressed volume S_0 is determined by the operating point, but is able to be controlled in the modified exponential model, where it is set to .035 mmHg/ml. Similarly, the logarithmic and modified logarithmic models are shown for three values of maximum volume V_m (110, 130, and 150 ml). For the logarithmic model, the stiffness S_0 is determined by the operating point, but is able to be controlled in the modified logarithmic model, where it is set to .035 mmHg/ml.

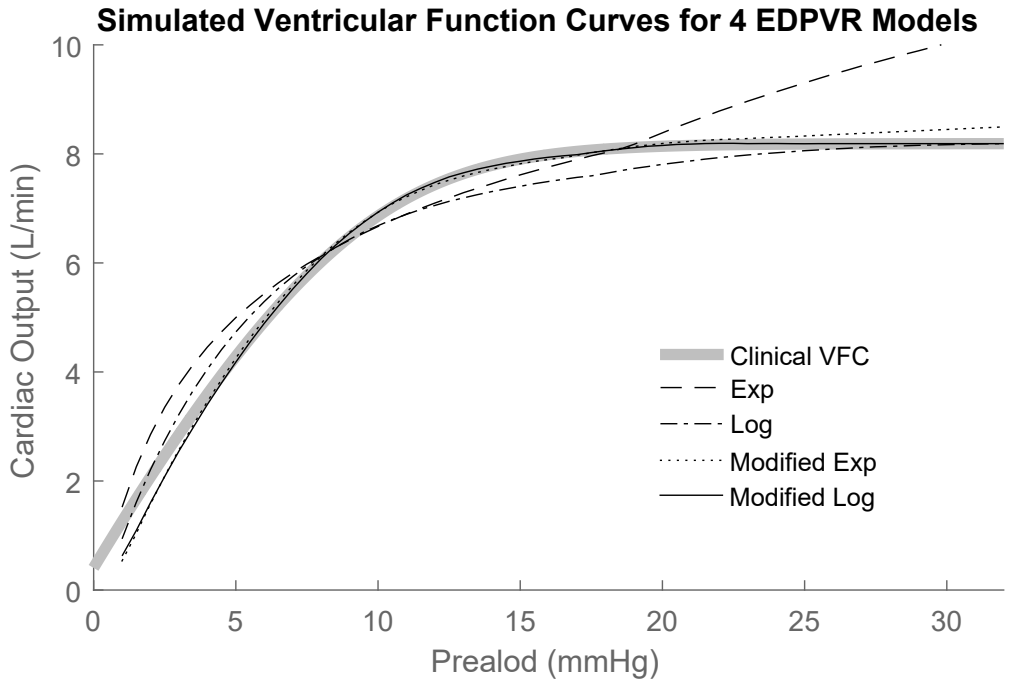

Figure 4.3: Simulated ventricular function curves. Cardiac output vs preload at constant afterload for the four different models of EDPVR. Excellent agreement between clinical data is obtained for the modified exponential and modified logarithmic models. As expected, the exponential model over predicts cardiac output at higher ventricular preloads, and the exponential and logarithmic have a higher slope at lower preloads than the clinical data suggests should be the case.

4.3 Summary and Conclusion

Modified exponential and logarithmic EDPVR curves have been proposed that have an additional degree of freedom to allow the slope at the unstressed volume to be adjusted. These curves have been shown to reproduce more physiologic ventricular function curves compared to the commonly used original exponential and logarithmic functions in lumped parameter simulations of the cardiovascular system. Physiological reproduction of ventricular function curves is important when assessing preload sensitivity with VAD support, especially at low preload values, when the slope of the elastance curve near the unstressed volume has a dominant effect on the cardiac output. Future research could focus on parameterizing these models with clinical pressure-volume data.

Part II

High-level Control

Chapter 5. High-Level 2PTP Control - Pump Function

This chapter provides an introduction to rotary piston pumps, identifies the constraints on the piston and torus geometry in a 2PTP, and develops ideal piston trajectory curves (velocity and position) to produce pulsatile pump ejections.

Chapter 6. High-Level 2PTP Control - Physiological Control

This chapter studies physiological control with the synchronous positive displacement pumping compared to continuous flow support by assessing preload sensitivity with ventricular function curves.

Chapter 5

High-Level 2PTP Control - Pump Function

This chapter provides an introduction to rotary piston pumps, identifies the constraints on the piston and torus geometry in a 2PTP, and develops ideal piston trajectory curves (velocity and position) to produce pulsatile pump ejections.

5.1 Rotary Piston Pump Introduction

This research focuses on a new pumping modality, a two-piston toroidal pump, which is a subset of the class of rotary piston pumps. Most rotary piston pumps that have been developed use a single rotating piston [11]. The most common example of this principle is the Wankel engine. Early prototypes of rotary piston blood pumps experienced thrombus issues in the axial gap between the rotor and pump housing and had seals which limited durability, caused blood clots to form, or required irrigation.

An alternative design has been developed that uses two independently controlled pistons within a toroidal pumping chamber, a two-piston toroidal pump (2PTP). This concept for a blood pump was originally patented by Dr. Alan Ulert [12], and original prototypes of the design were developed as part of Tom Pate's Master's thesis (under the supervision of Dr. Raul Longoria) in the Mechanical Engineering department at the University of Texas at Austin in 2005 [13]. It appears that this is the first realization of such a pump, although there is a patent by Newcomb from 1919 [61] that appears to be the first mention of this type of pumping mechanism (see Figure 5.1), but it does not appear that this pump was ever fabricated. Wankel also mentioned what he called a "stationary outer and inner chamber walls central-axis single-rotatating piston-machine" that takes a similar form in his book "Rotary Piston Machines" [62]. Additionally, there are some rotary piston engines share a similar architecture (see Figure 5.2). But again, the patent by Ulert and initial prototypes by Longoria and Pate appear to be the first realization of a two-piston toroidal pump. This

technology was subsequently transferred to Windmill Cardiovascular Systems (Austin, TX) for continued development, where the pump has been refined for clinical use and called the TORVAD (TORoidal Ventricular Assist Device). Preliminary feasibility testing for the TORVAD has been completed including 60-day animal experiment that has established this device as a potential improvement over existing CF technology, but significant challenges remain, particularity as it relates to the control of this new pumping modality.

5.1.1 Two-Piston Toroidal Pump (2PTP)

The 2PTP uses two independently controlled pistons to produce pulsatile ejections [14] (see Figure 1.2). Each piston is magnetically coupled to a position-controlled brushless DC motor that resides within the inner diameter of the toroidal pumping chamber. The pistons are suspended in the middle of the torus lumen with small ceramic microhydrodynamics bearings that serve to reduce wear and to control the gap between the piston and torus walls to minimize shear stress to the blood. The current version embodied in the TORVAD has a 30 ml stroke volume, but the device stroke volume could be scaled to adapt to different patient sizes and needs. The pump can synchronize to the cardiac cycle or can be run at a fixed flow rate up to 8 L/min.

The pistons of the two-piston toroidal pump (2PTP) are independently controlled to produce positive displacement pump ejections. One purpose of high-level control is to prescribe piston motions or trajectories to achieve a desired pump function. Two-piston toroidal pumping has two distinct phases: pumping (when fluid is simultaneously aspirated from the inflow and ejected to the outflow) and transition (when the pistons exchange functional roles in preparation for the next pumping stroke). These are demonstrated schematically in Figure 5.4.

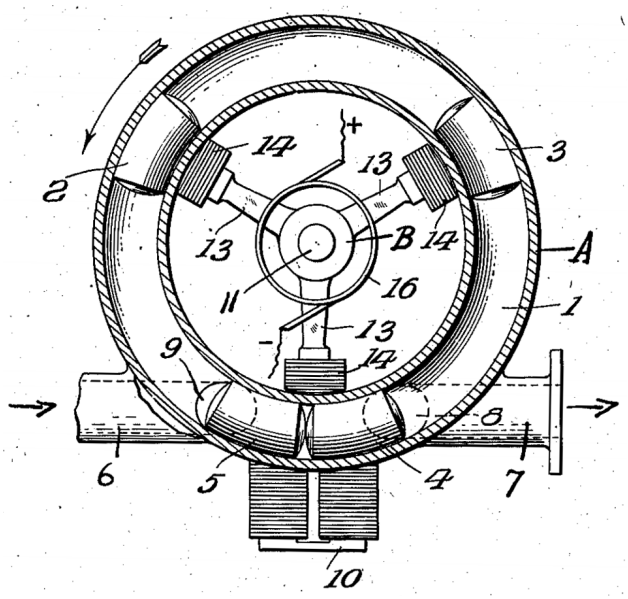

Figure 5.1: A figure from R.E. Newcomb's Fluid Pump patent 1,307,210 (1919)[61], with the following description:

The pump comprises a pump casing A having a chamber 1 which is in the form of a substantially circular or endless orbit in which a plurality of pistons 2, 3, 4, and 5 move by means to be hereinafter described. The pump chamber 1 has an inlet pipe 6 and an outlet pipe 7, the interiors of which communicate with the chamber 1, through ports 8 and 9. Rotating concentrically with the orbit of moment of the pistons is a rotor B driven by any suitable prime mover and carried on a shaft 11 journaled in bearings 12. The rotor B is provided with arms 13 carrying at their outer ends the magnets 14 energized by current supplied thereto by slip rings 15 and 16 from any extraneous source. Between the inlet and outlet ports 8 and 9, respectively, is a stationary magnet 10 which acts to momentarily retard the movement of each piston during passage between the two ports and until the adjacent preceding piston has advanced sufficiently to create a vacuum between the two pistons as, for instance, in the drawing, the piston 4 has been retarded while the piston 3 is now moving at its usual rate away from the inlet port 8; thus a vacuum is created between the two pistons 3 and 4 which draws the fluid in through the inlet port 8 and, at the same time, the piston 5 moving at its usual rate has displaced through the outlet port 9 that bulk of fluid which has been previously drawn in between pistons 4 and 5, and as the piston 2 continues it engages the piston 5 and thus forces the piston 5 out of range of the influence of the stationary magnet and itself becomes retarded thus repeating the cycle of operations and, in this way, substantially continuous streams of fluid are drawn into and discharged from the casing.

Figure 5.2: A cover from the January 1967 issue of Popular Science[63]

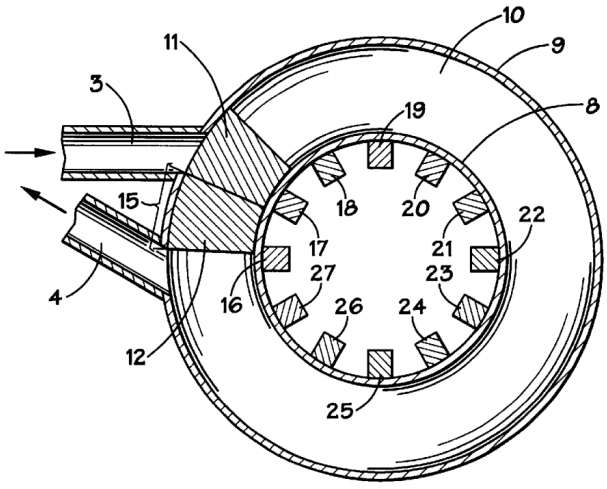

Figure 5.3: A figure from I.A. Ulert's Circular Artificial Heart patent 6,576,010 (2003) [12]

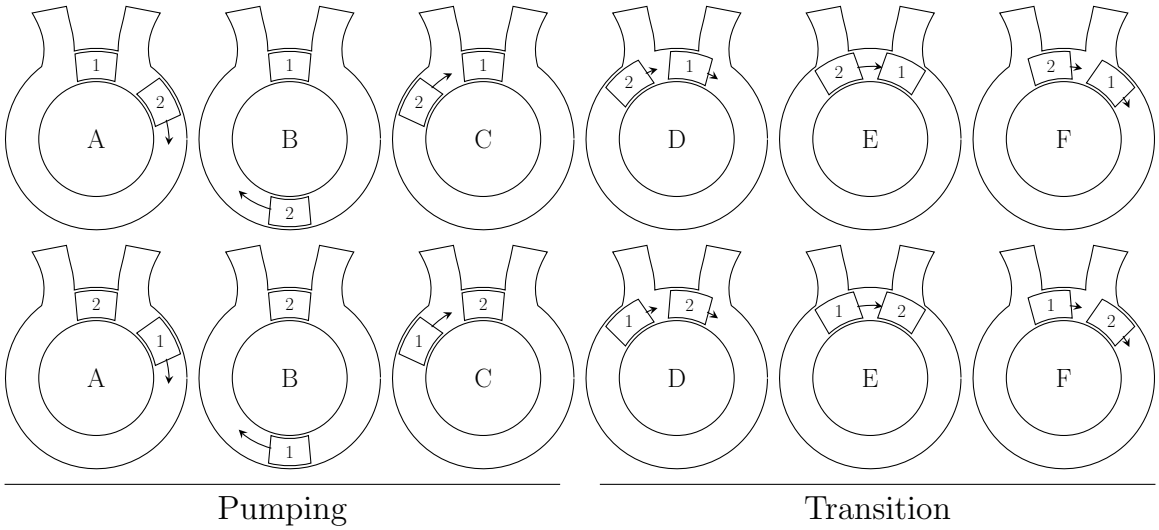

Figure 5.4: Schematics representations of two-piston toroidal pumping. There are two distinct phases - pumping (A-C) and transition (D-F). During pumping, one piston remains stationary in the region between the inflow and outflow ports (referred to as the 'hold' position), the other piston rotates around the torus simultaneously aspirating fluid through the inflow (on the right) and ejecting fluid through the outflow (on the left). At the end of the pumping stroke, the pistons move together, transition across the inflow and outflow ports, and exchange functional roles.

5.2 Pressure-Flow Curves

Pressure-flow curves (PQ curves) quantify the pressure versus flow rate relationship for different types of pumps. Most existing blood pump technologies are continuous flow which operate on axial or centrifugal principles. Understanding the PQ curves is especially important for CF pumps because the flow through the device is a function of the differential pressure across the device as well as the rotational speed of the device.

$$Q_{\text{CF}} = f(\omega[\text{rpm}], \Delta P) \tag{5.1}$$

The three most commonly used and FDA approved VADs are the centrifugal flow Abbott HeartMate 3 (HM3) and Medtronic HVAD and the axial flow Abbott HeartMate II (HMII). The centrifugal HVAD typically operates at speeds between 2400 and 3200 rpm [64], and the axial HMII's recommended operating speed is between 8600 and 9800 rpm [65]. Flow through a continuous flow device, whether it be centrifugal or axial, is a function not only of the pump speed, but also of the differential pressure across the pump. Pressure-flow curves for recommended speed ranges for these pumps can be seen in Figure 5.5. Axial flow pumps tend to have steeper PQ curves while centrifugal flow pumps tend to be shallower and more sensitive to pressure changes, but these can be altered through design.

The 2PTP operates very differently from other blood pumps. Positive displacement pumps like the 2PTP can deliver near-constant flow for any differential pump pressure (at least within the limits of the means of actuation, in this case the torque capabilities of the motors and magnetic coupling). Some leakage can occur that can affect the flow around 1-3% (depending on the piston-torus annular gap and the pressure), but in general, the mean flow rate is function of the number of pump ejections only, which could be expressed in terms of pump 'beats' per minute (bpm). This is evident in the PQ curves for the 2PTP in Figure 5.5, which are nearly vertical with a very slight slope due to the small amount of leakage.

$$Q_{\text{PD}} = SV \cdot \text{bpm} - Q_L(\omega, \Delta P) \tag{5.2}$$

where SV is the stroke volume of the pump and Q_L is the leakage, which is a function of the piston speeds w and the pressure across the pump ΔP.

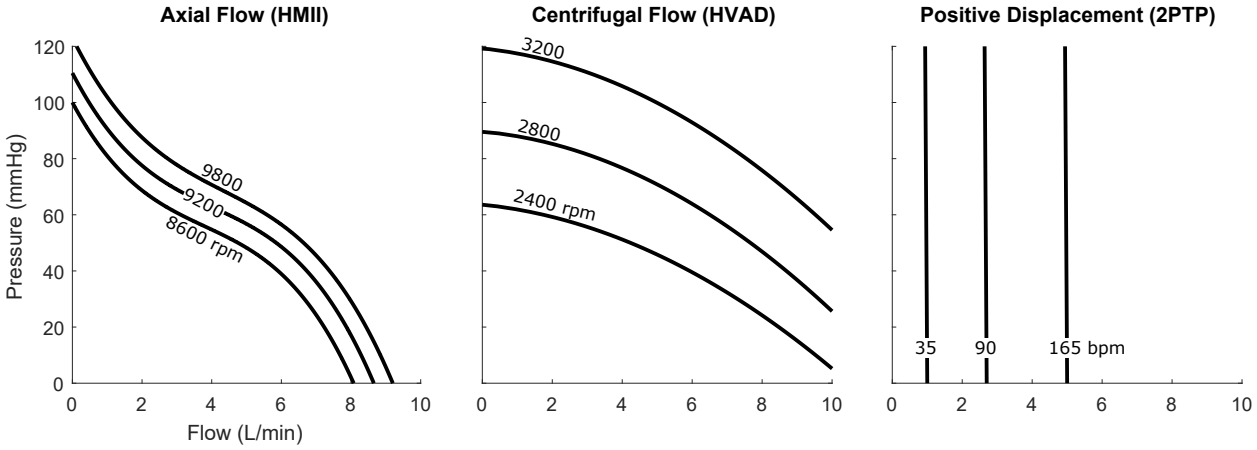

Figure 5.5: Pressure-flow curves (PQ or HQ curves) for axial (HMII) and centrifugal (HVAD) continuous flow pumps and for a positive displacement flow pump (2PTP). The HMII operates clinically between 8600 and 9800 rpm and the HVAD operates between 2400 and 3200 rpm. Flow through continuous flow pumps is a function of the differential pressure across the pump. For the 2PTP, which is a positive displacement pump, the pump operates at a fixed rate (bpm), delivering 30 ml per rotation minus a small amount of leakage flow at high pressures. As long as the torque does not exceed the capabilities of the motor, the pump operates at a near-constant average flow rate against for any differential pump pressure.

5.3 2PTP Pumping Criteria

Pressure-flow curves or the flow rate expressed in terms of pump bpm can provide information on mean flow rates, but do not provide any information on how the pistons should be controlled to produce pump ejections. To start to address this problem, two important criteria should be established.

1. **Pistons should not be allowed to contact**. The blood contacting surface of the pistons is made of Yttria-stabalized Zirconia, which is a relatively tough compared to other biocompatible ceramics like Silicone Nitride and Aluminia, but it can still fracture at high impact forces. Therefore, the pistons should maintain conservatively safe separation angles.
2. **Pistons position should not allow a backflow shunt**. Backflow can occur if the pistons are configured in such as way that allows direct fluid communication between the inflow and outflow ports. This could occur during the transition phase if the pistons are too close together or too far apart.

The two fault conditions that should be avoided (collision and shunt) are illustrated in Figure 5.6.

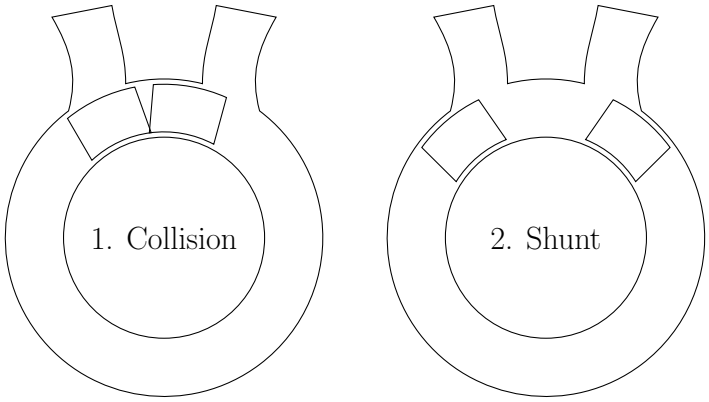

Figure 5.6: Schematic representations of two problematic events: 1) piston collision (left), which can chip ceramic pistons, and 2) a shunt condition (right), where unobstructed backflow can occur. Piston control should be designed to avoid these events.

5.4 2PTP Piston and Torus Geometry

Given the criteria above (collision and shunt avoidance), and taking into account angular requirements of the piston-motor magnetic coupling, angular assignments can be made for piston and torus geometries. Once the angular parameters of the pistons and torus are established, dimensions can be set for a given stroke volume.

5.4.1 Angular Parameters and Constraints

The restrictions of collision and shunting can provide guidance for the separation distance during the transition phase and for the size of the pistons and inflow and outflow ports. The angles of interest are defined in Figure 5.7.

For this analysis, it will be assumed that the outer radius piston angle θ_{po} will be less than or equal to the inner radius piston angle θ_{pi}. This helps facilitate streamlined flow on the leading and trailing faces to and from the ports which helps prevent regions of recirculation or stasis. This also sets the restriction that the separation angle is calculated from the inner radii of the pistons as shown in Figure 5.7.

$$\theta_{po} \leq \theta_{pi} \tag{5.3}$$

It is also assumed that the port angle θ_p is smaller than the angle at the outer radius of the piston so that the pistons completely occlude the port to stop flow during transition.

$$\theta_p \leq \theta_{po} \tag{5.4}$$

Shunt angles are defined as the angular sum of the opening at both the inflow and outflow in either the drive or hold shunt configuration and can be calculated using available geometries. The drive shunt angle θ_{sd} is defined as one that allows backflow around the drive portion of the torus.

$$\theta_{sd} = (2\theta_p + \theta_h) - (\theta_{pi} + \theta_{\text{sep}} + \theta_{po}) \tag{5.5}$$

The hold shunt θ_{sh} is defined as one that allows backflow through the hold portion of the torus, between the inflow and outflow ports.

$$\theta_{sh} = (\theta_{pi} + \theta_{\text{sep}} - \theta_{po}) - \theta_h \tag{5.6}$$

To simplify these relationships, it will be assume that the 'hold' angle is the same as the piston outer radius angle $\theta_{po} = \theta_h$.

$$\theta_{sd} = 2\theta_p - \theta_{pi} - \theta_{\text{sep}} \tag{5.7}$$

$$\theta_{sh} = \theta_{pi} + \theta_{\text{sep}} - 2\theta_{po} \tag{5.8}$$

To determine the angles of the pistons and ports, restrictions can be placed on the shunt angles. Positive shunt angles correspond to the maximum possible shunt angle during the transition. To avoid and protect from shunts, the shunt angle should be set to a negative value, not just zero, so that if the pistons are not exactly where they should be, a shunt still does not occur.

$$\theta_s = \theta_{sh} = \theta_{sd} \tag{5.9}$$

Another value that could be defined is the separation angle θ_{sep}. If the separation and shunt angles (θ_{sep} and θ_s) are defined, then two equations are still left with three unknowns: the port angle, inner radius piston angle, and the outer radius piston angle (θ_p, θ_{pi}, and θ_{po}).

$$\theta_s = 2\theta_p - \theta_{pi} - \theta_{\text{sep}} \tag{5.10}$$

$$\theta_s = \theta_{pi} + \theta_{\text{sep}} - 2\theta_{po} \tag{5.11}$$

Any of these three angles (θ_p, θ_{pi}, θ_{po}) can be selected to vary to obtain a family of possible solutions. In this case, the outer piston angle θ_{po} will be selected as the independent variable. Because it is smaller than the inner piston radius, it determines the angular width of the internal magnets. The equations can be rewritten to express the inner radius angle and port angle in terms of the outer radius angle.

$$\theta_{pi} = \theta_s - \theta_{\text{sep}} + 2\theta_{po} \tag{5.12}$$

$$\theta_p = \theta_s + \theta_{po} \tag{5.13}$$

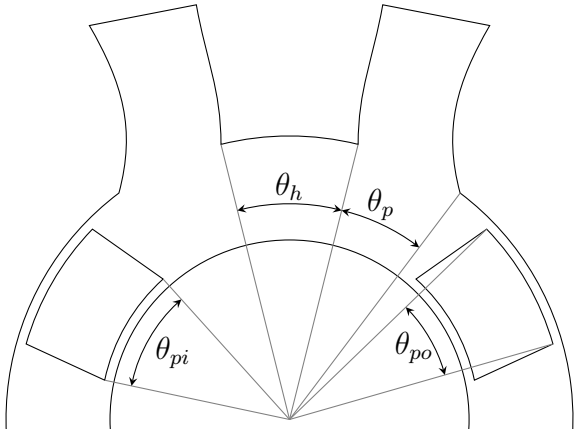

θ_{pi} Inner radius piston angle
θ_{po} Outer radius piston angle
θ_h 'Hold' angle between the ports
θ_p Inflow/outflow port angle

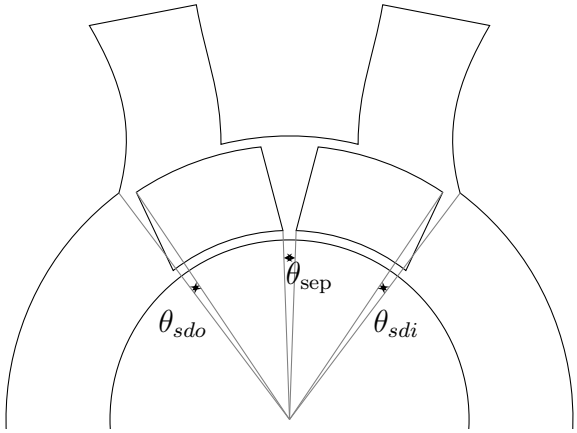

'Drive' shunt
θ_{sdi} Inflow drive shunt angle
θ_{sdo} Outflow drive shunt angle
$\theta_{sd} = \theta_{sdi} + \theta_{sdo}$ Drive shunt angle
θ_{sep} Separation angle

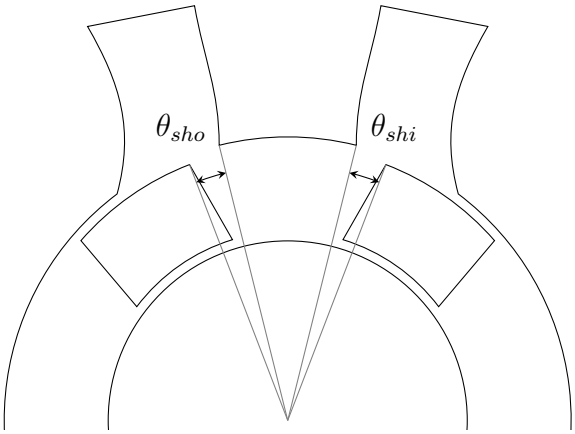

'Hold' shunt
θ_{shi} Inflow hold shunt angle
θ_{sho} Outflow hold shunt angle
$\theta_{sh} = \theta_{shi} + \theta_{sho}$ Hold shunt angle

Figure 5.7: Piston and torus angles.

Procedure for defining the angular geometry of the pistons and torus

1. Define a negative shunt angle to prevent backflow during transition

   $\theta_s = -5°$ (the total piston/port overlap should be 5°)

2. Define a separation angle between the pistons to minimize the risk of collision

   $\theta_{\text{sep}} = 15°$ (the pistons should stay 15° apart during transition)

3. Define the outer radius piston angle (internal magnet angle and piston geometry)

   $\theta_{po} = 28°$ (inner magnets of 25° plus ceramic thickness)

4. Calculate the inner radius piston angle using Equation 5.12

   $\theta_{pi} = \theta_s - \theta_{\text{sep}} + 2\theta_{po}$

   $\theta_{pi} = -5° - 15° + 2 \cdot 28°$

   $\theta_{pi} = 36°$

5. Calculate the port angle using Equation 5.13

   $\theta_p = \theta_s + \theta_{po}$

   $\theta_p = -5° + 28°$

   $\theta_p = 23°$

5.4.2 Geometric Parameters and Constraints

Once the piston and torus angles are assigned, the dimensions of the pistons and torus need to be determined to generate a desired stroke volume for each pump ejection. From inspection of the geometry and pumping stroke, the following relationship can be determined:

$$SV = V_T \left(\frac{360^\circ - 2\theta_{pi} - 2\theta_{\text{sep}}}{360^\circ} \right) \tag{5.14}$$

where the inner radius piston angle θ_{pi} and separation angle θ_{sep} are in degrees and where V_T is the torus volume, which can expressed using the cross sectional area A_C and the mean radius of the cross sectional area r_m.

$$V_T = 2\pi r_m A_c \tag{5.15}$$

The cross sectional area is a function of the inner and outer torus radius (r_i and r_o), the axial height of the torus cross section (h), and the fillet radius of the four corners of the torus r_f.

$$A_c = h(r_o - r_i) - (4 - \pi) r_f^2 \tag{5.16}$$

In this case, the mean radius of the cross sectional area is the average of the inner and outer radii.

$$r_m = \frac{r_o + r_i}{2} \tag{5.17}$$

The equation for the stroke volume can then be rewritten with these variables.

$$SV = 2\pi \left(\frac{r_o + r_i}{2} \right) \left[h(r_o - r_i) - (4 - \pi) r_f^2 \right] \left(\frac{360^\circ - 2\theta_{pi} - 2\theta_{\text{sep}}}{360^\circ} \right) \tag{5.18}$$

If a stroke volume and fillet radius are defined, there are still three unknowns: r_o, r_i, and h. The inner radius r_i can be set by the required radius of the brushless DC motors, which reside within the inner radius of the torus, at which point a family of solutions for r_o and h can be obtained, which can be selected based on other geometry constraints like motor height or piston aspect ratio (height divided by width).

$$h = \frac{1}{r_o - r_i} \left[\left(\frac{SV}{\pi(r_o + r_i)} \right) \left(\frac{360^\circ}{360^\circ - 2\theta_{pi} - 2\theta_{\text{sep}}} \right) + (4 - \pi) r_f^2 \right] \tag{5.19}$$

Procedure for defining the dimensional geometry of the pump

1. Identify the inner piston radius angle and separation angle
   $\theta_{pi} = 36°$ and $\theta_{\text{sep}} = 15°$
2. Define the stroke desired stroke volume, accounting for 3% leakage
   $SV = 1.03 \cdot 30 \text{ ml} = 1.03 \cdot 1.831 \text{ in}^3$
3. Define the fillet radius
   $r_f = 1/16$ in
4. Define the inner radius based on motor requirements
   $r_i = 0.85$ in
5. Relate h and r_o using Equation 5.19, and obtain a set of solutions. A example set of solutions for these dimensions can be found in Figure 5.8. Select a solution based on other factors like motor height, aspect ratio, and pump housing geometry.
   $h = 0.75$ in and $r_o = 1.365$ in for an aspect ratio of about 1.5 h/w

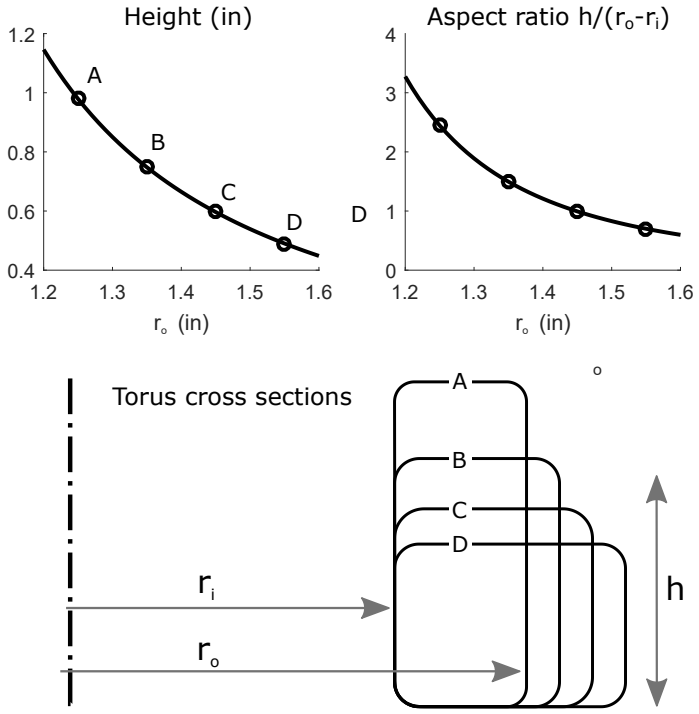

Figure 5.8: Torus cross section heights (h) and aspect ratios ($h/(r_o - r_i)$) as a function of various torus outer radius (r_o). Given $SV = 30$ ml, $r_i = 0.85$ in, $r_f = 1/16$ in, $\theta_{pi} = 36°$, and $\theta_{\text{sep}} = 15°$.

5.4.3 Summary of Parameters

The procedures above were used to determine the angular and geometric parameters for a 2PTP with a 30 ml stroke volume. Table 7.2 summarizes the results. These parameters represent only one family of solutions. Many variations are possible.

SV	30	ml	Pump stroke volume
θ_{sep}	15	deg	Minimum separation angle between pistons
θ_s	-5	deg	Shunt angle (negative prevents shunt)
r_i	0.85	in	Inner radius of the torus
θ_{pi}	36	deg	Inner radius piston angle
θ_{po}	28	deg	Outer radius piston angle
θ_p	23	deg	Port angle
h	0.75	in	Torus height
r_o	1.365	in	Outer radius of the torus
r_f	0.625	in	Fillet radius of the torus cross section
A_c	0.383	in^2	Cross sectional area of the piston/torus
r_m	1.1075	in	Mean radius of the piston cross sectional area
V_T	43.7	ml	Torus volume

Table 5.1: Pump dimensions and operation parameters.

5.5 2PTP Dynamic Flow Characteristics

The flow rate in and out of the pump is a function of the difference between the piston velocities (assuming leakage is small and can be ignored).

$$Q = \begin{cases} A_c r_m(\omega_2 - \omega_1) & \text{when piston 2 is the 'drive' piston} \\ A_c r_m(\omega_1 - \omega_2) & \text{when piston 1 is the 'drive' piston} \end{cases} \tag{5.20}$$

where A_c is the cross sectional area of the piston, r_m is the mean radius of the piston, and ω_1 and ω_2 are the rotational velocities of the pistons. During pumping, it will be assumed there is a 'hold' piston that moves slowly or remains stationary between the inflow and outflow ports to act like a virtual valve, and a 'drive' piston that rotates clockwise around the torus to perform the main pumping stroke. In that case, the equation for flow can be rewritten as:

$$Q = A_c r_m(\omega_d - \omega_h) \tag{5.21}$$

This difference in angular velocity will be defined as a pump angular velocity ω_p

$$\omega_p = \omega_d - \omega_h \tag{5.22}$$

Therefore, the flow can be expressed as a function of the pump angular velocity

$$Q = A_c r_m \omega_p \tag{5.23}$$

When considering how the piston should be driven to produce flow, it must first be decided what characteristics of flow are desired. From Figure 5.4, it is established that pump ejections are sequential: pump, transition, pump, transition, etc (assuming we're not interested in pumping backwards or half pump strokes). It can also be seen by inspection that during transition the inflow and outflow ports are completely occluded by the pistons, so that the flow must go to zero during that time (again, assuming negligible leakage flow). This sets up the first pumping restriction: if the flow goes to zero by port occlusion, it should also go to zero as a function of the differential piston velocities (ω_p should be zero during transition).

$$\omega_1 = \omega_2 \text{ and } \omega_p = 0 \quad \text{during transition (when ports are fully occluded)} \tag{5.24}$$

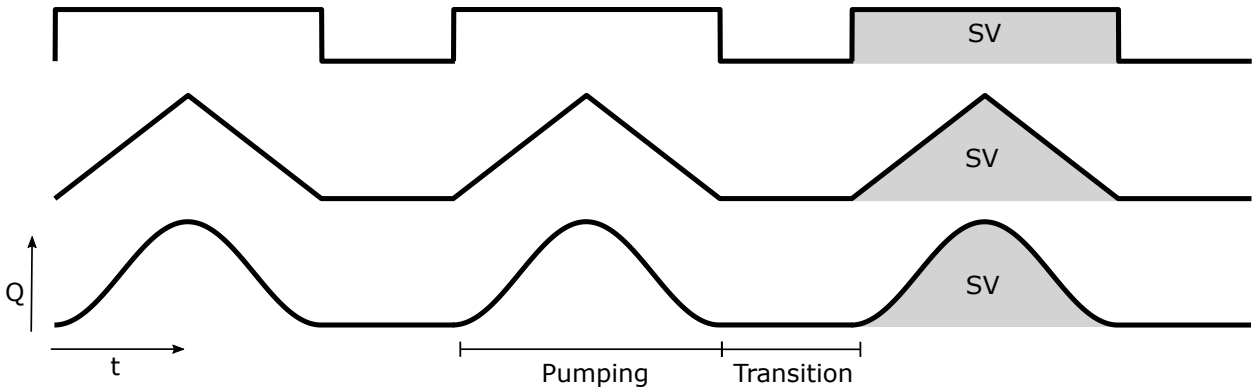

Figure 5.9: The 2PTP operates with sequential pumping-transition cycles. Transition is characterized by zero flow while the pistons occlude the inflow and outflow ports and exchange functional roles. The desired pump flow profiles could take a variety of forms, simple square waves, triangle waves, and sinusoidal curves are illustrated here as examples. Regardless of the desired profile chosen, the integrated region under each pumping cycle is the stroke volume of the device.

But what should the pump ejections look like? One could imagine any number of flow curve profiles being used: square waves, triangle waves, sinusoidal curves, etc. Some examples can be seen in Figure 5.9.

To decide how the flow profile should be shaped, the desired characteristics and limitations of pumping should be outlined and understood. One important feature of the dynamics that will be developed further in later chapters is the inertia of the blood in the pump and cannulas. Accelerating and decelerating the fluid requires effort (in this case motor torque).

$$\tau \sim I\dot{Q} = IA_cR_m\dot{\omega}_p. \tag{5.25}$$

Therefore, step changes in flow (like in the square wave) that result in 'infinite' acceleration should be avoided. Discontinuities or step changes in acceleration (like in the triangle wave) should also be avoided so that jerk, the derivative of acceleration, is not 'infinite'. Step changes in acceleration or jerk may also cause excess forces or vibration on the body - this is studied in Appendix A. Therefore, it would be good if the flow profile selected is twice differentiable to avoid discontinuities in acceleration. Functions composed of sine waves, which are infinitely differentiable, are one obvious choice. One such sinusoidal-based trajectory would be offset sine or cosine curves so that the normalized flow goes from 0 to 1

instead of -1 to 1. This can be done by offsetting a cosine and halving the amplitude:

$$Q = \frac{Q_m}{2}\left[1 - \cos\left(\pi \frac{t}{T_p}\right)\right] \tag{5.26}$$

This is also equivalent to the more simplified form using $\sin^2()$

$$Q = Q_m \sin^2\left(\frac{\pi}{2}\frac{t}{T_p}\right) \tag{5.27}$$

where Q_m is the maximum flowrate, t is the normalized time ($t = 0$ is the start of ejection, and T_p is the pump ejection time.

Furthermore, it might also be desired to shape the pulse, to skew the peak flow toward the beginning or end of the pump ejection for example, or to allow for a 'plateauing' of the peak flow. To accomplish this, piecewise functions can be used to for each case: the acceleration (a), maximum flow (m), and deceleration (d) regions.

$$Q = \begin{cases} Q_m \sin^2\left(\dfrac{\pi}{2}\dfrac{t}{\alpha_a T_p}\right) & \text{for} \quad 0 \le t < \alpha_a T_p \\ Q_m & \text{for} \quad \alpha_a T_p \le t < (\alpha_a + \alpha_m) T_p \\ Q_m - Q_m \sin^2\left(\dfrac{\pi}{2}\dfrac{t - (\alpha_a + \alpha_m)T_p}{\alpha_d T_p}\right) & \text{for} \quad (\alpha_a + \alpha_m) T_p \le t < T_p \end{cases} \tag{5.28}$$

The α ratios are defined by:

$$\begin{aligned} \alpha_a &= \frac{T_a}{T_p} \quad \text{acceleration time over total pumping time} \\ \alpha_m &= \frac{T_m}{T_p} \quad \text{time at max flow over total pumping time} \\ \alpha_d &= \frac{T_d}{T_p} \quad \text{decceleration time over total pumping time} \end{aligned} \tag{5.29}$$

where the sum of the ratios must equal 1.

$$\alpha_a + \alpha_m + \alpha_d = 1 \tag{5.30}$$

These ratios and the resulting flow are illustrated in Figure 5.10.

Allowing for different acceleration and deceleration times might be important for piston control or for cardiovascular hemodynamics. For example, if piston collision is most likely

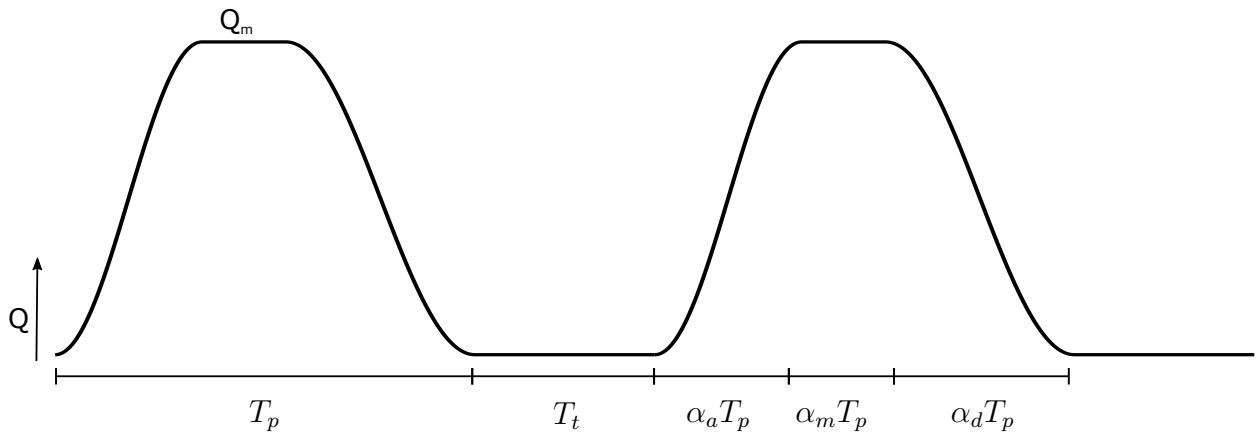

Figure 5.10: 2PTP sinusoidal flow profile. T_p is the pump time, T_t is the transition time. The pulsatile ejection has an acceleration time of $\alpha_a T_p$, time $\alpha_m T_p$ at max flow Q_m, and deceleration time of $\alpha_d T_p$. The acceleration and deceleration curves use piecewise $\sin^2()$ functions.

to occur during the deceleration phase, when the incoming driving piston is moving toward the the hold piston and where control errors can lead to contact, then to minimize the risk of collision, making the deceleration as gradual as possible might be desired. In terms of hemodynamics, it might be better to pump more quickly at the beginning or end of the pumping phase, depending on synchronous phasing or the desired ventricular unloading. Or it might be beneficial for achieving a high peak flow rate (by setting $\alpha_m = 0$). On the other hand, the eccentric mass of the piston generates centrifugal forces that might make it such that increasing α_m, which decreases the peak rotational velocity, is beneficial. These examples are meant to demonstrate the need for flexibility in defining the pump flow profile. Decisions will be need to be made regarding which aspects (hemodynamics, collision risk, centrifugal forces, power consumption, etc) are most important and how they should be balanced.

The maximum flow rate Q_m is related to the pumping time T_m because the stroke volume SV (the area under the curve) is known. The piecewise flow rate curves can be integrated and added to relate these terms.

$$\begin{aligned} SV = &\int_0^{\alpha_a T_p} Q_m \sin^2\left(\frac{\pi}{2}\frac{t}{\alpha_a T_p}\right) \mathrm{dt} + \int_{\alpha_a T_p}^{(\alpha_a+\alpha_m)T_p} Q_m \mathrm{dt} \\ &+ \int_{(\alpha_a+\alpha_m)T_p}^{T_p} Q_m - Q_m \sin^2\left(\frac{\pi}{2}\frac{t-(\alpha_a+\alpha_m)T_p}{\alpha_d T_p}\right) \mathrm{dt} \end{aligned} \tag{5.31}$$

$$SV = \left(\frac{\alpha_a}{2} + \alpha_m + \frac{\alpha_d}{2}\right) T_p Q_m \tag{5.32}$$

When the pumping time is defined, the max flow can be found by:

$$Q_m = \frac{SV}{\left(\frac{\alpha_a 1}{2} + \alpha_m + \frac{\alpha_d}{2}\right) T_p} \tag{5.33}$$

Knowing the desired pump flow profile is the first step, the next is to determine what piston rotational velocities are needed to create the profile. Again, because the pump is positive displacement, the flow is a function of the difference in velocity between the pistons, or the pumping velocity ω_p. The flow has been described using piecewise sinusoidal curves, so the pumping angular velocity will take the same form.

$$\omega_p = \begin{cases} \omega_m \sin^2\left(\dfrac{\pi}{2}\dfrac{t}{\alpha_a T_p}\right) & \text{for} \quad 0 \leq t < \alpha_a T_p \\ \omega_m & \text{for} \quad \alpha_a T_p \leq t < (\alpha_a + \alpha_m) T_p \\ \omega_m - \omega_m \sin^2\left(\dfrac{\pi}{2}\dfrac{t - (\alpha_a + \alpha_m) T_p}{\alpha_d T_p}\right) & \text{for} \quad (\alpha_a + \alpha_p) T_p \leq t < T_p \end{cases} \tag{5.34}$$

where the maximum velocity ω_m is found by

$$\omega_m = \frac{Q_m}{A_c r_m} = \frac{SV}{Ar\left(\frac{\alpha_a 1}{2} + \alpha_m + \frac{\alpha_d}{2}\right) T_p} \tag{5.35}$$

The pumping velocity ω_p has been defined, but now the driving and holding velocities of the different pistons need to be described to obtain the desired pumping velocity ($\omega_p = \omega_d - \omega_h$). One very simply solution to this problem is to break the pumping and transition into two discrete phases. For pumping, the drive piston could start from zero velocity, follow the same sinusoidal profile defined for the flow, then come to a stop near the outflow port. At that point, the pistons could move together through the transition phase and stop again once complete. But, this adds two unnecessary start/stop phases which adds time to the pump-transition cycle, and this method is inefficient in that it stops the incoming piston only to make it immediately start moving again into the transition phase and stops the outgoing drive piston only to make it immediately start moving again into the pumping phase. This would be like an incoming relay runner (drive piston) coming to a complete stop before

passing the baton and then the new runner (hold piston) not starting to run until after receiving the baton. Furthering this relay runner analogy, a much better approach is for the runners to reach some shared velocity, then pass the baton (transition), at which point the new runner (new drive piston) can proceed and the old runner (new hold piston) can come to a stop.

Geometric constraints also need to be considered when planning the piston velocities. Because the difference in piston velocity drives flow in and out of the pump, the pistons need to be moving the same velocity when the ports are fully occluded. Just as relay runners can only pass the baton within a restricted zone, the pistons can only transition over a restricted angle. The angles at which this happens are determined by piston, torus, and port geometries. Using geometric and velocity constraints, two important events can be described: 1) when the pistons start moving the same velocity at the start of transition, and 2) when the pistons stop moving the same velocity at the beginning of the next pumping period. This is illustrated in Figure 5.11.

The angle of separation between the pistons during transition θ_{sep} was defined above. Another angle that must be specified is the angle of the pistons when entering and exiting transition. When entering transition, the outgoing piston (piston 2 in Figure 5.11) cannot fully occlude the port before pumping ends because if the pistons are moving different velocities when the inflow is occluded, then the sudden occlusion will cause a waterhammer effect in the cannulas and pump. Therefore:

$$\theta_{ta} < \theta_p \quad \text{and} \quad \theta_{td} < \theta_p \tag{5.36}$$

θ_{ta} is defined here as the transition angle (the angle at which the outgoing piston reaches the transition velocity, and θ_{td} will be the angle that the incommoding piston will start to decelerate to a stop. θ_p is the port angle of the inflow and outflow ports. 0° corresponds to the 12 o'clock position (between the inflow and outflow ports) and the angle increases in the clockwise direction.

For a given pump profile defined above, pump ejection time T_p, and transition time T_t, piecewise function curves for both pistons can be defined. But first, the transition velocity ω_t,

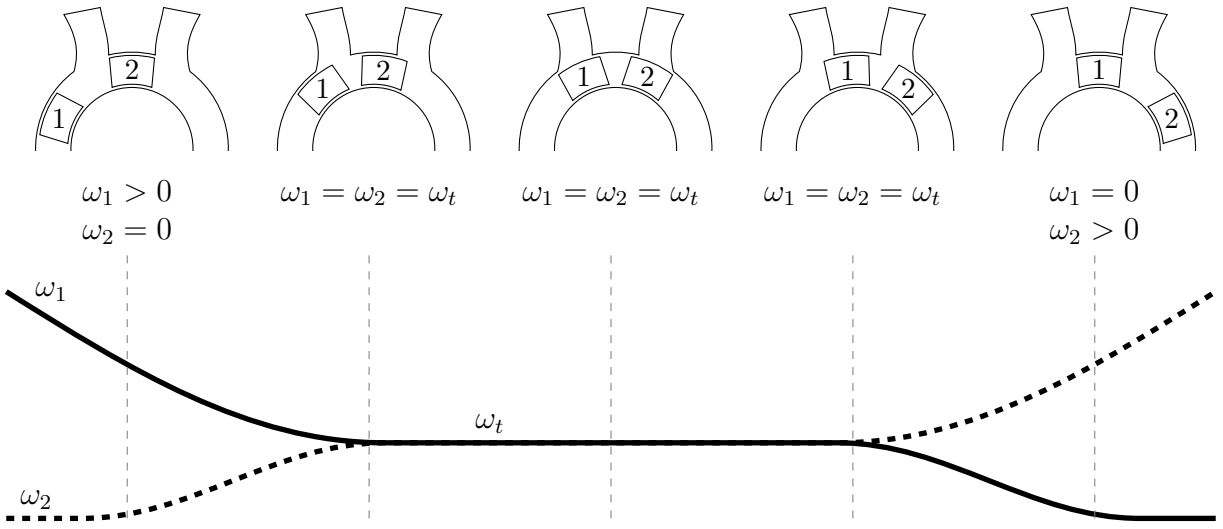

Figure 5.11: Piston velocities during transition. The stationary 'hold' piston (2 in this case) accelerates to the same velocity as the incoming 'drive' piston (1 in this case) before the inflow and outflow ports are occluded. By moving the same velocity, the flow in and out of the pump is zero (ignoring leakage), allowing the pistons to occlude the ports without causing a waterhammer effect.

acceleration angle θ_{ta} where the outgoing piston reaches the transition velocity, and deceleration angle θ_{td} where the incoming piston starts decelerates to stop need to be determined. One way to do this is to prescribe the acceleration and deceleration angles, at which point the piecewise curves can be fully defined. The transition velocity is found by

$$\omega_t = \frac{\theta_{pi} + \theta_{\text{sep}} - \theta_{ta} - \theta_{da}}{T_t} \tag{5.37}$$

The acceleration and deceleration times can be determined from the angles and transition velocity.

$$\theta_{ta} = \frac{1}{2}\omega_t T_{ta} \tag{5.38}$$

$$\theta_{td} = \frac{1}{2}\omega_t T_{td} \tag{5.39}$$

And then the acceleration and deceleration velocity profiles out of and into transition are:

$$\omega_{\text{ta}} = \omega_t \sin^2\left(\frac{\pi}{2}\frac{\hat{t}_{ta}}{T_{ta}}\right) \tag{5.40}$$

where $\hat{t}_{ta}$ is the normalized time from the start of the acceleration phase and $T_{ta} = 2\theta_t/\omega_t$
Deceleration is similar

$$\omega_{\mathrm{td}} = \omega_t \left[1 - \sin^2\left(\frac{\pi}{2}\frac{\hat{t}_{td}}{T_{td}}\right)\right] \tag{5.41}$$

where $\hat{t}_{td}$ is the normalized time from the start of the deceleration phase and $T_{td} = 2\theta_t/\omega_t$

Another option is to 1) minimize the acceleration and deceleration angles (to minimize port occlusion and therefore to minimize partial port resistance) while 2) not allowing the driving piston to change acceleration sign during the acceleration and deceleration portions of the pumping stroke. This can be accomplished by setting the the derivative of acceleration (jerk) for the transition acceleration and deceleration equal and opposite to the differential piston jerk at both the start and end of the pumping stroke.

Jerk at the start of the pumping acceleration

$$j_{pa} = \ddot{\omega}_p\Big|_{t=0} = 2\omega_m \left(\frac{\pi}{2}\right)^2 \frac{1}{T_a^2} \tag{5.42}$$

Jerk at the end of pump deceleration

$$j_{pd} = \ddot{\omega}_p\Big|_{t=T_p} = 2\omega_m \left(\frac{\pi}{2}\right)^2 \frac{1}{T_d^2} \tag{5.43}$$

Jerk of the acceleration of the 'hold' piston into transition

$$j_{ta} = \ddot{\omega}_h\Big|_{t=0} = 2\omega_t \left(\frac{\pi}{2}\right)^2 \frac{1}{T_{ta}^2} \tag{5.44}$$

Jerk of the deceleration of the new 'hold' piston from transition

$$j_{td} = \ddot{\omega}_h\Big|_{t=T_{td}} = 2\omega_t \left(\frac{\pi}{2}\right)^2 \frac{1}{T_{td}^2} \tag{5.45}$$

Now, to make it such that the driving piston acceleration does not change sign at the start of acceleration or end of deceleration, set

$$j_{pa} = j_{td} \quad \text{and} \quad j_{pd} = j_{ta} \tag{5.46}$$

$$2\omega_m \left(\frac{\pi}{2}\right)^2 \frac{1}{T_a^2} = 2\omega_t \left(\frac{\pi}{2}\right)^2 \frac{1}{T_{td}^2} \tag{5.47}$$

$$2\omega_m \left(\frac{\pi}{2}\right)^2 \frac{1}{T_d^2} = 2\omega_t \left(\frac{\pi}{2}\right)^2 \frac{1}{T_{ta}^2} \tag{5.48}$$

Equations 5.37, 5.38, 5.39, 5.47, and 5.48 can be combined. Two values (ω_m and T_p) are prescribed from which 5 unknowns (ω_t, θ_{ta}, θ_{td}, T_{ta}, and T_{td}) can be determined. First, T_{td} and T_{ta} can be isolated:

$$\frac{\omega_m}{2T_d^2}\left[1 + \frac{T_a}{T_d}\right] T_{ta}^3 + \frac{\omega_m T_t}{T_d^2} T_{ta}^2 - (\theta_{pi} + \theta_{\text{sep}}) = 0 \tag{5.49}$$

$$\frac{\omega_m}{2T_a^2}\left[1 + \frac{T_d}{T_a}\right] T_{td}^3 + \frac{\omega_m T_t}{T_a^2} T_{td}^2 - (\theta_{pi} + \theta_{\text{sep}}) = 0 \tag{5.50}$$

These cubic functions can be solved numerically to find T_{td} and T_{ta}, from which the transition velocity can be determined:

$$\omega_t = \frac{\omega_m T_{ta}^2}{T_d^2} = \frac{\omega_m T_{td}^2}{T_a^2} \tag{5.51}$$

And then the acceleration and deceleration angles can be found:

$$\theta_{ta} = \frac{1}{2}\omega_t T_{ta} \quad \text{and} \quad \theta_{td} = \frac{1}{2}\omega_t T_{td}$$

One limitation of this approach is that the acceleration and deceleration angles θ_{ta} and θ_{td} can become larger than the port (which would lead to waterhammer effects and difficulty in control) under some circumstances (specifically, when the transition time T_t becomes very short compared to the pump time T_p). This can be avoided when selecting the operation parameters.

An example of the velocity and acceleration curves for piston 1 and piston 2 can be seen in Figure 5.12. In this case, the pump time T_p was set to 0.35 seconds, the stroke rate (pump ejections per minute) was set to 80 bpm resulting in a transition time T_t of 0.4 seconds. The pump acceleration ratio α_a is set to 0.4 and the deceleration ratio α_d is set to 0.6. The resulting flow rate and fluid acceleration curves are also shown.

5.6 Reference Tracking Curves

From the constraints outlined above, velocity, position, and acceleration reference curves (also known as reference or tracking curves) can be generated for the drive and hold pistons for a single ejection cycle (pumping and transition).

5.6.1 Angular Velocity

Pump (p) angular velocity ($\omega_p = \omega_d - \omega_h$)

$$\omega_p = \begin{cases} \omega_m \sin^2\left(\frac{\pi}{2}\frac{t}{T_a}\right) \\ \omega_m \\ \omega_m\left[1 - \sin^2\left(\frac{\pi}{2}\frac{t-(T_a+T_m)}{T_d}\right)\right] \\ 0 \end{cases} \text{ for } \begin{array}{rcccl} 0 & \leq & t & < & T_a \\ T_a & \leq & t & < & T_a + T_m \\ T_a + T_m & \leq & t & < & T_p \\ T_p & \leq & t & < & T_p + T_t \end{array} \tag{5.52}$$

Hold piston (h) angular velocity

$$\omega_h = \begin{cases} \omega_t\left[1 - \sin^2\left(\frac{\pi}{2}\frac{t}{T_{td}}\right)\right] \\ 0 \\ \omega_t \sin^2\left(\frac{\pi}{2}\frac{t-(T_p-T_{ta})}{T_{ta}}\right) \\ \omega_t \end{cases} \text{ for } \begin{array}{rcccl} 0 & \leq & t & < & T_{td} \\ T_{td} & \leq & t & < & T_p - T_{ta} \\ T_p - T_{ta} & \leq & t & < & T_p \\ T_p & \leq & t & < & T_p + T_t \end{array} \tag{5.53}$$

Drive piston (d) angular velocity

$$\omega_d = \omega_p + \omega_h \tag{5.54}$$

where t is the normalized time from the beginning of pump ejection to the end of transition at $T_p + T_t$.

5.6.2 Angular Position

Angular position is found by integrating the angular velocity.

Pump (p) angular position ($\theta_p = \theta_d - \theta_h$)

$$\theta_p = \begin{cases} \omega_m\left[\frac{t}{2} - \frac{T_a}{2\pi}\sin\left(\pi\frac{t}{T_a}\right)\right] \\ \omega_m\left(t - T_a\right) + \omega_m\frac{T_a}{2} \\ \omega_m\left[\frac{t}{2} + \frac{T_d}{2\pi}\sin\left(\pi\frac{t-(T_a+T_m)}{T_d}\right) + \frac{T_m}{2}\right] \\ 360^\circ - 2\theta_{pi} - 2\theta_{\text{sep}} \end{cases} \text{ for } \begin{array}{rcccl} 0 & \leq & t & < & T_a \\ T_a & \leq & t & < & T_a + T_m \\ T_a + T_m & \leq & t & < & T_p \\ T_p & \leq & t & < & T_p + T_t \end{array} \tag{5.55}$$

Hold piston (h) angular position

$$\theta_h = \begin{cases} -\theta_{td} + \omega_t \left[\frac{t}{2} + \frac{T_{td}}{2\pi} \sin\left(\pi \frac{t}{T_{td}} \right) \right] & \text{for} \quad 0 \leq t < T_{td} \\ 0 & \text{for} \quad T_{td} \leq t < T_p - T_{ta} \\ \omega_t \left[\frac{t-(T_p-T_{ta})}{2} - \frac{T_{ta}}{2\pi} \sin\left(\pi \frac{t-(T_p-T_{ta})}{T_{ta}} \right) \right] & \text{for} \quad T_p - T_{ta} \leq t < T_p \\ \theta_{td} + \omega_t \left(t - T_p \right) & \text{for} \quad T_p \leq t < T_p + T_t \end{cases} \tag{5.56}$$

Drive piston (d) angular position

$$\theta_d = \theta_p + \theta_h \tag{5.57}$$

5.6.3 Angular Acceleration

Angular acceleration is found by taking the derivative of the angular velocity. These can be used in feedforward control to estimate the torque that will be required to accelerate and decelerate the fluid and rotational masses (piston and motors).

Pump (p) angular position ($\theta_p = \theta_d - \theta_h$)

$$\alpha_p = \begin{cases} \frac{4\omega_m}{\pi T_a} \sin\left(\frac{\pi}{2} \frac{t}{T_a} \right) \cos\left(\frac{\pi}{2} \frac{t}{T_a} \right) & \text{for} \quad 0 \leq t < T_a \\ 0 & \text{for} \quad T_a \leq t < T_a + T_m \\ -\frac{4\omega_m}{\pi T_a} \sin\left(\frac{\pi}{2} \frac{t-(T_a+T_m)}{T_d} \right) \cos\left(\frac{\pi}{2} \frac{t-(T_a+T_m)}{T_a} \right) & \text{for} \quad T_a + T_m \leq t < T_p \\ 0 & \text{for} \quad T_p \leq t < T_p + T_t \end{cases} \tag{5.58}$$

Hold piston (h) angular acceleration

$$\alpha_h = \begin{cases} -\frac{4\omega_t}{\pi T_{td}} \sin\left(\frac{\pi}{2} \frac{t}{T_{td}} \right) \cos\left(\frac{\pi}{2} \frac{t}{T_{td}} \right) & \text{for} \quad 0 \leq t < T_{td} \\ 0 & \text{for} \quad T_{td} \leq t < T_p - T_{ta} \\ \frac{4\omega_t}{\pi T_{ta}} \sin\left(\frac{\pi}{2} \frac{t-(T_p-T_{ta})}{T_{ta}} \right) \cos\left(\frac{\pi}{2} \frac{t-(T_p-T_{ta})}{T_{ta}} \right) & \text{for} \quad T_p - T_{ta} \leq t < T_p \\ 0 & \text{for} \quad T_p \leq t < T_p + T_t \end{cases} \tag{5.59}$$

Drive piston (d) angular acceleration

$$\alpha_d = \alpha_p + \alpha_h \tag{5.60}$$

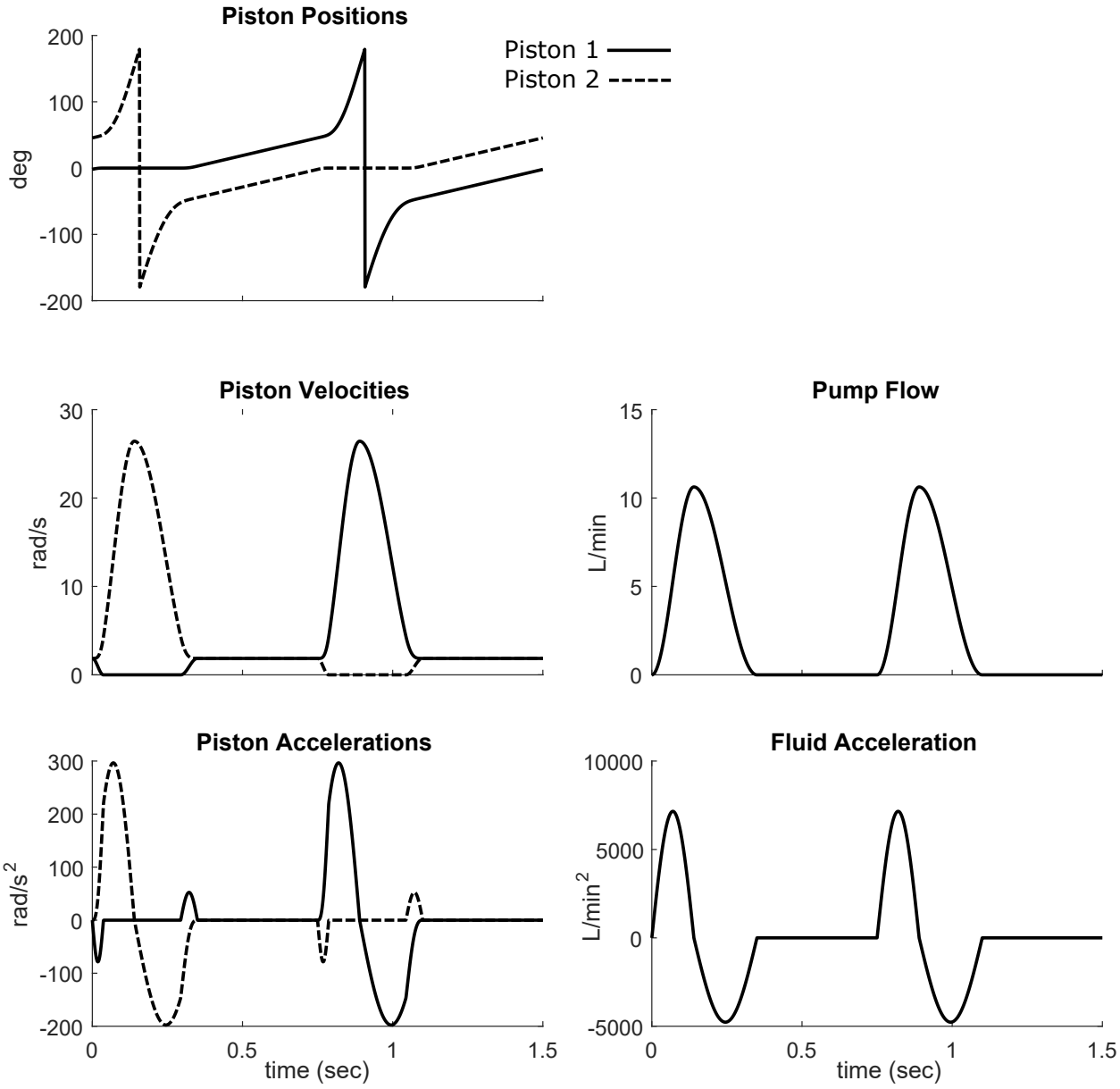

Figure 5.12: Example piston position, velocity, and acceleration reference curves for a pump time of 0.35 seconds, at a rate of 80 bpm. $\alpha_a = 0.4$ and $\alpha_d = 0.6$. The flow rate and fluid acceleration that result can be seen on the right.

Chapter 6

High-Level 2PTP Control - Physiological Control

This chapter studies physiological control with the synchronous positive displacement pumping compared to continuous flow support by assessing preload sensitivity with ventricular function curves.

6.1 Physiological Control

The primary purpose of a VAD is to increase cardiac output, but VADs should also ideally restore a physiological response to metabolic demand which can vary throughout the day depending on the patient's activity level or physiological status. As discussed in Chapter 2, the healthy heart balances flow by passively regulating cardiac output with the so-called Frank-Starling law of the heart [32]. In heart failure, the autoregulation of the Frank-Starling law is impaired, and even with increased preload and decreased afterload, the ventricle is unable to provide sufficient cardiac output to the system. VADs increase cardiac output, but the healthy Frank-Starling relationship of cardiac output vs preload is not necessarily restored. Continuous flow devices operating at constant speed have been shown to have half the preload sensitivity and three times the afterload sensitivity compared to the healthy heart [35].

Virtually all implanted VADs are continuous flow (CF) devices, either axial flow pumps like the Abbott HeartMate II (HMII) or centrifugal flow pumps like the Medtronic HVAD and Abbott HeartMate 3 [66]. Continuous flow devices are well known to be insensitive to ventricular preload. It has been estimated that CF devices have 30-50% the preload sensitivity compared to a healthy heart [35, 67]. This creates impaired autoregulation of cardiac output that is significantly altered and non-physiological [68]. Left-to-right flow balancing issues and left ventricular overpumping can quickly lead to suction events, ventricular septal-wall deviations, pulmonary edema, tricuspid valvular regurgitation, arrhythmias, and

if sustained, aortic valve leaflet fusion, right heart dysfunction, and ultimately right heart failure in 10-30% of patients [69, 70, 71, 72]. These conditions create a difficult clinical balancing act involving control of systemic vascular resistance and intravascular fluid volume with vasodilator and inotropic medications in an attempt to adjust left ventricular output and reduce ventricular suction events while maintaining viable right ventricular function [65].

The goal of physiological control of VADs is to restore the cardiac output autoregulation to provide phsyiological levels of support based on metabolic demand and to prevent overpumping and ventricular suction. High-level control adjusts pump mode (asynchronous or synchronous), phasing (where in the cardiac cycle to pump), or rotational speed for CF VADs. Control algorithms proposed for CF VADs adjust mean rpm using sensed or measured feedback, such as arterial blood pressure or ventricular preload, but none have been implemented in a clinical setting. Ideal physiological control might involve measuring preload (LV pressure), afterload (arterial pressure and/or impedance), heart rate, and ventricular ejection through the aortic valve to provide optimal flow. This is not currently a viable solution; indwelling blood or volume sensors are not robust in terms of long-term stability, and the additional instrumentation involved would be cumbersome. Other methods have been proposed such as maintaining a set differential pump pressure, pulsatility gradient, or pulsatility ratio [17], but these methods have all fallen well short of providing a healthy-like response [73]. Proposed methods have been limited to simple speed changes without considering the importance of pulsatility and synchronization and how these features should be adjusted to optimize LVAD *coordination* with the heart.

High-level control of a synchronous positive displacement pump like the 2PTP poses unique problems because there are many more variables that can be adjusted. Instead of a single setting (like pulsatile pump rate or CF rpm), the 2PTP has multiple pump variations including asynchronous or synchronous pumping (how much to pump), synchronous phasing within the the cardiac cycle (when to pump), and pump ejection time (how quickly to pump).

6.2 2PTP Physiological Control

The 2PTP provides sinusoidal pump flow ejections by controlling the piston reference trajectories, as described in the previous chapter. Pump aspiration and ejection occur simultaneously (flow into the pump equals flow out of the pump, there is no internal pump compliance). In its current embodiment (the TORVAD), the stroke volume is 30 ml. The pump has an integrated epicardial ECG lead to detect ventricular depolarization so that the pump ejections can be synchronized to the cardiac cycle. ECG feedback is used to assess heart rate and rhythm, which can be used to set the pump flow rate. The default mode, if the heart rate is within normal ranges and has a regular rhythm, is synchronous counterpulse support where the pump ejects in early diastole, just after the ventricular contraction. If the heart rate falls outside of normal ranges (for example, < 40 or > 140 bpm), if the rhythm is irregular or in ventricular fibrillation then the pump will operate in asynchronous mode at 5 L/min. These are the current settings of the TORVAD, but infinite variation is possible, and these settings could be manually adjusted by doctors, nurses, caregivers, or patients.

An illustrative explanation of counterpulse support is shown in Figure 6.1. Pump ejections have a stroke time T_{ST}. The peak ejection is timed to occur at a phase delay (PD) from the R-wave of the ECG signal. The RR-interval is the time from R-wave to R-wave, and is the inverse of the heart rate (RR = 60/HR). The pump controller senses the R-wave from the integrated ECG lead and adjusts the timing of the pump to obtain the desired phase delay so that the pump ejection occurs in early diastole. This control and these settings are customizable.

Counterpulse support with a 30 ml stroke volume was determined to provide comparable cardiac output to a continuous flow device (the HeartMate II) at a normal clinical setting (9,000 rpm) [74]. Counterpulse support maximizes cardiac output because it allows the ventricle to contract and eject blood through the aortic valve during systole. Then the pump ejection in early diastole serves to boost the cardiac output. If the pump ejects during systole (for example a phase delay of 20% in Figure 6.2), then much of the blood that would normally be ejected through the aortic valve is instead shunted through the pump, which results in a lower cardiac output compared to counterpulse support.

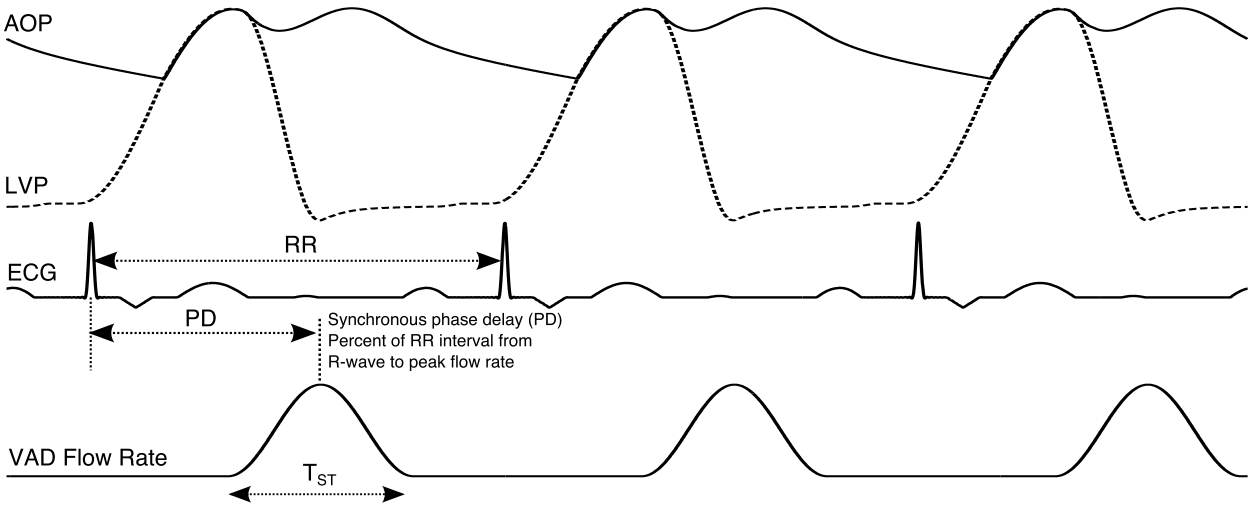

Figure 6.1: Hemodynamic plots of aortic pressure (AOP) and left ventricular pressure (LVP), a simulated representation of a typical electrocardiogram (ECG), and a plot of the 2PTP flow rate (VAD Flow Rate) are used to demonstrate the synchronous phasing operation of the pump. The R-wave of the ECG and a programmable phase delay (PD) are used to synchronize the peak flow rate of the pump to a predetermined time in the cardiac cycle, in this case early diastole. The effect of this early diastolic ejection (with stroke time T_{ST}) on the arterial pressure can be seen in the AOP trace. From [14].

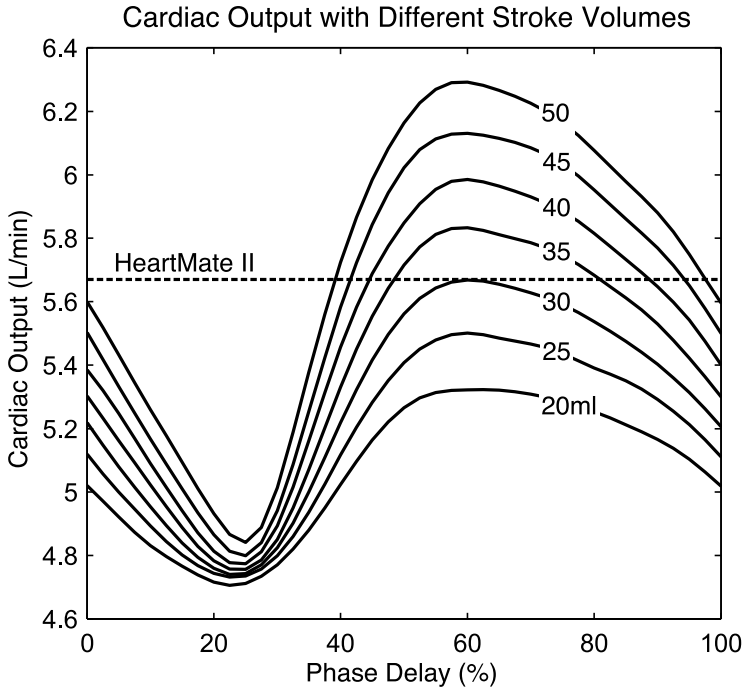

Figure 6.2: Cardiac output (CO) versus phase delay with 2PTP support at various stroke volumes. The CO when supported with a HeartMate II continuous flow (CF) is displayed as a dashed line. From this plot, it can be seen that a 30 mL stroke volume 2PTP operating with a phase delay of approximately 60 generates an equivalent CO to a CF device. The effect of phasing adjustments and stroke volume changes on CO support levels is also illustrated in this plot. From [14]

.

6.3 Passive Preload Sensitivity - CF vs 2PTP Counterpulse

This chapter will first study how cardiac output varies passively with different with continuous flow VADs and with the 2PTP in counterpulsation.

This study compares preload sensitivity of CF support to counterpulsation with a 2PTP, which is the primary operating mode of the TORVAD. Counterpulse support increases cardiac output while preserving aortic valve flow and provides ventricular unloading comparable to CF devices [14]. The 2PTP flow rate in synchronous mode is a function of heart rate alone and is not itself sensitive to preload or afterload, but the preserved aortic valve flow that results from counterpulse support is generated by remaining left ventricular function and is physiologically sensitive to changes in ventricular preload and afterload. Understanding how the positive displacement 2PTP ejection and the left ventricle work together by quantifying the combined response to preload and comparing it to the current CF standard of care is the purpose of this section.

6.3.1 Preload Sensitivity Simulation Methods

Lumped parameter models of the cardiovascular system are routinely used to simulate the hemodynamics that result from VAD support [36]. The two models developed in Chapter 3 were used for this study. First, an open-loop simulation of the systemic circulation was used to obtain ventricular function curves by isolating the systemic circulation and directly prescribing preload and afterload boundary conditions. Second, a closed-loop simulation that includes the pulmonary circulation was used to study the hemodynamic effects and risk of suction caused by changes to pulmonary vascular resistance, systemic vascular resistance, heart rate, inotropic state, and blood volume.

Four different conditions were modeled: healthy, heart failure, heart failure with CF support, and heart failure with 30ml 2PTP synchronous counterpulsation. Baseline hemodynamics and parameters are shown in Table 6.1.

The continuous flow device was modeled using pressure-flow curves for the HMII at 9,000 rpm. The 2PTP flow was generated using a prescribed sinusoidal flow rate pulse with a 30 ml stroke volume and with an ejection time of 300 ms in early diastole. Early diastole was

Condition	HR	CO	QVAD	QAO	MAP	LVESV	SW	SVR	PVR
	bpm	L/min	L/min	L/min	mmHg	ml	mmHg·ml	mmHg·s/ml	mmHg·s/ml
Healthy	70	5.6	-	5.6	90	92	7,768	0.895	0.045
Heart Failure (HF)	90	3.8	-	3.8	70	182	2,682	1.010	0.045
HF+CF(9kpm)	90	5.3	4.9	0.4	75	157	2,008	0.760	0.045
HF+2PTP	90	5.3	2.7	2.6	75	164	1,859	0.760	0.045

Table 6.1: Baseline hemodynamic parameters for four simulation conditions: healthy, heart failure (HF), heart failure with continuous flow (CF) support modeled as an axial flow pump at 9,000 rpm, and heart failure with 30 ml TO2PTPRVAD counterpulse support. Note that the cardiac output increases from 3.8 to 5.3 L/min with both CF and 2PTP support, even though the VAD flow rate is 4.9 L/min for the CF device and only 2.7 L/min for the 2PTP counterpulse device. This is because counterpulse support preserves 2.6 L/min of aortic valve flow by ventricular contraction, while the CF device pumps during systole and therefore diminishes aortic valve flow to 0.4 L/min.
HR heart rate, *CO* cardiac output, *QVAD* ventricular assist device mean flow rate, *QAO* mean flow rate through the aortic valve, *MAP* mean arterial pressure, *LVESV* left ventricular end-systolic volume, *SW* stroke work, *SVR* systemic vascular resistance, *PVR* pulmonary vascular resistance.

chosen as the primary operating mode of the device because it maximizes aortic valve flow while providing full support.

For the open-loop simulation, the model was simplified to the systemic circulation only, which was defined to include the pulmonary veins, left atrium and ventricle and valves, and the systemic arterial tree consisting of the larger elastic vessels, smaller arterioles, and capillaries. The pulmonary circulation was removed for this simulation, not because its function and response are unimportant, but rather to eliminate it as an additional variable so that the entire possible range of right-sided conditions (for example, elevated pulmonary vascular resistance, right heart failure, or pulmonary edema) could be studied by changing the boundary conditions of the left-sided model. Ventricular function curves were obtained by varying the preload pressure in the open-loop model from 2 to 25 mmHg in 0.5 mmHg increments at constant afterload resistance listed in Table 6.1. At each preload pressure, the model was simulated until cycle-to-cycle flows and pressures converged. Once the model stabilized, flow rates were averaged over the final cardiac cycle to assess the metrics of cardiac output, VAD flow, and aortic valve flow.

For the closed-loop simulation, the pulmonary circulation was included so that changes in pulmonary vascular resistance (PVR), systemic vascular resistance (SVR), heart rate (HR),

inotropic state, and blood volume could be studied to observe the response with different modalities of ventricular support. Changes in PVR are of particular interest because elevated PVR is common in VAD patients [37] and can also occur during postural changes or the Valsalva maneuver [39, 38] and changes in PVR are used in cardiovascular modeling to test the propensity of ventricular suction with VAD support [41, 40, 42].

In the closed-loop configuration, each of the four parameters were independently varied from baseline values. Pulmonary vascular resistance was adjusted from 0.02 to 0.50 mmHg s/ml by modifying the resistance of the pulmonary vascular tree (R_{pt}). Systemic vascular resistance was adjusted from 0.2 to 1.4 mmHg s/ml by changing the resistance of the systemic vascular tree (R_{st}). Heart rate was adjusted from 40 to 140 bpm by modifying the RR interval of the simulation. The inotropic state was adjusted from 50% to 150% of the baseline ventricular elastance by scaling the active elastance (E_m) of both left and right ventricular. Finally, blood volume was adjusted by adding and removing up to 750 ml blood volume from the closed-loop simulation. All four cardiovascular and support conditions were modeled (healthy, heart failure, CF, and 2PTP counterpulse support). Twenty-five simulations were run for each parameter that was varied using values that were spaced equally between the minimum and maximum described above. For each simulation, the parameter was changed and then the simulation was run until the cycle-to-cycle pressures and flows converged. The primary purpose of this study was to assess whether overpumping occurred for the different types of support. This was assessed by ventricular suction, which was defined as left ventricular volumes less than 15 ml, which is the approximate volume when the ventricular walls could start to be drawn inward past the diameter of the protruding inflow tip. Cardiac output (CO), mean arterial pressure (MAP), and left ventricular end-systolic volume (LVESV) were recorded after each simulation converged.

6.3.2 Preload Sensitivity Simulation Results

Ventricular function curves are used to quantify the relationship between cardiac output and left ventricular preload at a constant afterload resistance. All four conditions are displayed in Figure 6.3: healthy; heart failure; heart failure with CF support; and heart failure with 2PTP synchronous counterpulsation. The solid gray line represents the cardiac output re-

	Preload Sensitivity L/min/mmHg			**Cardiac Output** L/min		
	Preload mmHg			**Preload** mmHg		
Condition	**20**	**10**	**5**	**20**	**10**	**5**
Healthy	.084	.170	.342	5.9	4.7	3.3
Heart Failure (HF)	.068	.116	.265	3.0	2.2	1.4
HF+CF(9kpm)	.083	.080	.086	5.9	5.1	4.7
HF+2PTP	.086	.156	.306	5.8	4.7	3.5

Table 6.2: Preload sensitivity and cardiac output from the open-loop model simulation, reported at three different preload pressures (5, 10, and 20 mmHg) and for all four different conditions simulated (healthy, heart failure, heart failure with continuous flow (CF) support at 9,000 rpm, and heart failure with 30ml 2PTP counterpulse support).

sponse to changes in preload for heart failure and the dashed gray line represents the healthy condition and also provides an ideal target for VAD support. Both the CF device and 2PTP counterpulse support provided a substantial increase in cardiac output, but had different sensitivities depending on preload. Preload sensitivity is quantified by the slope of a tangent line of the ventricular function curve at a specific preload, and is expressed in terms of the change in cardiac output (L/min) per change in pressure (mmHg). Preload sensitivities for all four conditions at preloads of 5, 10, and 20 mmHg are listed in Table 6.2.

At higher preloads of 20 mmHg, both modalities of support provide similar cardiac outputs compared to the healthy heart (5.9 L/min for the healthy heart, 3.0 for heart failure, 5.9 with CF support, and 5.8 with 2PTP counterpulse support) and provide physiological responses to ventricular preload in terms of preload sensitivities (0.084 L/min/mmHg for the healthy heart, 0.068 for heart failure, 0.083 with CF support, and 0.086 with 2PTP counterpulse support). As preload decreases, the cardiac outputs and preload sensitivities of the different pumping modalities start to diverge. At nominal preloads of 10 mmHg, the cardiac outputs are still fairly similar (4.7 L/min for the healthy heart, 2.2 for heart failure, 5.1 with CF support, and 4.7 with 2PTP counterpulse support) but the sensitivity with 2PTP support increases to match the healthy heart while the preload sensitivity with CF support does not adjust (0.170 L/min/mmHg for the healthy heart, 0.116 for heart failure, 0.080 with CF support, and 0.156 with 2PTP counterpulse support). At low preloads of 5 mmHg, the CF device overpumps the circulation compared to the healthy heart and 2PTP

support (3.3 L/min for the healthy heart, 1.4 for heart failure, 4.7 with CF support, and 3.5 with 2PTP counterpulse support) and the difference in preload sensitivity between the modalities becomes even more pronounced (0.342 L/min/mmHg for the healthy heart, 0.265 for heart failure, 0.092 with CF support, and 0.306 with 2PTP counterpulse support). These CF sensitivities compare well to other published sensitivity values for the HMII in the literature, for example 0.095 L/min/mmHg reported by Khalil, et al (ref) and 0.09 reported by Salamonsen, et al [35].

This difference in cardiac output and preload sensitivity for the different modalities of support can be explained by the relationship between aortic valve flow and VAD flow, which is shown in Figure 6.4. With 2PTP counterpulse support, aortic valve flow is preserved because the VAD temporarily pauses pumping and allows the ventricle to contract in systole, and then the VAD provides an early diastolic counterpulse to boost cardiac output [74]. The preserved aortic valve flow is physiologically sensitive to preload, so cardiac output is automatically adjusted. This is demonstrated by the ventricular function curve with 2PTP support, which is almost a direct offset from the healthy heart failure curve. The 2PTP is positive displacement, so it provides a cardiac output offset to the ventricular function curve while allowing the native heart function and eject blood through the aortic valve to control the shape of the ventricular function curve. Continuous flow devices pump throughout the cardiac cycle, effectively shunting flow during systole so that the majority if not all of the cardiac output goes through the device, which is not able to provide an inherent physiological response to preload [35]. As a result, as preload pressure drops, the CF VAD provides too much flow compared to the failing or even healthy heart.

Baseline results for the closed-loop model with the initial SVR, PVR, and HR settings are provided in Table 6.1. From baseline heart failure, both CF and 2PTP counterpulse support boost cardiac output from 3.8 to 5.3 L/min, but the 2PTP does so with only half the VAD flow (2.7 for the 2PTP compared to 4.9 L/min for CF). This is because counterpulse support preserves more aortic valve flow (2.6 L/min with 2PTP compare to 0.4 L/min with CF). Ventricular unloading can be assessed for these different support modalities with left ventricular stroke work (LVSW), which is calculated as the area of the LV pressure-volume loop and represents the work done by the ventricle during one cardiac cycle. Both modalities

of support reduce stroke work from 2,682 mmHg ml in heart failure (down to 1,859 with 2PTP support and 2,008 with CF support). The difference and clinical significance between these two may be negligible, but is highlighted here because this may be somewhat counterintuitive given that the ventricle ejects more blood through the aortic valve with 2PTP counterpulse support. These results demonstrate that the 2PTP provides comparable unloading in terms of LVSW with only half the VAD flow compared to CF support. This is because the ventricle is still contracting and doing the work of ejecting blood with CF support except that it pumps through the VAD rather than through the aortic valve.

Results of PVR, SVR, HR, inotropic variation, and blood volume changes are shown in Figure 6.5. Mean cardiac output, aortic valve flow, VAD flow, left ventricular end-systolic volume, and left atrial pressure are shown as a function of the varied parameters (PVR, SVR, HR, and percent inotropic change). Of particular interest are the PVR results, which demonstrate the most difference between the different types of support. As PVR increases, cardiac output with CF support remains higher than cardiac output with 2PTP counterpulse support, as a result left ventricular suction (defined as left ventricular volume less than 15 ml) begins to occur when PVR is greater than 0.35 mmHg s/ml. This finding is confirmed by similar studies that experienced suction at a PVR of 0.375 mmHg s/ml [41].

The results of SVR, HR, inotropic state, and blood volume in Figure 6.5 all have similar results in terms of cardiac output, and demonstrate that the response to changes in SVR is fairly similar for the both CF and 2PTP counterpulse support and that both appear to be offsets from the heart failure curve. For low HR and inotropic state, CO with CF support is higher than 2PTP support, but never enough to cause left ventricular suction.

Figures 6.6 and 6.7 shows arterial and left ventricular pressure curves, aortic and VAD flow curves, and left ventricular pressure-volume loops for the closed-loop simulation with CF and 2PTP counterpulse support after a step change in PVR from 0.04 to 0.37 mmHg s/ml at 5 seconds on the plot. This simulation is included to provide an example of how changes in SVR alter hemodynamics and shift the left ventricular PV loops. With CF support, the small amount of aortic valve flow that was present before the PVR increase very quickly dropped to zero as the VAD flow took over the entire CO. Left ventricular volume continued

to drop significantly and with it the pressure the ventricle was able to generate. Eventually, suction events began to occur as the ventricular volume reached a critical minimum. With 2PTP counterpulse support, native aortic valve flow was preserved, allowing the left ventricle to provide a large margin of adjustment to CO when the preload dropped after the PVR increase. This reduction in CO demonstrates that the ventricle is not overpumped and no suction events occur.

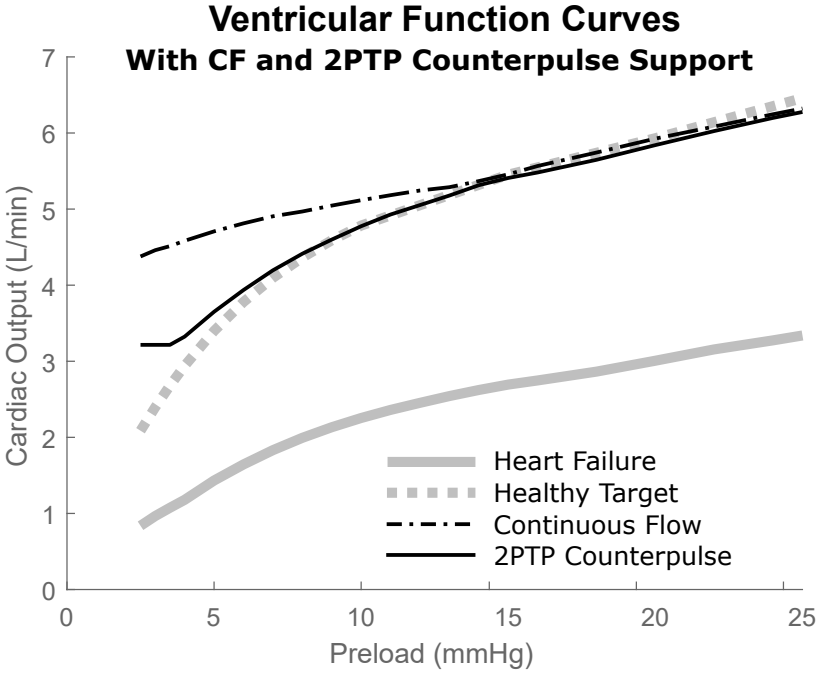

Figure 6.3: Simulated ventricular function curves from the open-loop cardiovascular system model with continuous flow (CF) support and 2PTP counterpulse support. As expected, both VADs boost cardiac output back to healthy levels, but the CF device overpumps the circulation at low preloads compared to a normal healthy response. 2PTP counterpulse support does not overpump at low preloads, but follows the healthy nonlinear response.

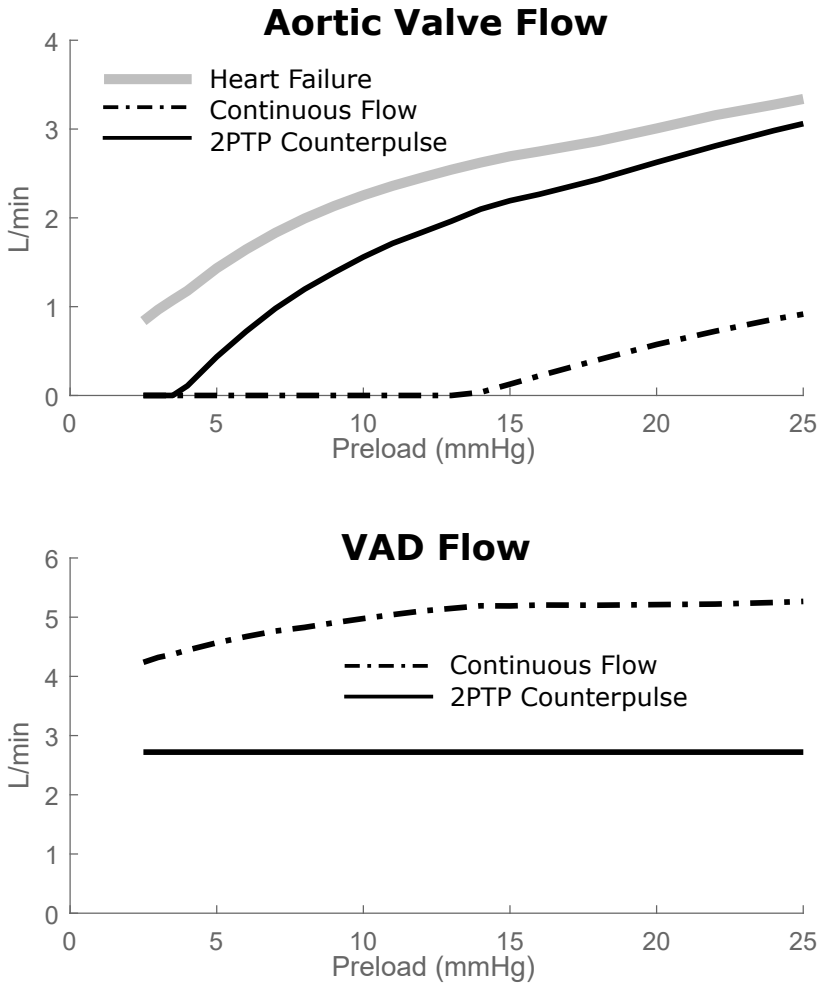

Figure 6.4: Aortic valve flow and VAD flow as a function of ventricular preload. With 2PTP counterpulse support, much of the native flow through the aortic valve is maintained. It is this flow that remains physiologically sensitive to preload changes and produces the nonlinear response seen in Figure 6.3. For CF support, aortic valve flow is significantly diminished and becomes zero at moderate preloads at which point the VAD takes over the entire cardiac output, which does not have physiological sensitivity to preload and causes overpumping at low preloads.

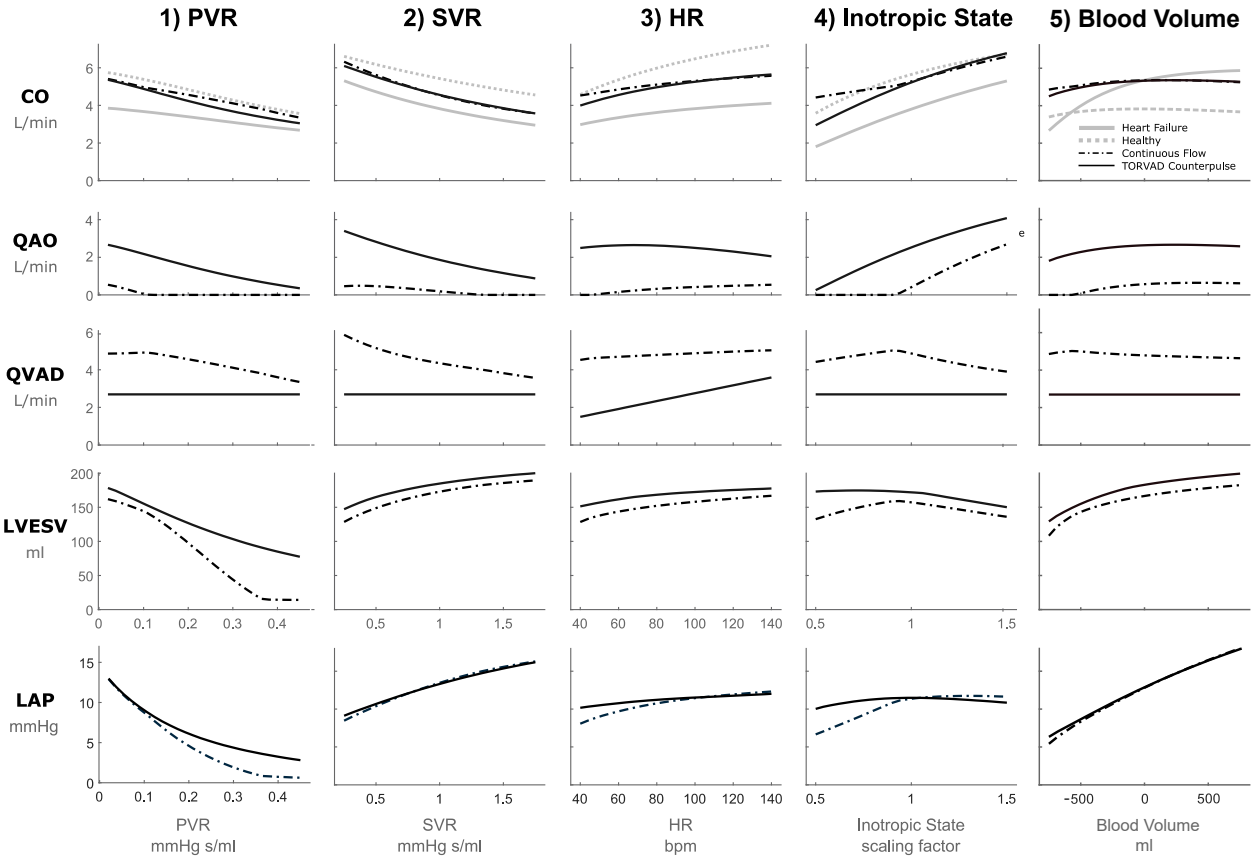

Figure 6.5: Cardiac output, aortic valve flow rate, VAD flow rate, left ventricular end-systolic volume (LVESV), and mean left atrial pressure (LAP) for CF and 2PTP (TORVAD) counterpulse support for changes in (1) PVR pulmonary vascular resistance (PVR), (2) systemic vascular resistance (SVR), (3) heart rate (HR), (4) inotropic state, and (5) blood volume. Healthy and heart failure cardiac output values are also displayed for comparison.

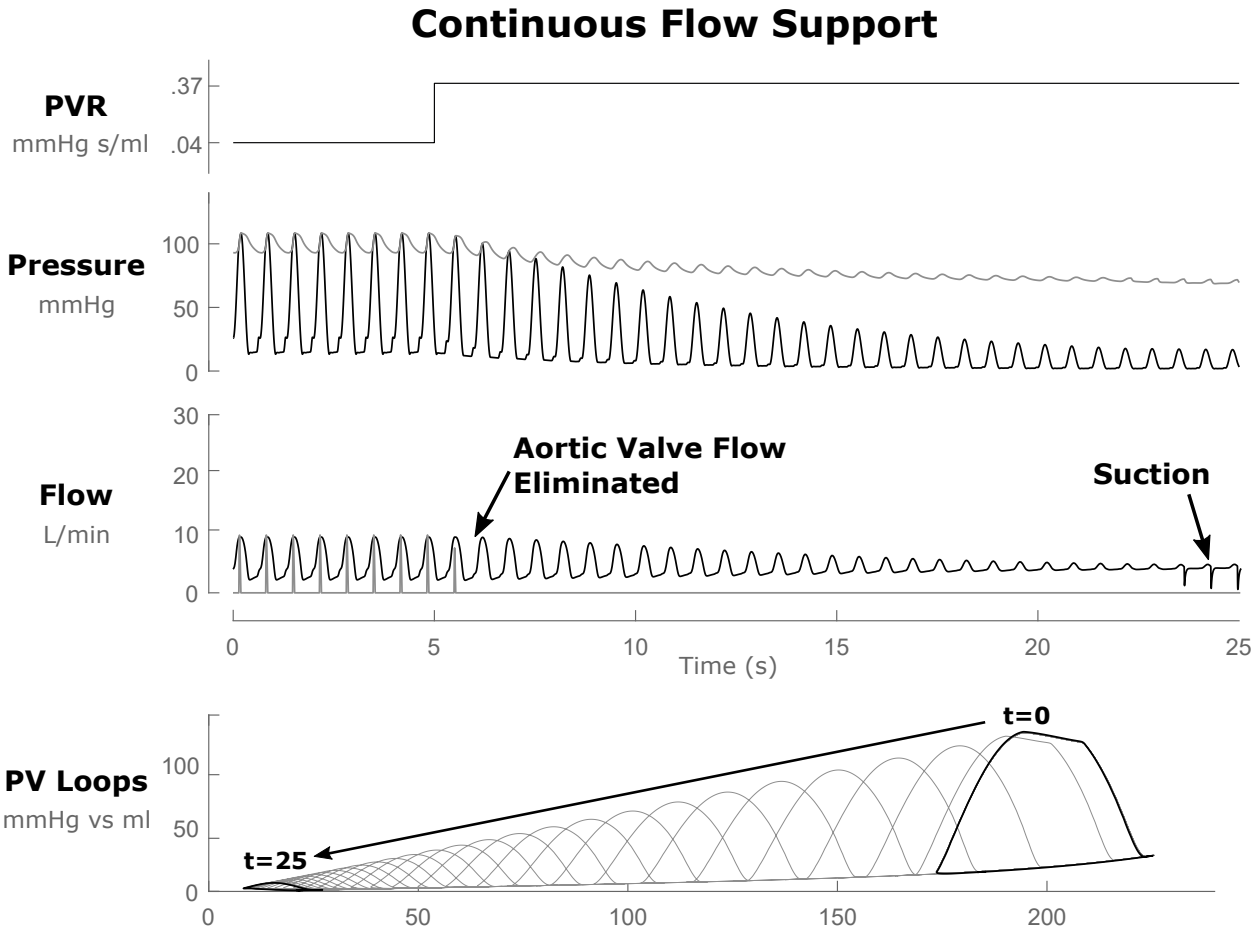

Figure 6.6: Hemodynamics (pressure and flow) and pressure-volume (PV) loop responses to a step-change in pulmonary vascular resistance in the closed-loop simulation. When pulmonary vascular resistance is increased from 1 to 2 Wood units, the continuous flow overpumps the circulation resulting in low ventricular volumes and ventricular suction events.

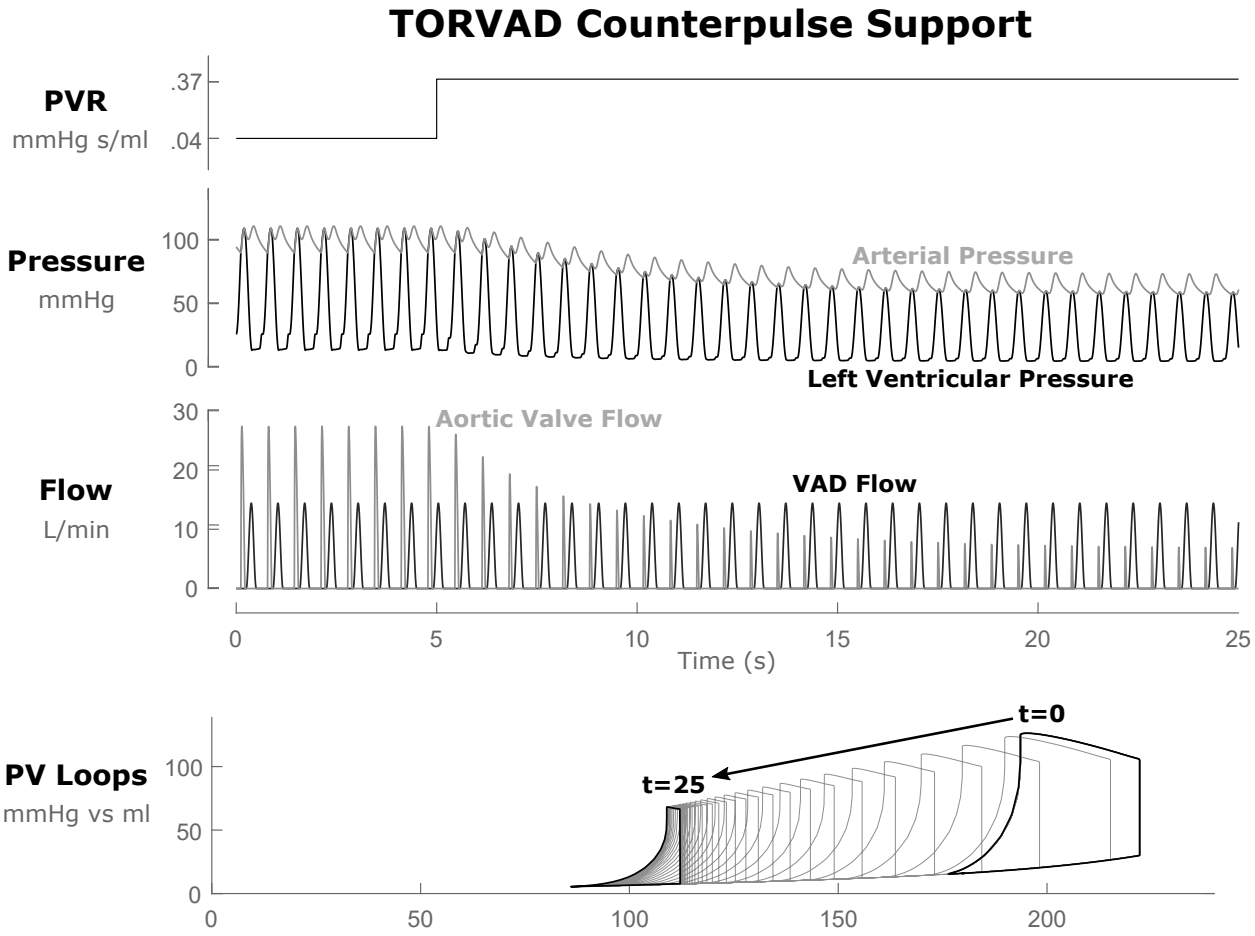

Figure 6.7: Hemodynamics (pressure and flow) and pressure-volume (PV) loop responses to a step-change in pulmonary vascular resistance in the closed-loop simulation. When pulmonary vascular resistance is increased from 1 to 2 Wood units, 2PTP (TORVAD) counterpulse support preserves aortic valve flow that physiologically responds to the change in preload, which reduces cardiac output and prevents overpumping.

6.3.3 Preload Sensitivity Simulation Discussion

Passive autoregulation of cardiac output by the left ventricle is critical for maintaining a healthy response to physiological feedback. Ventricular preload varies throughout the day depending on the patient's physical activity, volume status, or pathological state [32]. Continuous flow devices are set to a constant rotational speed by the clinician at periodic follow-up visits, but cannot automatically adjust flow throughout the day in response to physiological need.

Continuous flow VADs pump throughout the cardiac cycle. The highest VAD flow rate is during systole because blood that would normally be ejected by the left ventricle through the aortic valve is instead shunted through the VAD to the point where the aortic valve only opens sporadically or often not at all [75]. This can result in aortic valve commissural fusion, aortic insufficiency, and outflow tract and aortic root thrombus in CF VAD recipients [76, 77]. Additionally, when aortic valve flow is diminished and the entirety of the CO is taken over by the CF device, preload sensitivity significantly deviates from the normal response at low preloads, which can lead to overpumping. Active physiological control methods have been proposed that would modulate flow based on various feedback mechanisms to overcome this deficiency, but these methods have not yet been implemented in clinical practice [17, 73]. Many of these algorithms specifically try to recreate the Starling response using indwelling pressure transducers to measure preload and adjust pump flow to follow prescribed ventricular function curves [35, 78]. Some indwelling pressure sensors can be prone to thrombus formation and long term drift, which compromise accurate measurements, and long-term reliable solutions have not yet emerged [17]. Others have proposed estimation of preload using pump metrics such as the differential pump pressure or the pulsatility index to drive a Starling-like c,ontrol [79, 26, 38]. However, these methods also require indwelling sensors or rely on pump-derived estimations of pressure and flow that are prone to inaccuracies outside of steady-state conditions or due to viscosity variation.

Synchronous counterpulsation with the 2PTP device preserves native aortic valve flow. By operating the pump in this mode, the 2PTP briefly ceases to pump blood in systole allowing the ventricle to eject normally through the aortic valve. By preserving native aortic flow

with counterpulse support, patency of the native aortic valve is maintained and the autoregulatory aspect of the heart is preserved in the native aortic valve flow, thereby restoring the physiologic preload sensitivity of the cardiovascular system. Synchronous counterpulsation might be considered a form of both active and passive control. It's active in the sense that pump ejections are synchronized to the cardiac cycle such that the pump flow rate automatically changes based on the heart rate and the pump ejection occurs during diastole, but passive in the sense that cardiac output responds to preload due to the preservation of the native aortic ejection without the need for additional pressure sensors or pump flow rate changes.

One limitation of 2PTP counterpulse support is that preload sensitivity depends on the remaining preload response of the failing ventricle. The 2PTP has a fixed 30 ml stroke volume that is insensitive to changes in preload. It is only by preserving aortic valve flow with counterpulsation that a physiological response to preload remains. If ventricular function were to significantly deteriorate, then the 2PTP may need to operate asynchronously to take over the entire CO. Similarly, if ventricular function improves, then the 2PTP ejection could be adjusted to a different time in the cardiac cycle, or the pump could eject every other heart beat.

Salamonsen, et al., specified three requirements for Starling-like control [79]: (a) preload sensitivity should be comparable to that of the left ventricle; (b) it should be maximal at low preloads and fall nonlinearly and become negligible at high preloads; and (c) the amplitude of the Starling curve should scale to compensate for metabolic requirements during exercise or stress. The results demonstrated here for 2PTP counterpulse support satisfy the first two requirements. While preload sensitivity has been considered one of the most important aspect of regulating cardiac output, afterload, heart rate, and inotropic state are also important regulating mechanisms [32, 33]. The results of the closed-loop model in Figure 6 show that the response to changes in SVR is fairly similar for both CF and 2PTP counterpulse support. Both appear to be offsets from the heart failure curve and have the same general shape of the compared to the healthy or failure curves. This may seem to be in contrast to claims that CF devices have three to four times the afterload sensitivity of the healthy heart [80, 67], but the referenced study did not account for the increased preload that can also occur with increased

afterload. As CO drops, preload increases, which makes ventricular contractions stronger. Similar responses are also shown for increased heart rate and inotropic state compared to the healthy and failing heart, at least in terms of the general shape of the curves. There is a greater difference between the modalities of support as HR and inotropic state decrease where CF support produces more cardiac output than with 2PTP support, but these may not be clinically significant.

One of the limitations of this study is that SVR, PVR, HR, inotropic state, and blood volume were individually varied in the closed-loop study. This was done to isolate their effect from one another, but in reality they may vary simultaneously, along with other unaccounted for parameters such as vascular tone. A multivariable analysis may be helpful to answer these questions and motivates future work.

6.4 Summary and Conclusion

This chapter has studied baseline physiological control for a 2PTP pump with synchronous counterpulse support. By pumping in this way, the 2PTP works in cooperation with the heart to increase cardiac output and provide a physiological response to preload pressure by maintaining native aortic valve ejection during systole. Preload sensitivity is an important feedback mechanism for cardiac output autoregulation in response to metabolic demand, which varies from activity level, fluid volume, or pathological status. Continuous flow devices are less sensitive to preload compared to the normal healthy heart, especially at low preloads where they overpump the system. Counterpulse support with the 2PTP preserves aortic valve flow, provides physiological sensitivity across all preload conditions, and reduces the risk of suction at low preload pressures. This should prevent overpumping and minimize the risk of suction and septal wall shift.

In addition to providing physiological cardiac output preload sensitivity, the pump flow rate also automatically responds to heart rate changes in synchronous mode. Future research could study the hemodynamics that result from different operating modes such as asynchronous pumping, and could explore ways to detect and provide an increased cardiac output for exercise response.

Part III

2PTP Model

Chapter 7. 2PTP Variable Structure Model

This chapter develops a variable structure 2PTP model that can be used to simulate pump dynamics. An algorithmic bond graph approach is presented that is used to generate state equations and simulate the system.

Chapter 8. Reduced-Order Model

This chapter develops a simplified reduced-order linear 2PTP model of pumping and transition by ignoring nonlinear effects and the annular leakage between the piston and torus walls. This model is used to design control and estimation methods.

Chapter 7

2PTP Variable Structure Model

This chapter develops a variable structure 2PTP model that can be used to simulate pump dynamics. An algorithmic bond graph approach is presented that is used to generate state equations and simulate the system.

Models are helpful for understanding dynamics and designing and testing estimation and control of new or complex systems. The 2PTP is a new class of pump with several interacting dynamics. A model of the 2PTP would help for understanding and the quantify the dynamics of the pump and would serve as a basis for improving and testing the control of the device in simulation.

The 2PTP system has a few key components that need to be modeled:

- Brushless DC Motors
- Pistons
- Magnetic coupling between the motor and pistons
- Fluid flow and pressure in the pump and inflow and outflow cannulas

The dynamics involved with the motors, pistons, and magnetic coupling models are relatively straightforward and are briefly introduced in Section 7.1. The dynamics of the flow and pressure in the pump are more complicated, and are developed in Section 7.2.

7.1 Motor and Piston Model

Each piston is independently controlled by a brushless DC motor. The motor and the piston are magnetically coupled by magnets on an arm of the motor that interact with magnets sealed inside of the piston. The dynamic model for each element (motor, piston, and magnetic coupling) are developed individually and are then incorporated into subsystem models that are connected to the pump flow model developed in Section 7.2.

7.1.1 Motor Model

The pump uses two independent brushless DC motors. A bond graph (see Figure 7.1) is used to show the structure of the motor model. An input voltage V_{in} is applied to coils with electrical resistance R_e. Electrical inductance in the motors coils is small and ignored. Motor current i_m is electromagnetically converted to torque T_m by the motor gyrator constant k_e. The motor has mass moment of inertia J_m and damping b_m.

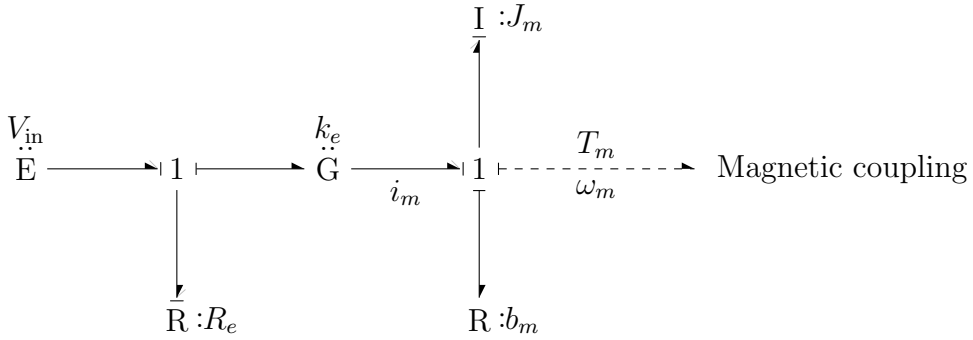

Figure 7.1: Bond graph model of a brushless DC motor. Causality assignments of the bond graph depend on the assignment of the power bond to the magnetic coupling, which will be shown later to return 'effort' to the motor subsystem.

From the bond graph and causality assignments, it can be seen that there is only one energetic state, the angular velocity of the motor.

$$J_m\dot{\omega}_m = k_e i_m - b_m\omega_m - T_m \tag{7.1}$$

The motor position is found integrating the velocity

$$\theta_m = \dot{\omega}_m \tag{7.2}$$

The torque from the magnetic coupling T_m will defined later. The motor current i_m is a function of the input voltage, back emf gyrator coefficient, and coil resistance

$$i_m = \frac{V_{\text{in}} - k_e\omega_m}{R_e} \tag{7.3}$$

Substituting the current into the dynamic equation for the rotational velocity, the state equations become

$$\dot{\omega}_m = \frac{1}{J_m}\left[\left(b_m + \frac{k_e^2}{R_e}\right)\omega_m - T_m + \frac{k_e}{R_e}V_{\text{in}}\right] \tag{7.4}$$

$$\theta_m = \dot{\omega}_m \tag{7.5}$$

7.1.2 Piston Model

The pistons are zirconia ceramic on the external surfaces and are suspended in the middle of the torus lumen using two zirconia rails on the axial faces of the torus so that there is a 3-4 mil (75-100 μm) annular gap between the piston and torus walls. Controlling this gap minimizes shear stress in the blood. The rail also serves to constrain piston motion within the toroidal chamber to one degree of freedom, the angular position θ_p, and prevents zirconia piston interaction with the titanium torus walls. The zirconia-zirconia interaction at the small interface generates micro-hydrodynamic lubrication by way of lubrication with a plasma-gel that provides a thin protective protein buffer between the ceramic surfaces [81, 82, 83, 84]. While this mixed-lubrication minimizes wear, there is still friction that should be accounted for in the model.

Many attempts have been made over the years to model friction (viscous, Coulomb, Stribeck, rising static friction, frictional memory, pre-sliding displacement, etc) and to control for its effects (stiff control, model based feedforward, adaptive strategies, variable structure control, etc) [85]. More recently, observer-based techniques have been implemented [86, 87, 88]. Frictional torque should be minimal in the device compared to the other sources of torque (the pressure across the piston and torque from the magnetic coupling for example), so the model should strive for simplicity in approach. For the time being, a linear friction coefficient is assumed.

A bond graph (see Figure 7.2) was used to develop the model for pistons dynamics. The piston has mass moment of inertia J_p, and frictional damping b_p.

From the bond graph and causality assignments, it can be seen that there is only one state, the angular velocity of the piston.

$$\dot{\omega}_p = \frac{1}{J_p}\left(T_m - b_p\omega_p - ArP\right) \tag{7.6}$$

The torque from the magnetic coupling T_m will defined later. A and r are the area and radius of the piston, and P is the pressure on across the piston which will be defined in the section on the pump model.

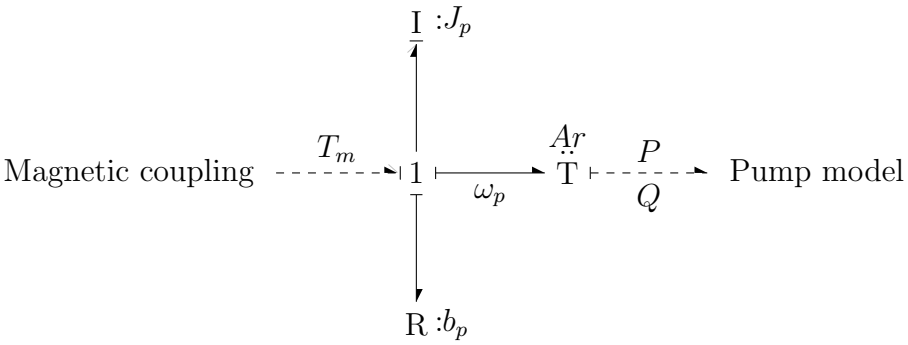

Figure 7.2: Bond graph model of the piston dynamics. Causality assignments of the bond graph depend on the assignment of the power bond to the magnetic coupling, which will be shown later to return 'effort' to the piston subsystem, as well as the assignment to the pump model, which will be shown later to return 'effort' the piston subsystem as well.

Piston position is found by integrating the velocity

$$\theta_p = \dot{\omega}_p \tag{7.7}$$

7.1.3 Magnetic Coupling Model

The motor and pistons are coupled by magnets. Magnets are configured in Halbach arrays to maximize the magnetic flux in the gap, increase magnetic coupling torque, and minimize angular displacement between the piston and motor. An illustrated schematic of this coupling is shown in Figure 7.3.

The magnetic coupling has been simulated with finite element modeling (FEM) to which a sinusoidal curve is fit (see Figure 7.4). This provides the nonlinear torque-displacement constitutive relationship.

$$T_m = T_{\max} \sin\left(2\pi \frac{\theta}{4 \cdot \theta_{\mathrm{e}}}\right) \tag{7.8}$$

where $T_{\max}$ is the maximum torque, θ is the displacement angle between the motor and piston, and θ_e is the displacement angle when the piston 'escapes' the motor (when the piston and motor become decoupled). This model is only valid from $-\theta_e < \theta < \theta_e$, but the magnetic coupling should be strong enough so that the the piston and motor never decouple, so the model does not need to operate beyond this point.

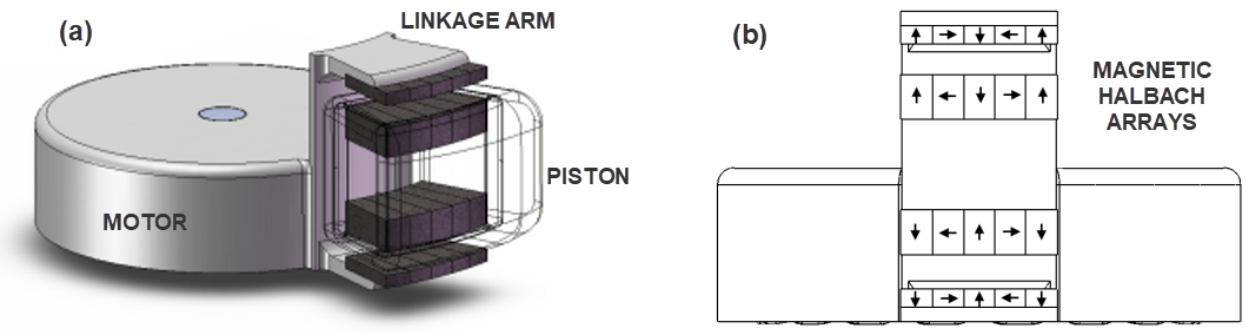

Figure 7.3: Illustration of the magnetic coupling between the motor and the piston. The motor has a linkage arm, with magnets above and below the piston. There are also magnets within the piston. These magnets interact with each other through the pump housing (not shown) to couple the motor and piston motion and position. Magnetic Halbach arrays are used to concentrate flux in the coupling gap and maximize the flux density.

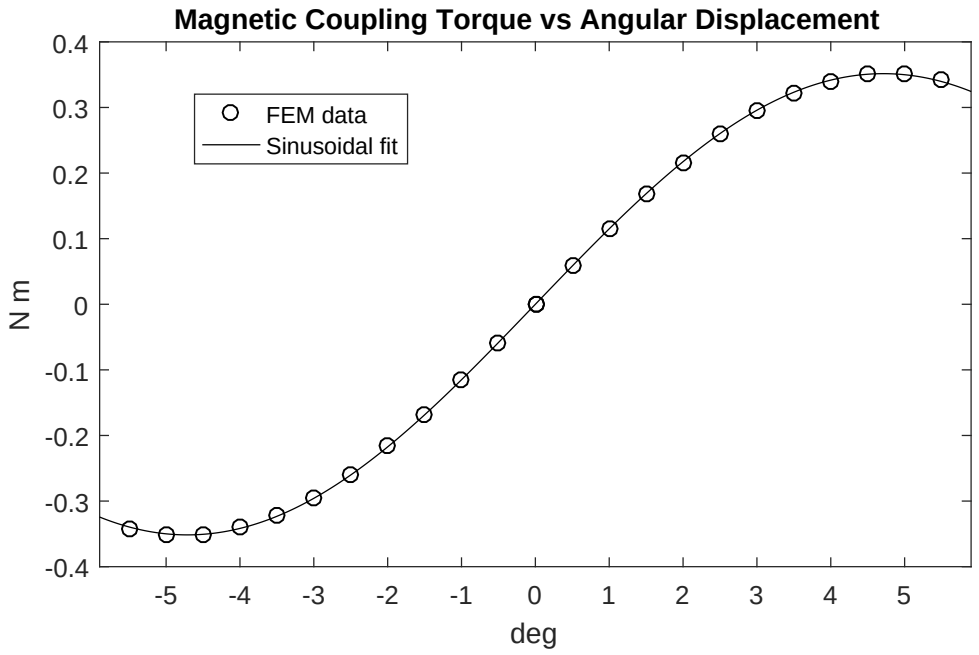

Figure 7.4: Magnetic coupling torque vs angular displacement between the motor and piston. Finite element modeling (FEM) was performed to estimate the torque for angular displacements at 0.5 degree intervals. A sinusoidal approximation fits the data very well. Piston decoupling (or 'escape') is when the piston and motor separate from each other. This occurs at ± 5 degrees, at which point the slope of the coupling torque reverses and becomes unstable.

A complete bond graph for the motors, pistons, and magnetic coupling between them is shown in Figure 7.5. Causality is assigned with the assumption that the piston will provide flow (Q) to the pump model and receive effort (P), this will be shown to be the case later in the pump model section. In actuality, the entire model should be drawn before causality is assigned, but has been done so here in anticipation of the final form so that the independent states of the motor-piston subsystem can be seen.

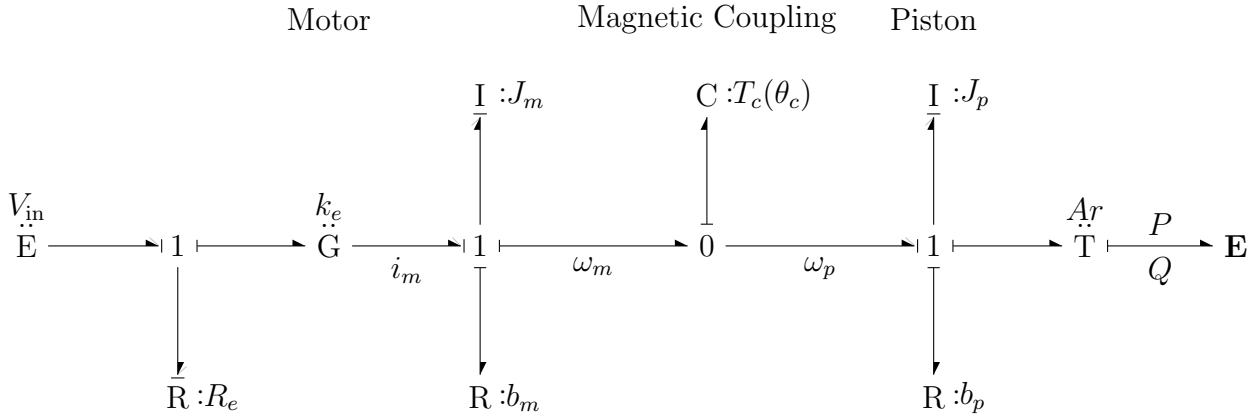

Figure 7.5: Bond graph model for the motor, magnetic coupling, and piston dynamics. This model could couple to the pump model by giving the flow Q and receiving the back-pressure on the piston P.

7.1.4 Motor and Piston State Equations

The motor-piston subsystem has three energetic states, the angular velocities of the motor ω_m and piston ω_p, and the angular displacement between the motor and piston ($\theta_c = \theta_p - \theta_m$). The absolute positions of the motor and pistons will be tracked as well, which adds an 'information state'. The state equations for the motor and piston subsystem are:

$$\dot{\omega}_m = \frac{1}{J_m}\left[\left(b_m + \frac{k_e^2}{R_e}\right)\omega_m - T_{\max}\sin\left(2\pi\frac{\theta_m - \theta_p}{4\cdot\theta_{\text{e}}}\right) + \frac{k_e}{R_e}V_{\text{in}}\right] \tag{7.9}$$

$$\dot{\omega}_p = \frac{1}{J_p}\left[T_{\max}\sin\left(2\pi\frac{\theta_m - \theta_p}{4\cdot\theta_{\text{e}}}\right) - b_p\omega_p - ArP\right] \tag{7.10}$$

$$\dot{\theta}_m = \omega_m \tag{7.11}$$

$$\dot{\theta}_p = \omega_p \tag{7.12}$$

7.2 Pump Flow and Pressure Model

The motor-piston subsystem developed above describes how the input (motor voltage) drives the piston motion. The pistons move within the toroidal pumping chamber to produce flow in and out of the pump. A schematic of the pump is shown in Figure 7.6.

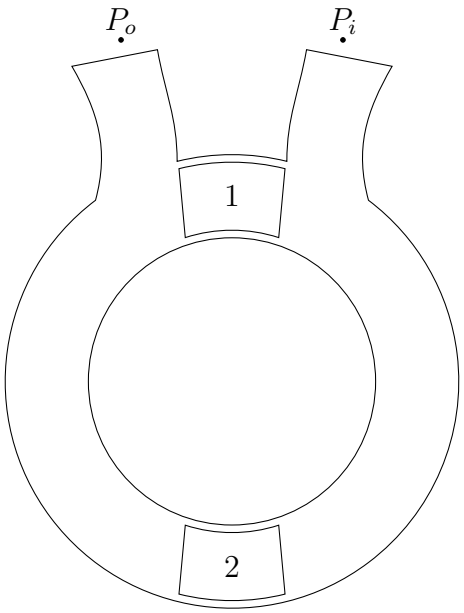

Figure 7.6: 2PTP schematic. Two pistons, labeled 1 and 2, are within the toroidal shaped pumping chamber. The pump inflow is on the right with inflow pressure P_i and the pump outflow is on the left with outlet pressure P_o.

Two-piston pumping in a toroidal chamber is not straightforward, there are many issues to be considered:

- Leakage flow in the annular gap between the piston and torus
- Fluid inertia and resistance effects throughout the torus and cannulas
- The effects of inflow and outflow occlusion as the pistons transition across the ports.

To understand these effects, a model of the flow and pressure in the pump was developed. The input to this subsystem is the piston 'flow' from the motor-piston subsystem described above. The systems will be linked by this 'power bond', which will return an 'effort' (pressure) to the motor-piston subsystem.

7.2.1 Pumping Modes

Under normal operation, the pump has two repeating sequential modes: pumping and transition. A third mode fault mode (shunting) can occur if the pistons are not controlled well. These three modes are described below and are schematically illustrated in Figure 7.7.

1 - Pumping. In this mode, one piston remains stationary in the 'hold' position while the other piston (the 'drive' piston) rotates around the torus, simultaneously aspirating blood from the inflow (left ventricle) and ejecting blood to the outflow (aorta). Piston motion is coupled to the fluid in the inflow and outflow and directly relates to flow in and out of the pump.

2 - Transition. This mode occurs between pumping strokes when the pistons move together to exchange functional roles. During this mode, the inflow and outflow ports are partially or totally occluded.

3 - Shunt. This is a possible fault mode that should not happen during normal operation of the pump. If the pistons are controlled poorly, there is a potential for a shunt to develop between the inflow and outflow ports which would allow backflow. A robust model of the pump may need to include this mode if the effects of poor control need to be quantified.

This pumping mechanism is complex. The pistons exchange functional roles causing the pressure differential to change sign on the pistons, the pistons transition across the inflow and outflow ports affecting the fluid resistance and introducing leakage pathways that appear and disappear, and the pistons allow annular leakage. The pistons are controlled by magnetically coupled motors which much be precisely controlled to avoid piston collision, shunts, and harsh vibrations. A model of the pump would help for designing that control. The purpose of this chapter is to develop that model and to identify which elements are important to include.

1) Pumping (one piston pumps while the other remains stationary to act as a virtual valve)

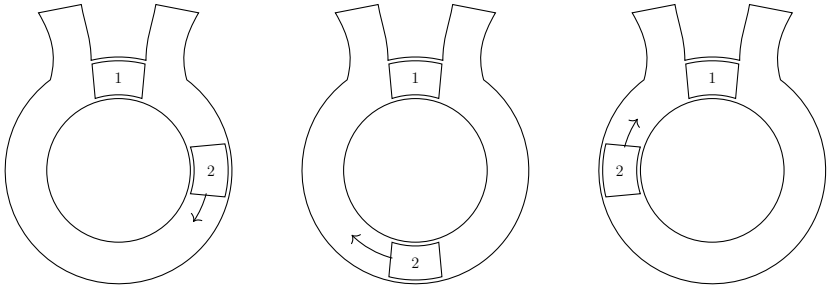

2) Transition (this mode occurs when the pistons are exchanging functional roles)

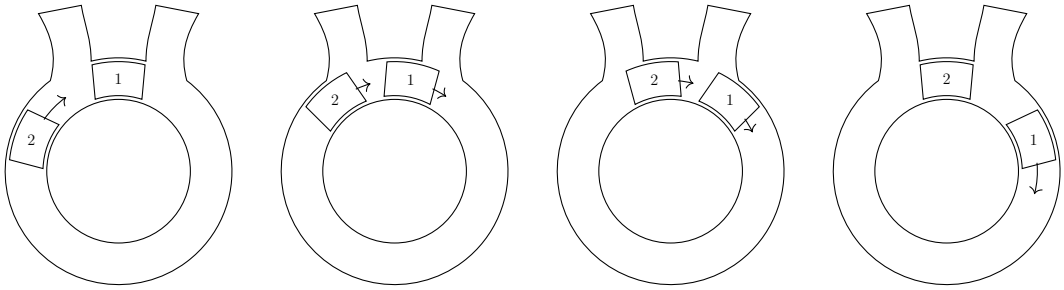

3) Shunt (this is a special case, and should not occur if the pistons are controlled well)

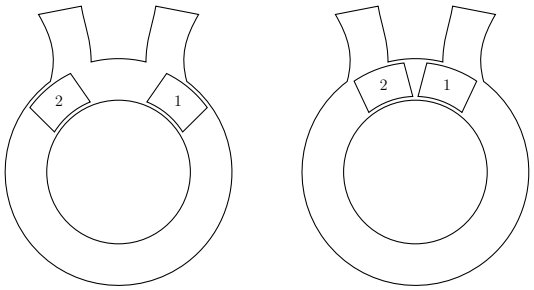

Figure 7.7: Schematics representations of the three pumping modes

7.3 Building the Pump Flow and Pressure Model

This section assembles the pump flow and pressure model in stages. Starting from a simple positive displacement model, and then adding pieces along the way to include effects such as leakage, port occlusion, and switching.

7.3.1 A Simple Positive Displacement Model

To start, a simple model of a positive displacement pump was formulated. This model assumes zero leakage around the pistons and a common pressure in the torus fluid volumes between the pistons. A bond graph for this model and a schematic of the pump is shown in Figure 7.8. For the purposes of the pump model, it is assumed that piston flows Q_1 and Q_2 are provided by the piston model (this will be shown later to be the case).

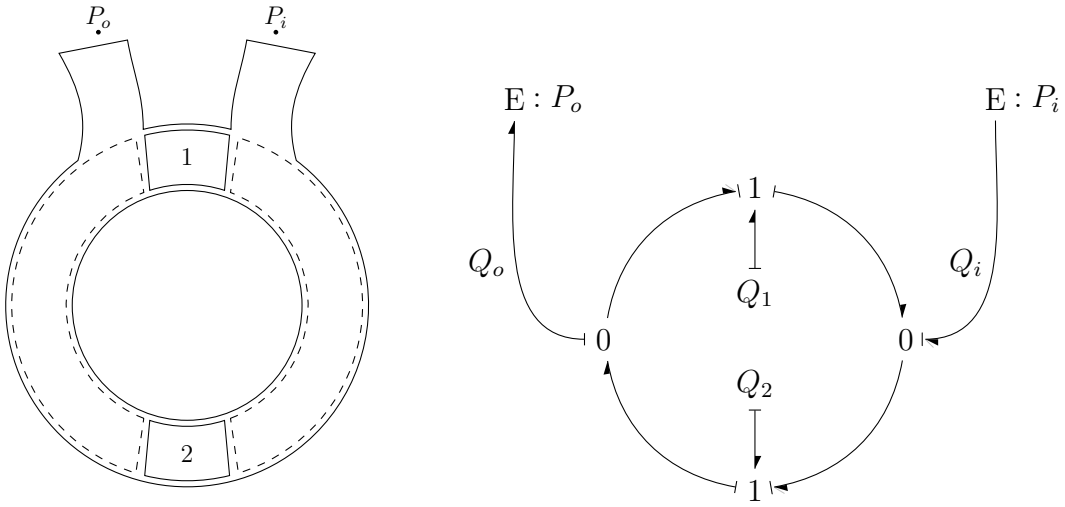

Figure 7.8: A simple positive-displacement pump model. The model is deterministic. There are no independent states. Piston flows Q_1 and Q_2 are provided by the piston model. The flow in and out of the pump is simply $Q_i = Q_o = Q_2 - Q_1$

7.3.2 Incorporate Piston Leakage

There is a annular gap between the piston and torus wall that keeps the surfaces separated to prevent wear and also reduces blood damage by minimizing shear produced in the gap. Blood is a mixture of cells (red blood cells, white blood cells, platelets) and plasma (a fluid which has the viscosity of water, but which also contains several dissolved proteins). The interaction of these different components makes blood behave in a non-Newtonian way, with a higher viscosity at very low shear rates. But this phenomenon is only important at extremely low shear rates, and for the purposes of this model, blood is assumed to be a Newtonian fluid with a density of 1025 kg/m^3 and viscosity of .0035 Pa·s.

The Reynolds number ($R_e = \rho U h/\mu$) quantifies the inertial forces relative to the viscous forces. For low Reynolds numbers, viscous flow dominates and laminar flow could be assumed. For a gap of 100 μm and a velocity of 1 m/s (approximate maximum velocity of the piston), the Reynolds number is very low (29). For parallel plates, the entrance length can be estimated by $L_e = .06hR_e$.

The Reynolds number is low ($R_e < 100$) and the entrance length is short ($L_e/L << 1$), therefore fully-developed laminar flow is assumed [89]. With that assumption, the leakage around the pistons can be analytically estimated by two mechanisms: Couette (motion-driven) and Poiseuille (pressure-driven) flow. The length of the gap varies as a function of the radius and the swept angle of the pistons, but for simplicity, the mean piston radius r_m and mean swept angle θ_m will be used. The velocity profile in the gap is defined by

$$u = \frac{1}{2\mu}\frac{\Delta P}{r_m\theta_m}\left(y^2 - yh\right) + \frac{r_m\omega_p y}{h} \tag{7.13}$$

where ΔP is the pressure drop across the piston, h is the gap height, and y is the location across the gap from 0 at the torus wall to h at the piston wall.

The velocity profile can be integrated across the gap and multiplied by the piston circumference C to obtain the leakage flow rate.

$$Q_L = C\int_0^h u dy \tag{7.14}$$

$$Q_L = C\int_0^h \left[\frac{1}{2\mu}\frac{\Delta P}{r_m\theta_m}\left(y^2 - yh\right) + \frac{r_m\omega_p y}{h}\right] dy \tag{7.15}$$

$$Q_L = C\left[\frac{1}{2\mu}\frac{\Delta P}{r_m\theta_m}\left(\frac{y^3}{3} - \frac{y^2 h}{2}\right) + \frac{r_m\omega_p y^2}{2h}\right]_{y=0}^{y=h} \tag{7.16}$$

$$Q_L = C\left[-\frac{h^3}{12\mu}\frac{\Delta P}{r_m\theta_m} + \frac{r_m\omega_p h}{2}\right] \tag{7.17}$$

The leakage flow through the annular gap produces a viscous drag on the piston. The shear stress on the piston can be found by taking the partial derivative of the velocity with respect to y evaluated at the piston surface.

$$\tau = \mu\left[\frac{\partial u}{\partial y}\right]_{y=h} \tag{7.18}$$

$$\tau = \mu\frac{\partial}{\partial y}\left[\frac{1}{2\mu}\frac{\Delta P}{r_m\theta_m}\left(y^2 - yh\right) + \frac{r_m\omega_p y}{h}\right]_{y=h} \tag{7.19}$$

$$\tau = \mu\left[\frac{1}{2\mu}\frac{\Delta P}{r_m\theta_m}\left(2y - h\right) + \frac{r_m\omega_p}{h}\right]_{y=h} \tag{7.20}$$

$$\tau = \frac{h}{2}\frac{\Delta P}{r_m\theta_m} + \frac{\mu r_m\omega_p}{h} \tag{7.21}$$

Shear stress can be converted to a torque on the piston by multiplying it by the circumferential piston area A_C and the mean piston radius r_m

$$T = A_c r_m\left(\frac{h}{2}\frac{\Delta P}{r_m\theta_m} + \frac{\mu r_m\omega_p}{h}\right) \tag{7.22}$$

Note how both the viscous torque T and leakage flow Q_L are functions of the piston velocity ω_p and differential pressure ΔP.

$$Q_L = Q_L(\omega_p, \Delta P) \tag{7.23}$$

$$T = T(\omega_p, \Delta P) \tag{7.24}$$

This relationship can be used to form a two-port resistor in the bond graph. A bond graph for a single piston with leakage flow incorporated is shown in Figure 7.9. The leakage model is then incorporated into the bond graph of the full pump in Figure 7.10.

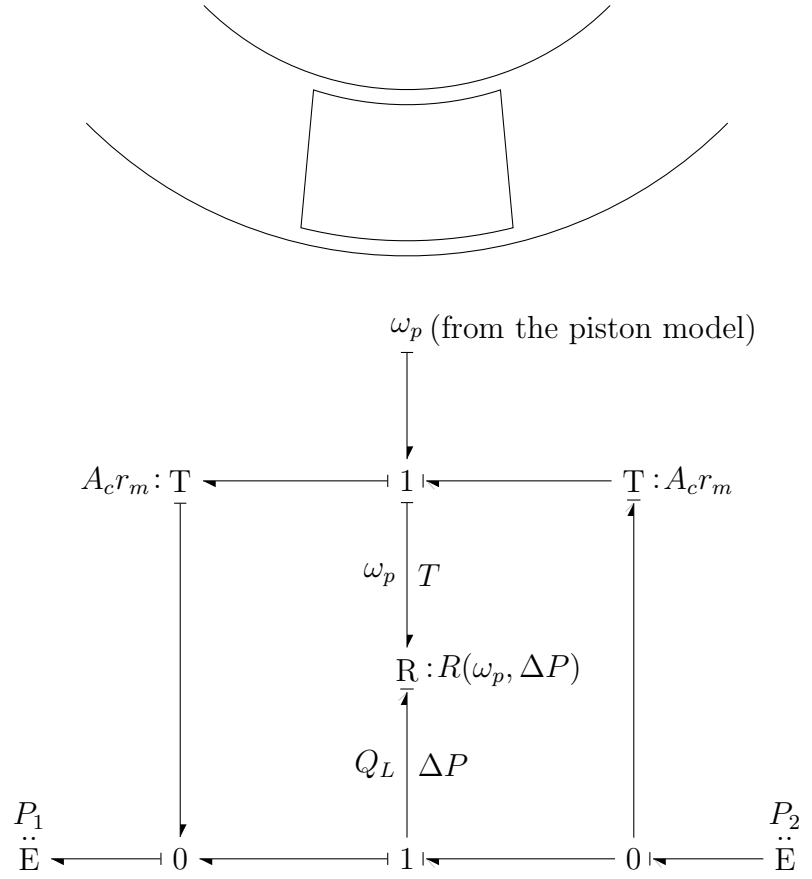

Figure 7.9: Leakage model for a single piston that incorporates the Couette (motion-driven) and Poiseuille (pressure-driven) flows. Leakage caused by the piston motion and torque from the viscous drag accounted for using a two-port R.

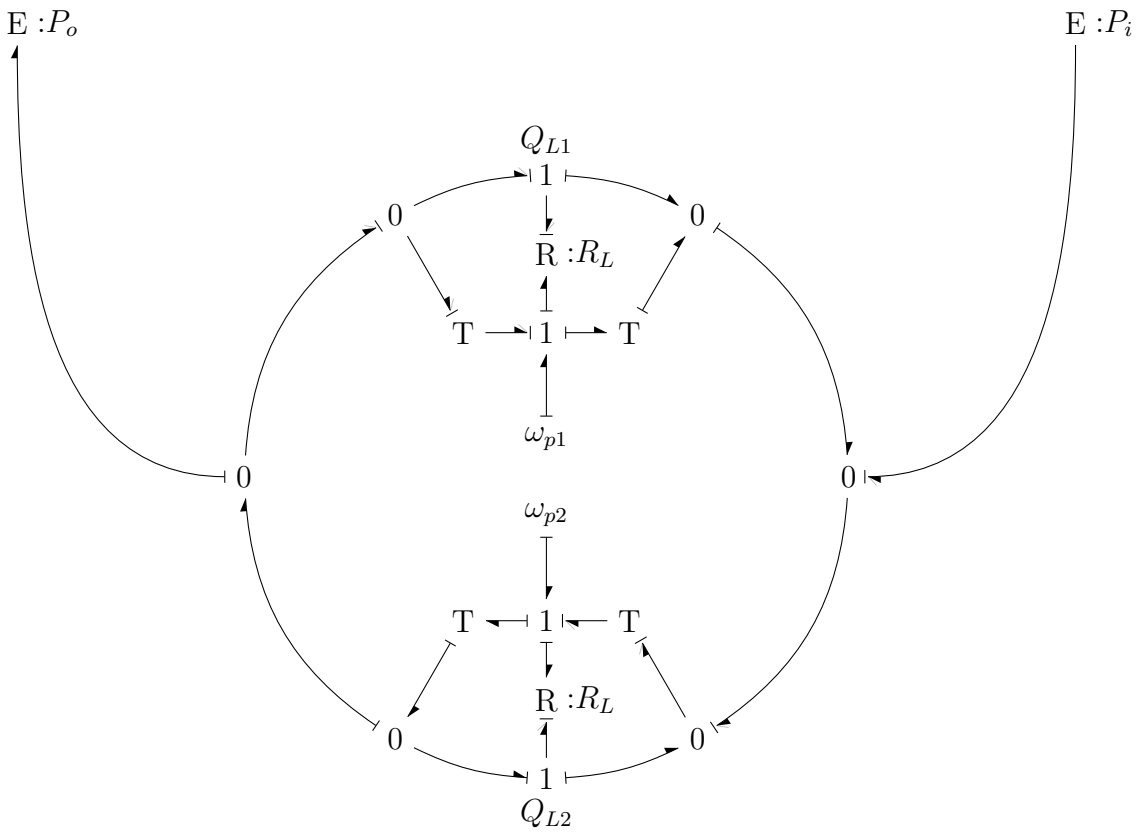

Figure 7.10: Bond graph of a positive displacement pump with leakage. R_L is a two-port resistor, and is a function of both ω_p and ΔP. This subsystem model is still completely deterministic when the inlet and outlet pressure and piston flows are prescribed (or determined from the piston subsystem model).

7.3.3 Fluid Inertance and Resistance

The next piece of the model to consider is whether the fluid in the torus stores energy, and if so, how (either potentially with a compliance or kinetically with an inertance). Many pump models operate at very high pressures and the compliance of the fluid needs to be taken into account. But pressures in the 2PTP are very low relative to many hydraulic applications (100 mmHg blood pressure is only about 2 psi), and blood is typically treated as incompressible in most lumped parameter simulations of the cardiovascular simulation or computational fluid dynamic simulations of blood pump. The kinetic energy of the fluid mass (inertance), on the other hand, is not negligible, especially in the 2PTP which is a pulsatile pump and accelerates and decelerates fluid each pump stroke.

The fluid in the torus as well as the inflow and outflow has inertance, and the flow through the torus and inflow and outflow has viscous resistance. To determine the effects, distinct regions of separate flow must be defined. There are two clear distinct volumes that could be defined; one on either side of the pistons. But these volumes do not necessarily have the same flow rate or flow direction. To account for the different flows, an additional demarcation can be added where the flow enters or exits the pump. Therefore four distinct volumes are defined. These volumes are shown in Figure 7.11.

The flow of each volume in the torus and for the inflow and outflow would be defined by the pressure on either side, the inertance of the fluid in the torus, and the viscous resistance to flow.

$$P_{\text{in}} - P_{\text{out}} = I(V_i)\dot{Q}_i + R(V_i)Q_i \tag{7.25}$$

where P_{in} is the pressure at the 'inflow' of the volume, P_{out} is the pressure at the 'outflow' of the volume, V_i is the volume, $I(V_i)$ is the fluid inertance as a function of the volume, and $R(V_i)$ is the viscous resistance as a function of the volume.

These partitioned volumes can be included in the model for the pump. The bond graph with these four volumes and flows (A, B, C, and D) and associated inertance and resistance is shown in Figure 7.13.

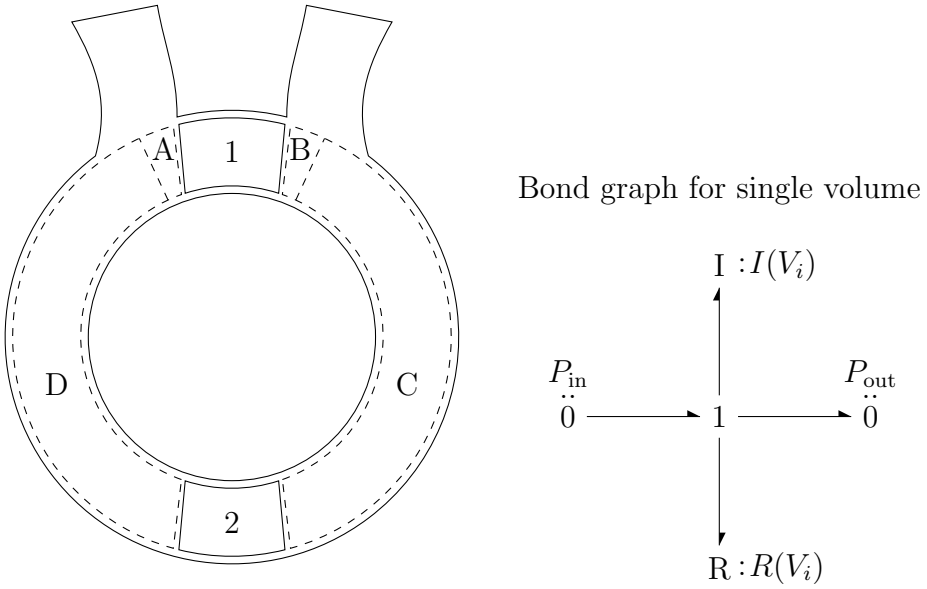

Figure 7.11: The torus volume can be split into four distinct segments. Each segment has an associated fluid inertance and resistance that changes with the volume of each segment as the pistons move. The pressure boundaries of each segment represent either the leading or trailing piston faces, or the pressure at the inflow and outflow.

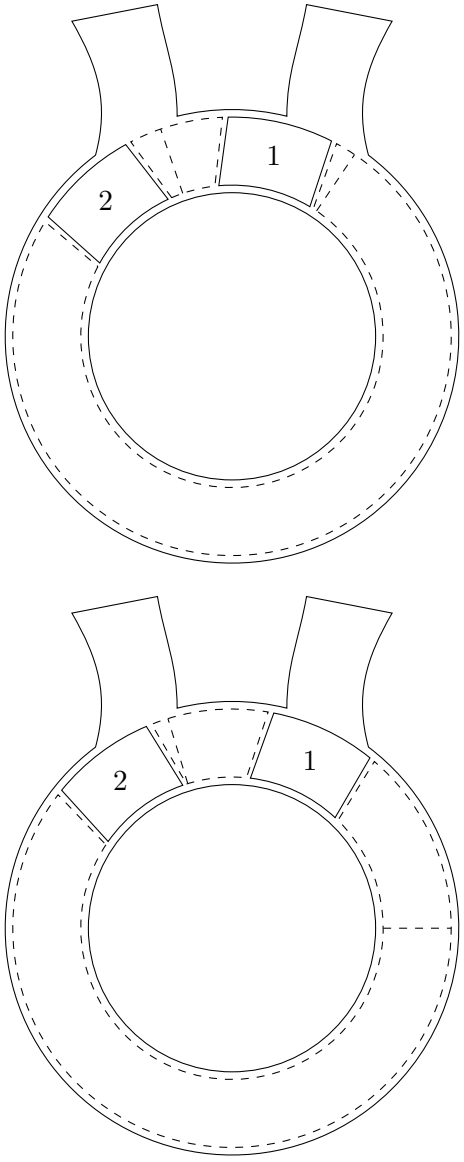

Figure 7.12: Partitioning the torus volume during transition.

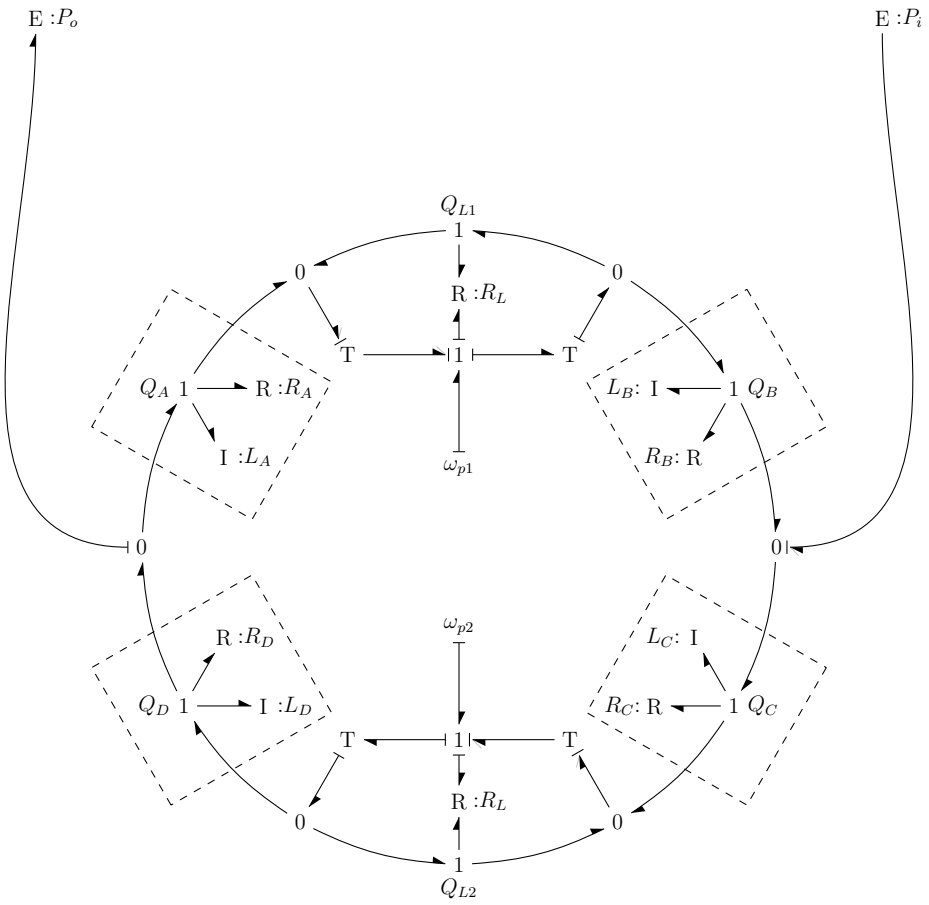

Figure 7.13: Bond graph of the 2PTP with four distinct volumes and flows (A, B, C, and D). Each of the four volumes have resistance R and inertance I that vary with volume.

7.3.4 Inflow and Outflow Resistance

As the pistons transition across the inflow and outflow ports, the area between the pump volumes and inflow and outflow ports decreases to zero during transition, and then opens back up again after transition. The fluid resistance caused by this area change could behave like an orifice resistor.

$$\Delta P = R(A_o)Q|Q| \tag{7.26}$$

where ΔP is the pressure drop across the resistor, Q is the flow through the resistor, and where a orifice resistance term R would change as a function of the orifice area A_o. For a rectangular orifice, the resistance can be expressed as a function of the fluid density ρ, orifice area A_o, and a discharge coefficient C_d

$$R(A_o) = C_d \frac{\rho}{A_o^2} \tag{7.27}$$

The resistance will go to infinity as the orifice approaches zero when the pistons occlude the inflow and outflow ports. This could cause a problem depending on the causality of the bond graph. If the resistor 'receives' flow and 'returns' pressure, this will cause problems with the model:

$$P \to \infty \text{ as } A_o \to 0 \text{ when } P = R(A_o)Q|Q| \tag{7.28}$$

In this case, when the port is occluded the resistance would need to be limited or the resistance would need to be removed from the model and a new model formulated. These options will be explored more later. If the resistor causality is such that it 'receives' pressure and 'returns' flow, this model formulation will be fine because

$$Q \to 0 \text{ as } A_o \to 0 \text{ when } Q = \text{sgn}(\Delta P)\sqrt{\frac{|\Delta P|}{R(A_o)}} \tag{7.29}$$

This resistance can be incorporated into the bond graph as seen in Figure 7.14.

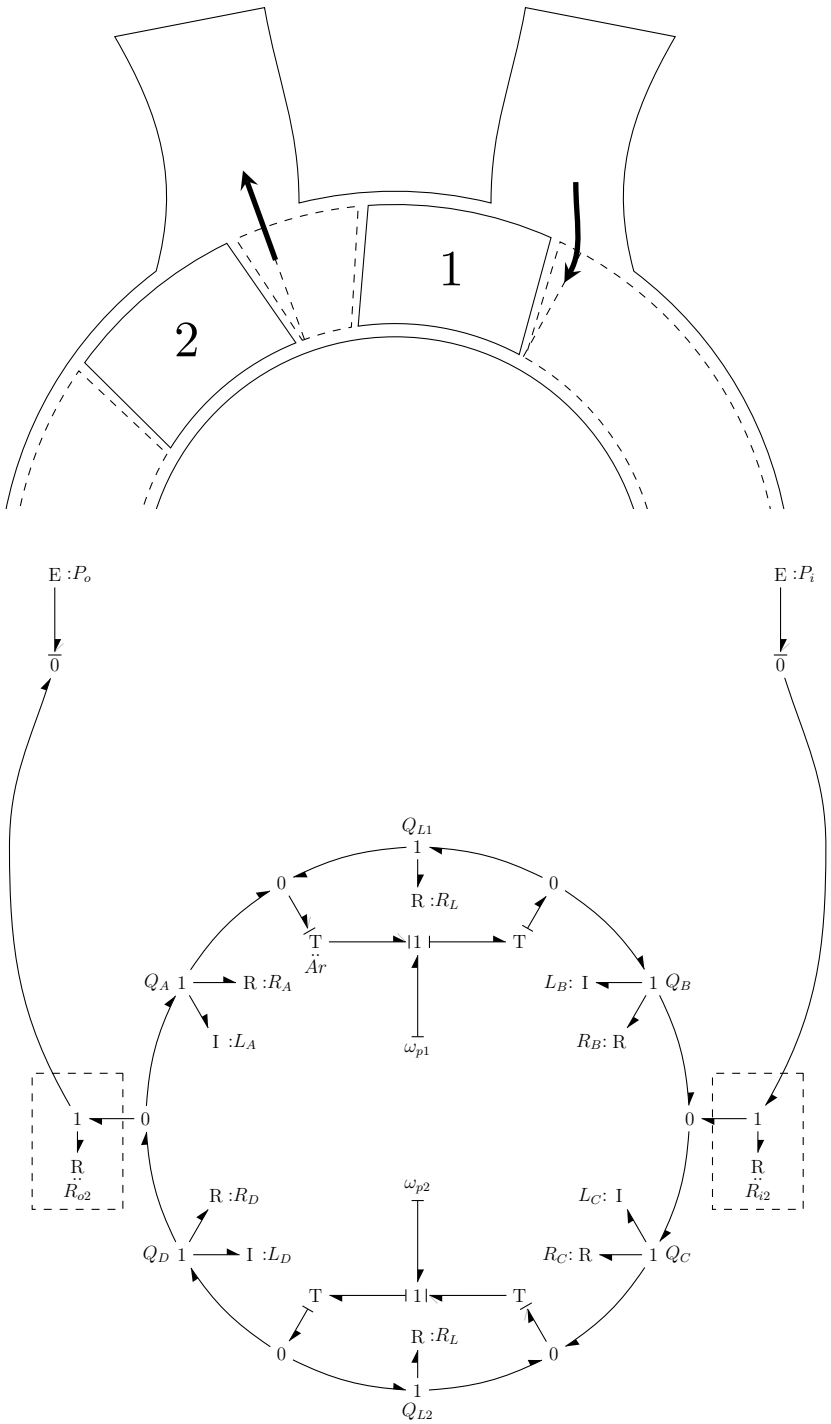

Figure 7.14: Bond graph model of the 2PTP with inflow and outflow port resistance. The flow into the torus from the inflow port and out of the torus through the outflow will be restricted by the orifice area as the pistons transition across and occlude the inflow and outflow ports.

7.3.5 Transition

During transition, the inflow and outflow ports are occluded, the pistons exchange functional roles, and the volumes between the pistons come into 'fluid communication' with the opposite port. There are two options for handling this:

1. Include all flow paths and resistances into a single model and allow the resistances to go to infinity (or some limited value) when the ports are occluded. For this model, arbitrary causality assignments will result, which will need to be implicitly solved each time step. Alternatively, a parasitic capacitance could added to the pressure zeros (0) in the torus, though doing so will require assigning very inelastic properties to the fluid that make the differential equations very stiff. The bond graph for this option is shown in Figure 7.15.
2. A hybrid model or variable structure model. In this case, there would be a different dynamic models: one model would be used for when piston 2 is pumping, another used when the ports are fully occluded, and another when piston 1 is pumping. The three bond graphs representing the three models can be seen in Figure 7.16.

One problem with either modeling approach is that the pressure across the pump does not manifest itself on the pistons during the transition phase. Quasistatic models can be used to determine this. When the dynamics are removed, the pressure across the pistons is equal to the differential pressure across the pump during the pumping phases, but zero during the transition phase. This is due to the fact that when the ports are occluded, in either model approach, there is no way for the model to account for any pressure differential across the pump to 'reach' the pistons. This results in a step change in pressure when the ports are occluded and when they are opened. This is illustrated in Figure 7.17. One would expect the differential piston pressure to transition smoothly from one extreme to the other across the occlusion.

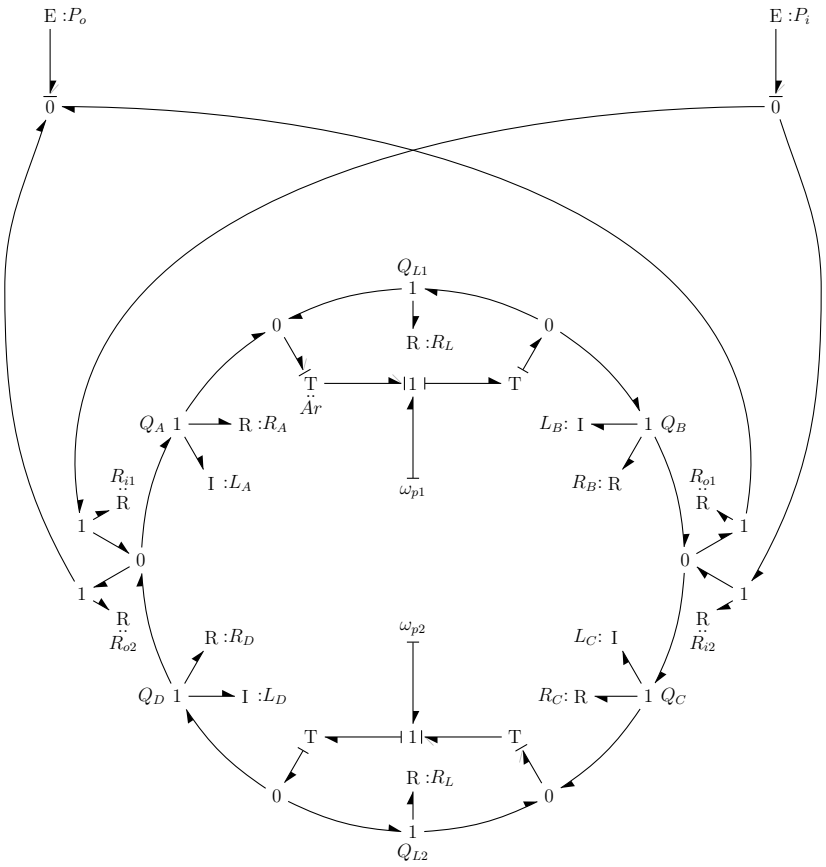

Figure 7.15: Bond graph incorporating the resistances for both inflow and outflow ports into a single model. This creates arbitrary assignments that would need to be implicitly solved, or a parasitic compliance could be added into the torus volume.

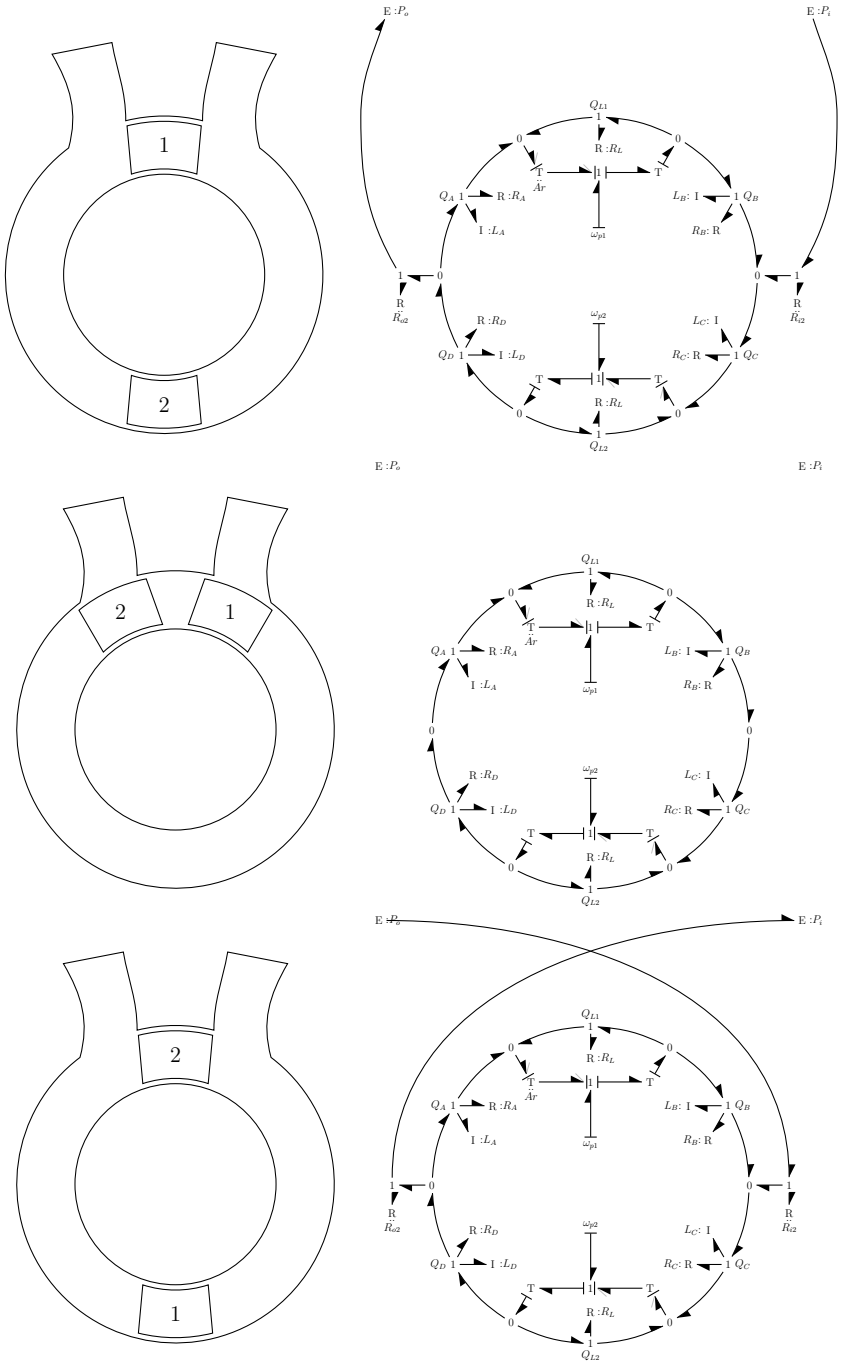

Figure 7.16: Three separate modes of variable structure : 1) piston 2 is the pumping piston, 2) transition when the inflow and outflow are occluded, and 3) piston 1 is the pumping piston.

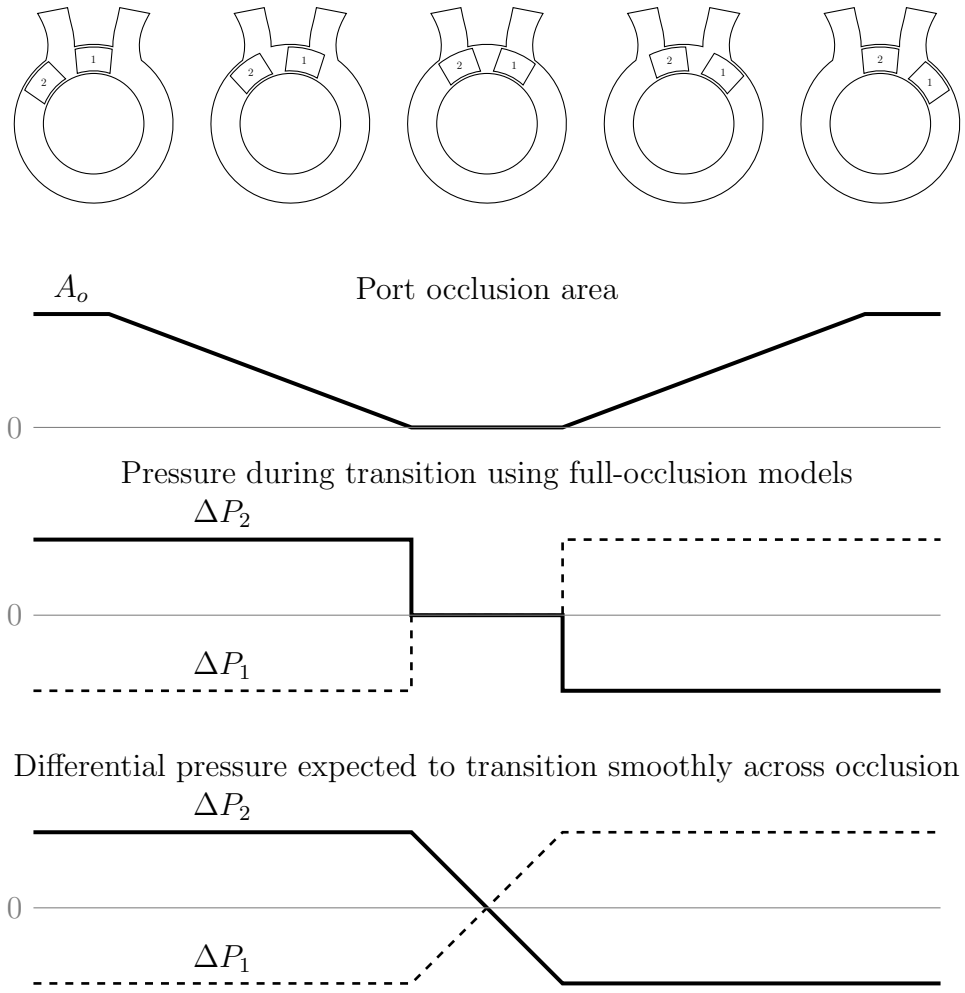

Figure 7.17: Quasistatic pressure across the piston during transition. In the full-occlusion model with no leakage, the pressure across the pistons is equal to the differential pressure across the pump when the port area is non-zero, and the pressure is zero during transition when the ports are fully occluded. This creates a step change in pressure to zero when the ports are occluded and a step change to the differential pressure ΔP when the ports are opened. This is not a realistic model. Instead, the pressure is expected to change smoothly during transition.

7.3.6 Occlusion Leakage

As the pistons start transition across the ports, there is an additional leakage pathway that has not yet been accounted for between the torus volumes and the ports. An example of these additional leakage pathways are shown in Figure 7.18. These leakage pathways are from the inflow and outflow ports to the leading and/or trailing faces of the pistons, depending on piston location. For small leakage gaps where flow is laminar, a linear resistance is assumed.

$$\Delta P = R(\theta_p)Q \tag{7.30}$$

These resistances would be a function of the arc length overlap of the piston and torus walls. When the leakage gap is much smaller than the length ($h/L << 1$), which is predominately the case, fully developed Poiseuille flow is used to model the leakage flow.

$$Q = \frac{\Delta P h^3}{12\mu r_o \theta_o} \tag{7.31}$$

where ΔP is the pressure gradient across the piston, h is the gap height, μ is the viscosity of blood, r_o is the outer piston radius, and θ_o is the overlap angle of the piston and torus wall.

$$R(\theta_o) = \frac{12\mu r_m \theta_o}{h^3} \tag{7.32}$$

At small overlap angles, the resistance would go to zero, which would produce the same problems outlined above when the occlusion area goes to zero. Similarly, the resistance would need to have a practical maximum value set for small values of θ_o.

Depending on the position of the pistons, there are twelve separate flows into or out of the pump. But these flows are not all present at the same time. For example, when piston 1 is in the trap and piston 2 is the pumping piston, then the volume between the leading face of piston 2 and the trailing face of piston 1 is in fluid communication with the outflow, but not the inflow. Therefore the flow from that volume to the inflow is deactivated when the pistons are in that position. The modeling challenge is in deciding how to deactivate that flow.

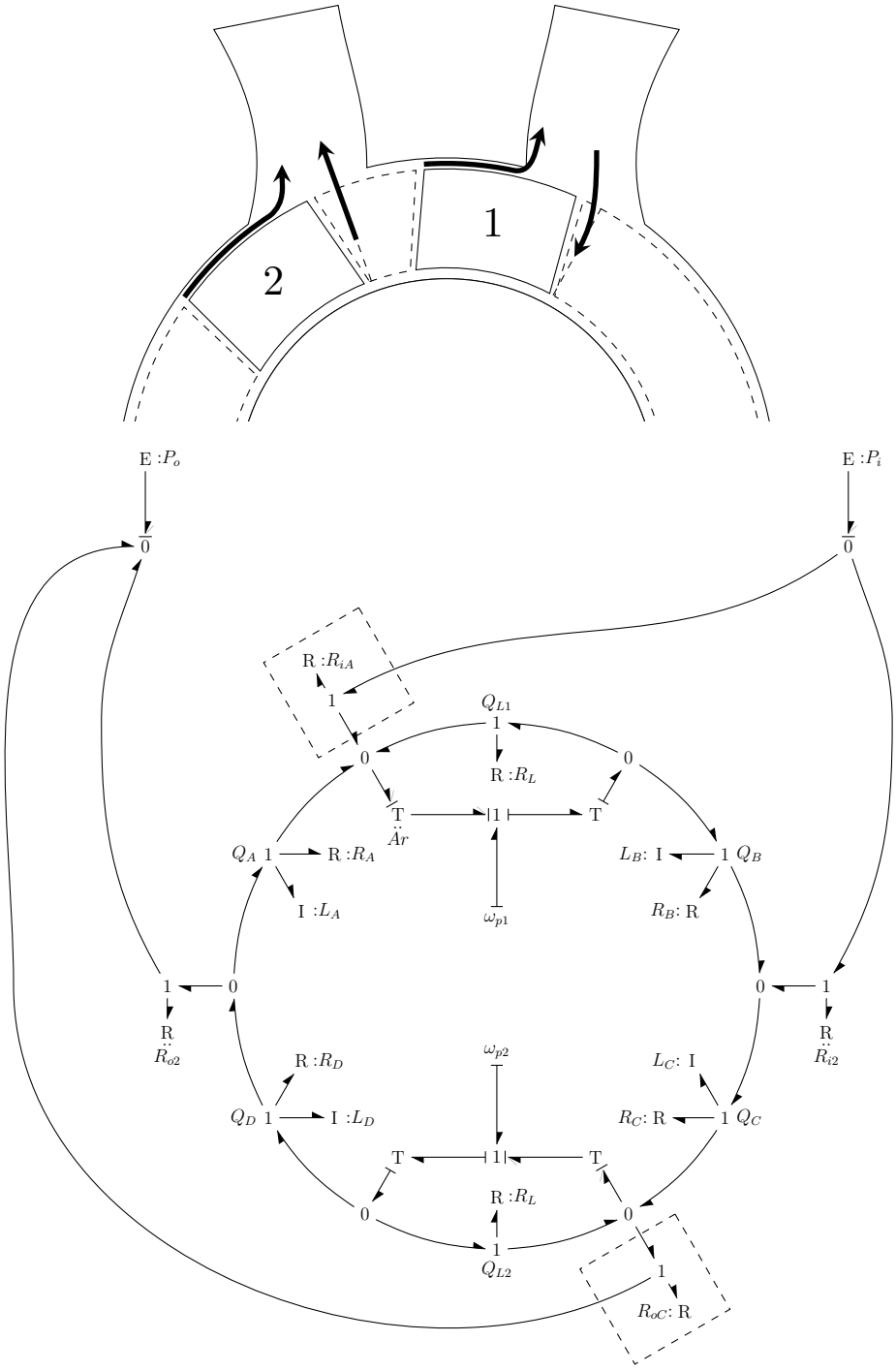

Figure 7.18: There are numerous pathways for flow into and out of the 2PTP, depending on piston position. These pathways will have variable resistance as the pistons transition across the ports. This is an example of two additional leakage pathways (highlighted with dashed boxes) that could be accounted for when the pistons transition across the inflow and outflow ports.

7.3.7 Special Case - Shunt

A shunt occurs if the pistons are ever in positions such that direct 'fluid communication' occurs between the inflow and outflow ports. Depending on how well the pistons are controlled, this scenario can happen briefly during transition. To account for the shunt flow, an additional control volume and flow Q_s will be added to the torus. Figure 7.19 illustrates this.

This addition control volume only appears when the shunt appears. It is zero otherwise. Practically speaking, this mode should never happen, so it may not be important to include in the simulation. It may not be important to model fault modes, especially if the dynamics that occur in those modes are not important to understand, and it is unreasonable to consider and model every possible fault mode. This shunt mode has been included for model completeness, but it is unlikely to be needed in the practical implementation of the simulation or in the design of the control.

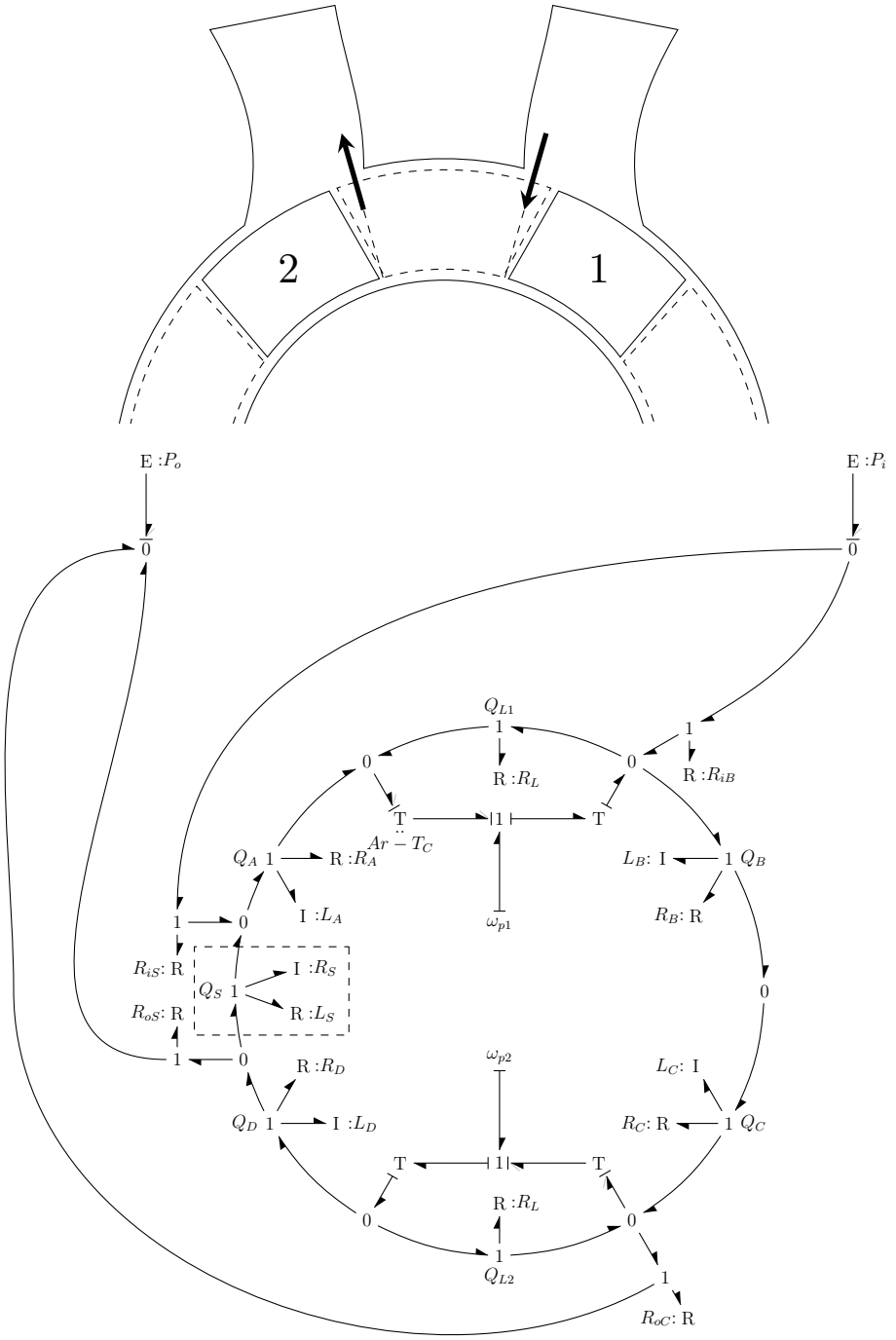

Figure 7.19: Shunt condition

7.3.8 Inflow and Outflow Effects

The inflow and outflow ports and cannulas add coupled inertance and resistance. These effects can be included in the differential pressure across the pump ΔP_p.

$$P_o - P_i = \Delta P_p = (I_o + I_i)\dot{Q}_p + (R_i + R_o)Q_p + P_{ao} - P_{LV} \tag{7.33}$$

where I_i and I_o are the inflow and outflow inertance, R_i and R_o are the inflow and outflow resistance, P_{ao} is the aortic pressure (outflow), and P_{LV} is the left ventricular pressure (inflow). The inertance and resistance are functions of the cannula diameters and lengths.

$$I_i = \frac{\rho L_i}{\pi D_i^2} \tag{7.34}$$

$$I_o = \frac{\rho L_o}{\pi D_o^2} \tag{7.35}$$

$$R_i = \frac{128\pi L_i \mu}{\pi^2 D_i^4} \tag{7.36}$$

$$R_o = \frac{128\pi L_o \mu}{\pi^2 D_o^4} \tag{7.37}$$

where μ and ρ are blood viscosity and density, L_i and L_o are the inflow and outflow cannula lengths, and D_i and D_o are the inflow and outflow cannula diameters.

The flow in and out of the pump Q_p is a linear function of the states, which changes for each structure (i).

$$Q_p = f_i(Q_A, Q_B, Q_C, Q_D) \tag{7.38}$$

$$\dot{Q}_p = f_i(\dot{Q}_A, \dot{Q}_B, \dot{Q}_C, \dot{Q}_D) \tag{7.39}$$

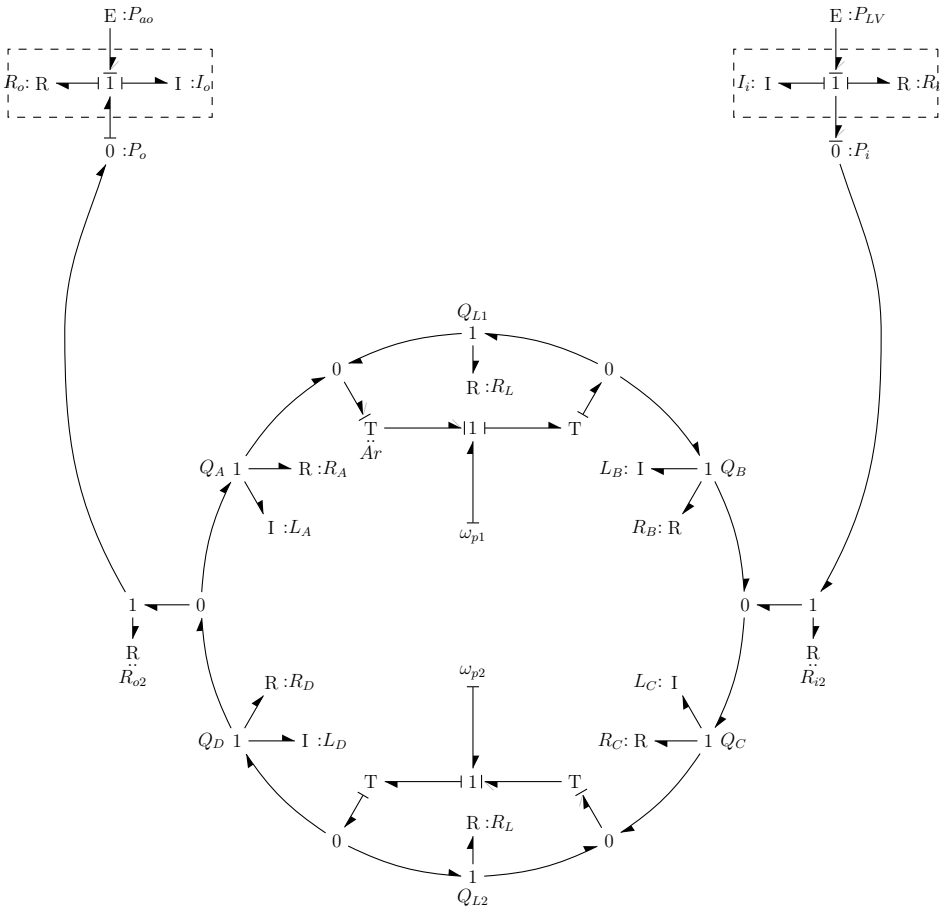

Figure 7.20: Coupling the inflow and outflow to the system. The inductor (I) has derivative causality, so the fluid momentum in the cannulas is not an independent state. When the cannulas are included, the pressure in becomes the left ventricular (LV) pressure and pressure out becomes the aortic (ao) pressure.

7.4 Variable Structure Model

The previous sections assembled the model in stages - first, the motor and piston dynamics were described, and then the pump flow model was derived starting from a simple model of a positive displacement pump, to which leakage was added, then fluid inertance and resistance in the pump, followed by the port resistance and leakage during transition. What resulted is the bond graph shown in Figure 7.21, which accounts for all possible pumping modes (piston 2 pumping, piston 1 pumping, or transition), and which shows all of the different flow and leakage pathways in and out of the pump. There are twelve possible flows in or out of the pump, but they are not all active at the same time. These paths are given the abbreviations below.

Main flow path when Piston 2 is pumping:

i2	From the inflow to the 0 between the V_B and V_C
o2	From the outflow to the 0 between the V_D and V_A

Main flow path when Piston 1 is pumping:

i1	From the inflow to the 0 between the V_D and V_A
o1	From the outflow to the 0 between the V_B and V_C

Port occlusion leakage paths

iA	From the inflow trailing face of piston 1
iB	From the inflow leading face of piston 1
iC	From the inflow trailing face of piston 2
iD	From the inflow leading face of piston 2
oA	From the outflow trailing face of piston 1
oB	From the outflow leading face of piston 1
oC	From the outflow trailing face of piston 2
oD	From the outflow leading face of piston 2

These pathways appear or disappear depending on the position of the pistons. The challenge in modeling is in deciding how to treat the inactive flow paths. Two methods could be used:

1. Include all flow paths and resistances into a single model and add parasitic compliance or solve implicit equations simultaneously.
2. Use a variable structure or hybrid modeling approach where the structure is determined by the position of the pistons and is represented by a separate set of dynamic equations.

These methods each carry their own set of problems or challenges. The first method, disabling the flow paths by increasing the resistance terms, results in numerous arbitrary causal

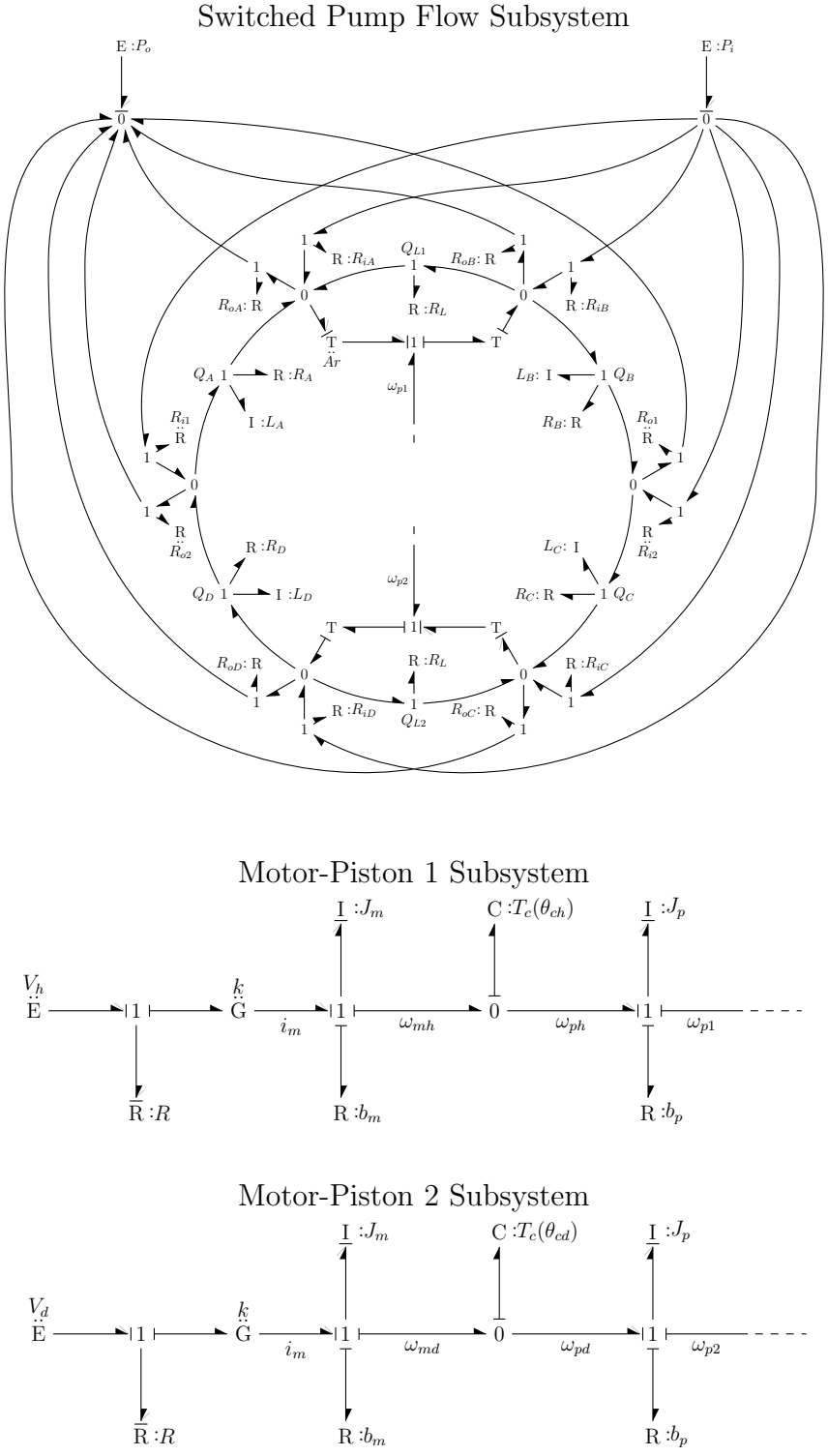

Figure 7.21: The complete bond graph model of the 2PTP pump.

assignments in the bond graph, which would results in numerous implicit integration terms that require iterative calculation schemes such as Newton-Raphson at each timestep. To get around this arbitrary assignment problem, *ad hoc* parasitic compliance can be added to each pressure-node (0) in the pumping chamber. But the fluid pumped in this case is blood, which, like water, is usually treated as an incompressible fluid, especially within the relatively low pressure changes that would occur in a blood pump such as this. The parasitic compliance terms would be extremely stiff, and could add significant computational time and/or noise to the model.

On the other hand, the variable structure approach requires that the model be reformulated and re-initialized between each structure. In this case, there are 49 distinct structures (see Figure 7.22 - note that there are 64 structures shown, but the right column and top row are just mirrored with from the left column and bottom row respectively). Each of these structures corresponds to a different model that can be represented with a different bond graph (see Figure 7.23). Of the 49 structures, 14 result in piston overlap and are not physically possible (indicated with red labels in Figure 7.22), and 9 result in a shunt condition (indicated with gray labels in Figure 7.22). 5 of the shunts are considered very unlikely to occur. This leaves 30 unique structures that needed to be determined.

Another way these modes can be visualized is by mapping the piston positions relative to each other during a stroke, shown in Figure 7.24. Zero degrees corresponds to the 'hold' position, when the piston is directly between the inflow and outflow ports. The x-axis is the piston 1 position and the y-axis is the piston 2 position from -180 to 180 degrees. The dashed line represents the relative piston positions during two consecutive strokes. The plot repeats itself (-180 degrees also equals 180 degrees). This plot is helpful for illustrating which modes occur during typical operation and how narrow the window is between shunt conditions.

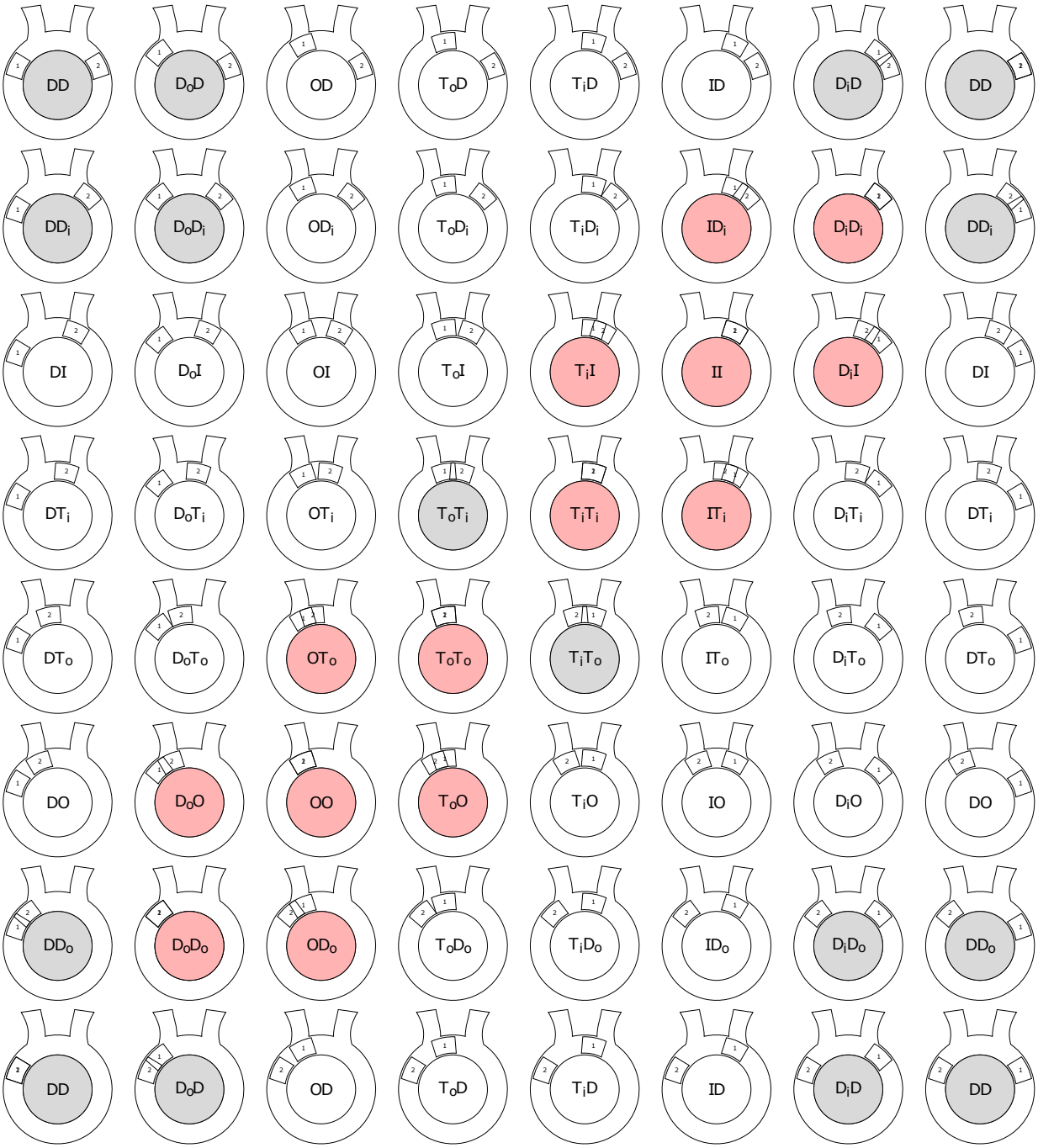

Figure 7.22: Schematic representations of 64 possible model structures depending on piston position. The first letter in the label corresponds to piston 1 position, and the second letter corresponds to the piston 2 position. D - drive position, D_o - drive position with partial outflow occlusion, O - outflow occlusion, T_o - trap position with partial outflow occlusion, T_i - trap position with partial inflow occlusion, I - inflow occlusion, D_i - drive position with partial inflow occlusion. There are only 49 unique modes; the leftmost and rightmost rows are the same, as well as the top and bottom rows. Because the pistons rotate, the pattern is repeating. Red labels indicate modes of piston overlap (not physically possible) and the gray labels indicate zones where shunting occurs (special cases).

Figure 7.23: Bond graphs of 64 possible model structures, corresponding to the schematics represented in Figure 7.22.

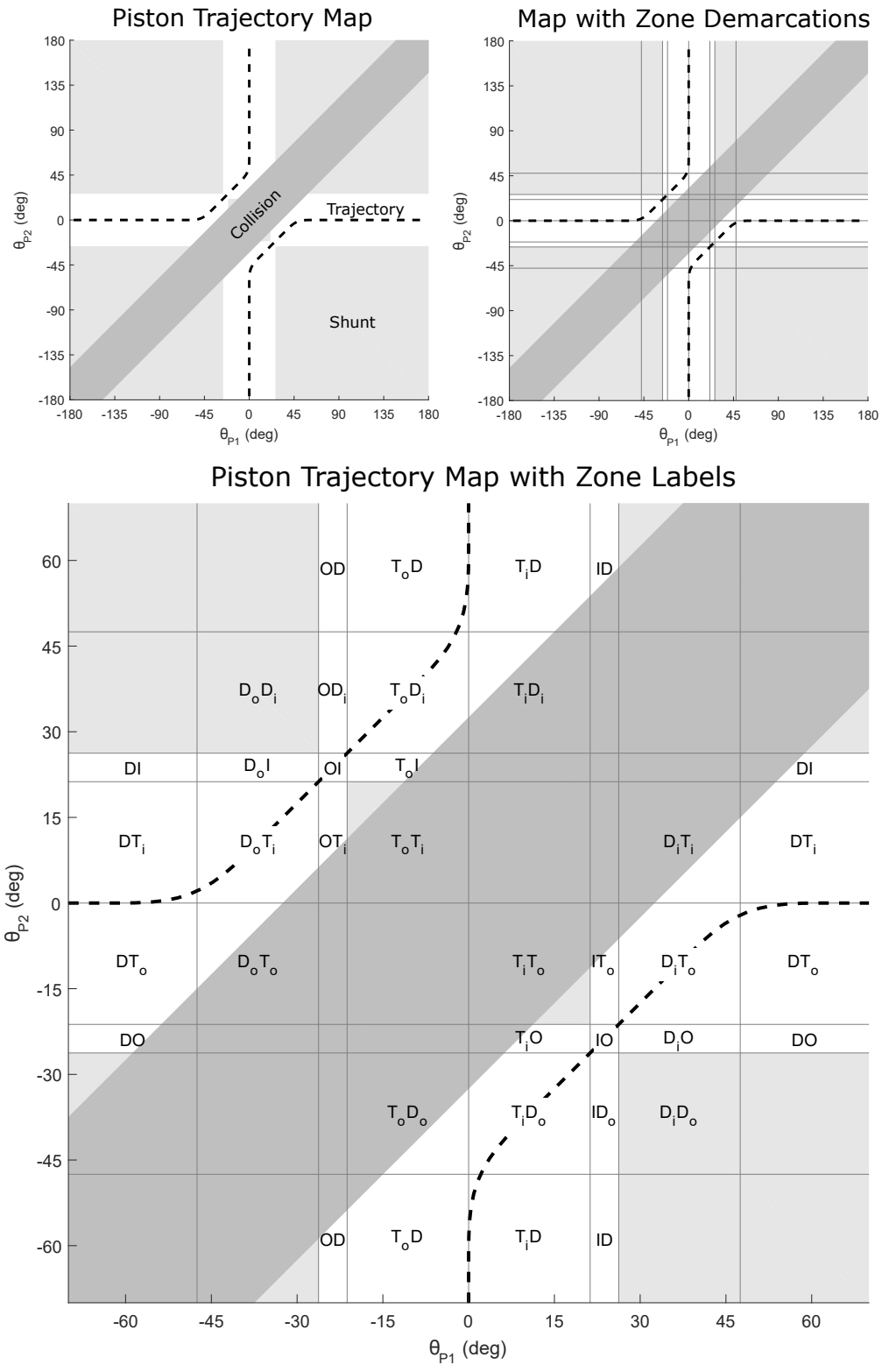

Figure 7.24: Piston trajectory map. State equations are different for each zone. The dashed line represents the typical trajectory of the pistons in relative piston position space.

7.5 State Equations

The state equations for a switched system can be represented by a family of systems

$$\dot{\mathbf{x}} = f_i(\mathbf{x}) \tag{7.40}$$

where i is an index to the family of subsystems for each possible structure.

There are 13 states that define the motor, piston, and flow dynamics:

$$\mathbf{x} = [\theta_{m1}\ \ \omega_{m1}\ \ \theta_{p1}\ \ \omega_{p1}\ \ \theta_{m2}\ \ \omega_{m2}\ \ \theta_{p2}\ \ \omega_{p2}\ \ Q_A\ \ Q_B\ \ Q_C\ \ Q_D\ \ Q_S]^T \tag{7.41}$$

The state equations for the motors and pistons are the same. First, for motor and piston 1:

$$\dot{\omega}_{m1} = \frac{1}{J_m}\left[\left(b_m + \frac{k_e^2}{R_e}\right)\omega_{m1} - T_{\max}\sin\left(2\pi\frac{\theta_{m1}-\theta_{p1}}{4\cdot\theta_{\mathrm{e}}}\right) + \frac{k_e}{R_e}V_{\mathrm{in},1}\right] \tag{7.42}$$

$$\dot{\omega}_{p1} = \frac{1}{J_p}\left[T_{\max}\sin\left(2\pi\frac{\theta_{m1}-\theta_{p1}}{4\cdot\theta_{\mathrm{e}}}\right) - b_p\omega_{p1} - T_{p1}\right] \tag{7.43}$$

$$\dot{\theta}_{m1} = \omega_{m1} \tag{7.44}$$

$$\dot{\theta}_{p1} = \omega_{p1} \tag{7.45}$$

And motor and piston 2:

$$\dot{\omega}_{m2} = \frac{1}{J_m}\left[\left(b_m + \frac{k_e^2}{R_e}\right)\omega_{m2} - T_{\max}\sin\left(2\pi\frac{\theta_{m2}-\theta_{p2}}{4\cdot\theta_{\mathrm{e}}}\right) + \frac{k_e}{R_e}V_{\mathrm{in},2}\right] \tag{7.46}$$

$$\dot{\omega}_{p2} = \frac{1}{J_p}\left[T_{\max}\sin\left(2\pi\frac{\theta_{m2}-\theta_{p2}}{4\cdot\theta_{\mathrm{e}}}\right) - b_p\omega_{p2} - T_{p2}\right] \tag{7.47}$$

$$\dot{\theta}_{m2} = \omega_{m2} \tag{7.48}$$

$$\dot{\theta}_{p2} = \omega_{p2} \tag{7.49}$$

The torque from the pressure on the faces of the pistons is a function of the fluid flow and piston velocity, the formulation of which depends on the structure.

$$T_{p1} = f_{p1}(\omega_{p1}, Q_A, Q_B) \tag{7.50}$$

$$T_{p2} = f_{p2}(\omega_{p2}, Q_C, Q_D) \tag{7.51}$$

Details for each structure can be found in Appendix C.

Next, there are the torus flow states $Q_A - Q_D$ and the shunt flow Q_S. But not all of the flow states are always active. For example, in some configurations flows Q_B and Q_C or Q_A and Q_D will directly couple such that one state is redundant. Also, the shunt flow Q_S are only active in certain structures. When modeling, each dynamic equation will be carried through, but the order of the system will changes based on the structure of the model (redundant states reduce the order by 1).

#	Zone	θ_{m1}	ω_{m1}	θ_{p1}	ω_{p1}	θ_{m2}	ω_{m2}	θ_{p2}	ω_{p2}	Q_A	Q_B	Q_C	Q_D	Q_S	Order
1	OD	✓	✓	✓	✓	✓	✓	✓	✓	✓	✓	-	-	-	10
2	T_oD	✓	✓	✓	✓	✓	✓	✓	✓	✓	✓	✓	-	-	11
3	T_iD	✓	✓	✓	✓	✓	✓	✓	✓	✓	✓	✓	-	-	11
4	ID	✓	✓	✓	✓	✓	✓	✓	✓	✓	✓	-	-	-	10
5	T_oD_o	✓	✓	✓	✓	✓	✓	✓	✓	✓	✓	✓	✓	-	12
6	T_iD_o	✓	✓	✓	✓	✓	✓	✓	✓	✓	✓	✓	✓	-	12
7	ID_o	✓	✓	✓	✓	✓	✓	✓	✓	✓	✓	-	✓	-	11
8	D_iD_o	✓	✓	✓	✓	✓	✓	✓	✓	✓	✓	-	✓	✓	12
9	DO	✓	✓	✓	✓	✓	✓	✓	✓	✓	-	-	✓	-	10
10	T_iO	✓	✓	✓	✓	✓	✓	✓	✓	✓	✓	✓	-	-	11
11	IO	✓	✓	✓	✓	✓	✓	✓	✓	✓	✓	-	-	-	10
12	D_iO	✓	✓	✓	✓	✓	✓	✓	✓	✓	✓	-	✓	-	11
13	DT_o	✓	✓	✓	✓	✓	✓	✓	✓	✓	-	✓	✓	-	11
14	DT_o	✓	✓	✓	✓	✓	✓	✓	✓	✓	✓	✓	✓	-	12
15	T_iT_o	✓	✓	✓	✓	✓	✓	✓	✓	✓	✓	✓	-	✓	12
16	IT_o	✓	✓	✓	✓	✓	✓	✓	✓	✓	✓	✓	-	-	11
17	D_iT_o	✓	✓	✓	✓	✓	✓	✓	✓	✓	✓	✓	✓	-	12
18	DT_o	✓	✓	✓	✓	✓	✓	✓	✓	✓	-	✓	✓	-	11
19	D_oT_o	✓	✓	✓	✓	✓	✓	✓	✓	✓	✓	✓	✓	-	12
20	OT_i	✓	✓	✓	✓	✓	✓	✓	✓	✓	✓	-	✓	-	11
21	T_oT_i	✓	✓	✓	✓	✓	✓	✓	✓	✓	✓	-	✓	✓	12
22	D_iT_i	✓	✓	✓	✓	✓	✓	✓	✓	✓	✓	-	✓	-	11
23	DI	✓	✓	✓	✓	✓	✓	✓	✓	✓	-	✓	-	-	10
24	D_oI	✓	✓	✓	✓	✓	✓	✓	✓	✓	✓	✓	-	-	11
25	OI	✓	✓	✓	✓	✓	✓	✓	✓	✓	✓	-	-	-	10
26	T_oI	✓	✓	✓	✓	✓	✓	✓	✓	✓	✓	-	✓	-	11
27	D_oD_i	✓	✓	✓	✓	✓	✓	✓	✓	✓	✓	✓	-	✓	12
28	OD_i	✓	✓	✓	✓	✓	✓	✓	✓	✓	✓	✓	-	-	11
29	T_oD_i	✓	✓	✓	✓	✓	✓	✓	✓	✓	✓	✓	✓	-	12
30	T_oD_i	✓	✓	✓	✓	✓	✓	✓	✓	✓	✓	✓	✓	-	12

Table 7.1: There are 30 possible model structures. This table shows how many and which states are active for a given model structure. The piston and motors states (θ_m, ω_m, θ_p, and ω_p) are always active. The pump flows (Q_A, Q_B, Q_C, and Q_D) will sometimes directly couple, so one or more states will be redundant. Redundant flow states are eliminated with a dash. The shunt flow Q_s is only present in special cases.

From the trajectory map in Figure 7.24, it can be seen that there are 30 operating structures that should be accounted for. State equations need to be found for each of those structures. To do so, the bond graph for each mode is drawn using an algorithmic approach. These bond graphs can be seen in Appendix C. A few observations:

- Only zero or one (never two) external bonds is ever connected to a single torus or piston pressure node (0).
- Arbitrary causality occurs any time a port is completely occluded, creating an algebraic loop, but the associated resistances of partial port occlusion are linear so an explicit solution can be obtained.
- Causality assignments in each mode made it such that the external bonds deliver a pressure to the piston or torus pressure node (0), and never a flow.

Given the observations above, the following algorithm can be used to determine the state equations for each structure.

Algorithm for determining structure state equations:

First, determine if there are any coupled flows (A, B, C, or D). Coupled flows occur when there are no external bonds from the inflow or outflow bonds between the flow nodes (1). Depending on how many flows are coupled, this will determine the number of states. Then, for each flow (A, B, C, D, and S):

1. Identify the first external bond in the counter-clockwise direction (for convenience, CC-bond) and the first external bond in the clockwise direction (CW-bond).
2. The differential equation for each flow will take the same form:

$$\dot{Q}_n = \left[\hat{p}\Delta P - R_n Q_n + R_{cc} Q_{cc} - R_{cw} Q_{cw}\right]/L_n \tag{7.52}$$

   where n is the flow (A, B, C, D, or S), $\hat{p}$ is either 1, -1, or 0 depending on the CC and CW bonds, R_n is the viscous torus resistance, L_n is the inertia in the torus, $R_{cc}Q_{cc}$ is the pressure from the inflow or outflow resistance at the CC-node, and $R_{cw}Q_{cw}$ is the pressure from the inflow or outflow resistance at the CW-node.
3. Determine $\hat{p}$

3.1. $\hat{p} = 1$ if the CC-node is connected to the outflow and the CW-node is connected to the inflow. In this case, the differential pressure across the pump increases the fluid momentum.

3.2. $\hat{p} = -1$ if the CC-node is connected to the inflow and the CW-node is connected to the outflow. In this case, the differential pressure across the pump decreases the fluid momentum.

3.3. $\hat{p} = 0$ if the CC-node and CW-node are connected to the same port (either inflow or outflow). In this case, the differential pressure across the pump does not affect the fluid momentum.

4. Calculate the resistance R_n and inertance L_n, which are functions of the control volume for n plus any coupled control volume. For example, if A and B are coupled, then $R_A = R_B = R(V_A + V_B)$ and $L_A = L_B = L(V_A + V_B)$.
5. Identify the CC-node pressure from resistance $R_{cc}Q_{cc}$ and $R_{cw}Q_{cw}$. The resistances are functions of the partial occlusion leakage swept angle or port area of the inflow and outflow. The flows are functions of the states.

This procedure was implemented algorithmically in LaTeXto obtain symbolic state equations. Appendix C shows the results of this. Similarly, this algorithmic approach was used in Matlab to simulate the model rather than individually solving and writing the differential equations of each state for all 30 structures.

7.6 Structure Switching

Variable structure models have certain characteristics:

- The number of state variables is structure dependent. In this case, there are as many as five independent flow states (Q_A, Q_B, Q_C, Q_D, and Q_S) which can become become coupled depending on the structure.
- When the model changes structure at discrete events, the states must often be reinitialized.
- Event conditions or state events are those that trigger structure changes based on state values. Time events are those that occur at known time instances. In this case the piston positions (states) determine the structure, so we're concerned with state events.

Once sets of differential equations are obtained for each structure, they can easily be solved using standard solution techniques such as Matlab's built-in differential equation solvers like `ode45()` or `ode23s()`. Two problems must be handled when the structure changes: 1) the structure change must be detected and 2) the states must be re-initialized.

7.6.1 Event Detection

First, structure changes need to be detected. These are defined as *state events* because the structure changes as a function of state (in this case, as a function of both piston 1 and piston 2 positions). Looking at the trajectory map in Figure 7.24, it can be seen that a state event occurs any time the dual-piston trajectory crosses a zone boundary line. Matlab's built-in event detection is used to accomplish this.

7.6.2 Re-initialization

States need to be re-initialized as flows become coupled or decouple due to inflow and outflow pathways vanishing or being introduced. By inspection of the schematic illustrations and bond graphs, the following rules can be applied:

- When the piston is in the hold position, partial port occlusion flow will move from one side of the piston to the other as the pistons moves across zero degrees. In this case the partial port occlusion flow starts affecting the flow on the opposite side of the piston.

- If the pumping piston moves from partial port occlusion to pumping, the flow on either side of the piston will be coupled, and the leakage flow resistance will be modified.

One way to visualize these rules is to to overlay the ports that get switched on and off over the schematic structures. This is shown in Figure 7.25.

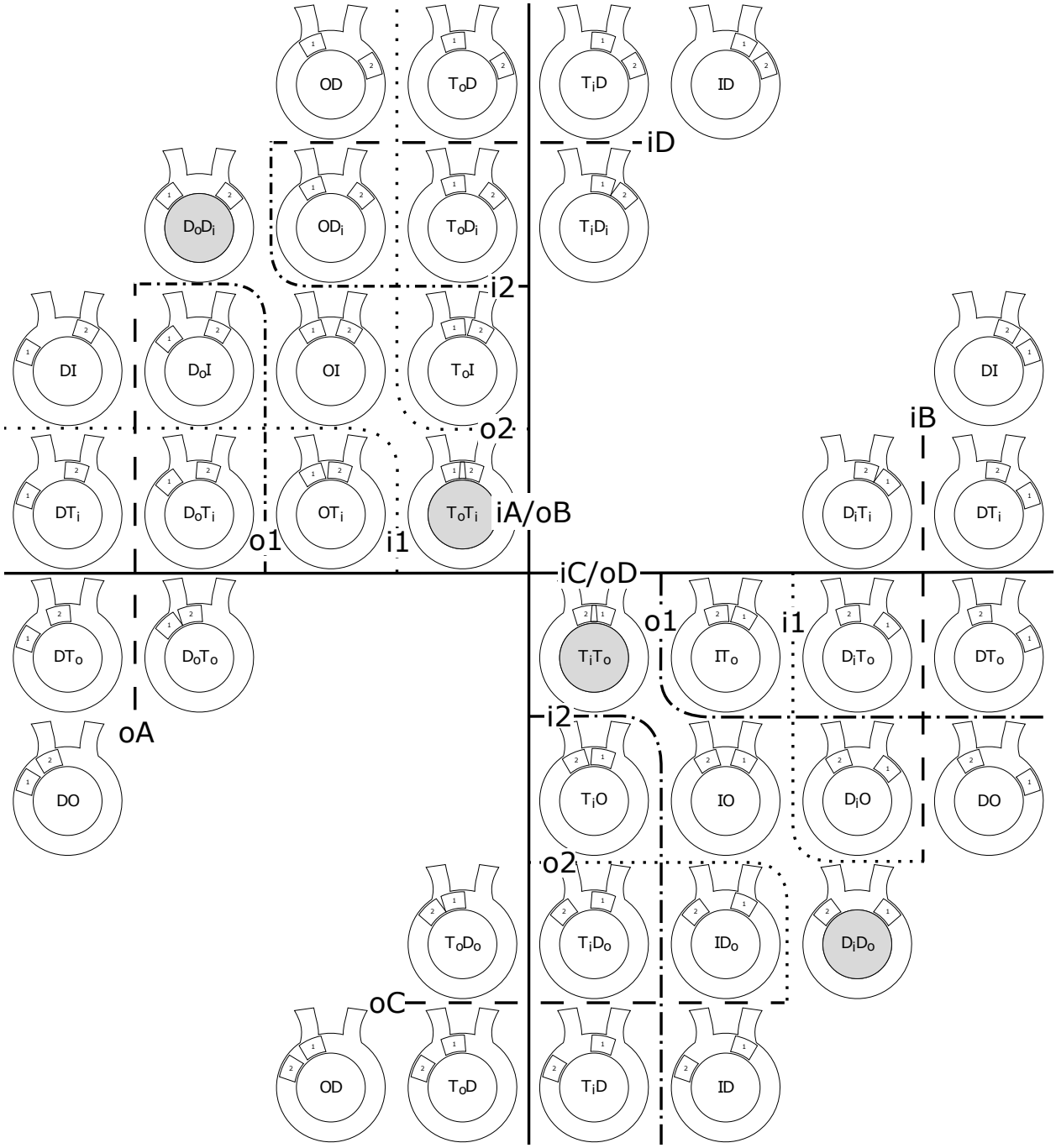

Figure 7.25: Schematic representations of the variable structures of the model with boundaries are drawn when flows either appear or disappear. When these boundaries are crossed, the states must be reinitialized.

7.7 Pump Parameters

Pump geometry was determined in Chapter 5 and listed in Table 7.2. Other parameters that are needed to simulate the model such as piston and motor characteristics, blood properties, and inflow and outflow parameters are listed below.

J_p	1.07e-6	kg m^2	Piston mass moment of inertia
B_p	5e-3	N m s	Piston linear damping coefficient
J_m	4.2e-6	kg m^2	Motor mass moment of inertia
B_m	1.75e-4	N m s	Motor linear damping coefficient
k_e	0.11	N m / Amp	Motor gyrator coefficient
R_e	2.2	Ohms	Motor electrical resistance
$T_{\max}$	0.34	N	Magnetic coupling magnitude (for sine function)
θ_e	5	deg	Escape angle when the piston and motor decouple
k_c	0.08	N m / deg	Magnetic coupling linear stiffness
h	0.0035	in	Piston/torus gap height
ρ	1025	kg / m^3	Blood density
μ	0.0035	Pa s	Blood viscosity
C_d	0.7		Port area resistance discharge coefficient
L_i	12.5	cm	Inflow cannula length
L_o	30	cm	Outflow cannula length
D_i	14	mm	Inflow cannula diameter
D_o	14	mm	Outflow cannula diameter

Table 7.2: Pump parameters.

7.8 Simulation Results

Matlab's ODE solvers were used to simulate the variable structure model developed in this chapter. Because of the leakage flow and dynamics, the system is stiff so `ode23()` and `ode45()` hang up and do not solve. All of the stiff solvers work relatively well, but `ode23tb()` seems to be the most stable and solve most quickly. Simulating three pump cycles usually takes about 10 to 15 seconds of computational time, the majority of which seems to be due to the switching events where the ODE solve stops and reinitializes.

First, a quasistatic simulation is performed to see how the pressure changes as the pistons occlude the inflow and outflow ports. To do this, the differential pump pressure is set to 100 mmhg and the simulation is run over a very large timestep (20 seconds) so that the pistons move very slow and the dynamic effects (such as pressure due to inertance) are negligible. The results of this simulation can be seen in Figure 7.26 and should be compared to the expected results shown in Figure 7.17. As expected, the pressure changes smoothly from positive 100 mmHg to negative 100 mmHg for Piston 1, and vice versa for Piston 2. This is due to the inclusion of the partial port occlusion leakage model during transition and helps provide a justification for the inclusion of these extra terms in the complicated variable structure format.

Next, the idealized pump flow and pressure are simulated by directly controlling the piston motion. To do this, the pistons velocity is directly prescribed and the motor, piston, and magnetic coupling dynamics are ignored. The results can be seen in Figure 12.6. The angular position and pump flow plots follow ideal trajectories and are as expected. To note are the bottom-left plot which shows 15° piston separation during transition, and the bottom-right plot that shows the dynamic pressure across the piston during pumping and transition. The differential pressure across the pump is a constant 100 mmHg, but the pressure across the pistons has additional dynamic pressures associated with the inertia and resistance of the fluid flow in the cannulas and torus. Another thing to note is that the pressure changes smoothly from positive to negative during transition (when pump flow is zero).

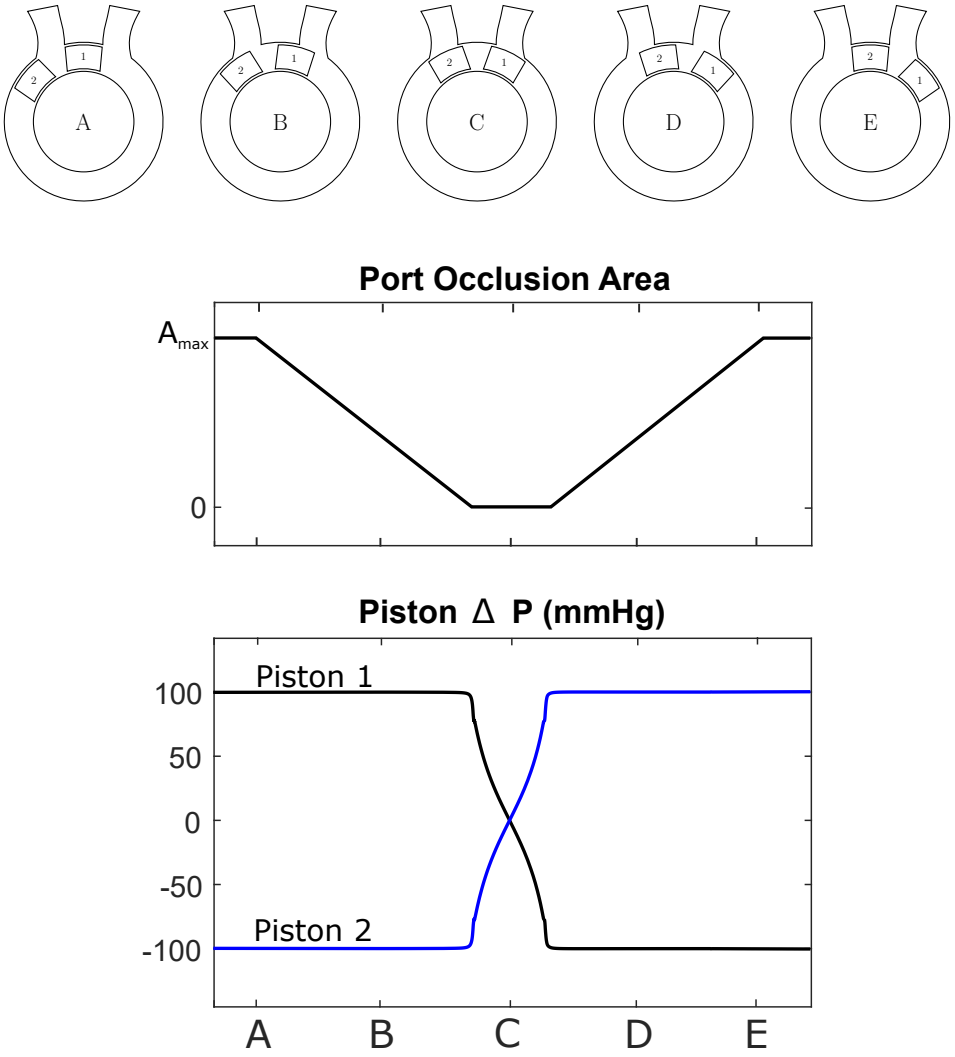

Figure 7.26: Simulated quasistatic pressure across the piston during transition. The pressure changes smoothly as the pistons transition across the inflow and outflow ports.

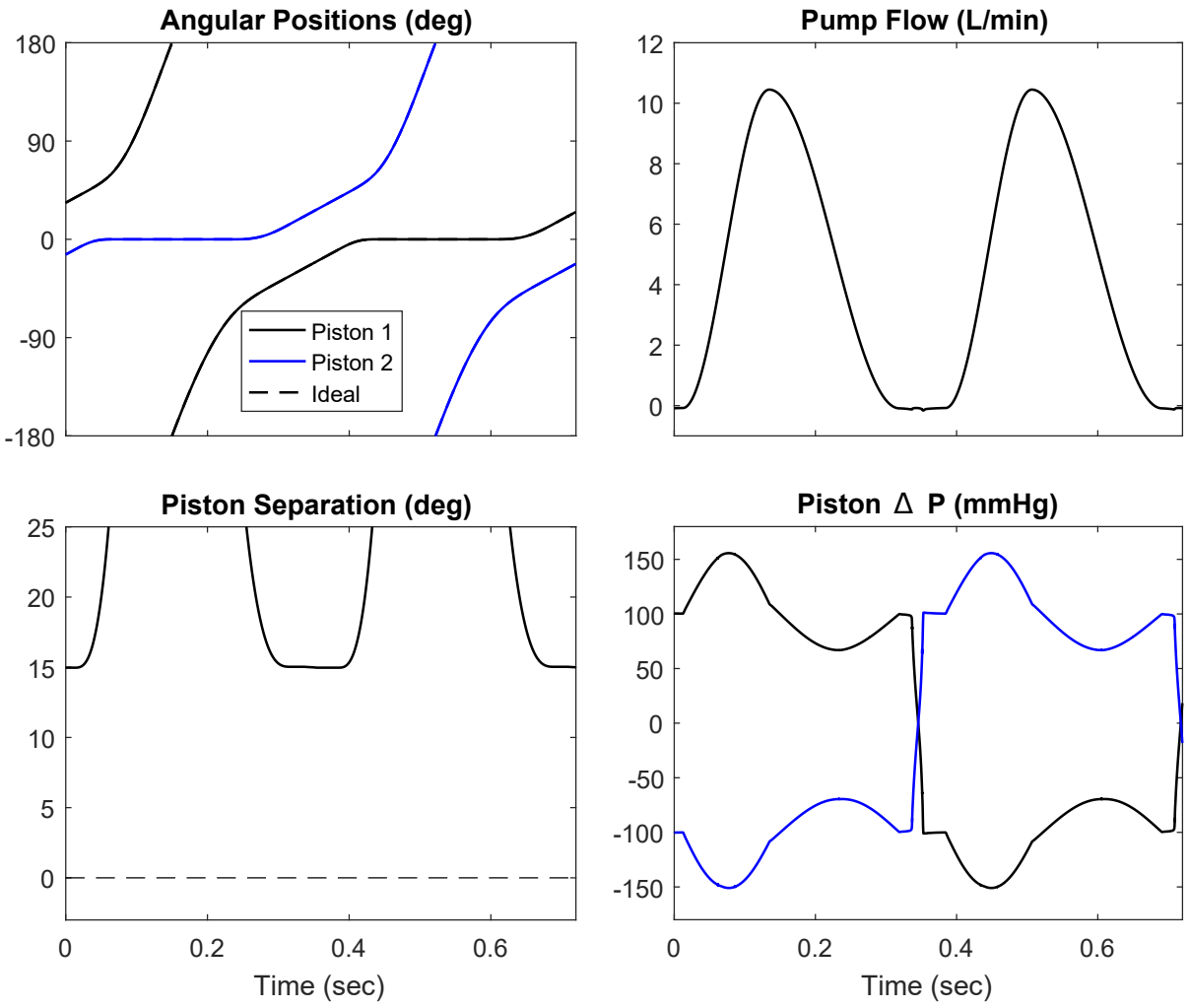

Figure 7.27: Ideal 2PTP pressure and flow at 5 L/min against a constant differential pump pressure of 100 mmHg. In this model, piston motion is prescribed (the motor, piston, and magnetic dynamics are not included).

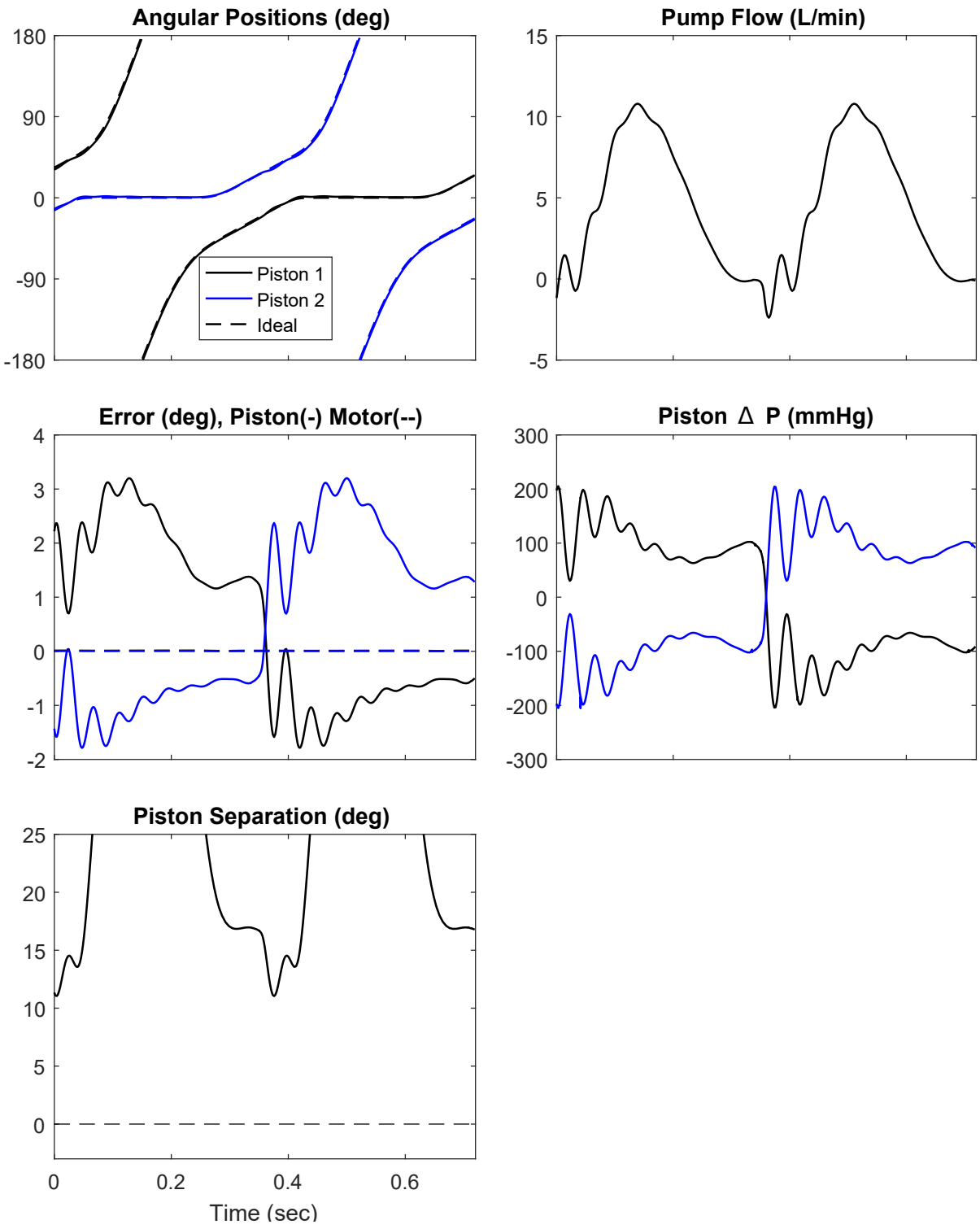

Figure 7.28: 2PTP pressure and flow at 5 L/min against a constant differential pump pressure of 100 mmHg with ideal motor control. In this model, motor motion is prescribed and the piston dynamics and magnetic coupling determine how well the pistons follow.

Chapter 8

Reduced-Order Model

This chapter develops a simplified reduced-order linear 2PTP model of pumping and transition by ignoring nonlinear effects and the annular leakage between the piston and torus walls. This model is used to design control and estimation methods.

One approach to low-level control design is to utilize well developed control methods for linear systems. For this approach, a linearized model of the pump was needed. Linearizing each of the 30 separate modes would be tedious and require burdensome tracking and control mode switching during operation. A better approach could be to develop linear models for only the two general pumping modes:

1. Pumping (one piston is pumping, either 1 or 2, while the other piston is holding)
2. Transition (when the pistons are moving together and the ports are occluded)

To reduce the order and simply the models, a few simplifications were made:

1. Leakage flow is ignored. Experimental studies with a prototype 2PTP have demonstrated leakage flow less than 3% of the total flow. By eliminating the leakage flow, the flow in the torus and the piston motion become directly coupled. As will be shown, this eliminates five states (pump flows A, B, C, D, and S).
2. Nonlinear port flow is ignored. When the ports are open, the pressure generated by the nonlinear resistance is very small compared to the viscous resistance of the cannulas or differential pressure across the pump. Linear models would either have fully open ports or fully closed ports.
3. Magnetic coupling is linearized. The magnetic coupling is represented by a sinusoidal torque-displacement relationship. For the linear model, a simple linear angular spring constant is used instead.
4. Shunt mode is ignored. This mode is a special case that should not happen if the pump is controlled reasonably well.

8.1 Reduced-Order Model for Pumping

First, the simplified model when one piston is the 'drive' or pumping piston, while the other piston is the 'hold' piston will be considered. To start, the bond graph for the system is developed from the analysis in previous sections, with the modification that leakage flow is removed, partial port occlusion is neglected, and nonlinear port resistance is ignored. This simplified bond graph is shown in Figure 8.1

When the leakage is neglected, and piston flow is determined by the motor/piston/magnetic-coupling subsystem model, then the inertance of the fluid in the torus and the ports receives derivative causality, which means no additional states are added, but also means that the fluid inertance is directly coupled to the pistons.

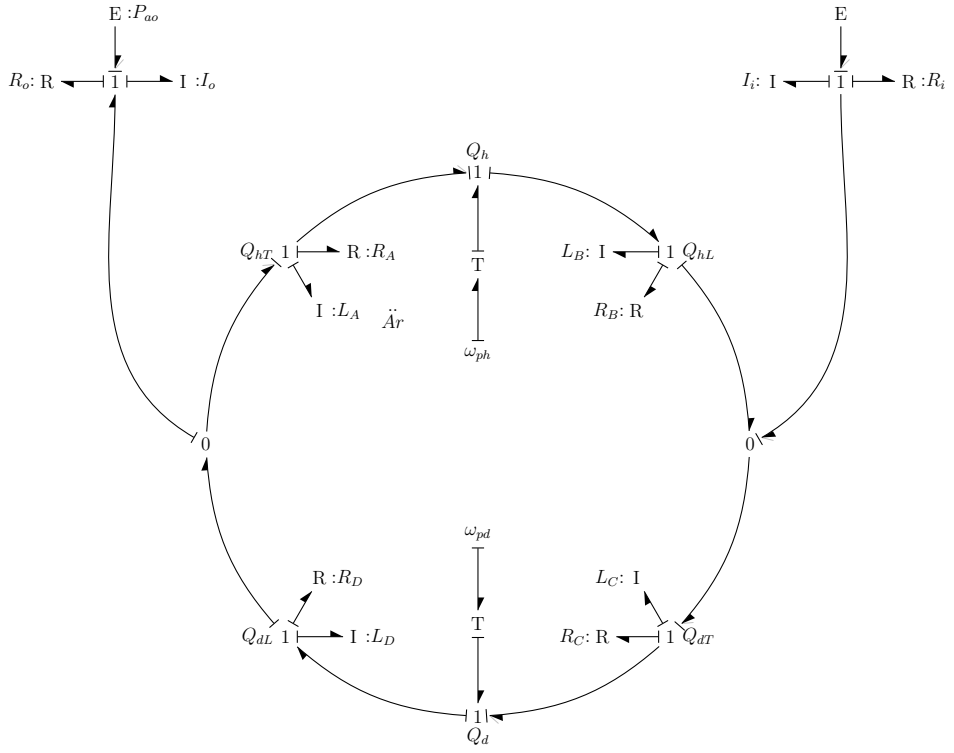

Figure 8.1: Simplified model of the 2PTP. When flow is determined by the motor/piston/magnetic-coupling model, then no additional states are added for the flow in the torus (all pump flow energy storage elements have derivative causality).

It can be seen by inspection of the torus that for the 'hold' piston the fluid volume leading (hL) and trailing (hT) change at equal and opposite rates as the piston moves as long as

the piston stays relatively within the 'hold' region and does not move far. Therefore, the sum of the inertia and resistance are constant and assigned the values L_h and R_h where the subscript h signifies the 'hold' position. The same analysis can be done for the 'drive' piston. Volumes dL and dT will change at equal and opposite rates so the sum is constant and the inertia and resistance are set to L_d and R_d. The bond graph can be simplified as well and can be seen in Figure 8.2, which also includes the subsystems for each motor-piston coupling, which together make up the complete simplified model.

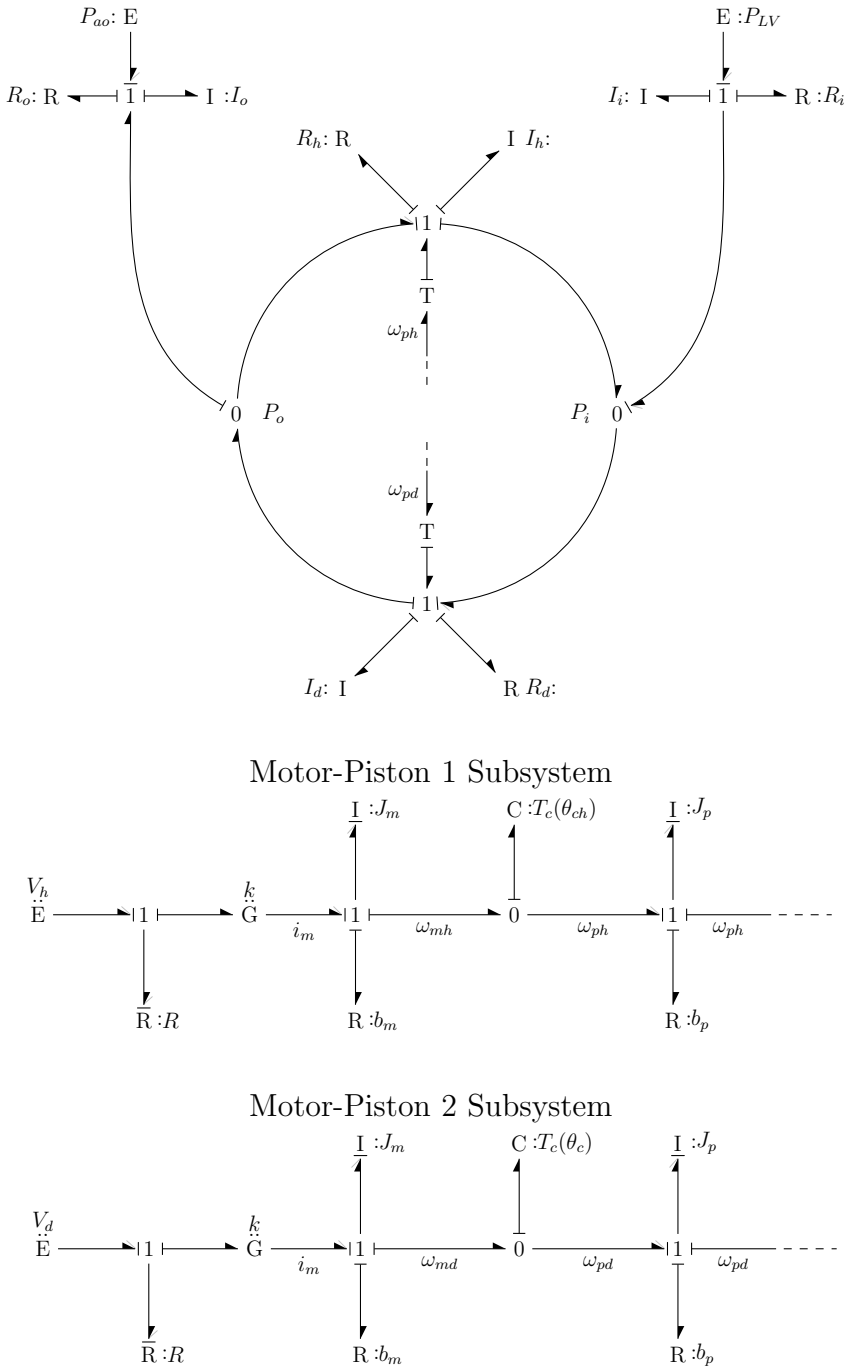

Figure 8.2: Simplified model of the 2PTP with motor subsystems. The two motor-piston subsystems are illustrated separately for ease of viewing, but are coupled to the pump flow model at the dashed power bonds, making a complete coupled system.

8.1.1 Linearization

To create a linearized model, the magnetic coupling torque $T_c(\theta_c)$ is linearized by replacing the sinusoidal magnetic coupling with a linear rotational spring constant k_c.

$$T_c(\omega_m - \omega_p) = T_{\max} \sin\left(2\pi \frac{\theta_m - \theta_p}{4 \cdot \theta_e}\right) \approx k_c(\omega_m - \omega_p) \tag{8.1}$$

8.1.2 State Equations

State equations can be derived from the bond graph in Figure 8.2. First, the state equations from the motor-piston subsystems from Section 7.1.1 remain unchanged for the 'hold' motor-piston:

$$\dot{\omega}_{mh} = \frac{1}{J_m}\left[\frac{V_h k_e - k_e^2 \omega_{mh}}{R} - b_m \omega_{mh} - k_c(\theta_{ph} - \theta_{mh})\right] \tag{8.2}$$

$$\dot{\omega}_{ph} = \frac{1}{J_p}\left[k_c(\theta_{mh} - \theta_{ph}) - b_p \omega_{ph} - T_{ph}\right] \tag{8.3}$$

$$\dot{\theta}_{mh} = \omega_{mh} \tag{8.4}$$

$$\dot{\theta}_{ph} = \omega_{ph} \tag{8.5}$$

And for the 'drive' motor-piston:

$$\dot{\omega}_{md} = \frac{1}{J_m}\left[\frac{V_d k_e - k_e^2 \omega_{md}}{R} - b_m \omega_{md} - k_c(\theta_{pd} - \theta_{md})\right] \tag{8.6}$$

$$\dot{\omega}_{pd} = \frac{1}{J_p}\left[k_c(\theta_{md} - \theta_{pd}) - b_p \omega_{pd} - T_{pd}\right] \tag{8.7}$$

$$\dot{\theta}_{md} = \omega_{md} \tag{8.8}$$

$$\dot{\theta}_{pd} = \omega_{pd} \tag{8.9}$$

The inertial elements in the torus and cannula are all dependent (all fluid inertance elements have derivative causality). The inertance and the resistance from the torus flow will be coupled through the differential piston pressures in the piston-motor state equations above (T_{ph} and T_{pd}), which can derived using the bond graph.

$$T_{ph} = Ar\left[I_h \dot{Q}_h + R_h Q_h + P_i - P_o\right] \tag{8.10}$$

$$T_{pd} = Ar\left[I_d\dot{Q}_d + R_dQ_d + P_o - P_i\right] \tag{8.11}$$

P_i and P_o are the pressures at the inflow and outflow ports, which depend on the flow dynamics as well as the pressures in the left ventricle P_{LV} and aorta P_{ao}.

$$P_o = P_{ao} + I_o(\dot{Q}_d - \dot{Q}_h) + R_o(Q_d - Q_h) \tag{8.12}$$

$$P_i = P_{LV} - I_i(\dot{Q}_d - \dot{Q}_h) - R_o(Q_d - Q_h) \tag{8.13}$$

The difference between the outflow and inflow pressure can be found by subtraction.

$$P_o - P_i = \Delta P + I_c(\dot{Q}_d - \dot{Q}_h) + R_c(Q_d - Q_h) \tag{8.14}$$

where

$$I_c = I_i + I_o \ , \quad R_c = R_i + R_o \ , \text{ and } \quad \Delta P = P_{ao} - P_{LV}$$

Flow are related to the piston rotational velocity by the cross sectional area of the piston A and the mean piston radius r.

$$Q_h = Ar\omega_{ph} \tag{8.15}$$

$$Q_d = Ar\omega_{pd} \tag{8.16}$$

The state equations for the piston velocities can now be rewritten incorporating the pump pressures, resistance, and dependent inertance.

$$(J_p + J_h + J_c)\,\dot{\omega}_{ph} = k_c(\theta_{mh} - \theta_{ph}) - (b_p + b_h + b_c)\,\omega_{ph} + Ar\Delta P + J_c\dot{\omega}_{pd} + b_c\omega_{pd} \tag{8.17}$$

$$(J_p + J_d + J_c)\,\dot{\omega}_{pd} = k_c(\theta_{md} - \theta_{pd}) - (b_p + b_d + b_c)\,\omega_{pd} - Ar\Delta P + J_c\dot{\omega}_{ph} + b_c\omega_{ph} \tag{8.18}$$

where

$$J_h = I_h(Ar)^2 \ , \quad J_d = I_d(Ar)^2 \ , \text{ and } \quad J_c = I_c(Ar)^2$$

$$b_h = R_h(Ar)^2 \ , \quad b_d = R_d(Ar)^2 \ , \text{ and } \quad b_c = R_c(Ar)^2$$

These are implicit differential equations ($\dot{\mathbf{x}} = f(\dot{\mathbf{x}}, \mathbf{x}, \mathbf{u})$), which can be made explicit ($\dot{\mathbf{x}} = f(\mathbf{x}, \mathbf{u})$) through algebraic manipulation in this case because all of the terms are linear. This

can be done by hand or using the symbolic equation capabilities of Matlab. Either way, solving for $\dot{\omega}_{pd}$ and $\dot{\omega}_{ph}$ produces the following differential equations for the rotational piston velocity.

$$\begin{bmatrix}\dot{\omega}_{pd}\\ \dot{\omega}_{ph}\end{bmatrix} = \begin{bmatrix}\frac{1}{\hat{J}_d} & \frac{1}{\hat{J}_c}\\ \frac{1}{\hat{J}_c} & \frac{1}{\hat{J}_h}\end{bmatrix} \begin{bmatrix}k_c(\theta_{md}-\theta_{pd}) - \hat{b}_d\omega_{pd} - Ar\Delta P + b_c\omega_{ph}\\ k_c(\theta_{mh}-\theta_{ph}) - \hat{b}_h\omega_{ph} + Ar\Delta P + b_c\omega_{pd}\end{bmatrix} \tag{8.19}$$

where

$$\hat{J}_h = J_p + J_h + J_c - \frac{J_c^2}{J_p + J_d + J_c} \tag{8.20}$$

$$\hat{J}_d = J_p + J_d + J_c - \frac{J_c^2}{J_p + J_h + J_c} \tag{8.21}$$

$$\hat{J}_c = \frac{1}{J_c}\left(J_p + J_d + J_c\right)\left(J_p + J_h + J_c\right) - J_c \tag{8.22}$$

$$\hat{b}_d = b_p + b_d + b_c \tag{8.23}$$

$$\hat{b}_h = b_p + b_h + b_c \tag{8.24}$$

8.1.3 State Space Representation

By eliminating the leakage flow and directly coupling the flow to the piston velocity, and by ignoring the special shunt flow case, the model has been reduced from 13 states to 8 states, and can be represented in state space form

$$\dot{\mathbf{x}} = A\mathbf{x} + B\mathbf{u} + W\mathbf{w}$$

There are eight states $\mathbf{x}$, the piston and motor velocities, and piston and motor positions.

$$\mathbf{x} = \begin{bmatrix}\theta_{m1} & \theta_{m2} & \omega_{m1} & \omega_{m2} & \theta_{p1} & \theta_{p2} & \omega_{p1} & \omega_{p2}\end{bmatrix}^T$$

States

1	θ_{m1}	Motor 1 angular position
2	θ_{m2}	Motor 2 angular position
3	ω_{m1}	Motor 1 angular velocity
4	ω_{m2}	Motor 2 angular velocity
5	θ_{p1}	Piston 1 angular position
6	θ_{p2}	Piston 2 angular position
7	ω_{p1}	Piston 1 angular velocity
8	ω_{p2}	Piston 2 angular velocity

There are two linear conditions to consider: when piston 1 is the 'drive' piston, and when piston 2 is the 'drive' piston. Different state matrices will be used depending on how the pump is operating.

When piston 1 is the driving piston, the linear system will take the form:

$$\dot{\mathbf{x}} = A_1\mathbf{x} + B\mathbf{u} + W_1\Delta P \tag{8.25}$$

Similarly, when piston 2 is the driving piston, the linear system will take the form:

$$\dot{\mathbf{x}} = A_2\mathbf{x} + B\mathbf{u} + W_2\Delta P \tag{8.26}$$

In this way, the state order remains the same regardless of pump configuration.

From the linearized equations in the previous section, the state matrices can be found.

$$A_1 = \begin{bmatrix} 0 & 0 & 1 & 0 & 0 & 0 & 0 & 0 \\ 0 & 0 & 0 & 1 & 0 & 0 & 0 & 0 \\ -\frac{k_c}{J_m} & 0 & -\frac{b_m + \frac{k_e^2}{R}}{J_m} & 0 & \frac{k_c}{J_m} & 0 & 0 & 0 \\ 0 & -\frac{k_c}{J_m} & 0 & -\frac{b_m + \frac{k_e^2}{R}}{J_m} & 0 & \frac{k_c}{J_m} & 0 & 0 \\ 0 & 0 & 0 & 0 & 0 & 0 & 1 & 0 \\ 0 & 0 & 0 & 0 & 0 & 0 & 0 & 1 \\ \frac{k_c}{\hat{J}_d} & \frac{k_c}{\hat{J}_c} & 0 & 0 & -\frac{k_c}{\hat{J}_d} & -\frac{k_c}{\hat{J}_c} & -\frac{\hat{b}_d}{\hat{J}_d} + \frac{b_c}{\hat{J}_c} & -\frac{\hat{b}_h}{\hat{J}_c} + \frac{b_c}{\hat{J}_d} \\ \frac{k_c}{\hat{J}_c} & \frac{k_c}{\hat{J}_h} & 0 & 0 & -\frac{k_c}{\hat{J}_c} & -\frac{k_c}{\hat{J}_h} & -\frac{\hat{b}_d}{\hat{J}_c} + \frac{b_c}{\hat{J}_h} & -\frac{\hat{b}_h}{\hat{J}_h} + \frac{b_c}{\hat{J}_c} \end{bmatrix}$$

$$A_2 = \begin{bmatrix} 0 & 0 & 1 & 0 & 0 & 0 & 0 & 0 \\ 0 & 0 & 0 & 1 & 0 & 0 & 0 & 0 \\ -\frac{k_c}{J_m} & 0 & -\frac{b_m + \frac{k_e^2}{R}}{J_m} & 0 & \frac{k_c}{J_m} & 0 & 0 & 0 \\ 0 & -\frac{k_c}{J_m} & 0 & -\frac{b_m + \frac{k_e^2}{R}}{J_m} & 0 & \frac{k_c}{J_m} & 0 & 0 \\ 0 & 0 & 0 & 0 & 0 & 0 & 1 & 0 \\ 0 & 0 & 0 & 0 & 0 & 0 & 0 & 1 \\ \frac{k_c}{\hat{J}_h} & \frac{k_c}{\hat{J}_c} & 0 & 0 & -\frac{k_c}{\hat{J}_h} & -\frac{k_c}{\hat{J}_c} & -\frac{\hat{b}_h}{\hat{J}_h} + \frac{b_c}{\hat{J}_c} & -\frac{\hat{b}_d}{\hat{J}_c} + \frac{b_c}{\hat{J}_h} \\ \frac{k_c}{\hat{J}_c} & \frac{k_c}{\hat{J}_d} & 0 & 0 & -\frac{k_c}{\hat{J}_c} & -\frac{k_c}{\hat{J}_d} & -\frac{\hat{b}_h}{\hat{J}_c} + \frac{b_c}{\hat{J}_d} & -\frac{\hat{b}_d}{\hat{J}_d} + \frac{b_c}{\hat{J}_c} \end{bmatrix}$$

The input matrix B is the same regardless of which piston is the driving piston

$$B_1 = B_2 = B = \begin{bmatrix} 0 & 0 \\ 0 & 0 \\ \frac{k_e}{R_e J_m} & 0 \\ 0 & \frac{k_e}{R_e J_m} \\ 0 & 0 \\ 0 & 0 \\ 0 & 0 \\ 0 & 0 \end{bmatrix}$$

And the disturbance matrix W will change depending on which piston is the driving piston

$$W_1 = \begin{bmatrix} 0 \\ 0 \\ 0 \\ 0 \\ 0 \\ 0 \\ -\frac{Ar}{\hat{J}_d} + \frac{Ar}{\hat{J}_c} \\ \frac{Ar}{\hat{J}_h} - \frac{Ar}{\hat{J}_c} \end{bmatrix} \qquad W_2 = \begin{bmatrix} 0 \\ 0 \\ 0 \\ 0 \\ 0 \\ 0 \\ \frac{Ar}{\hat{J}_h} - \frac{Ar}{\hat{J}_c} \\ -\frac{Ar}{\hat{J}_d} + \frac{Ar}{\hat{J}_c} \end{bmatrix}$$

8.1.4 Controllability and Observability

Controllability and observability are important properties of the system. To control the states, whether that be the position of the pistons or motors, or the velocities of the pistons and motors, the system must be controllable by the two motor voltage inputs. Observability is important in this case because all of the states are not measureable. To design an observer with limited measurable states, the system must be observable so that the unmeasured states can be estimated.

To determine these properties for the linearized system, the controllability matrix $\mathcal{C}$ and the observability matrix $\mathcal{O}$ are found by the standard approach.

$$\mathcal{C} = [B \;\; AB \;\; A^2B \;\; ... \;\; A^7B]$$

$$\mathcal{O} = \begin{bmatrix} C \\ CA \\ CA^2 \\ ... \\ CA^7 \end{bmatrix}$$

Each need to have a rank equal to the number of rows of the state matrix A (8) for for the system to be both controllable and observable [1]. Matlab was used to calculate the rank of each matrix, which is eight for both, confirming controllability and observability for the linearized pumping model.

[1]The state matrix, A, is an 8x8 matrix but only has rank 6 because only the differential position (piston minus motor, $\theta_p - \theta_m$) is an energetic state. That is allowable, A need not be full rank, but the controllability and observability matrices must be.

8.2 Linear Model of Transition

During transition, the inflow and outflow ports are occluded. In the linear approximation, when leakage is neglected, it is assumed that the ports are completely closed, and the bond graph simplifies to that seen in Figure 8.3. When the power bond to the inflow and outflow ports is removed, the pistons are directly coupled, and the order of the system is reduced by one.

8.2.1 State Equations

State equations can be derived form the bond graph in Figure 8.3. First, the state equations from the motor-piston subsystems from Section 7.1.1 remain unchanged for the 'hold' motor-piston:

$$\dot{\omega}_{mh} = \frac{1}{J_m}\left[\frac{V_h k_e - k_e^2 \omega_{mh}}{R} - b_m \omega_{mh} - k_c(\theta_{ph} - \theta_{mh})\right] \tag{8.27}$$

$$\dot{\omega}_{ph} = \frac{1}{2J_p + J_h + J_d}\left[k_c(\theta_{mh} - \theta_{ph}) + k_c(\theta_{md} - \theta_{pd}) - b_h \omega_{ph} - b_d \omega_{pd}\right] \tag{8.28}$$

$$\dot{\theta}_{mh} = \omega_{mh} \tag{8.29}$$

$$\dot{\theta}_{ph} = \omega_{ph} \tag{8.30}$$

And for the 'drive' motor-piston:

$$\dot{\omega}_{md} = \frac{1}{J_m}\left[\frac{V_d k_e - k_e^2 \omega_{md}}{R} - b_m \omega_{md} - k_c(\theta_{pd} - \theta_{md})\right] \tag{8.31}$$

$$\dot{\omega}_{pd} = \frac{1}{2J_p + J_h + J_d}\left[k_c(\theta_{mh} - \theta_{ph}) + k_c(\theta_{md} - \theta_{pd}) - b_h \omega_{ph} - b_d \omega_{pd}\right] \tag{8.32}$$

$$\dot{\theta}_{md} = \omega_{md} \tag{8.33}$$

$$\dot{\theta}_{pd} = \omega_{pd} \tag{8.34}$$

The differential equations for the piston velocities (ω_{ph} and ω_{pd}) are identical because the pistons are directly coupled. In this case, the order of the system reduces from six energetic states in the pumping case to five in the transition.

8.2.2 State Space

The linear model can be represented in state space

$$\dot{\mathbf{x}} = A_T\mathbf{x} + B\mathbf{u} + W_T\mathbf{w}$$

There are eight states as before,

$$\mathbf{x} = \begin{bmatrix}\theta_{m1} & \theta_{m2} & \omega_{m1} & \omega_{m2} & \theta_{p1} & \theta_{p2} & \omega_{p1} & \omega_{p2}\end{bmatrix}^T$$

But in this case, the velocity of the pistons are directly coupled ($\omega_{p1} = \omega_{p2}$).

$$A_T = \begin{bmatrix} 0 & 0 & 1 & 0 & 0 & 0 & 0 & 0 \\ 0 & 0 & 0 & 1 & 0 & 0 & 0 & 0 \\ -\frac{k_c}{J_m} & 0 & -\frac{b_m + k_e^2/R}{J_m} & 0 & \frac{k_c}{J_m} & 0 & 0 & 0 \\ 0 & -\frac{k_c}{J_m} & 0 & -\frac{b_m + k_e^2/R}{J_m} & 0 & \frac{k_c}{J_m} & 0 & 0 \\ 0 & 0 & 0 & 0 & 0 & 0 & 1 & 0 \\ 0 & 0 & 0 & 0 & 0 & 0 & 0 & 1 \\ \frac{k_c}{J_t} & \frac{k_c}{J_t} & 0 & 0 & -\frac{k_c}{J_t} & -\frac{k_c}{J_t} & -\frac{b_t}{2J_t} & -\frac{b_t}{2J_t} \\ \frac{k_c}{J_t} & \frac{k_c}{J_t} & 0 & 0 & -\frac{k_c}{J_t} & -\frac{k_c}{J_t} & -\frac{b_t}{2J_t} & -\frac{b_t}{2J_t} \end{bmatrix}$$

where

$$J_t = 2J_p + J_d + J_h;$$

$$b_t = 2b_p + b_h + b_d;$$

The input matrix is the same as before.

$$B_T = \begin{bmatrix} 0 & 0 \\ 0 & 0 \\ \frac{k_e}{R_e J_m} & 0 \\ 0 & \frac{k_e}{R_e J_m} \\ 0 & 0 \\ 0 & 0 \\ 0 & 0 \\ 0 & 0 \end{bmatrix}$$

In this case, when the inflow and outflow ports are assumed to be completely blocked, the differential pressure does not contribute to the system. Therefore the disturbance matrix is zero

$$W_T = 0$$

8.2.3 Controllability and Observability

To determine these properties for the linearized transition system, the controllability matrix $\mathcal{C}$ and the observability matrix $\mathcal{O}$ are found using Matlab.

$$\text{rank}(\mathcal{C}) = 6 \tag{8.35}$$

$$\text{rank}(\mathcal{O}) = 8 \tag{8.36}$$

The system is observable, but not controllable. This is because the pistons have been coupled together and can no longer be independently controlled with the two inputs. What are the implications of this? During transition when the ports are completely occluded (and leakage is neglected), the pistons are not independently controllable. If they enter the transition at 10 degrees separation, then they would remain at 10 degrees separation through the transition and move at the same velocity. This is true in this simplified model where leakage is neglected, but not necessarily true for the actual system. And this is not a problem as long as the desired piston angles move together during transition and the desired piston velocities stay the same during transition - then the system is fully controllable because the piston position and velocity states are directly coupled.

8.3 Reduced-Order Model Zones

Just as in the switched model, the demarcations between the different modes can be visualized using a structure-space map. In this case, there are only three structures:

- **1**. Piston 1 is the driving piston, and piston 2 is the hold piston
- **2**. Piston 2 is the driving piston, and piston 1 is the hold piston
- **T**. Transition - either or both ports are completely occluded

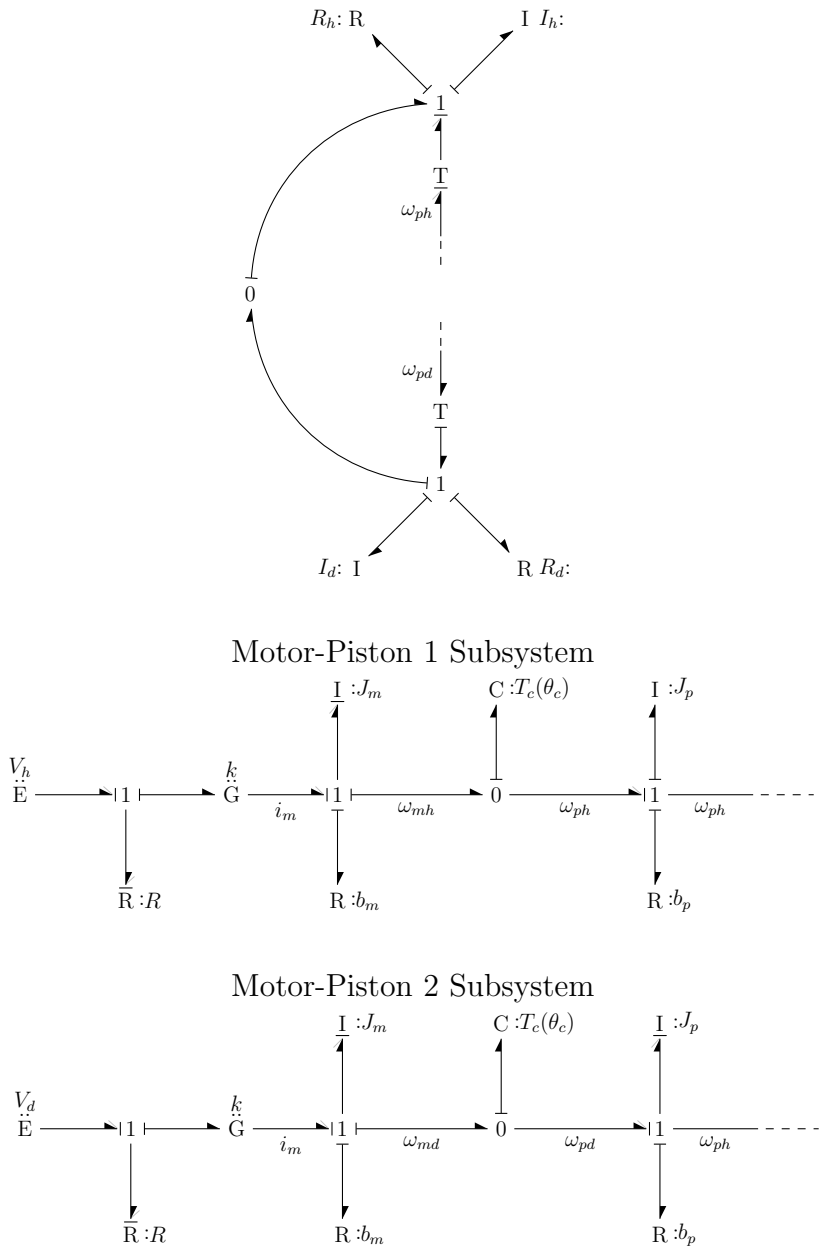

Figure 8.3: Simplified linear model of the 2PTP transition. When the inflow and/or outflow ports have been occluded, the pistons become directly coupled. In this case, one of the pistons has derivative causality and the number of states is reduced compared to the linear pumping system.

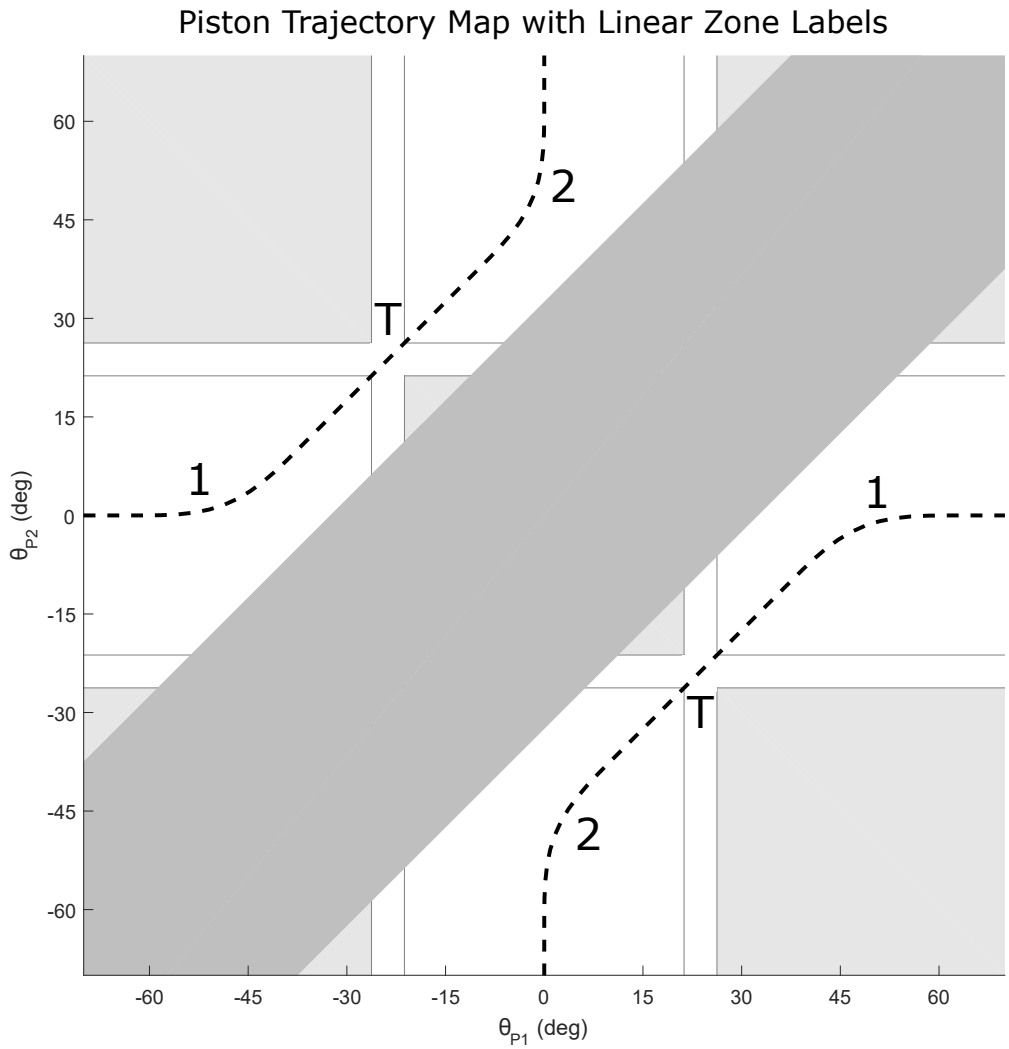

Figure 8.4: Piston trajectory map. The differential state equations are different for each zone as the pistons transition past the inflow and outflow ports.

8.4 Coupling

The difficulty in formulating the reduced-order for both the pumping and transition modes arises due to the coupling of the flow. For the pumping case, the acceleration of one of the pistons directly influences the acceleration of the other due to the inertance of the fluid in the cannulas. This can be seen in the coupled state equations for piston velocity.

$$\begin{bmatrix} \dot{\omega}_{pd} \\ \dot{\omega}_{ph} \end{bmatrix} = \begin{bmatrix} \frac{1}{\hat{J}_d} & \frac{1}{\hat{J}_c} \\ \frac{1}{\hat{J}_c} & \frac{1}{\hat{J}_h} \end{bmatrix} \begin{bmatrix} k_c(\theta_{md} - \theta_{pd}) - \hat{b}_d\omega_{pd} - Ar\Delta P + b_c\omega_{ph} \\ k_c(\theta_{mh} - \theta_{ph}) - \hat{b}_h\omega_{ph} + Ar\Delta P + b_c\omega_{pd} \end{bmatrix} \tag{8.37}$$

If the off-diagonal components of the inverted mass moment of inertia matrix were zero, then the pistons would be completely decoupled and each motor/piston subsystem could be treated completely independently. When the off-diagonal component becomes larger, the pistons become more directly coupled. In the extreme case of infinitely long cannulas, the pistons would be directly coupled as in the transition case.

How coupled the pistons are to each other changes how they should be controlled, and changes the complexity of the observer model that is needed to estimate the unmeasured states. The decoupled system (zero cannula length) would consist of two systems with 4 states, whereas the coupled system consists of 8 states. For the sake of simplicity, it would be good to ignore the coupling, but this would seem to depend on the length of the cannulas. A quantification of the degree of coupling would be helpful.

One way to assess the degree of coupling is the look at the effective mass moments of inertia in the coupled piston velocity equations above. The piston velocity dynamic equations can each be expressed as the sum of torques on each piston.

$$\begin{bmatrix} \dot{\omega}_{pd} \\ \dot{\omega}_{ph} \end{bmatrix} = \begin{bmatrix} \frac{1}{\hat{J}_d} & \frac{1}{\hat{J}_c} \\ \frac{1}{\hat{J}_c} & \frac{1}{\hat{J}_h} \end{bmatrix} \begin{bmatrix} T_d \\ T_h \end{bmatrix} \tag{8.38}$$

where

$$T_d = k_c(\theta_{md} - \theta_{pd}) - \hat{b}_d\omega_{pd} - Ar\Delta P + b_c\omega_{ph} \tag{8.39}$$

$$T_h = k_c(\theta_{mh} - \theta_{ph}) - \hat{b}_h\omega_{ph} + Ar\Delta P + b_c\omega_{pd} \tag{8.40}$$

The state equations are rewritten in terms of these torques:

$$\dot{\omega}_{pd} = \frac{1}{\hat{J}_d} T_d + \frac{1}{\hat{J}_c} T_h \tag{8.41}$$

$$\dot{\omega}_{ph} = \frac{1}{\hat{J}_h} T_h + \frac{1}{\hat{J}_c} T_d \tag{8.42}$$

These equations can be rearranged by introducing a dimensionless variable γ

$$\dot{\omega}_{pd} = \frac{1}{\hat{J}_d} \left(T_d + \gamma_d T_h \right) \tag{8.43}$$

$$\dot{\omega}_{ph} = \frac{1}{\hat{J}_h} \left(T_h + \gamma_h T_d \right) \tag{8.44}$$

where

$$\gamma_h = \frac{1/\hat{J}_c}{1/\hat{J}_h} \tag{8.45}$$

$$\gamma_d = \frac{1/\hat{J}_c}{1/\hat{J}_d} \tag{8.46}$$

This dimensionless variable represents the degree of coupling. If $\gamma = 0$, then the torque on one piston does not influence the dynamics of the other. If $\gamma = 1$, then the equations become identical and the pistons are directly coupled. Therefore, γ becomes a helpful dimensionless variable that can be used to determine whether or not the fluid coupling should be included or could be ignored. The coupling variable γ is a ratio of the mass moments of the coupled inertias, which are a function of the length of the cannulas. Figure 8.5 shows how the inverse effective mass moments of inertia for the drive piston ($1/\hat{J}_d$), the hold piston ($1/\hat{J}_h$), and for the coupled flow ($1/\hat{J}_c$). The figure also shows the dimensionless variables γ_d and γ_h, which increase with increasing cannula length as expected, and are zero when the cannula length is zero and the flows are completely decoupled.

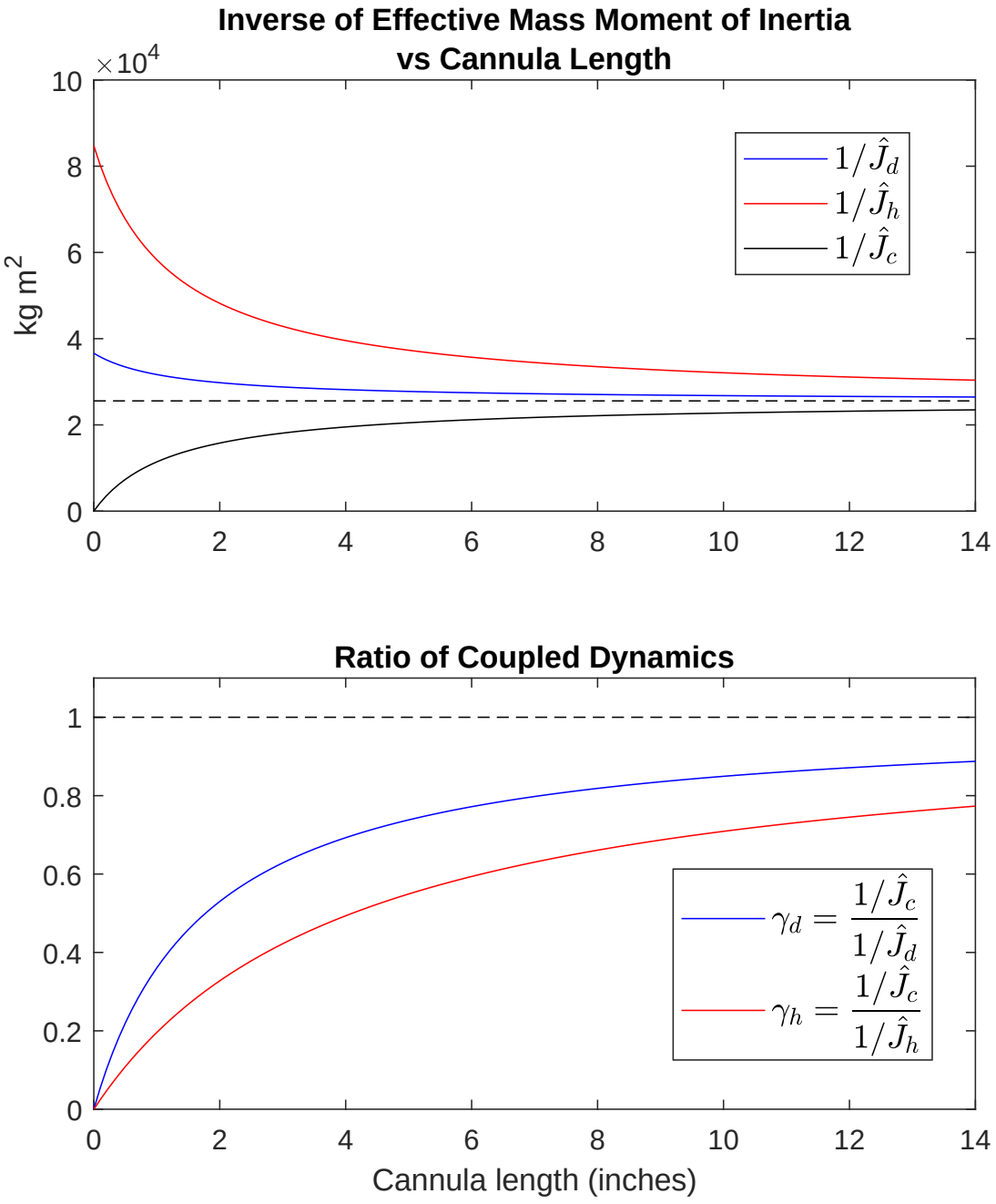

Figure 8.5: Effective coupled mass moment of inertias vs cannula length. Note that as the cannula length goes to zeros, the effective coupled inertia ($\hat{J}_c$) goes to infinity, and so $1/\hat{J}_c$ goes to zero, which removes the off diagnoal terms from the coupled differential equations and effectively decouples the flows. Note also that all of the effective inertias asymptote at the same value, which is $2J_p + J_d + J_h$

Part IV

Low-Level Control and Estimation

Chapter 9. Low-Level Control

This chapter uses the reduced-order linear 2PTP model to develop improved control with linear methods (specifically LQR) and assess the results compared to previous PID control in simulations using the 30-structure 2PTP model.

Chapter 10. State Estimation

This chapter develops estimation methods for unmeasurable states in the 2PTP. Kalman filter techniques are utilized and the suboptimal steady state gain is used to minimize computational time so that the observer can run in real-time on the pump controller.

Chapter 11. Stability and Robustness

This chapter studies the stability and robustness of the compensated system (control with estimation). Matlab robustness tools are used as well as a pole plot cloud to determine the sensitivity to parameter uncertainty.

Chapter 12. Experiments

This chapter studies results from preliminary experiments in passive and active mock circulatory loops to verify similarity with the model, test the improved control, and confirm pressure and flow estimation.

Chapter 9

Low-Level Control

This chapter uses the reduced-order linear 2PTP model to develop improved control with linear methods (specifically LQR) and assess the results compared to previous PID control in simulations using the 30-structure 2PTP model.

The motion and position of the pistons in the 2PTP are controlled by two independent brushless DC motors via a magnetic coupling. The position of the motors is measured using diametrically magnetized cylinders bonded to the motor rotors and 12-bit 2D hall effects sensors (0.088° resolution) [31]. Currently, the motors are driven to follow piece-wise sinusoidal reference curves using simple proportional-integral (PI) control on the error signal ($e = \theta_{\text{ref}} - \theta_m$), where the error ($e$) is calculated from the desired angular position (θ_{ref}) minus the actual position of the motor (θ_m) obtained from the angular magnetic sensor. This method works reasonably well, but is not robust and experiences problems when blood pressure is high or when the pump tries to pump at high flow rates. Problems especially arise when the pistons are moving close together during the transition period. During this time when the pistons are transversing the inflow and outflow ports, large impulses can occur as the blood pressure switches from one side of the piston to the other. This poor transition control can lead to the pistons colliding, as seen in experimental data seen in Figure 1.4.

Improving 2PTP control is critical for:

1. Providing precisely timed pulsatile ejections that are important for maximizing the benefits of synchronous flow
2. Preventing collision if the pistons are too close together during transition that could result in damage to the pistons, pump failure, and possibly patient death
3. Preventing shunting and back flow if the pistons are too far apart during transition.
4. Minimizing vibration that could cause patient discomfort.
5. Reducing power, which may be unecessarily high due to poor control.

9.1 Linear Quadratic Regulator

Many methods are available for improving the dynamic piston control of the 2PTP. One common approaches is linear quadratic regulation (LQR). The linear reduced-order models developed for pumping and transition that were developed in the previous chapter can be used to design this type of control. LQR is a form of optimal control that provides weighting functions to states and inputs. By having weighting available, particular states (for example piston position) can be given more priority than others (for example motor position). In addition to the benefits of weighting, LQR also improves the dynamic response of the system using feedback from all of the states.

The first step to develop LQR control is to define a performance index to be minimized. The controller for the pump will run indefinitely, so the problem will be formulated with 'infinite horizon'. Also, in this case, the piston states follow reference trajectories $\mathbf{x}_r(t)$. The state error is the difference between the state and reference

$$\mathbf{e} = \mathbf{x} - \mathbf{x}_r \tag{9.1}$$

Then, rather than regulate states to zero, the LQR will be be formulated to regulate the error to zero. The performance index (PI) is then defined to be:

$$J = \frac{1}{2}\int_0^\infty \left[\mathbf{e}^T Q \mathbf{e} + \mathbf{x}^T R \mathbf{x}\right] dt$$

The state weights Q and input weights R are matrices (assuming no off-diagonal terms will be applied), whose values will be assigned based on desired performance characteristics.

$$Q = \begin{bmatrix} q_{\theta_{m1}} & 0 & 0 & 0 & 0 & 0 & 0 & 0 \\ 0 & q_{\theta_{m2}} & 0 & 0 & 0 & 0 & 0 & 0 \\ 0 & 0 & q_{\omega_{m1}} & 0 & 0 & 0 & 0 & 0 \\ 0 & 0 & 0 & q_{\omega_{m2}} & 0 & 0 & 0 & 0 \\ 0 & 0 & 0 & 0 & q_{\theta_{p1}} & 0 & 0 & 0 \\ 0 & 0 & 0 & 0 & 0 & q_{\theta_{p2}} & 0 & 0 \\ 0 & 0 & 0 & 0 & 0 & 0 & q_{\omega_{p1}} & 0 \\ 0 & 0 & 0 & 0 & 0 & 0 & 0 & q_{\omega_{p2}} \end{bmatrix} \qquad R = \begin{bmatrix} r_{V_1} & 0 \\ 0 & r_{V_2} \end{bmatrix}$$

For LQR, the closed-loop control input is defined by

$$\mathbf{u} = -R^{-1}B^T(S\mathbf{x}) = -G\mathbf{x} \tag{9.2}$$

where R, B, and $\mathbf{x}$ are known or determined by the dynamics. S is unknown, but can be found using the Matrix Ricatti Equation:

$$\dot{S} = -A^T S - SA + SBR^{-1}B^T S - C^T QC$$

Where $\dot{S} = 0$ for the infinite horizon problem.

$$0 = -A^T S - SA + SBR^{-1}B^T S - C^T QC$$

The steady state Matrix Ricatti Equation can be solved in Matlab using `are()`.

```
S = are(A,B*inv(R)*B',Q);
```

Once S is determined, the feedback gain G is found by

$$G = R^{-1}B^T S \tag{9.3}$$

which is used for the control

$$\mathbf{u} = -G\mathbf{x} \tag{9.4}$$

9.1.1 LQR Weights

To determine LQR feedback gains G, the weights Q and R must be assigned. As a starting point, a general rule of thumb is to set the weights inversely proportional to the square of the maximum allowable error:

$$q_i = \frac{1}{e^2_{x_i,\max}} \quad \text{and} \quad r_i = \frac{1}{e^2_{u_i,\max}}$$

Piston position and velocity reference trajectories were derived in Chapter 5, and would be followed closely if possible. A good starting point might be 2 degrees error allowed from the ideal angular position trajectory.

The piston velocity and motor position and velocity will by necessity follow closely due to the magnetic coupling, so we might not want to weight the motors at all to allow more dynamic motion to achieve low piston trajectory error. The input voltage is usually limited by the

power supply. In this case, 15V saturation will be assumed. This results in the following assignments.

$$q_{\theta_m} = 0$$

$$q_{\omega_m} = 0$$

$$q_{\theta_p} = \frac{1}{(3 \text{ deg})^2} = .111 \text{ deg}^{-2}$$

$$q_{\omega_p} = 0$$

$$r_V = \frac{1}{(15 \text{ V})^2} = .0044 \text{ V}^2$$

One the feedback gain G is determined, the poles of the closed-loop system for pumping control can be determined using `eig(A-B*K)`

$$\lambda_{1,2} = -118 \pm 947i$$

$$\lambda_{3,4} = -114 \pm 777i$$

$$\lambda_{5,6} = -321 \pm 261i$$

$$\lambda_{7,8} = -101 \pm 98i$$

And for transition control:

$$\lambda_{1,2} = -121 \pm 942i$$

$$\lambda_{3,4} = -216 \pm 786i$$

$$\lambda_{5,6} = -318 \pm 261i$$

$$\lambda_{7,8} = 0$$

Note the zero poles were introduced for transition because the order of the system was reduced in the linear transition model, due to the piston velocities and positions being directly coupled (by an offset).

9.2 Disturbance / Exogenous Variable Rejection

The pressure is a disturbance on the system, whose influence could be rejected by incorporating it into the control if it was a known quantity. The pressure is not currently measured by the device, but it could be estimated. Whether or not and how this estimation might be done will be discussed more in the next chapter. For this section, it will be assumed that the pressure is known. If known, the pressure effects can be included in the linear quadratic regulator formulation such that it can be assigned as feedback gain to adjust the control based on its value.

First, write the states in terms of the controllable states $\mathbf{x}$ and the exogenous pressure states $\mathbf{x}_p$,

$$\left[\begin{array}{c} \dot{\mathbf{x}} \\ \hline \dot{\mathbf{x}}_p \end{array}\right] = \left[\begin{array}{c|c} A & W \\ \hline 0 & A_p \end{array}\right] \left[\begin{array}{c} \mathbf{x} \\ \hline \mathbf{x}_p \end{array}\right] + \left[\begin{array}{c} B \\ \hline 0 \end{array}\right] \mathbf{u} \tag{9.5}$$

Define these state partitioned matrices as

$$A_d = \begin{bmatrix} A & W \\ 0 & A_p \end{bmatrix} \quad B_d = \begin{bmatrix} B \\ 0 \end{bmatrix} \tag{9.6}$$

Similarly, let

$$C_d = \begin{bmatrix} C & 0 \\ 0 & C_p \end{bmatrix} \quad Q_d = \begin{bmatrix} Q & 0 \\ 0 & 0 \end{bmatrix} \quad R_d = \begin{bmatrix} R & 0 \\ 0 & 0 \end{bmatrix} \quad \text{and} \quad S_d = \begin{bmatrix} S_1 & S_2 \\ S_2^T & S_3 \end{bmatrix} \tag{9.7}$$

Note that the lower right quadrant of the Q_d matrix is set to zero. This must be done because the pressure is not controllable and therefore the quadratic pressure cannot be minimized through the control.

Next, the Matrix Ricatti Equation is written for the system that includes the exogenous variables

$$\dot{S}_d = -A_d^T S_d - S_d A_d + S_d B_d R^{-1} B_d^T S_d - C_d^T Q_d C_d \tag{9.8}$$

which can be rewritten in terms of the partitioned matrices

$$\begin{aligned} \begin{bmatrix} \dot{S}_1 & \dot{S}_2 \\ \dot{S}_2^T & \dot{S}_3 \end{bmatrix} = &- \begin{bmatrix} A^T & 0 \\ W^T & A_p^T \end{bmatrix} \begin{bmatrix} S_1 & S_2 \\ S_2^T & S_3 \end{bmatrix} - \begin{bmatrix} S_1 & S_2 \\ S_2^T & S_3 \end{bmatrix} \begin{bmatrix} A & W \\ 0 & A_p \end{bmatrix} \\ &+ \begin{bmatrix} S_1 & S_2 \\ S_2^T & S_3 \end{bmatrix} \begin{bmatrix} B \\ 0 \end{bmatrix} R^{-1} \begin{bmatrix} B^T & 0 \end{bmatrix} \begin{bmatrix} S_1 & S_2 \\ S_2^T & S_3 \end{bmatrix} \\ &- \begin{bmatrix} C^T & 0 \\ 0 & C_p^T \end{bmatrix} \begin{bmatrix} Q & 0 \\ 0 & 0 \end{bmatrix} \begin{bmatrix} C & 0 \\ 0 & C_p \end{bmatrix} \end{aligned}$$

Performing the linear algebra, the four partitions can be written:

$$\dot{S}_1 = -A^T S_1 - S_1 A + S_1 B R^{-1} B^T S_1 - C^T Q C \tag{9.9}$$

$$\dot{S}_2 = -A^T S_2 - S_2 A_p - S_1 W + S_1 B R^{-1} B^T S_2 \tag{9.10}$$

$$\dot{S}_3 = -W^T S_2 - A_p^T S_3 - S_3 A_p - S_2^T W + S_2^T B R^{-1} B^T S_2 \tag{9.11}$$

Similarly, the feedback control can be partitioned into state and exogenous state feedback

$$\mathbf{u} = -R^{-1} \begin{bmatrix} B^T & 0 \end{bmatrix} \begin{bmatrix} S_1 & S_2 \\ S_2 & S_3 \end{bmatrix} \begin{bmatrix} \mathbf{x} \\ \mathbf{x}_p \end{bmatrix} \tag{9.12}$$

$$\mathbf{u} = -R^{-1} \left(B^T S_1 \mathbf{x} + B^T S_2 \mathbf{x}_p \right) \tag{9.13}$$

Or, in terms of the feedback gain G

$$\mathbf{u} = G_d \mathbf{x}_d = G\mathbf{x} + G_p \mathbf{x}_p \tag{9.14}$$

where

$$G = -R^{-1} B^T S_1 \quad \text{and} \quad G_p = R^{-1} B^T S_2 \tag{9.15}$$

Note that the feedback gain G for the states $\mathbf{x}$ is a function of S_1 only, and from above it can be seen that S_1 is decoupled from the disturbance matrix W as well as the disturbance Ricatti solutions S_2 and S_3.

The feedback gain for the pressure G_p is a function of S_2, the solution of which is a function of S_1. Interestingly, S_3 falls out and is not needed to determine the state and disturbance feedback gains.

Another way to demonstrate that the state feedback is decoupled is by looking at the eigenvalues of the feedback state control, and observing that it is not altered by the inclusion of the exogenous variables.

$$A_d - B_d G_d = \begin{bmatrix} A & W \\ 0 & 0 \end{bmatrix} - \begin{bmatrix} B \\ 0 \end{bmatrix} \begin{bmatrix} G & G_p \end{bmatrix} = \begin{bmatrix} A - BG & W - BG_p \\ 0 & 0 \end{bmatrix} \tag{9.16}$$

The eigenvalues are found by

$$|\lambda I - (A_D - B_d G_d)| = \begin{vmatrix} \lambda I - (A - BG) & -(W - BG_p) \\ 0 & \lambda I_m \end{vmatrix} = \lambda^m \left[\lambda I - (A - BG) \right] = 0$$

(9.17)

The closed-loop eigenvalues are decoupled from the exogenous variables and their feedback. And, there have been m zero eigenvalues introduced where m is the number of exogenous variables.

This disturbance rejection functions in such a way as to remove steady state error from the system. Another way to do this is to include an integrator in the control formulation.

9.3 Feedforward

Feedback control with LQR on the reference trajectory error and disturbance rejection can only take the control so far. One benefit of prescribing reference trajectories (in terms of not only position, but velocity and acceleration as well), is that the input required to drive the system along a prescribed trajectory can be anticipated and fed forward.

It will be shown that feeding velocity and acceleration terms forward will be helpful, therefore it is desirable that the position curve is twice differentiable and that the velocity and acceleration curves are smooth (no step changes). These requirements were already enforced in Chapter 5.

For feedforward, it will be assumed that the motor and piston position, velocity, and acceleration are the same. This will compensate for the low order dynamics of the system, but ignore the higher order effects of the mangetic coupling. This is acceptable because the feedforward is not meant to be an ideal input that compensates for all of the dynamics. It's intention is to predict, to a reasonable extent, the input that will be required from the low order dynamics of the system, and then to let the feedback control compensate for the rest.

Feedforward assumptions:

1. θ_r (reference trajectory) is of class C2 ($\dot{\theta}_r$ and $\ddot{\theta}_r$ exist and are continuous)
2. $\theta_m \approx \theta_p$ (higher order magnetic coupling dynamics ignored)
3. $\omega_m \approx \omega_p$ (higher order magnetic coupling dynamics ignored)
4. $\alpha_m \approx \alpha_p$ (higher order magnetic coupling dynamics ignored)

9.3.1 Fluid and Piston Feedforward

Much of the power required to produce pulsatile flow is due to the piston torque required for the acceleration and deceleration of the fluid in the pump and in the cannulas. This torque can be anticipated and quantified by looking at the coupled dynamic equations for the piston motion.

$$\begin{bmatrix} \dot{\omega}_{pd} \\ \dot{\omega}_{ph} \end{bmatrix} = \begin{bmatrix} \frac{1}{\hat{J}_d} & \frac{1}{\hat{J}_c} \\ \frac{1}{\hat{J}_c} & \frac{1}{\hat{J}_h} \end{bmatrix} \begin{bmatrix} T_d^p - \hat{b}_d \omega_{pd} + b_c \omega_{ph} \\ T_h^p - \hat{b}_h \omega_{ph} + b_c \omega_{pd} \end{bmatrix} \tag{9.18}$$

where T^p is the torque required to drive the piston at a known acceleration and velocity, and where the effective mass moments of inertia were previously defined as:

$$\hat{J}_h = J_p + J_h + J_c - \frac{J_c^2}{J_p + J_d + J_c} \tag{9.19}$$

$$\hat{J}_d = J_p + J_d + J_c - \frac{J_c^2}{J_p + J_h + J_c} \tag{9.20}$$

$$\hat{J}_c = \frac{1}{J_c} \left(J_p + J_d + J_c \right) \left(J_p + J_h + J_c \right) - J_c \tag{9.21}$$

To solve for T_d^p and T_h^p the inverse mass moment of inertia matrix can be inverted

$$\begin{bmatrix} \frac{1}{\hat{J}_d} & \frac{1}{\hat{J}_c} \\ \frac{1}{\hat{J}_c} & \frac{1}{\hat{J}_h} \end{bmatrix}^{-1} \begin{bmatrix} \dot{\omega}_{pd} \\ \dot{\omega}_{ph} \end{bmatrix} = \begin{bmatrix} T_d^p - \hat{b}_d \omega_{pd} + b_c \omega_{ph} \\ T_h^p - \hat{b}_h \omega_{ph} + b_c \omega_{pd} \end{bmatrix} \tag{9.22}$$

$$\begin{bmatrix} J_p + J_d + J_c & -J_c \\ -J_c & J_p + J_h + J_c \end{bmatrix} \begin{bmatrix} \dot{\omega}_{pd} \\ \dot{\omega}_{ph} \end{bmatrix} = \begin{bmatrix} T_d^p - \hat{b}_d \omega_{pd} + b_c \omega_{ph} \\ T_h^p - \hat{b}_h \omega_{ph} + b_c \omega_{pd} \end{bmatrix} \tag{9.23}$$

Then the torques T_d^p and T_h^p can be expressed as a function of the desired acceleration:

$$T_d^p = \left(J_p + J_d + J_c \right) \dot{\omega}_{pd} - J_c \dot{\omega}_{ph} + \hat{b}_d \omega_{pd} - b_c \omega_{ph} \tag{9.24}$$

$$T_h^p = \left(J_p + J_h + J_c \right) \dot{\omega}_{ph} - J_c \dot{\omega}_{pd} + \hat{b}_h \omega_{ph} - b_c \omega_{pd} \tag{9.25}$$

Torque can be converted to voltage by the relationship

$$V^p = \frac{R}{k_e} T^p \tag{9.26}$$

Again, the higher order dynamics of the magnetic spring coupling and ignored and the assumption is made that input will drive these torques directly through the motor and that the feedback control can compensate for the higher-order effects. Note also that the feedforward term contains the desired velocity terms as well as acceleration. In this way, the piston friction and fluid resistance are fed forward as well.

9.3.2 Electrical back emf and Motor Dynamics

Similarly, the torque required to drive the motor at a known acceleration and velocity can be determined using the dynamic equiations for the motors.

$$\dot{\omega}_{md} = \frac{1}{J_m}\left[\frac{V_d k_e - k_e^2 \omega_{md}}{R} - b_m \omega_{md} - k_c(\theta_{pd} - \theta_{md})\right] \tag{9.27}$$

$$\dot{\omega}_{mh} = \frac{1}{J_m}\left[\frac{V_h k_e - k_e^2 \omega_{mh}}{R} - b_m \omega_{mh} - k_c(\theta_{ph} - \theta_{mh})\right] \tag{9.28}$$

Again, ignoring the higher order dynamics of the magnetic coupling, the torques from the magnetic spring can be replaced by the torques required to drive the pistons and fluid:

$$\dot{\omega}_{md} = \frac{1}{J_m}\left[\frac{V_d k_e - k_e^2 \omega_{md}}{R} - b_m \omega_{md} - T_d^p\right] \tag{9.29}$$

$$\dot{\omega}_{mh} = \frac{1}{J_m}\left[\frac{V_h k_e - k_e^2 \omega_{mh}}{R} - b_m \omega_{mh} - T_h^p\right] \tag{9.30}$$

From these, the input voltages V_d and V_h can be expressed as a function of the desired acceleration and velocities:

$$V_d = \frac{R}{k_e}\left[J_m \dot{\omega}_{md} + \frac{k_e^2 \omega_{md}}{R} + b_m \omega_{md}\right] \tag{9.31}$$

$$V_h = \frac{R}{k_e}\left[J_m \dot{\omega}_{mh} + \frac{k_e^2 \omega_{mh}}{R} + b_m \omega_{mh}\right] \tag{9.32}$$

9.3.3 Combining the Fluid, Piston, and Motor Feedforward

The total feedforward is a sum of the piston feedforward voltage V^p and motor feedforward voltage V^m

$$V_d = V_d^p + V_d^m \qquad \text{and} \qquad V_h = V_h^p + V_h^m \tag{9.33}$$

The terms are added to get

$$V_d = \frac{R}{k_e}\left[J_m\dot{\omega}_{md} + \frac{k_e^2\omega_{md}}{R} + b_m\omega_{md} + (J_p + J_d + J_c)\,\dot{\omega}_{pd} - J_c\dot{\omega}_{ph} + \hat{b}_d\omega_{pd} - b_c\omega_{ph}\right] \quad (9.34)$$

$$V_h = \frac{R}{k_e}\left[J_m\dot{\omega}_{mh} + \frac{k_e^2\omega_{mh}}{R} + b_m\omega_{mh} + (J_p + J_h + J_c)\,\dot{\omega}_{ph} - J_c\dot{\omega}_{pd} + \hat{b}_h\omega_{ph} - b_c\omega_{pd}\right] \quad (9.35)$$

Then, as discussed above, when higher order dynamics of the magnetic coupling are ingored, the motor velocity and accelerations are treated as the same ($\omega_p \approx \omega_m$ and $\dot{\omega}_p \approx \dot{\omega}_m$), the equations can be simplified:

$$V_d = \frac{R}{k_e}\left[(J_p + J_d + J_c + J_m)\,\dot{\omega}_d - J_c\dot{\omega}_h + \left(\frac{k_e^2}{R} + b_m + \hat{b}_d\right)\omega_d - b_c\omega_h\right] \quad (9.36)$$

$$V_h = \frac{R}{k_e}\left[(J_p + J_d + J_c + J_m)\,\dot{\omega}_h - J_c\dot{\omega}_d + \left(\frac{k_e^2}{R} + b_m + \hat{b}_h\right)\omega_h - b_c\omega_d\right] \quad (9.37)$$

Now these voltages can be fed forward as functions of the desired velocities ω and acceleration $\dot{\omega}$ of the drive (d) and hold (h) piston/motor subsystems.

9.4 Simulation Results

Computational simulations are used to determine the effectiveness of LQR control compared to PID. The switched variable structure model is used as a test environment to simulate the actual pump dynamics (motor, piston, and flow), and then PID and LQR derived from the reduced-order model are implemented for control. For LQR, it is assumed that all states (motor position and velocities and piston position and velocities) are known. In reality, only motor position is measured. In practice, an observer (which is developed in the next chapter) is needed to estimate the unmeasurable states. For now, as an ideal test of the control, it is assumed that all states are known.

First, the model is simulated with PID control. Figure 9.1 shows simulation results for 5 L/min flow against a constant differential pump pressure of 100 mmHg with PID control. Significant deviation of the pistons positions from the reference trajectory (piston error) can be seen. During transition, when the pressure changes signs on the piston, the tracking error changes sign as well as the piston swings across the ideal trajectory. During this time, the pistons are transitioning and are ideally separated by 15°, but when the pressure changes

sides on both of the pistons, the pistons move toward each other, and collide (separation angle of zero degrees). While this piston position cannot be measured experimentally, during these high flow and pressure conditions, audible collisions of the piston ceramic material has been heard in prototype experiments, corresponding to the collision shown here.

Next, the model is simulated with LQR control. Figure 9.2 shows simulation results for 5 L/min flow against a constant differential pump pressure of 100 mmHg with LQR control. The piston position error from the reference trajectory has been drastically improved. The difference is especially notable in the plot of piston separation angle. With PID control, the pistons collide during transition, whereas they remain about 13° separated with LQR control (again, 15° is ideal).

Figure 9.3 compares PID and LQR by showing the piston angular position error from the reference trajectory as well as the control voltage input at simulated 5 L/min against 100 mmHg differential pump pressure. As noted above, LQR improves the position error from over 10° with PID control to about 1° with LQR control. Control input voltage is also plotted to demonstrate that the input requirements are not significantly affected by the change of control. Most of the power requirements are needed for the hydraulic load.

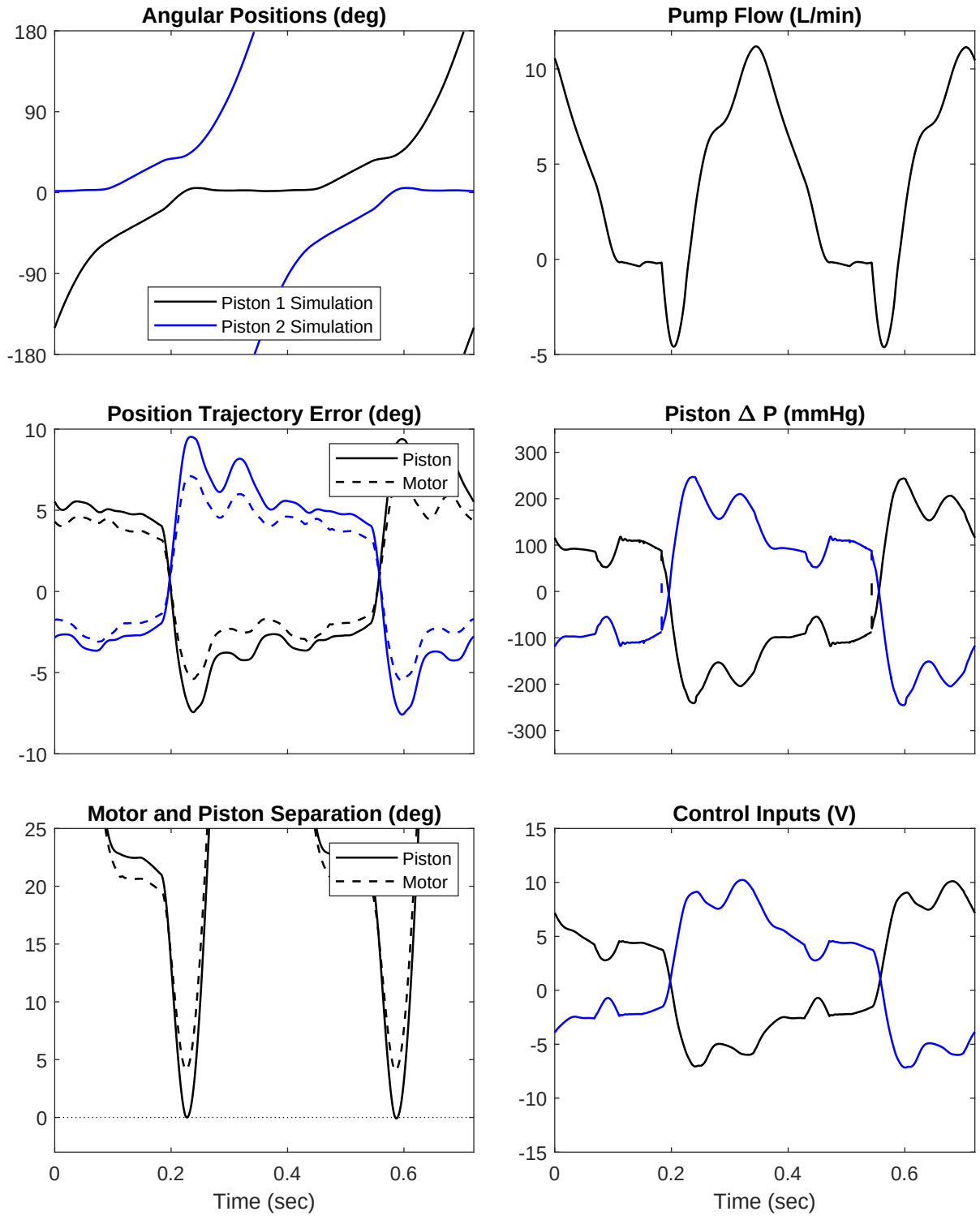

Figure 9.1: Simulated PID control at 5 L/min against 100 mmHg differential pump pressure. In this scenario, the pistons collide after transition when the differential pressure changes signs across the piston. Collision at high pressure has been observed experimentally.

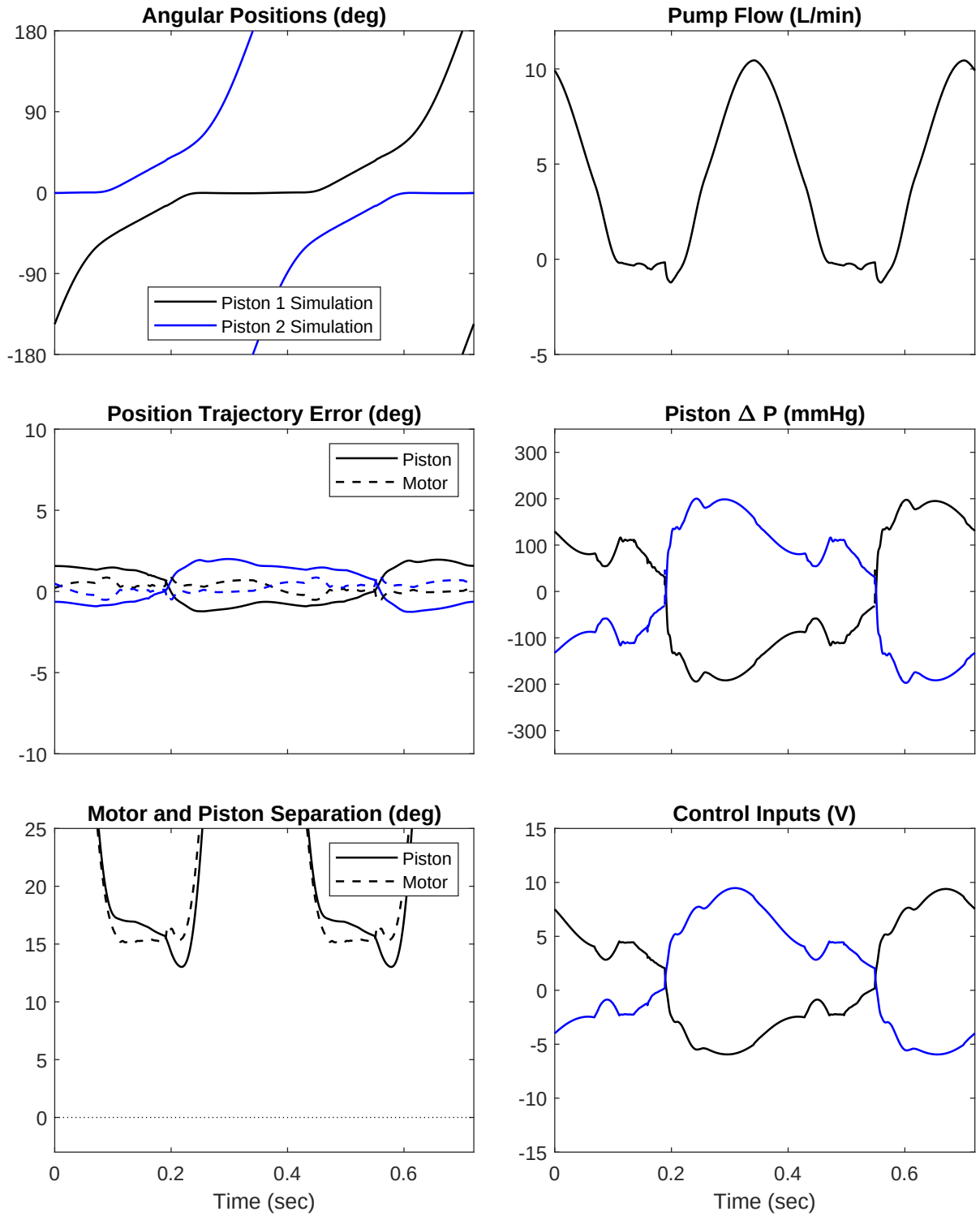

Figure 9.2: Simulated LQR control at 5 L/min against 100 mmHg differential pump pressure. LQR drastically improves the control of the pistons compared to PID control.

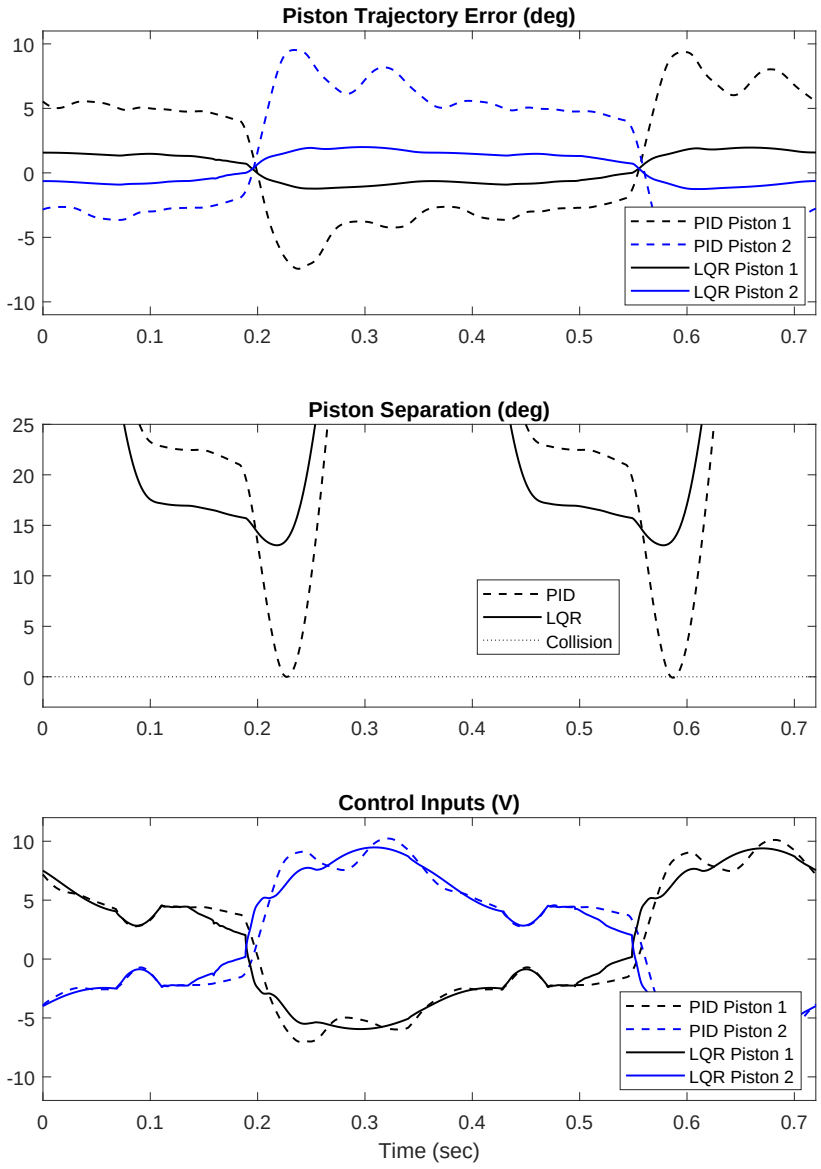

Figure 9.3: Piston trajectory error, piston separation, and input voltage for PID and LQR control at 5 L/min against 100 mmHg differential pump pressure. LQR drastically improves the trajectory control and prevents collision without requiring any significant additional input power.

Chapter 10

State Estimation

This chapter develops estimation methods for unmeasurable states in the 2PTP. Kalman filter techniques are utilized and the suboptimal steady state gain is used to minimize computational time so that the observer can run in real-time on the pump controller.

The control methods developed in the previous chapter assume that all of the states are known. In reality, only the motor positions are measured. The angular motor positions are measured using two 12-bit two-dimensional Hall effects sensor that detect the orientation of a diametrically magnetized cylindrical magnets bonded to the motor rotor shafts. The motor velocity is not measured and the pistons are contained within the toroidal pumping chamber and there is no straightforward way to measure their position or velocity. In addition, the exogenous disturbance (in this case the differential pressure across the pump) is not directly measured, but would be good to know for diagnostic purposes as well as disturbance rejection control. In order to make use of full-state or optimal control feedback methods developed in the previous chapter, an estimation of the unmeasured states must be developed.

An observer or reduced-order observer could be used to estimate the unmeasurable states, but arbitrary pole placement methods for placing the poles of the observer can lead to control feedback instability in the presence of measurement and process noise and uncertainty. Instead, a Kalman filter (which is an optimal observer) is a useful tool that can be used to formulate the observer instead, by taking into account the expected measurement and process noise of the system.

10.1 Kalman Filter

The Kalman filter is a well developed tool and a detailed description of it's formulation will not be included here. Briefly, the Kalman filter consists of three steps: 1) prediction, 2) covariance propagation, and 3) measurement update.

1. Prediction

The first step is to make a prediction of the states from time t_{k-1} to t_k. This prediction is based on the dynamics of the system and can be based on a linear or nonlinear model of the system. In the linear form, the discrete formulation can be used:

$$\hat{\mathbf{x}}_k^- = A_k \hat{\mathbf{x}}_{k-1}^+ + B_k \mathbf{u}_k \tag{10.1}$$

where A_k and B_k are in the discrete form. The minus (-) and plus (+) indicate whether the values are before (-) or after (+) the measurement update.

2. Covariance Propagation

The covariance grows between measurements, which is a function of the system dynamics (represented in A_k) as well as the estimation of the process noise Q_k.

$$P_k^- = A_k P_{x-1}^+ A_k^T + Q_k \tag{10.2}$$

3. Measurement update

When a measurement z_k is performed, the estimation $\hat{x}$ and covariance P can be updated (the estimation is improved and the covariance can be decreased based with the new information).

The measurement is a function of the states

$$z_k = C_k x_k \tag{10.3}$$

The Kalman gain K_k is a function of the covariance and measurement noise R_k

$$K_k = P_k^- C_k^T \left(C_k P_k^- C_k^T + R_k \right)^{-1} \tag{10.4}$$

Once the Kalman gain is defined, the innovation (the difference between the measurement and the expected value) is used to update the estimated state $\hat{x}$

$$\hat{x}_k^+ = \hat{x}_k^- + K_k \left(z_k - C_k \hat{x}_k^- \right) \tag{10.5}$$

The measurement adds information, so the covariance decreases. The update is defined by:

$$P_k^+ = \left(I - K_k C_k \right) P_k^- \tag{10.6}$$

10.2 2PTP Kalman Filter Setup

The reduced-order model will be used as the basis of the 2PTP Kalman filter. The reduced-order model has 8 states: the motor angular positions (2), motor angular velocities (2), piston angular positions (2), and piston angular velocities (2). In addition, there is an unknown pressure disturbance (ΔP) on the system. One option is to add the pressure as a 9th state so that it can be estimated using a Kalman filter. But, there are also unknown friction terms on each piston and complications that arise from transitioning. When all unknown disturbances from pressure and friction are lumped together, then piston stiction (high friction when the piston velocity is zero) can also create problems here and the friction has been shown to be nonlinear as well as position dependent and different from piston-to-piston. It's difficult to predict and model these changing friction forces, so they can instead be treated as process noise that the Kalman filter estimates. When each piston's friction as well as the pressure disturbance on the system is lumped into one disturbance, it makes it difficult to separate friction from pressure. Therefore, it's helpful to add two process disturbance terms (one for each piston) to 'cover' all of the uncertainty. This way, each process disturbance includes the pressure disturbance on the pistons, any nonlinear or variable friction, as well as any unaccounted for dynamics or uncertainty.

The linearized reduced-order model of the 2PTP is

$$\dot{\mathbf{x}} = A_i\mathbf{x} + B\mathbf{u} + W\Delta P \tag{10.7}$$

Because leakage was ignored, and pump flow was directly coupled to piston velocity, the pump dynamics are represented by an eighth order system. The state matrix A_i changes depending on which mode the pump is in, whether when piston 1 is pumping (A_1), piston 2 is pumping (A_2) or transition (A_T). The states are:

$$\mathbf{x} = \begin{bmatrix}\theta_{m1} & \theta_{m2} & \omega_{m1} & \omega_{m2} & \theta_{p1} & \theta_{p2} & \omega_{p1} & \omega_{p2}\end{bmatrix} \tag{10.8}$$

To formulate the Kalman filter, the differential pressure across the pump ΔP as well as piston friction can be included as two torque disturbances, one on each piston, and the estimated system dynamics become.

$$\dot{\hat{\mathbf{x}}} = A\hat{\mathbf{x}} + B\mathbf{u} + Gw \tag{10.9}$$

where the estimated metastate now includes the process disturbance torques T_1 and T_2.

$$\hat{\mathbf{x}} = \begin{bmatrix} \theta_{m1} & \theta_{m2} & \omega_{m1} & \omega_{m2} & \theta_{p1} & \theta_{p2} & \omega_{p1} & \omega_{p2} & T_1 & T_2 \end{bmatrix} \tag{10.10}$$

and G quantifies the process noise using the white noise component w, which gets added to the process torques T_1 and T_2

$$G = \begin{bmatrix} 0 & 0 & 0 & 0 & 0 & 0 & 0 & 0 & 1 & 1 \end{bmatrix}^T \tag{10.11}$$

Measurement noise must also be included in the formulation of the Kalman filter. This can be represnted by a white Gaussian vector $\mathbf{v}$ added to the measurement:

$$\mathbf{z}_i = C\mathbf{x}_i + \mathbf{v}_i \tag{10.12}$$

10.3 Process and Measurement Noise

The process noise Q and measurement noise R were selected based on the known dynamics of the system. The process torque disturbance is comprised of the differential pressure across the pump as well as any dynamics or friction that have not been accounted for the in the model formulation. These effects are represented as a first-order Markov process with Q =(50 mmHg)^2 process noise and a time constant of 0.02 sec. Motor position measurement noise can occur due to sensor noise and digital bit flips, therefore R was set to R =(0.2 deg)^2.

10.4 Switching

The reduced-order model has state-dependent switching, determined by the positions of the pistons in the torus. One option for dealing for this in the Kalman filter is to change the state matrix A_i at the switch points (A_1 for piston 1 pumping, A_2 for piston 2 pumping, and A_T for transition), and then allow the covariance and Kalman gain dynamically converge after each switch. Because the reduced order model is linear, the covariance and Kalman gain will reach steady-state after each switch. The dynamics of this transition depend on the state dynamics captured in A_i, but are independent of the states themselves.

Figure 10.1 shows the response of the covariance in time at each switch event. These are normalized, where each term is divided by it's value at steady state for comparison. This is

a tenth-order estimation system with a 10x10 symmetric covariance matrix, so there are 55 independent covariances shown in each plot. The covariance dissipates to steady state quickly in each case, approximately 0.02 seconds for both pumping into transition and transition into pumping. Also of note, though unsurprising, is that the transition from piston 1 pumping to transition is the same as piston 2 pumping to transition and, and likewise for the reverse.

Figure 10.2 shows the Kalman gains that can be computed from the covariances in Figure 10.1. Similar convergence in time is seen (reaching steady state at around 0.02 seconds). There are two measurements with ten estimation states, so there are 20 independent Kalman gains plotted. Again, they are shown normalized (divided by their steady state value), so that the time rate response of all 20 gains can be shown on the same plot.

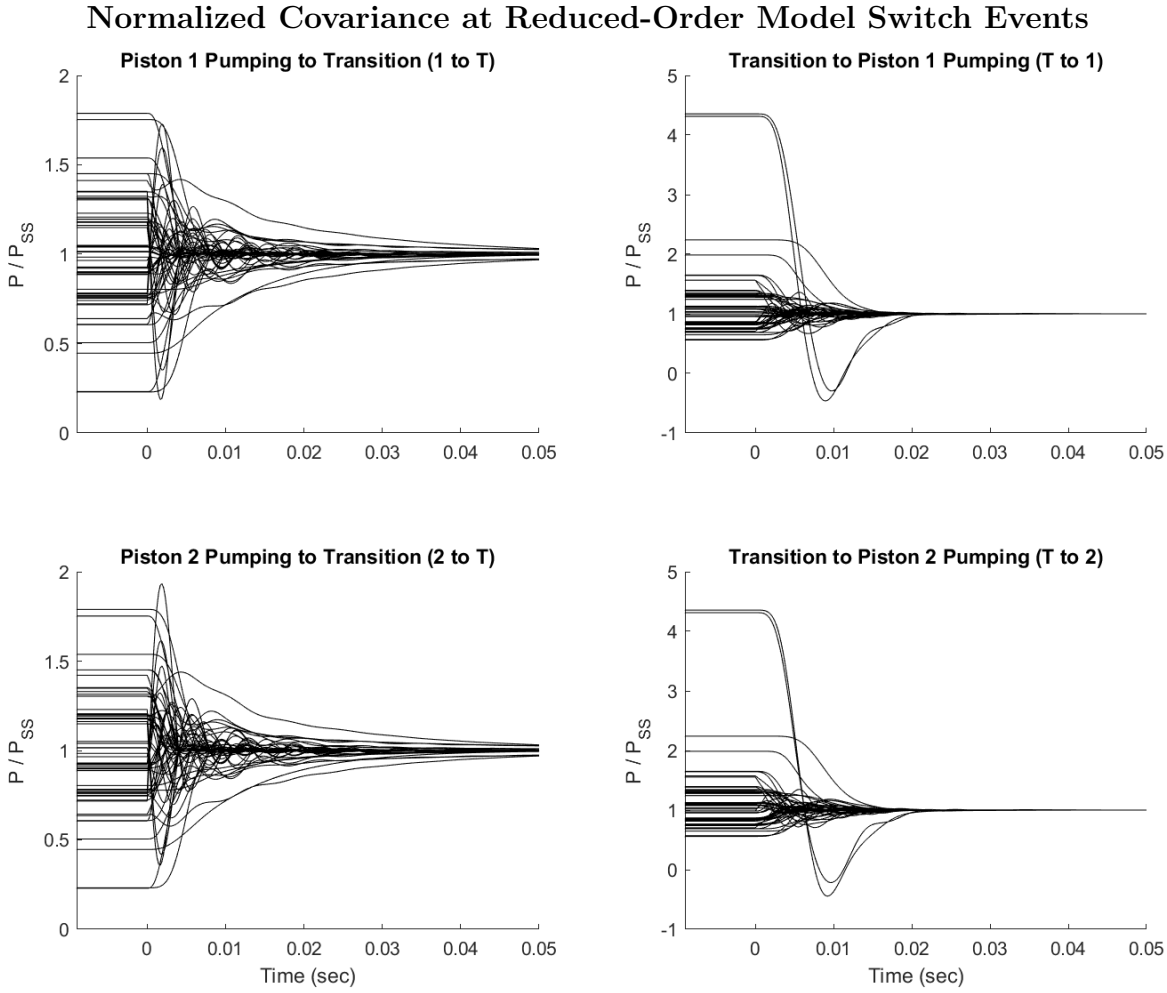

Figure 10.1: Normalized covariance (defined as the covariance divided by the covariance at steady state) at the four switch events: from pumping (either piston 1 pumping or piston 2 pumping) to transition, and from transition to pumping. Covariance is a 10x10 matrix, so there are 55 unique values shown in each plot.

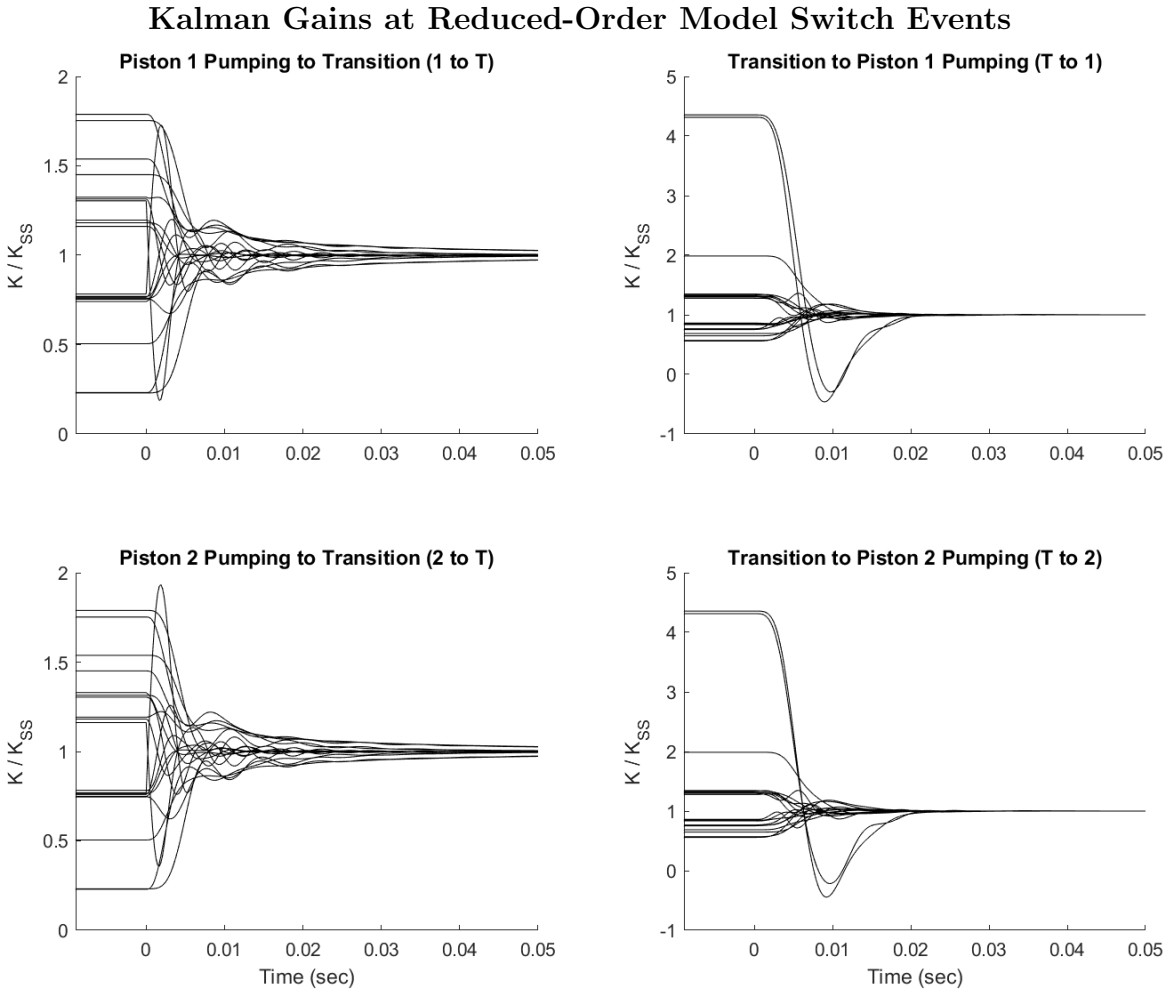

Figure 10.2: Normalized Kalman gains (defined as the Kalman gain divided by the Kalman gain at steady state) at the four switch events: from pumping (either piston 1 pumping or piston 2 pumping) to transition, and from transition to pumping. There are two measurements and 10 states, so there are 20 unique gain values shown in each plot.

10.5 Practical Application - Suboptimal Kalman Filter

The coupled reduced-order model has ten states. In practice, a model this large requires numerous calculations when implemented in real-time on a microcontroller. The covariance propagation, inversion, and Kalman gain calculation especially require numerous multiplications. For this model, when there are ten states and two measurements (the motor positions), the number of multiplications that the controller would have to implement is 654. Only 140 of these (21%) are needed for the state prediction update and state update, which would need to be done for any model-based observer approach. The dynamic Kalman filter with covariance propagation, matrix inversion, and covariance measurement update requires and additional 514 multiplication operations, which increases the computational time required to run the algorithm on the controller by over 350%. The number of multiplications required by a ten-state system with two measurements can be found in Table 10.1. For some controllers or at some operational frequencies, this may be acceptable. But if the control operates at a high frequency, or computational time on the microcontroller is limited by other operational requirements, then this might produce too great a burden on the controller.

	Multiplications for:	
Step	Optimal Kalman Filter	Suboptimal Observer
State predication update	120	120
Covariance propagation	200	-
Kalman gain	214	-
State update	20	20
Covariance update	100	-
Total multiplications	**654**	**140**

Table 10.1: Number of multiplications for the real-time implementation of a tenth order model Kalman filer with 2 outputs (assumes that C is 2x10 and that y is a function of only one state in $\hat{x}$).

To overcome the computational burden of high-order Kalman filters, some computational tricks can be used to reduce the number of operations such square-root methods [90]. Other options include reducing the number of states (for example if the motor and piston could be modeled as directly coupled, then four of the ten states could be eliminated), pre-filtering (when measurements are obtained more frequency than needed and the Kalman filter is run

at a lower frequency), or decoupling states (for example, if the two motor/piston subsystems could be treated separately and the coupling fluid effects could be ignored, then the system could be treated as two separate 5-order systems) [90].

An alternative to implementing the Kalman filter in real time, or making any of the accommodations listed above, is to use a suboptimal filter. Suboptimal filter design makes use of Kalman filtering principles by precomputing the error covariance (the most computationally burdensome step). Then, the Kalman gain can be precomputed as well, and stair stepped solutions or time-dependent lookup tables can be used for the observer gain matrix.

The suboptimal Kalman filter approach is particularly suited for linear time-invariant systems that operate for longer indefinite periods of time and when the steady-state response (after the Kalman filter covariance has settled) is of the most interest. If the system is nonlinear, and methods like the extended Kalman filter or particle filters are used, then the covariance will dynamically change with the states, and this approach would not be well suited. This approach is also not appropriate when the initial transitory dynamics of Kalman filter of of interest. In the linear time-invariant steady-state case, the Kalman filter acts like nothing more than an optimal observer with a constant time-invariant gain K. This is a good approach for a linear observer design when process and measurement noise can be quantified, it allows for a more optimal approach for the observer design than something like arbitrary pole-placement methods, which don't anticipate measurement or process noise in their formulation, and so might be prone to instabilities in practice.

To save computational time, the suboptimal Kalman filter is implemented. Steady state Kalman gain values for each mode (piston 1 pumping, piston 2 pumping, and transition) are used when the reduced-order model is operating in those modes. This is suboptimal (as the name of the approach implies), but it may be an adequate approach when the controller isn't able to perform the computational requirements involved with covariance propogation and measurement updates.

Figure 10.3 shows all 20 Kalman gains propogated from piston 2 pumping mode, into transition mode, and then into piston 1 pumping mode. The solid lines show the ideal Kalman gains and the dashed lines show the suboptimal approach taken in this research.

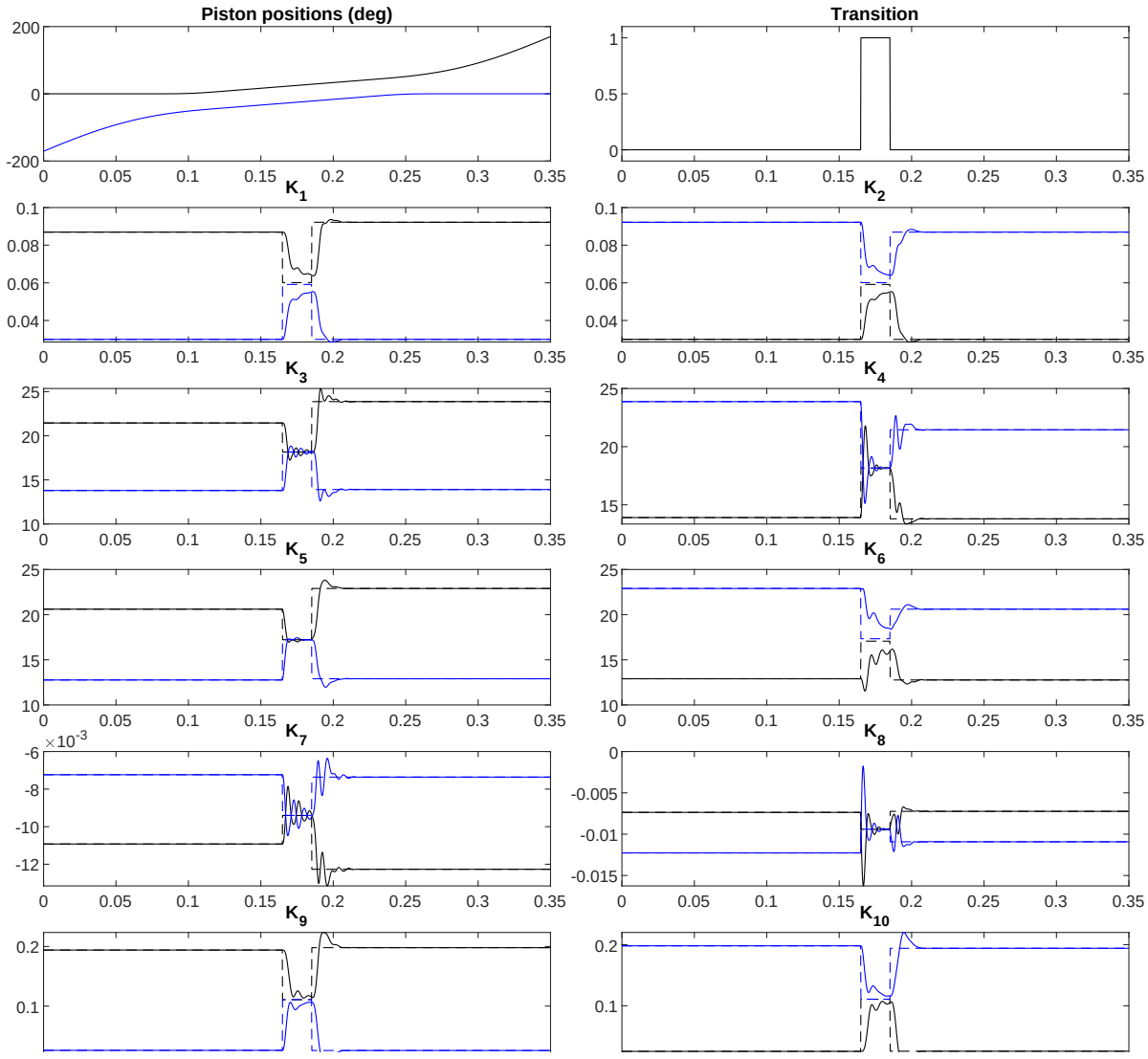

Figure 10.3: Kalman gains vs time for one pump cycle at 5 L/min. Solid lines are the dynamic results, while dashed lines represent the suboptimal steady-state solution used for this research.

The suboptimal Kalman filter is implemented on the microcontroller of a prototype 2PTP at 4800 Hz. The discrete time transition matrix A_k and input matrix B_k derived from the reduced-order models are loaded into the memory of the microcontroller for each mode (piston 1 pumping, piston 2 pumping, and transition). Corresponding suboptimal Kalman (observer) gains are loaded as well. Results will be discussed in Chapter 12.

Chapter 11

Stability and Robustness

This chapter studies the stability and robustness of the compensated system (control with estimation). Matlab robustness tools are used as well as a pole plot cloud to determine the sensitivity to parameter uncertainty.

Stability is always of interest for modeled systems. The open-loop stability of the system itself (as represented by the variable structure model) and reduced-order system model is important, as well as the stability of the compensated system when estimation and control are added. This chapter assesses the stability of:

1. The 30-Structure 2PTP Model
2. The Reduced-Order Linear 2PTP Model
3. Compensator Model (with Estimation and Control)

After baseline stability is established, this chapter also assesses robustness of the compensated system to see how unexpected noise and parameter inaccuracies can affect the stability of the system.

11.1 Switched Variable Structure Model Stability

The system dynamics are best captured by the switched variable structure model developed in Chapter 7. The stability characteristics of this model would be good to assess to to know whether or not the unforced 2PTP system is stable.

In order to determine the stability of the 30-structure, 13-state model, stability of switched systems needs to be understood. Many switched systems depend on time or some other external forcing function to switch between structures. But in this case, the switched system is what is known as state-dependent, which means that the structure depends on the values of one or more of the states. For the 2PTP, those states are the angular piston positions.

Fortunately, stability in state-dependent systems is relatively straightforward. According to Liberzon, if each subsystem (in this case, each structure) is asymptotically stable within the bounds within which it operates, then the system as a whole is asymptotically stable [91]. Therefore, to determine whether or not the 2PTP system model is stable, the stability of each structure needs to be individually assessed.

One method to demonstrate the stability of each of the possible structures (which are nonlinear) is to determine the Lyapunov stability near an equilibrium point x_e. The First Lyapunov method for stability (or reduced method) consists of assessing the eigenvalues of the Jacobian of $f_i(x)$ at the equilibrium x_e.

$$\tilde{A} = \frac{df_i(x)}{x}\bigg|_{x_e} \tag{11.1}$$

This linearizes the differential equations about the equilibrium:

$$\dot{\tilde{x}} = \tilde{A}\tilde{x} + \tilde{B}\tilde{u} \tag{11.2}$$

If the eigenvalues of $\tilde{A}$ are negative, then the equilibrium point is stable.

A more thorough approach is the Second Lyapunov Method (or the Direct Method), which defines a positive definite (PD) scalar function $V(x)$. When the following conditions are true, the system is assume to be asymptotically stable in the sense of Lyapunov at the equilibrium point.

Conditions for Lyapunov stability:

1. $V(x) = 0$ when $x = x_e$
2. $V(x) \neq 0$ when $x \neq x_e$ (the first two conditions describe a PD function)
3. $\dot{V}(x) = \sum_{i=1}^{N} \frac{\partial V}{\partial x_i} f_i(x) \leq 0$ for $x \neq x_e$

$V(x)$ can be any PD function. The equation for the potential and kinetic energy in the system is often good to use. To obtain an energy equation, each energy storage element can be identified.

Magnetic Coupling Potential Energy. The magnetic coupling torque is a sinusoidal function of the angle between the motor and piston. The potential energy can be found by

integrating the torque equation to get:

$$\mathrm{PE_{mc}} = \frac{4T_{\max}\theta_c}{2\pi}\left[1 - cos\left(2\pi\frac{\theta_m - \theta_p}{4\theta_c}\right)\right] \tag{11.3}$$

Motor Kinetic Energy. The kinetic energy of the rotational mass of the motor is

$$\mathrm{KE_m} = \frac{1}{2}J_m\omega_m^2 \tag{11.4}$$

Piston Kinetic Energy. Similarly, the kinetic energy of the rotational mass of the piston is

$$\mathrm{KE_p} = \frac{1}{2}J_p\omega_p^2 \tag{11.5}$$

The equations above suffice to quantify the energy from the rotation of the motor and piston and the magnetic coupling. The other energy in the system is from the fluid flow.

$$\mathrm{PE_Q} = \frac{1}{2}\left(I_A Q_A^2 + I_B Q_B^2 + I_C Q_C^2 + I_D Q_D^2 + I_S Q_S^2\right) \tag{11.6}$$

We can use the energies to describe the P.D. function $V(x)$

$$V(X) = \mathrm{PE_{mc}} + \mathrm{KE_m} + \mathrm{KE_p} + \mathrm{PE_Q} \tag{11.7}$$

$$V(x) = \frac{4T_{\max}\theta_c}{2\pi}\left[1 - cos\left(2\pi\frac{\theta_{m1} - \theta_{p1}}{4\theta_c}\right)\right] + \frac{1}{2}J_m\omega_{m1}^2 + \frac{1}{2}J_p\omega_{p1}^2 \tag{11.8}$$

$$+ \frac{4T_{\max}\theta_c}{2\pi}\left[1 - cos\left(2\pi\frac{\theta_{m2} - \theta_{p2}}{4\theta_c}\right)\right] + \frac{1}{2}J_m\omega_{m2}^2 + \frac{1}{2}J_p\omega_{p2}^2 \tag{11.9}$$

$$+ \frac{1}{2}\left(I_A Q_A^2 + I_B Q_B^2 + I_C Q_C^2 + I_D Q_D^2 + I_S Q_S^2\right) \tag{11.10}$$

It can be shown that for each structure, an equilibrium point x_e is when the flows, piston and motor angular velocities, and magnetic coupling angle are zero.

$$\theta_{m1} = \theta_{p1} \qquad \theta_{m2} = \theta_{p2} \tag{11.11}$$

$$\omega_{m1} = \omega_{m2} = \omega_{p1} = \omega_{p2} = Q_A = Q_B = Q_C = Q_D = Q_S = 0 \tag{11.12}$$

From these, it can easily be shown that $V(x)$ is P.D. because it is zero at the equilibrium point ($V(x_e) = 0$) and greater than zero otherwise, with the restriction that $|\omega_m - \omega_p| > \theta_c$, which restricts the magnetic coupling angle to the angle $\pm\theta_c$ which is the angle when the piston would 'escape' the motor magnets and the system model would break down. This satisfies the first two Lyapunov conditions

1. $V(x_e) = 0$
2. $V(x \neq x_e) > 0 \qquad \text{for } |\omega_m - \omega_p| > \theta_c$

To use $V(x)$ to determine the stability, the derivative $\dot{V}(x) = \sum_{i=1}^{N} \frac{\partial V}{\partial x_i} f_i(x)$ must be shown to be less than zero (the third Lyapunov condition). To find $\dot{V}(x)$, the first step is to solve the partial of $V(x)$ with respond to the state x.

$$\frac{\partial V(x)}{\partial x} = \begin{bmatrix} T_{\max} \sin\left(2\pi \frac{\theta_{m1}-\theta_{p1}}{2\theta_c}\right) \\ T_{\max} \sin\left(2\pi \frac{\theta_{m2}-\theta_{p2}}{2\theta_c}\right) \\ J_m \omega_{m1} \\ J_m \omega_{m2} \\ -T_{\max} \sin\left(2\pi \frac{\theta_{m1}-\theta_{p1}}{2\theta_c}\right) \\ -T_{\max} \sin\left(2\pi \frac{\theta_{m2}-\theta_{p2}}{2\theta_c}\right) \\ J_m \omega_{p1} \\ J_m \omega_{p2} \\ I_A Q_A \\ I_B Q_B \\ I_C Q_C \\ I_D Q_D \\ I_S Q_S \end{bmatrix}^T \tag{11.13}$$

This partial derivative is a row vector which is multiplied by the state equations $f(x)$, which can be represented as a column vector, as shown below.

$$f(x) = \dot{x} = \begin{bmatrix} \dot{\theta}_{m1} \\ \dot{\theta}_{m2} \\ \dot{\omega}_{m1} \\ \dot{\omega}_{m2} \\ \dot{\theta}_{p1} \\ \dot{\theta}_{p2} \\ \dot{\omega}_{p1} \\ \dot{\omega}_{p2} \\ \dot{Q}_A \\ \dot{Q}_B \\ \dot{Q}_C \\ \dot{Q}_D \\ \dot{Q}_S \end{bmatrix} = \begin{bmatrix} \omega_{m1} \\ \omega_{m2} \\ \frac{1}{J_m}\left[-\frac{k_e^2}{R}\omega_{m1} - b_m \omega_{m1} - T_{\max} \sin\left(2\pi \frac{\theta_{m1}-\theta_{p1}}{2\theta_c}\right)\right] \\ \frac{1}{J_m}\left[-\frac{k_e^2}{R}\omega_{m2} - b_m \omega_{m2} - T_{\max} \sin\left(2\pi \frac{\theta_{m1}-\theta_{p1}}{2\theta_c}\right)\right] \\ \omega_{p1} \\ \omega_{p2} \\ \frac{1}{J_p}\left[T_{\max} \sin\left(2\pi \frac{\theta_{m1}-\theta_{p1}}{2\theta_c}\right) - b_p \omega_{p1} - f\left(\omega_{p1}, Q_A, Q_B\right)\right] \\ \frac{1}{J_p}\left[T_{\max} \sin\left(2\pi \frac{\theta_{m2}-\theta_{p2}}{2\theta_c}\right) - b_p \omega_{p2} - f\left(\omega_{p2}, Q_C, Q_D\right)\right] \\ \dot{Q}_A \\ \dot{Q}_B \\ \dot{Q}_C \\ \dot{Q}_D \\ \dot{Q}_S \end{bmatrix} \tag{11.14}$$

Multiplying the 1x13 row vector by the 13x1 column vector results in a scalar term

$$\begin{aligned}
\dot{V}(x) = \frac{\partial V(x)}{f(x)}\dot{x} =& T_{\max}\sin\left(2\pi\frac{\theta_{m1}-\theta_{p1}}{2\theta_c}\right)\omega_{m1} \\
&+ T_{\max}\sin\left(2\pi\frac{\theta_{m2}-\theta_{p2}}{2\theta_c}\right)\omega_{m2} \\
&+ J_m\omega_{m1}\frac{1}{J_m}\left[-\frac{k_e^2}{R}\omega_{m1} - b_m\omega_{m1} - T_{\max}\sin\left(2\pi\frac{\theta_{m1}-\theta_{p1}}{2\theta_c}\right)\right] \\
&+ J_m\omega_{m2}\frac{1}{J_m}\left[-\frac{k_e^2}{R}\omega_{m2} - b_m\omega_{m2} - T_{\max}\sin\left(2\pi\frac{\theta_{m1}-\theta_{p1}}{2\theta_c}\right)\right] \\
&- T_{\max}\sin\left(2\pi\frac{\theta_{m1}-\theta_{p1}}{2\theta_c}\right)\omega_{p1} \\
&- T_{\max}\sin\left(2\pi\frac{\theta_{m2}-\theta_{p2}}{2\theta_c}\right)\omega_{p2} \\
&+ J_m\omega_{p1}\frac{1}{J_p}\left[T_{\max}\sin\left(2\pi\frac{\theta_{m1}-\theta_{p1}}{2\theta_c}\right) - b_p\omega_{p1} - f_{p1}\left(\omega_{p1}, Q_A, Q_B\right)\right] \\
&+ J_m\omega_{p2}\frac{1}{J_p}\left[T_{\max}\sin\left(2\pi\frac{\theta_{m2}-\theta_{p2}}{2\theta_c}\right) - b_p\omega_{p2} - f_{p2}\left(\omega_{p2}, Q_C, Q_D\right)\right] \\
&+ I_A Q_A\dot{Q}_A \\
&+ I_B Q_B\dot{Q}_B \\
&+ I_C Q_C\dot{Q}_C \\
&+ I_D Q_D\dot{Q}_D \\
&+ I_S Q_S\dot{Q}_S
\end{aligned}$$

This can be simplified

$$\begin{aligned}
\dot{V}(x) =& -\frac{k_e^2}{R}\omega_{m1}^2 - b_m\omega_{m1}^2 - \frac{k_e^2}{R}\omega_{m2}^2 - b_m\omega_{m2}^2 - b_p\omega_{p1}^2 - b_p\omega_{p2}^2 \\
&- f_{\mathrm{T1}}\left(\omega_{p1}, Q_A, Q_B\right)\omega_{p1} - f_{\mathrm{T2}}\left(\omega_{p2}, Q_C, Q_D\right)\omega_{p2} \\
&+ I_A Q_A\dot{Q}_A + I_B Q_B\dot{Q}_B + I_C Q_C\dot{Q}_C + I_D Q_D\dot{Q}_D + I_S Q_S\dot{Q}_S
\end{aligned}$$

Clearly the top row is always negative when the damping coefficients are positive (k_e, R, b_m, and b_p). This is consistent with the the linearized model and the motor/piston are a pair of coupled spring-mass-dampers, so this result is expected.

The fluid flow terms $\dot{Q}$ and the torque on each of the pistons as a function of the pressures caused by the flows (f_{p1} and f_{p2}) adds quite a bit of complexity, not in the sense of math-

ematical rigor or complexity, but just in terms of tedious calculations. Without recreating or typing pages and pages of equations, it can be shown that for all 30 possible structures, with any positive viscous linear resistance R_i and positive nonlinear port resistance R_{ii}, each term of $\dot{V}(x)$ will be negative, which completes the third requirement for Lyapunov stability.

Switched Variable Structure Model Stability Summary

Using the potential and kinetic energy of the system to define a PD function $V(x)$, it can be shown that $\dot{V}(x)$ is negative for all positive parameter values of (k_e, R, b_m, b_p, R_i, and R_{ii}) for each of the 30 possible structures. Further, because the structure is state-dependent, the system as a whole is asymptotically stable (as demonstrated by Liberzon [91]).

This result is not surprising. The pistons and motors are coupled spring-mass-damper systems, which are themselves stable systems, and the fluid flow that couples the pistons is damped by either linear or nonlinear resistance terms, only the magnitude of which changes as the piston position and structure change. Therefore, one can expected these damped systems to be stable when coupled.

11.2 Open-Loop Stability of the Reduced-Order Model

There are two reduced-order models. One for pumping and another for transition (when one or both of the ports are completely occluded). These reduced-order models are linear ($\dot{x} = Ax + Bu$), so it's straightforward to find the eigenvalues of the unforced system using the state matrix A.

11.2.1 Open-Loop Stability of the Reduced-Order Model of Pumping

For the reduced-order model of pumping, the eigenvalues (λ) are found using the Matlab function `eig()`:

$$\lambda_{1,2} = -113.7 \pm 776.9i$$
$$\lambda_{3,4} = -87.1 \pm 927.2i$$
$$\lambda_5 = -107.0$$
$$\lambda_6 = -12.5$$
$$\lambda_{7,8} = 0$$

This system is critically stable. There are two poles at zero that are are due the inclusion of the absolute angular positions in the state formulation. Of the 8 states, 2 are information (the absolute position of each motor/piston coupling) and 6 are energetic (the momenta of the pistons and motors as well as the magnetic coupling angles).

11.2.2 Open-Loop Stability of the Reduced-Order Model of Transition

Similary, eigenvalues for the reduced-order model of transition can be found:

$$\lambda_{1,2} = -117.8 \pm 763.3i$$
$$\lambda_{3,4} = -87.3 \pm 924.5i$$
$$\lambda_5 = -105.8.0$$
$$\lambda_{6,7,8} = 0$$

This system too is critically stable. As before, there are two poles at zero that are are due the inclusion of the absolute angular positions in the state formulation. There is also a third because one of the states is redundant (the piston velocities are identical in the model when leakage is neglected). Of the 8 states, 2 are information (the absolute position of each motor/piston coupling) and 1 is redundant, so there are five energetic states (the velocity or momenta of the pistons and motors as well as the magnetic coupling displacement).

11.2.3 Discussion on the Open-Loop Stability of the Reduced-Order Model

It is interesting to note how similar the poles of the pumping and transition reduced order models are. Many of the dynamics remain the same, including the magnetic coupling, motor damping, piston friction, and mass moments of inertia of the motor, piston, and torus fluid. Any differences between the two are due to the inclusion or exclusion of the cannula flow, which couples in to the piston velocities in the pumping model, but uncouples in the transition model. It is also interesting to note that the pole at -12.5 in the pumping model disappears from the transition model, indicating that this must be the pole that represents the pump flow rate in the cannulas (also the difference in velocities between the pistons), and that it is the slowest pole in the pumping system.

The other poles have large imaginary components. This would be caused by the magnetic coupling between the piston and motors, and show that the system is underdamped ($\zeta_{1,2} = .15$ and $\zeta_{3,4} = .09$).

11.3 Closed-Loop Stability of the Reduced-Order Model

The control and observer alter the dynamics. These were formulated using the reduced-order linear model of the pump during pumping and transition. These models are also state-dependent (based on the piston position), so as above, the stability of the switched linear system can be analyzed by looking only at the stability of the individual subsystems.

11.3.1 Separation Principle

The compensated linear system is

$$\dot{x} = Ax - BG\hat{x} \tag{11.15}$$

where $\hat{x}$ are the estimated states, found by the observer

$$\dot{\hat{x}} = \hat{A}\hat{x} - \hat{B}G\hat{x} + K\left(Cx - C\hat{x}\right) \tag{11.16}$$

In this case, $\hat{A}$ and $\hat{B}$ represent the predicted system dynamics, where A and B represent the actual system dynamics.

In state space form, the compensator can be expressed as

$$\begin{bmatrix}\dot{x}\\ \dot{\hat{x}}\end{bmatrix} = \begin{bmatrix}A & -BG\\ KC & \hat{A}-\hat{B}G-KC\end{bmatrix}\begin{bmatrix}x\\ \hat{x}\end{bmatrix} \tag{11.17}$$

When the predicted system dynamics and actual system dynamics are identical ($A = \hat{A}$ and $B = \hat{B}$), and when the observer error is expressed $e = x - \hat{x}$, then the compensator can be expressed as

$$\begin{bmatrix}\dot{x}\\ \dot{e}\end{bmatrix} = \begin{bmatrix}A-BG & BG\\ 0 & A-KC\end{bmatrix}\begin{bmatrix}x\\ e\end{bmatrix} \tag{11.18}$$

The matrix on the right hand side is triangular, so the eigenvalues of the control are those of $A-BG$ and the eigenvalues of the observer error are those of $A-KC$. This is the separation principle [92], which allows for the control and estimation to be derived independently, even for stochastic systems [90]. In this way, the eigenvalues of the control and estimation decouple, and the linear quadratic control gain G can be determined as if all of the states were readily available, and then the Kalman filter observer gain K can be found that can be used to estimate the states.

11.3.2 Poles Plots

One useful way of assessing the stability of the system is to visualize the poles. There are two models: pumping a transition, each of which have their own state dynamics (A and B) and gains (control G and estimation K).

	Pumping	Transition
State dynamics	A_p	A_t
Input dynamics	B_p	B_t
Control gains	G_p	G_t
Estimation gains	K_p	K_t

11.3.2.1 Pumping and Transition Pole Plots

Pumping Poles

For pumping, the open-loop poles are found using

$$\dot{x} = A_p x \tag{11.19}$$

The control poles are found using

$$\dot{x} = (A_p - B_p G_p)\, x \tag{11.20}$$

The estimation poles are found using

$$\dot{e} = (A_p - K_p C)\, e \tag{11.21}$$

And the compensator poles are found using

$$\begin{bmatrix} \dot{x} \\ \dot{\hat{x}} \end{bmatrix} = \begin{bmatrix} A_p & -B_p G_p \\ K_p C & A_p - B_p G_p - K_p C \end{bmatrix} \begin{bmatrix} x \\ \hat{x} \end{bmatrix} \tag{11.22}$$

Transition Poles

For transition, the open-loop poles are found using

$$\dot{x} = A_t x \tag{11.23}$$

The control poles are found using

$$\dot{x} = (A_t - B_t G_t)\, x \tag{11.24}$$

The estimation poles are found using

$$\dot{e} = (A_t - K_t C)\, e \tag{11.25}$$

And the compensator poles are found using

$$\begin{bmatrix} \dot{x} \\ \dot{\hat{x}} \end{bmatrix} = \begin{bmatrix} A_t & -B_t G_t \\ K_t C & A_t - B_t G_t - K_t C \end{bmatrix} \begin{bmatrix} x \\ \hat{x} \end{bmatrix} \tag{11.26}$$

The poles for pumping and transition are shown in Figure 11.1. Open-loop poles are shown as circles and the closed-loop compensated system poles are shown as X's. The compensator poles are a combination of the control poles (shown as C's) and Kalman filter estimation poles (shown as K's). In this case, the control and estimation poles are equal to the compensator poles because in this analysis, the actual system dynamics (A and B) are the same as the estimated system dynamics. All of the poles are stable (in the left plane).

One interesting thing to note is that the estimation poles are slower (are more to the right) than the control poles. Typically, it's helpful to have the observer poles respond much more quickly than the control, but in this case, where the observer poles are determined by the stochastic noise of the processes and sensors, they cannot be placed at arbitrary locations. Because the observer or estimation poles are slower than the control poles, they will limit the dynamic response of the system.

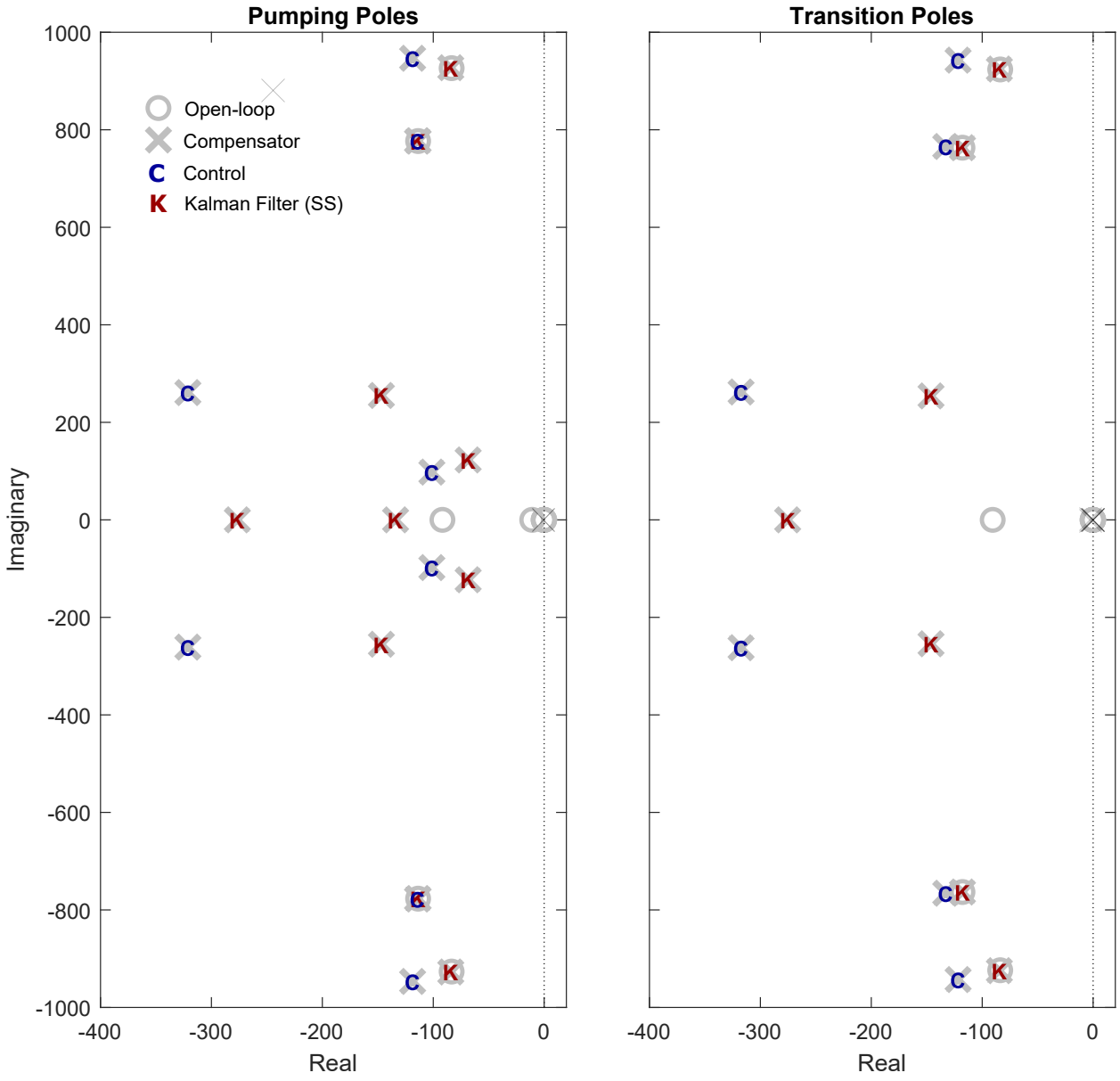

Figure 11.1: Pole locations for the open-loop system (O) and the compensated system (X), which are driven by the control poles (C) and steady state Kalman filter poles (K).

11.3.2.2 Switched Pole Plots Stability

Ideally, the pumping gains are used when the system dynamics are consistent with pumping, and the transition gains are used when the system dynamics are consistent with transition. But it could be the case that the transition gains (control and estimation) are using during pumping when the ports aren't occluded, or that the pumping gains are used during transition. This could happen if there is significant error between the actual piston position and estimated piston position such that occlusion (transition) starts or stops sooner or later than expected. To assess the stability of using the wrong gains at the wrong time, the two following compensated systems can be studied:

Pumping dynamics with transition gains

$$\begin{bmatrix} \dot{x} \\ \dot{\hat{x}} \end{bmatrix} = \begin{bmatrix} A_p & -B_p G_t \\ K_t C & A_t - B_t G_t - K_t C \end{bmatrix} \begin{bmatrix} x \\ \hat{x} \end{bmatrix} \tag{11.27}$$

Transition dynamics with pumping gains

$$\begin{bmatrix} \dot{x} \\ \dot{\hat{x}} \end{bmatrix} = \begin{bmatrix} A_t & -B_t G_p \\ K_p C & A_p - B_p G_p - K_p C \end{bmatrix} \begin{bmatrix} x \\ \hat{x} \end{bmatrix} \tag{11.28}$$

The poles of these mis-matched compensated systems are shown in Figure 11.2 along with the poles of the correctly compensated systems. Stability issues arise if the transition gains are used during puming (bottom left plot). Two of the poles are slightly positive. This is likely due to the fact that the pistons can move independently in when pumping, but the transition gains assumes that they'll move together. The other condition (transition with pumping gains), remains stable. This suggests that using the transition gains during pumping should be avoided if at all possible. This could be done by always using the pumping gains (which could lead to diminished performance during transition) or by underestimating the region which transition occurs (to make sure the pump is actually experiencing transition dynamics in that operating region).

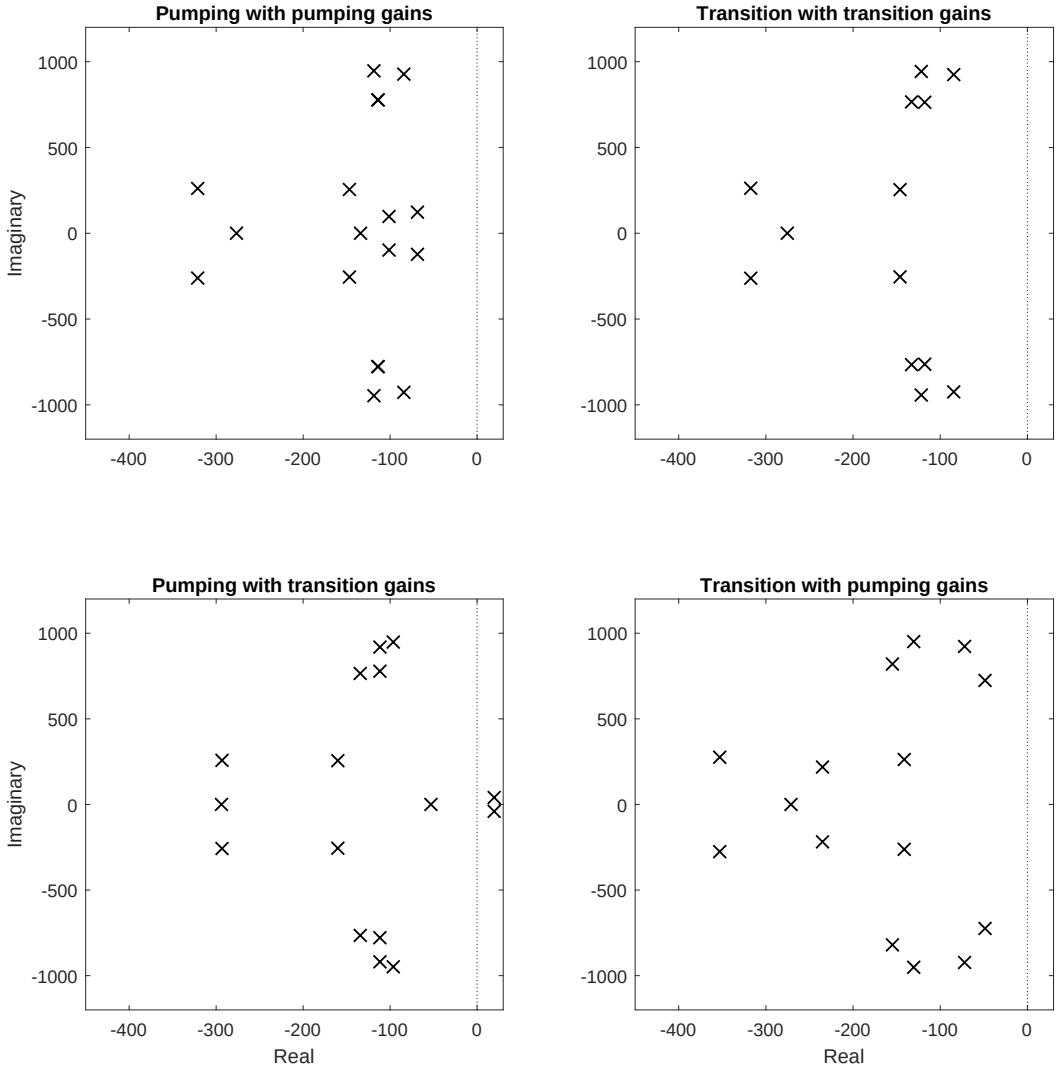

Figure 11.2: Compensator pole locations for the pumping/transition switched system. As was already shown, pumping with pumping gains and transition with transition gains are stable reduced-order systems. But when transition gains are used during pumping (bottom left plot), the system can become unstable. If pumping gains are used during transition (bottom right plot), the system remains stable.

11.3.3 Robustness

The separation principle above assumed that the actual and predicted system dynamics are identical ($A = \hat{A}$ and $B = \hat{B}$). This is almost never the case. The actual system dynamics, represented here by A and B, may vary due to parameter uncertainty, neglected or higher-order dynamics, and unanticipated noise. The robustness of the compensator can be determined by assessing the stability of the compensated system when taking these uncertainties into account.

For robust analysis, the compensated system will be analyzed.

$$\begin{bmatrix} \dot{x} \\ \dot{\hat{x}} \end{bmatrix} = \begin{bmatrix} A & -BG \\ KC & \hat{A} - \hat{B}G - KC \end{bmatrix} \begin{bmatrix} x \\ \hat{x} \end{bmatrix} \tag{11.29}$$

Several assumptions were made in the design of the control and observer, such as the parameter values (motor damping, piston friction, cannula length, etc), a linear system assumption (ignoring nonlinear flow resistance, friction, etc), and assumptions about the process and measurement noise magnitude. These may be relatively good assumptions, and the system could be relatively immune to deviations in the real system , or it could be the case that small parameter uncertainty or unexpected noise could quickly lead to compensator instability. One tool for analyzing robustness is the Mu Stability toolbox in Matlab.

11.3.3.1 Mu Analysis

Control and estimation are designed with assumed parameter values, but parameter uncertainty could make the system unstable. Matlab has built in functionality for assessing the robustness of controlled systems with parameter uncertainty. First, the uncertain parameters and uncertainty values are specified

Parameter		**Uncertainty (±)**
Motor mass moment of inertia	J_m	2%
Motor damping coefficient	b_m	5%
Piston mass moment of inertia	J_p	2%
Piston damping coefficient	b_p	5%
Motor gyrator coefficient	k_e	5%
Motor electrical resistance	R_e	5%
Magnetic coupling constant	k_c	5%
Cannula Length	L_C	10%

Two different methods can be used. The first is Matlab's built in functionality to assess robust stability `robstab()`. To assess robust stability, variable uncertanties are defined, the uncertain state matrix A_u and input matrix B_u are created from them, and then the compensated system constructed. Again, four scenarios are tested. Pumping model with pumping gains (P:P), transition model with transition gains (T:T), pumping model with transition gains (P:T) that we already know to be unstable, and transition model with pumping gains (T:P).

P:P - pumping model with pumping gains

$$\begin{bmatrix} \dot{x} \\ \dot{\hat{x}} \end{bmatrix} = \begin{bmatrix} A_{up} & -B_{up}G_p \\ K_pC & A_p - B_pG_p - K_pC \end{bmatrix} \begin{bmatrix} x \\ \hat{x} \end{bmatrix} \tag{11.30}$$

T:T - transition model with transition gains

$$\begin{bmatrix} \dot{x} \\ \dot{\hat{x}} \end{bmatrix} = \begin{bmatrix} A_{ut} & -B_{ut}G_t \\ K_tC & A_t - B_tG_t - K_tC \end{bmatrix} \begin{bmatrix} x \\ \hat{x} \end{bmatrix} \tag{11.31}$$

P:T - pumping model with transition gains

$$\begin{bmatrix} \dot{x} \\ \dot{\hat{x}} \end{bmatrix} = \begin{bmatrix} A_{up} & -B_{up}G_t \\ K_tC & A_t - B_tG_t - K_tC \end{bmatrix} \begin{bmatrix} x \\ \hat{x} \end{bmatrix} \tag{11.32}$$

T:P - transition model with pumping gains

$$\begin{bmatrix} \dot{x} \\ \dot{\hat{x}} \end{bmatrix} = \begin{bmatrix} A_{ut} & -B_{ut}G_p \\ K_pC & A_p - B_pG_p - K_pC \end{bmatrix} \begin{bmatrix} x \\ \hat{x} \end{bmatrix} \tag{11.33}$$

The compensated closed-loop state matrix is used to create a system using Matlab's `ss()` function, which is used in Matlab's robust stability function `robstab()`. The output of this analysis is a lower gain bound, upper gain bound, and critical frequency at which point the system becomes unstable. Result for each model are below. Again, the pumping model with transition (P:T) is already unstable, so no robust stability analysis was performed.

	Model:Gains			
	P:P	T:T	P:T	T:P
LowerBound	1.2188	1.3866	-	1.0695
UpperBound	1.2342	1.4061	-	1.0927
CriticalFrequency	715.30	890.95	-	677.66

These results mean, for example, that when pumping and using pumping gains, the system can withstand 21.9% to 38.7% *more* uncertainty than tested.

Next, to assess which variables affect stability the most, the sensitivity option in Matlab can be turned on, which generates the following output:

	Model:Gains			
	P:P	T:T	P:T	T:P
Parameter	Pumping	Transition	Transition	Pumping
J_m	0	2	-	0
J_p	18	30	-	183
L_c	47	49	-	48
R_e	20	29	-	41
b_m	0	1	-	0
b_p	0	2	-	0
k_c	0	3	-	0
k_e	5	0	-	4

These values indicate how much a changing the values of each parameter to their maximum uncertainty values affected the normalized stability margin. So for example, when pumping with pumping gains, a change in the length of the cannulas by 10% (the specified uncertainty range), will affect a change of 47% in the stability margin.

Clearly, uncertainty in the mass moment of inertia of the piston J_p, the length of the cannulas L_c, and the electrical resistance of the motor R_e cause the most change in the stability margin. This indicates which variables are most important to estimate accurately, and which are not as critical.

Uncertainty Pole Plot

Another way to assess the stability is too look at the pole plot with the uncertain parameters. To do this, a state matrix $A_{u,i}$ and input matrix $B_{u,i}$ are created at each possible combination of the maximum uncertainty of each parameter. This generates 2^8 possible matrices (8 is the number of parameters of uncertainty). Poles are obtained for each possible combination from 1 to 2^8. Each pole combination is plotted (along with the nominal pole locations). The results are shown in Figure 11.3.

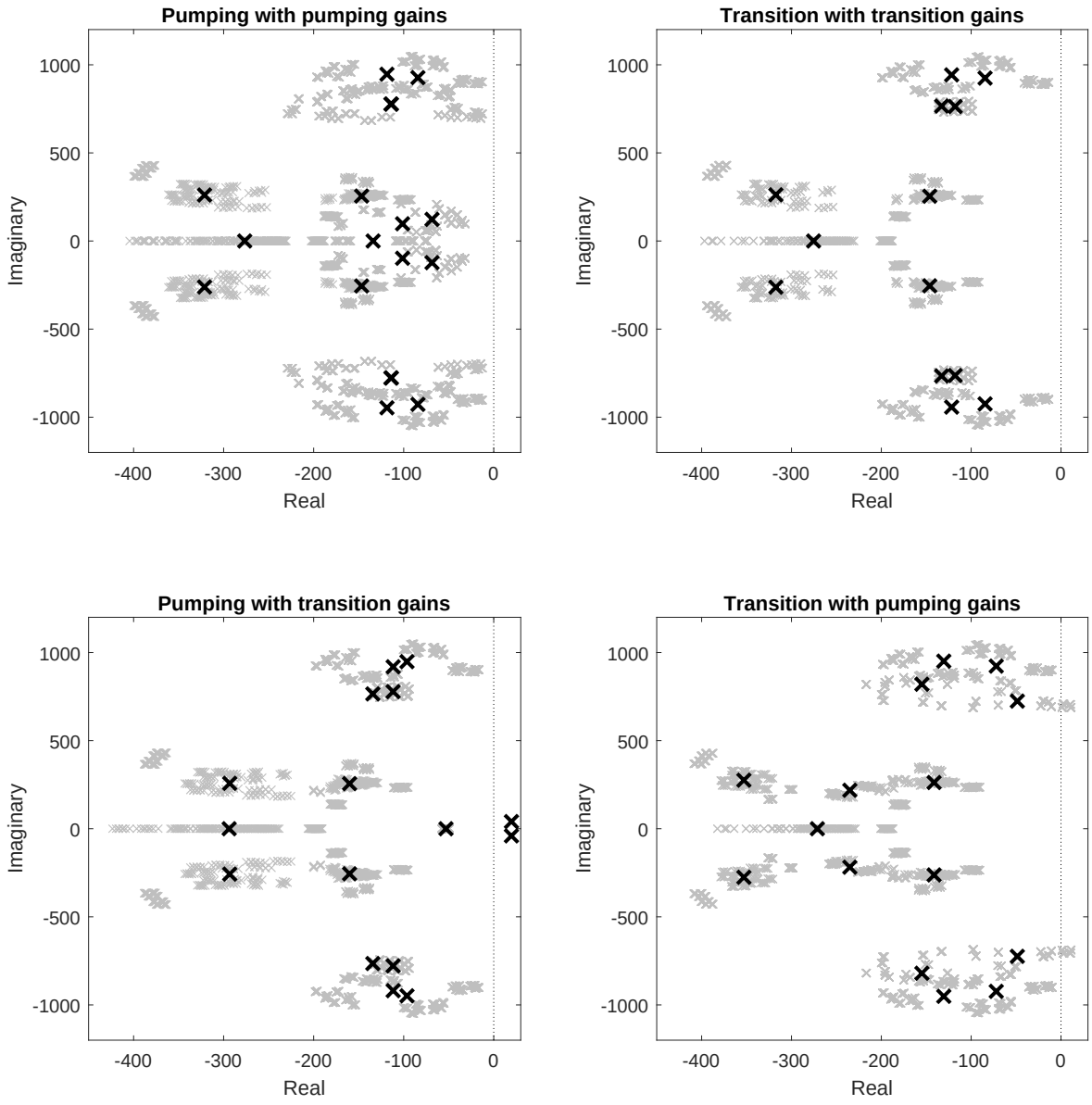

Figure 11.3: Compensator poles with parameter uncertainty for each of the combinations of models and gains.

11.4 Stability Summary and Discussion

The switched structure variable model was shown to be stable using Lyapunov's Direct Method. The reduced-order linear models were also shown to be linear for transition and pumping. Neither of these results is surprising. While there is some complicated coupling and leakage dynamics, the system is basically two double inertial spring-mass-damper systems with the addition of a resistive hydraulic network. Both of which are generally stable on their own.

Of more interest is the stability and robustness of the compensated system. It was shown that the dynamic response would be limited mostly by the estimator (steady state Kalman filter gains), that the compensated system during pumping and transition is stable, but that if transition gains are used during pumping, the system can become unstable.

Stability analysis (using Matlab's built in `robstab()` function and a pole cloud plot), showed that the system was robust to expected parameter uncertainties and that the variables that would effect the robustness the most were the mass moment of inertia of the piston J_p, the length of the cannulas L_c, and the electrical resistance of the motor R_e, so it is important to estimate these variables correctly.

Chapter 12

Experiments

This chapter studies results from preliminary experiments in passive and active mock circulatory loops to verify similarity with the model, test the improved control, and confirm pressure and flow estimation.

Experiments were conducted in two different mock circulatory loops with a prototype 2PTP pump. One mock circulatory loop was 'passive' and the second was 'active'. Schematic representations of these mock loop can be seen in Figure 12.2.

The passive mock circulatory loop is a simple fluid RC circuit. The capacitor is a large sealed air chamber and is made sufficiently large so that pressure is nearly constant when a pulsatile input flow is supplied. This simple setup allows quick and easy experiments to be run at constant flow rates and constant pressure differentials.

The active mock loop is a hybrid mock circulatory loop that can generate physiological differential pressure across the pump. There are two pressure chambers, one to represent the left ventricle and one the systemic arteries. Voice coil actuators (Moticont GVCM-095-089-01S06) with sealed piston interfaces (2.25" diameter, HD Slippers Enerseal LP022-57, 0-095-A-10) transform actuator force to pressures. The inflow of the 2PTP is connected to a flow port on the left ventricular pressure chamber and the outflow is connected to a flow port on the arterial pressure chamber. A backflow gear pump (Marco UP9-P 3.2 gpm, PTFE gears, VITON O-Ring) is connected between the pressure chambers that is used to maintain adequate volumes in each chamber. Measurements of the voice coil piston location, chamber pressures, and 2PTP flow rate are obtained by a MyRIO which is used to simulate and controls physiological left ventricular and arterial pressure for any cardiovascular operating condition (change in heart rate, ventricular contraction force, systemic vascular resistance, etc). Details and verification of this system are left to other graduate students working on this system and are outside the scope of the research questions of interest in this dissertation.

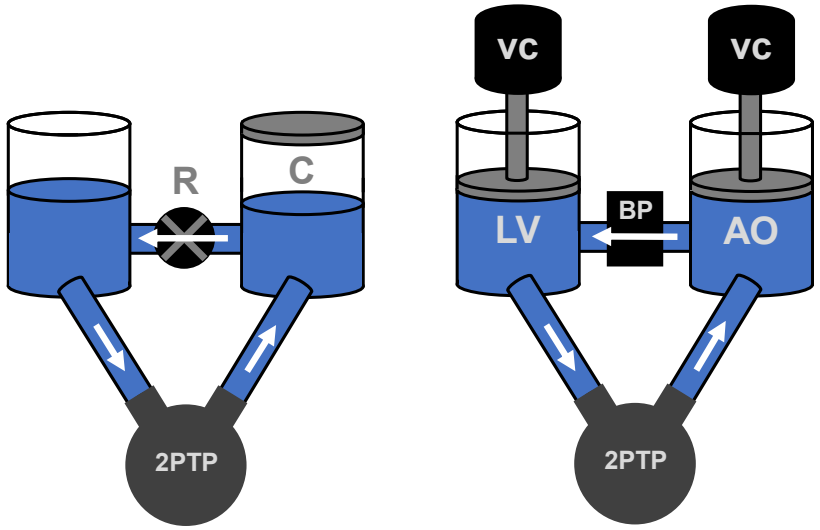

Figure 12.1: Schematics of the mock loops used for experimental testing. The passive mock loop consists of a simple RC circuit and is used for steady state experiments against a constant pressure head that is manually adjusted with a resistor. The active mock loop uses a computational simulation of the cardiovascular system define dynamic pressures on the 2PTP inlet (LV left ventricular pressure) and outlet (AO aortic pressure).

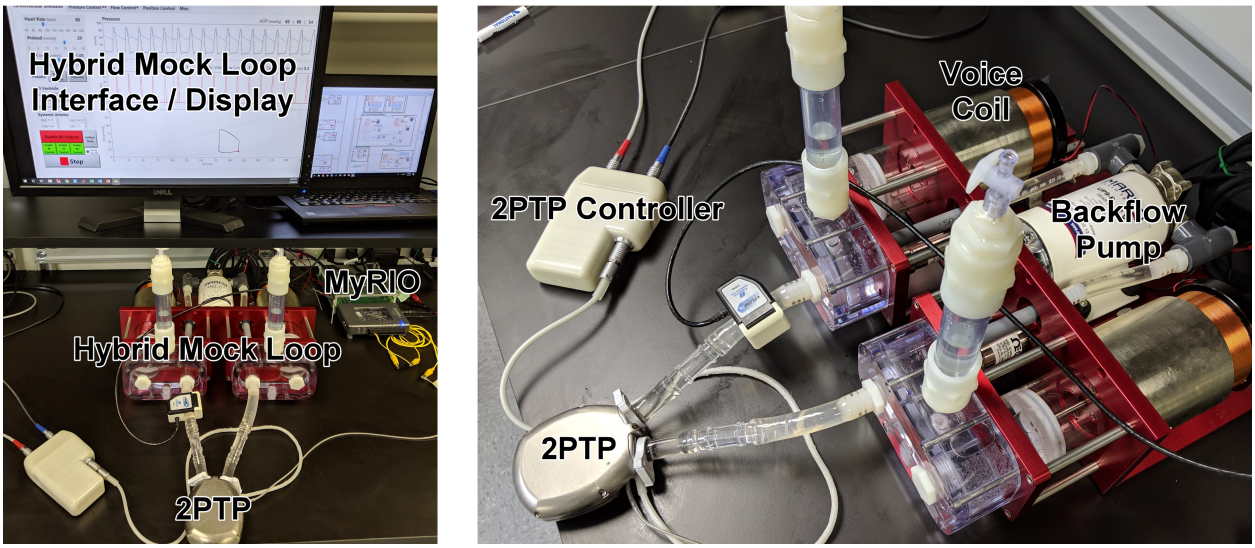

Figure 12.2: Hybrid mock loop experimental setup. The 2PTP is connected to a hybrid mock loop that is used to load the pump with cardiovascular pressure. The hybrid mock loop uses voice coils to control pressure and a backflow pump to maintain volume in each pressure chamber. The system is controlled with a MyRIO, which can simulate variation in HR, preload, afterload, and ventricular contraction.

12.1 Step Response

The interaction between the pistons due to the fluid coupling is an important aspect of the model and control. As a first experiment to observe these coupled dynamics, a simple step experiment was performed to verify baseline PID control and system dynamics. A prototype 2PTP was setup in the passive mock loop, with both chambers set to atmospheric pressure (zero pressure differential across the pump). The cannulas were 1/2" tygon tubing with an inflow length of 6" and outflow length of 12".

One piston (the hold piston) was placed between the inflow and outflow ports, and the other piston (the drive piston) was placed 180° opposite. Proportional control was used and the desired position of the drive piston was given a 10° step. Motor positions were measured, and the error was calculated. Results were compared with a simulation of the same experiment. Figure 12.3 shows the error plots for each both motor positions for the simulation and experiment.

$$e = \theta_m^{\text{desired}} - \theta_m^{\text{actual}} \tag{12.1}$$

There is very good agreement between the simulation and the experimental results. There is similar error magnitude, frequency response, and damping between the simulation and experiment, which provides evidence that the model recreates the dynamics of the system well and also provides evidence that the values were chosen well for the various model parameters (damping coefficients, mass moments of inertia, etc.).

This experiment also confirms that there is significant coupling between the pistons. In this experiment, only one piston is given the 10° step. The other piston (in the hold position) is only controlled to stay in place. The motion from the drive piston creates fluid flow and pressure that creates a force on the other piston due to the fluid coupling. This confirms that the coupling effect is strong (as was expected and shown in the development of the reduced-order model) and that accounting for and anticipating this coupling is important for the control of the pistons a coupled system.

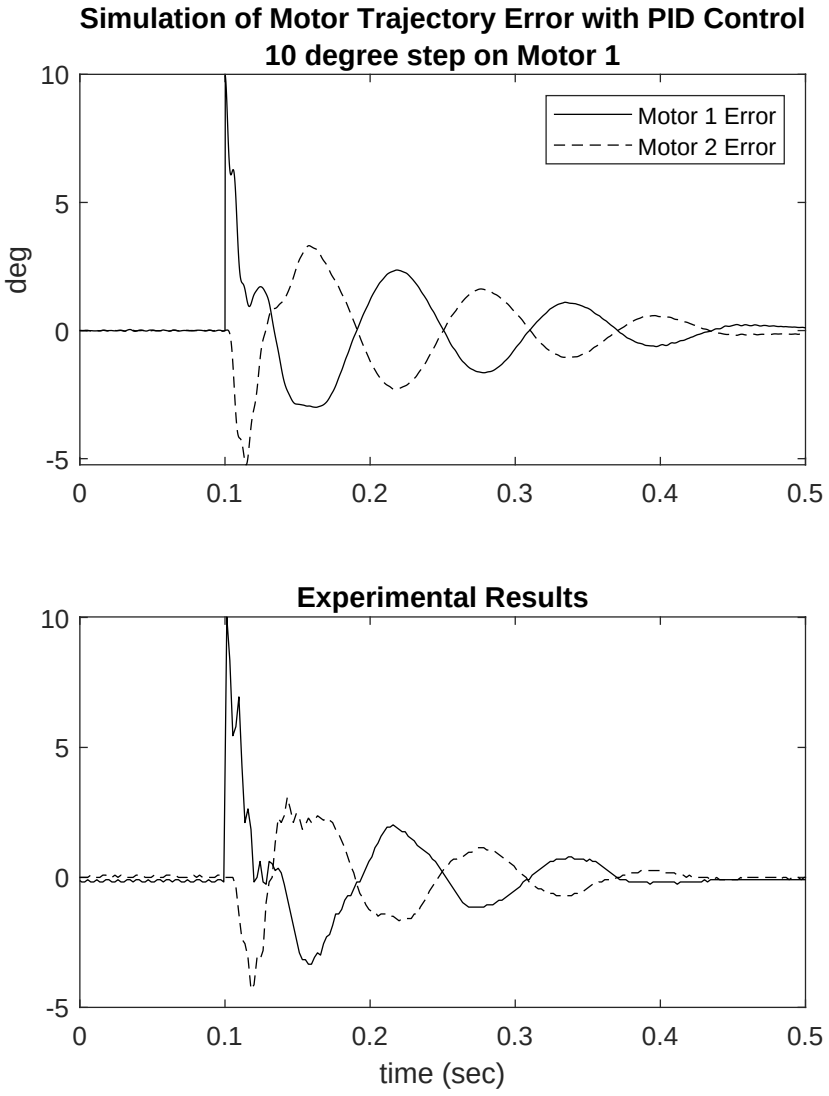

Figure 12.3: Simulation vs experimental results for a 10° reference trajectory step input on only one piston with proportional control. This experiment verified the coupling effects between the pistons as well as the damping effects of the piston and coupled inertia from the cannulas.

12.2 PID vs LQR Control

The step change discussed in the previous section did not require any switching of the model, and was a very basic test for comparing the model to experimental results. Therefore, the next experiment was the run the pump at a known flow rate and compare the experimental and simulation results.

With the 2PTP still setup in the passive mock loop (with 1/2" cannulas, 6" inflow, and 12" outflow), the pump flow rate was set to 5 L/min asynchrnous mode and the resistor was tuned until the differential pressure was 100 mmHg mean (103 max / 97 min). The suboptimal observer (based on steady state Kalman filter gains) was implemented on the controller to estimate unmeasureable pump states (motor velocity, piston position and velocity, and disturbance torque). The same conditions were run in the simulation against at constant differential pump pressure of 100 mmHg.

The simulation and experimental results are shown in Figure 12.4. The simulation results are solid lines and the experimental results are dashed. Motor/Piston 1 is black and Motor/Piston 2 is blue. Two complete pumping strokes are shown in the plots. The angular position plot (top-left) shows the motor positions throughout the two pump strokes. The motor trajectory error (middle-left) shows the deviation in the motor positions from the ideal trajectories. This error is used for the proportional control. Maximum error is about 7.5 degree and occurs just after transition and just before the pump ejection begins. Because this large error occurs at the end of transition when the motors and pistons are close together, the motors move much closer together than intended. This is shown in the motor separation plot (bottom-left), which shows that the motors come within 5 degrees of one another (the ideal trajectory is 15 degree separation). This is likely caused by the pressure change that occurs through transition. The pressure goes from pushing the pistons apart before transition to together after transition. This pressure change is shown in the plot of pressure (middle-right). When the pistons are pushed together after transition, it also creates a brief period of backflow, which is shown

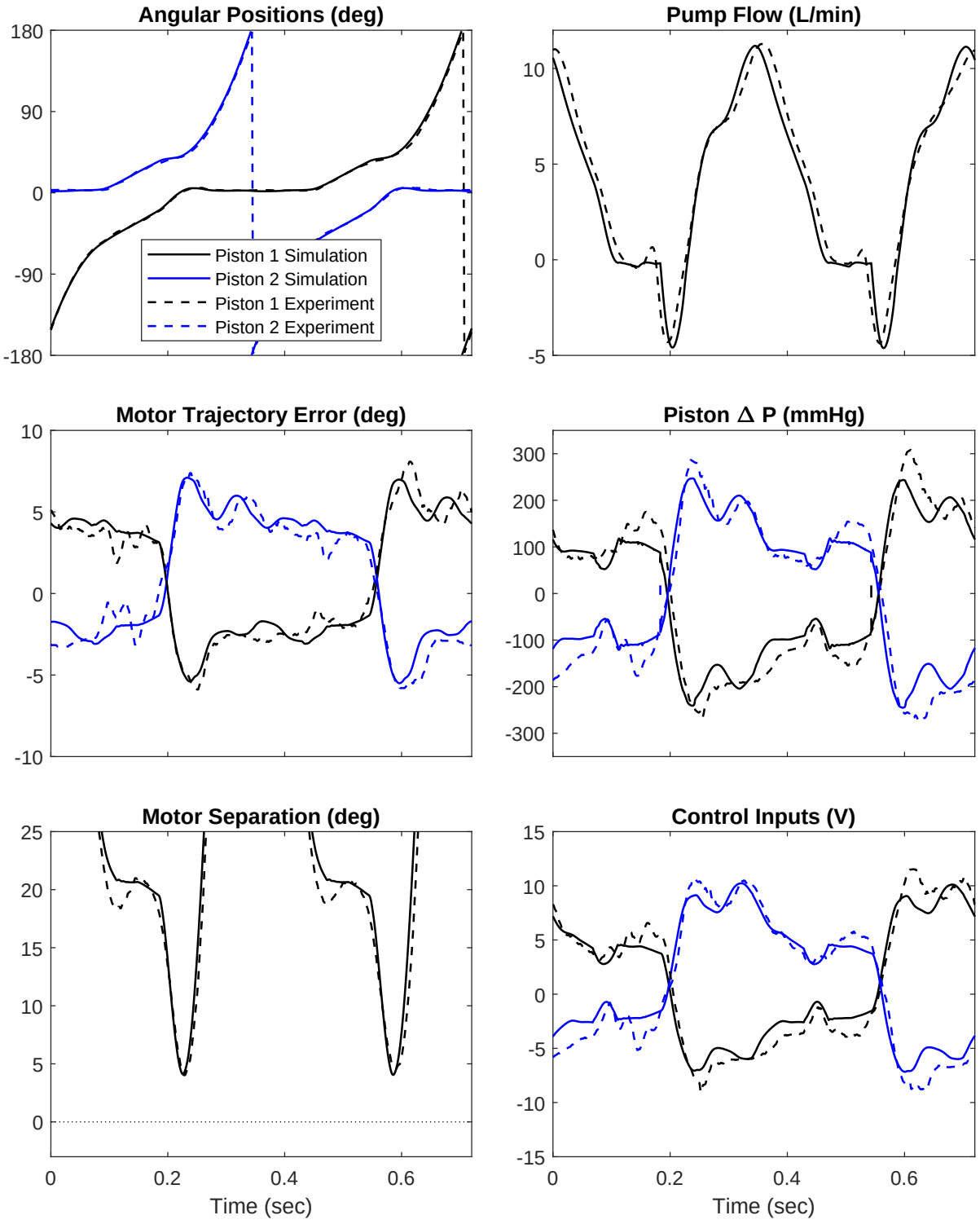

Figure 12.4: Simulated model compared to experimental results at 5 L/min with PID control.

One of the goals of this research was to use the model to improve the low-level control of the pistons. In order to accomplish this, linear quadratic control with a suboptimal observer were designed. The control gains and observer were implemented in the prototype 2PTP controller. The same experiment from the previous section was repeated (5 L/min against 100 mmHg differential pressure), but this time with the improved control method. Experimental results (dashed lines) are compared to simulation results (solid lines) in Figure 12.5. As expected, the improved control reduced the maximum trajectory error from approximately 7.5 deg to 1 degree, and the separation angle between the motors stays very near the ideal trajectory separation of 15 degrees. Once again, there is very good agreement between the experiment and simulation, with the exception of one large pressure/control spike in the experiment just before transition. The control does not seem affected by this model deviation.

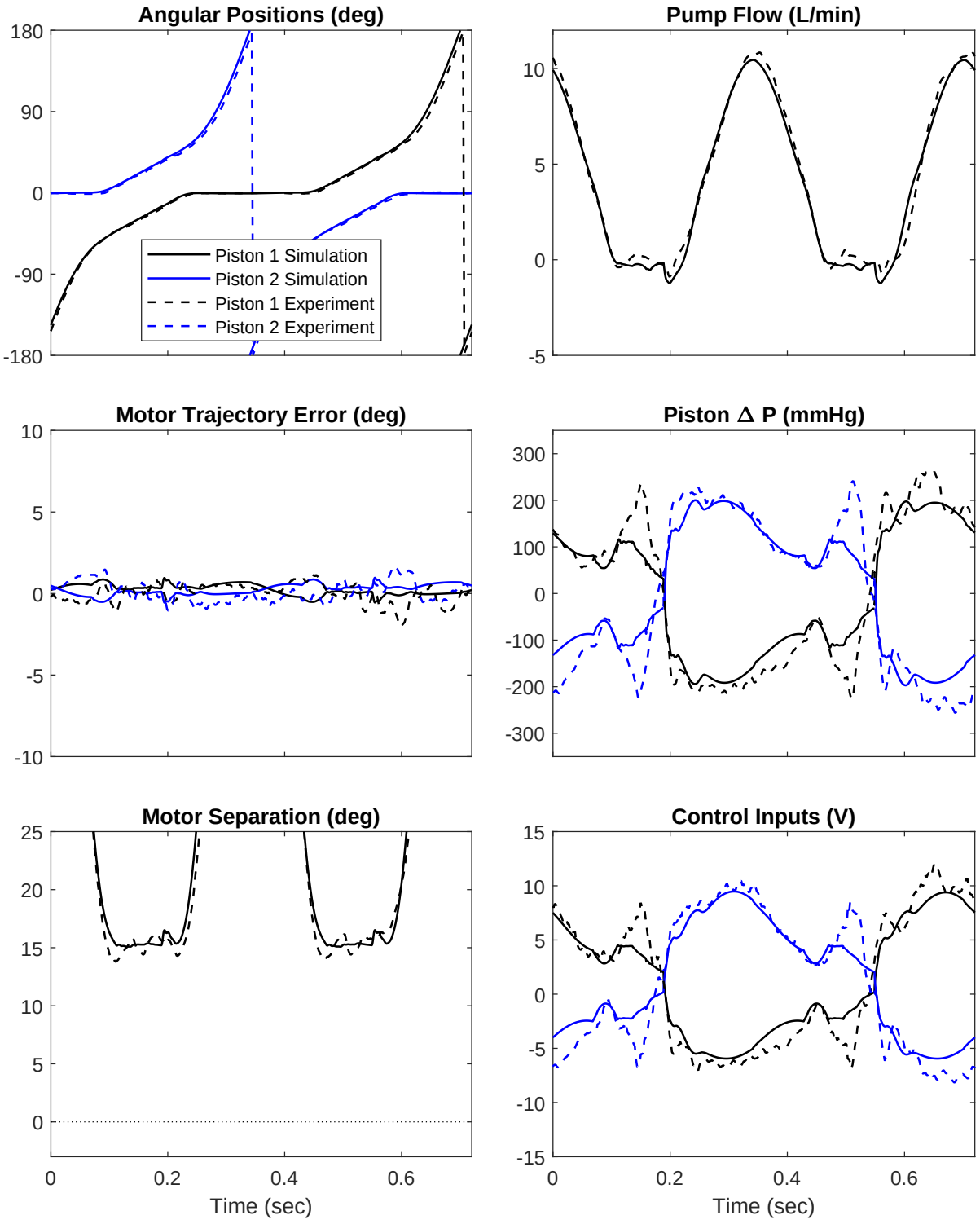

Figure 12.5: Simulated model compared to experimental results at 5 L/min with LQR control.

The two examples above demonstrated the effectiveness of LQR compared to PID control one flow and pressure (5 L/min against 100 mmHg pressure). PID vs LQR experiments were repeated over the range of pump flows (from zero to eight L/min when possible) at differential pressures of zero, 50, and 100 mmHg. A table of experiments is shown in Table 12.1. Experiments could not be run at 8 L/min against 50 mmHg or at 7 and 8 L/min at 100 mmHg because this required more hydraulic power than the the controller was capable of supplying.

	Asynchronous Flow Rate (L/min)							
Pressure (mmHg)	1	2	3	4	5	6	7	8
0	✓	✓	✓	✓	✓	✓	✓	✓
50	✓	✓	✓	✓	✓	✓	✓	-
100	✓	✓	✓	✓	✓	✓	-	-

Table 12.1: Asynchronous flow rates and pressures. Checkmarks indicate if an experiment was performed. Experiments could not be run at 8 L/min against 50 mmHg or at 7 and 8 L/min at 100 mmHg because this required more hydraulic power than the the controller was capable of supplying.

As a measure of the effectiveness of the control, the max motor position error from the ideal trajectory was measured for each experiment. This was chosen because it was an actual measurement (as opposed to the piston trajectory error which can be estimated with an observer but is not actually measured). The minimum distance between the motors during transition was also measured for each experiment. Figure 12.6 shows the results from these experiments for each flow rate and pressure condition. Results with PID control are indicated by circles and with LQR conrol are indicated by stars. At no loading pressure (0 mmHg), both controls perform well and keep the motor trajectory error small and piston separation large (with the exception of 8 L/min with PID control, when the hydraulic power requirements begin to exceed the supply capability and the input saturates). As pressure increases, so too does the trajectory error, but much more so for PID control.

As expected, LQR drastically improves the control across a wide range of operating flow rates and loading pressures, at least in terms of minimizing error from the ideal trajectory and maintaining the desired separation between the pistons during transition.

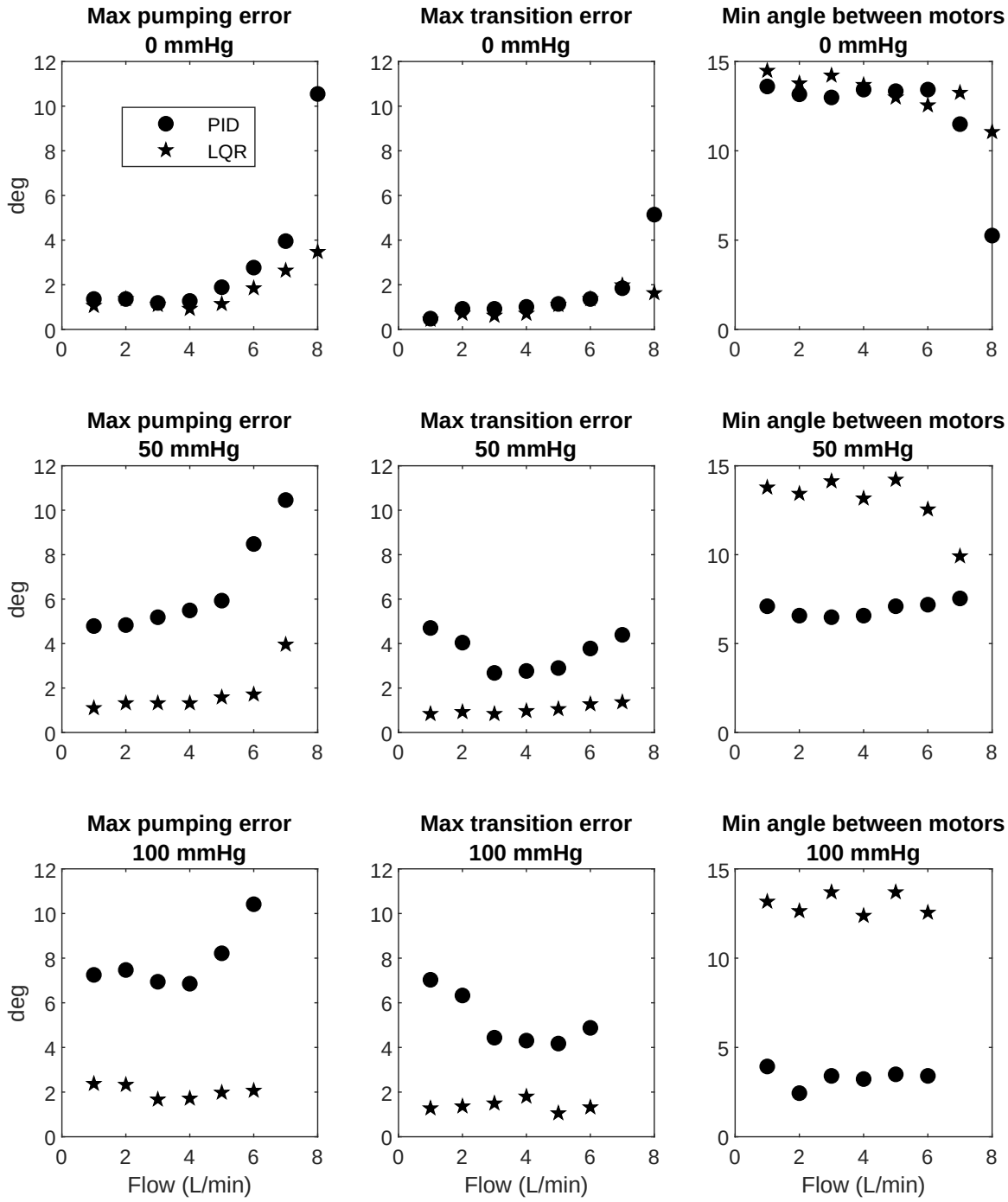

Figure 12.6: Motor position error from ideal trajectory for PID vs LQR at various flow rates and differential pump pressures. LQR control, made possible by suboptimal Kalman filter estimation, does a much better job of tracking the ideal trajectory compared to PID control on the motor position alone.

12.3 Pressure and Flow Estimation

Besides the unmeasurable pump states (motor velocity and piston position and velocity), the suboptimal Kalman filter-based observer on the pump controller is able to estimate pump flow rate (from estimated piston velocities) and differential pump pressures (from the estimation of the process disturbance).

$$\hat{Q} = Ar\left(\hat{\omega}_d - \hat{\omega}_h\right) \tag{12.2}$$

$$\Delta\hat{P} = \frac{\hat{T}_d - \hat{T}_h}{2Ar} \tag{12.3}$$

where $\hat{\omega}_d$ is the estimated drive piston velocity, $\hat{\omega}_d$ is the estimated hold piston velocity, $\hat{T}_d$ is the estimated torque disturbance on the drive piston, and $\hat{T}_h$ is the estimated torque disturbance on the hold piston. If the model and pump were perfect, $\hat{T}_d$ and $\hat{T}_h$ would be equal and opposite of one another, but due to frictional variation and other unaccounted for dynamics, they will be different, so the equation above has the effect of taking the average of the two disturbance values.

To test the estimation of the differential pressure, the pump was run from 1 to 6 L/min in 1 L/min increments in the passive mock loop. The resistor was adjusted by hand until the pressure was either 50 or 100 mmHg. The estimated pressure was compared to the actual pressure. The results are plotted in Figure 12.7. For all flow rates, the estimation error was less than 5 mmHg.

Next, to test the ability of the dynamic capabilities of the pressure estimation and pump flow estimation, the pump was set to run in the active mock circulatory loop. Heart failure was simulated at with a heart rate of 90 bpm. The hybrid mock loop generated a simulated ECG signal which the pump measured to synchronize pump ejections to the cardiac cycle. Dynamic differential pump pressure and flow rate were measured in the hybrid mock loop and compared to values obtained from the estimation algorithm. Results are shown in Figure 12.8. There is good agreement between the measured and estimated flow and pressure.

This pressure and flow information can provide valuable feedback for physiological control, could be used to estimate other cardiovascular parameters such as systemic vascular resistance, and could provide diagnostic information to doctors to monitor patient status.

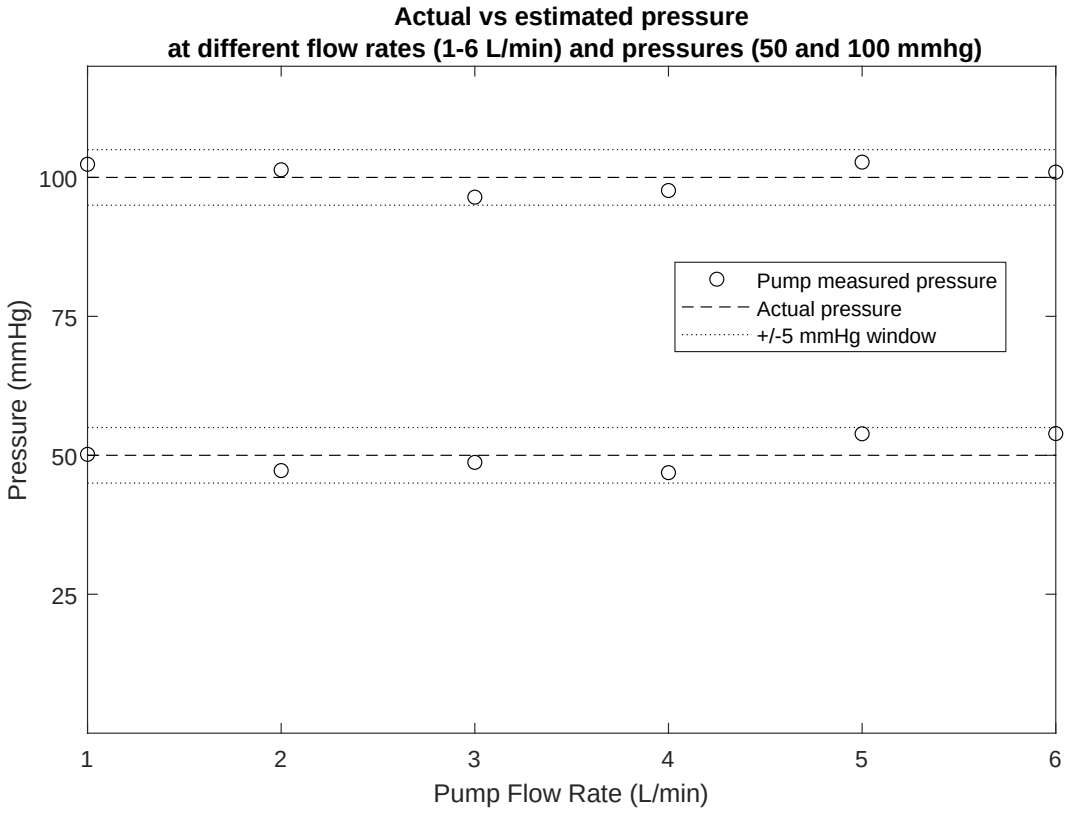

Figure 12.7: Pump estimated pressure against an mean pressure head at various flow rates (1-6 L/min) and at two different pressures (50 and 100 mmHg).

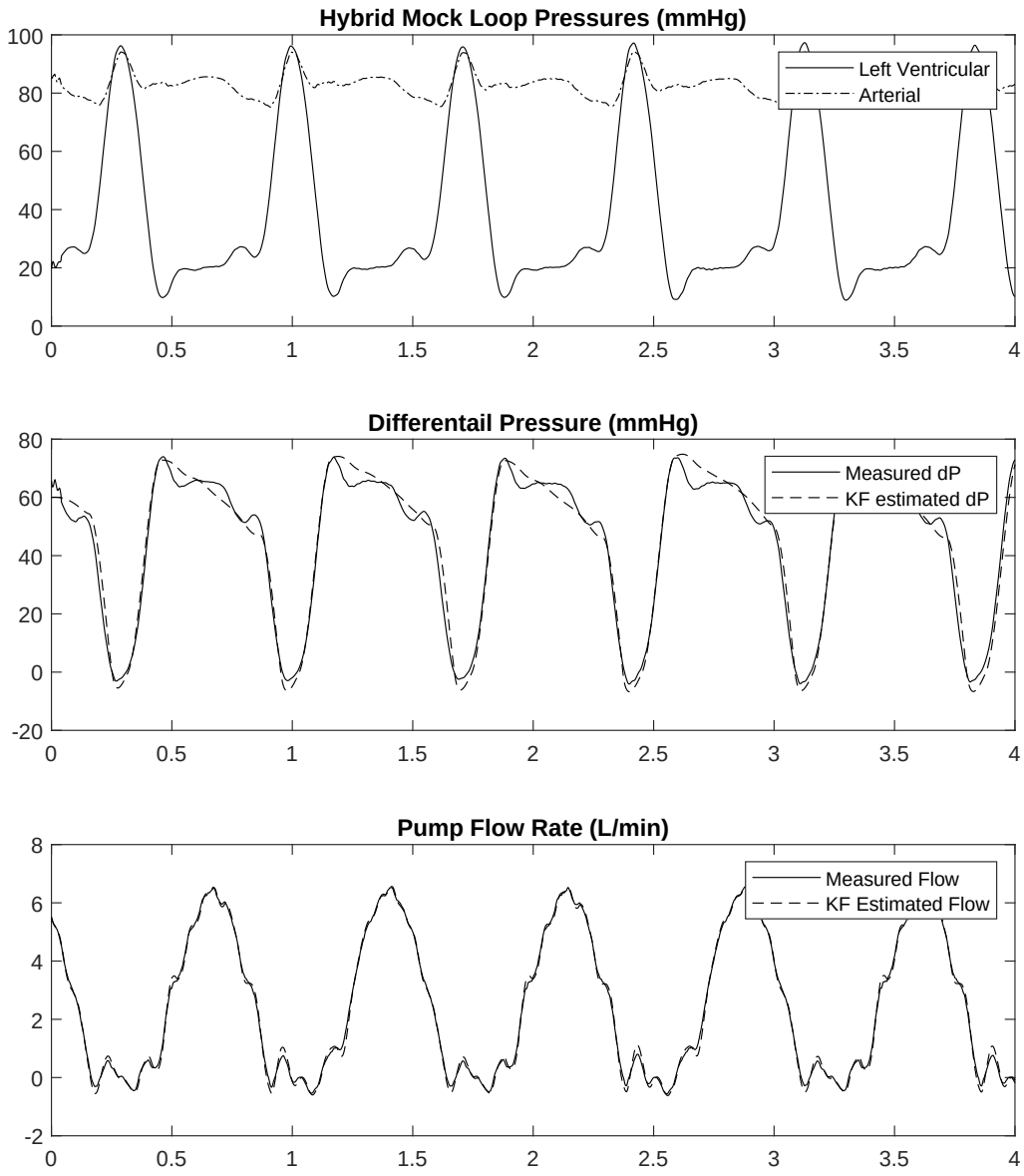

Figure 12.8: Measured vs KF estimated dynamic differential pump pressure and flow from the active mock loop at 90 bpm with synchronous counterpulse 2PTP flow.

Chapter 13

Discussion and Conclusions

The 2PTP is a new class of blood pump with unique capabilities. Besides the prototype TORVAD device, no 2PTP has been realized. Therefore, there are new challenges associated with two-piston pumping that have not been studied before, particularly as it relates to high-level physiological control with synchronous pumping and low-level piston control with pumping and transition switching. This research attempted to explore those challenges by studying hierarchical control of a 2PTP. This chapter provides a summary list of the research contributions, in the order of the four research aims outlined in the introduction.

Contributions

1 - Cardiovascular Modeling

- An new method for assessing preload and afterload sensitivity with ventricular assist device support was proposed. This method uses ventricular function curves obtained in an open-loop model of the cardiovascular system where preload and afterload boundary conditions are directly prescribed. This model enables ventricular function curves to be used as a metric for preload sensitivity with different types of VAD support.
- A new mathematical model for left ventricular filling (EDPVR) has been proposed that combines two features from established models: the stiffness of the ventricle at the unstressed volume and the exponential increase at high ventricular volumes. By adding this degree of freedom to either the typical exponential or logarithmic models, more physiological ventricular function curves are reproduced, which is important for studying the cardiac output response at low preloads with different kinds of VAD support.

2 - High-Level Physiological Control

- Methods were developed to specify geometric relationships and restrictions for the 2PTP architecture. Formulaic procedures were created for specifying parameters (such as piston and port angles and torus dimensinons) from specified requirements and restrictions (stroke volume, inner torus radius, and separation angle during transition).
- The 2PTP creates sequential pump ejections using the combined motion from two pistons. In order to control the shape of the pump ejections, path planning formulas were created from specified restrictions (sinusoidal pump ejection, twice differentiable position reference functions, no backwards motion, angles when transition starts/stops).
- The cardiovascular model was used to study preload sensitivity of two types of VAD support: continous flow vs 2PTP synchronous counterpulsation. Ventricular function curves generated in this case study demonstrated that counterpulsation provides a more physiological preload response, which could minimize the risk of ventricular suction and the progression to right heart failure.
- Though not a main focus of this research, vibration/forces on the surrounding tissue were studied (this work appears in the appendices). The combined dynamic forces inside the pump (motor/piston eccentric and rotational forces) with the hydraulic pressure forces imposed by the cannulas created an interesting modeling problem that required the formulations of a Lagrange subsystem with conservative exogenous efforts. This appears to be a unique formulation of the Lagrange subsystem formulation.

3- 2PTP Modeling

- A variable structure model of the 2PTP was developed. This is the first formulation of a switched model for this class of pump. The switched system consisted of 30 possible structures. State equations were derived for each structure using an algorithmic approach that could be applied to similar fluid network problems.
- A reduced-order model of the pump was developed that accounted for the coupling dynamics between the pistons due to the cannula flow. An interesting inertial fluid coupling problem for branched flow resulted from the reduced-order model. A generalized approach that quantifies the inertial coupling effects of branched flow was outlined in the appendix.

4 - Low-Level Control

- The reduced-order model of the 2PTP was utilized to take advantage of linear techniques for control (LQR) and estimation (Kalman filtering) to improve the control of the piston as compared to simple PID control of the motor positions.
- Experiments were conducted to verify the model and control. Position tracking error was reduced from 7.5 to 1 degree at 5 L/min flow rate against a differential pump pressure of 100 mmHg. Similar improvements were seen across a range of operating flows and pressures.
- Estimation of the pump flow rate and differential pump pressure was verified experimentally. Estimating the differential pressure provides disturbance rejection to improve control, but could also be used to improve physiological control methods as well as provide diagnostic information to physicians. Responsiveness to patient physiological need during exercise, rest, or pathological state is a growing field and this work on estimation contributes to the field by providing a method for obtaining important physiological feedback.

13.1 Limitations

Reticulation and the selection of dynamics are the art of modeling. As the expression goes, "all models are wrong but some are useful". This is true in the broader sense that all models are an approximation of reality, but also in the narrower sense in that many phenomenon are neglected or ignored. Simplifying to 2PTP to a lumped parameter model ignores three dimensional fluid dynamic and unsteady flow effects that might be more accurately captured with a three dimensional computational fluid dynamic model that uses the immersed boundary method for the moving pistons. But solving this model would be very time intensive, and the formulation of the model would not help in the design of control. There are other dynamics that could have been added to the lumped parameter model such as unsteady flow, fluid momentum associated with the changing flow directions into and out of the ports, centrifugal flow forces, non-Newtonian fluid properties, cannula compliance, and wave reflection in the cannulas (to name just a few). But the line has to be drawn somewhere.

Appendices

Appendix A

High-Level 2PTP Control - Vibration Concerns

Continuous flow pumps have a single rotating impeller that operates at constant speed. Even so, patients have reported discomfort caused by motion and vibration of the device. "All I felt was this vibration on my stomach, and I didn't understand what was going on ... It kept me awake at night because there was like a swooshing" [93]. How much more significant and problematic might this vibration be for a pulsatile device that has eccentric rotating masses and dynamic pumping strokes? What will be the forces on the surrounding tissue? What forces are allowable before the patient starts to feel the motion? How should the pistons and motors be driven to minimize these forces? These issues have not been studied before. A thorough search of the literature did not yield any results of forces or motion of implantable medical devices. This appendix will develop a model to start to answer these questions.

A.1 2PTP and Tissue Model of Motion and Vibration

First, a model of the pump and tissue is needed. The model should include a few key elements:

1. Eccentric mass of the pistons and motors
2. Viscoelastic properties of the surrounding tissue
3. Dynamic momentum and pressure forces associated with fluid entering and exiting the pump

A.1.1 Eccentric Masses

The pistons and the motors are magnetically coupled through a magnetic linkage. For this simple model, this magnetic coupling will be modeled as ideal (piston position = motor position). In this simplified model, the coupled piston and motor could be modeled as an

eccentric mass. A schematic of this system can be found in Figure A.1.

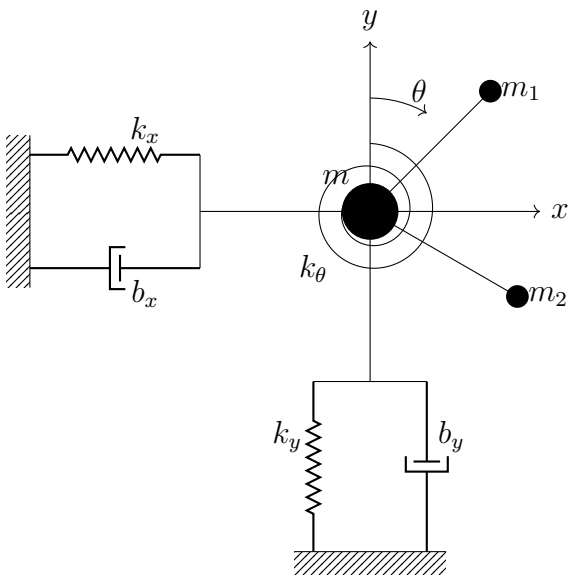

Figure A.1: A schematic representation of the pump in tissue. Two eccentric masses (m_1 and m_2 at radius r) rotate around a central pump mass m. The surrounding tissue is modeled as a Kelvin-Voigt material (parallel spring-damper system).

Of interest to this model is the force and torque exerted on the tissue and the motion of the pump. Multibody Lagrange subsystem analysis, explained in more detail later, can be used to derive the dynamic equations.

A.1.2 Tissue Model

Numerous simple models have been proposed to represent the viscoelastic properties of soft tissue including the Kelvin Voigt model, Maxwell model, and standard solid model [94]. These models consist of springs and dampers in various configurations (see Figure A.2). For this analysis, the Kelvin-Voigt model is used.

A.1.3 Fluid Momentum and Pressure Forces

A control volume must be established to understand the effects of fluid momentum and pressure forces on the pump. The control volume for the 2PTP is drawn around the pump up and includes the inflow and outflow ports (which are rigid) but not the inflow and outflow cannulas (which can bend and deflect). This control volume is shown in Figure A.3.

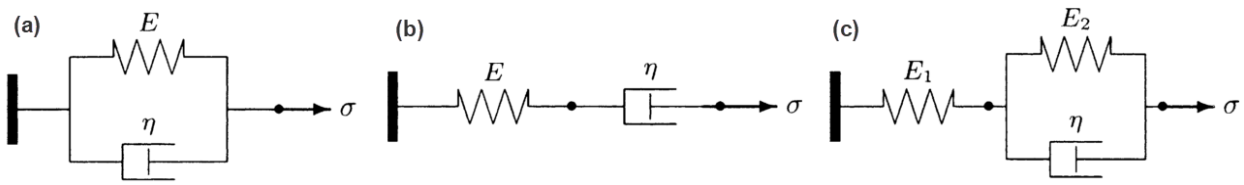

Figure A.2: Common tissue models: Kelvin-Voigt (a), Maxwell (b), and standard solid (c) (from [94])

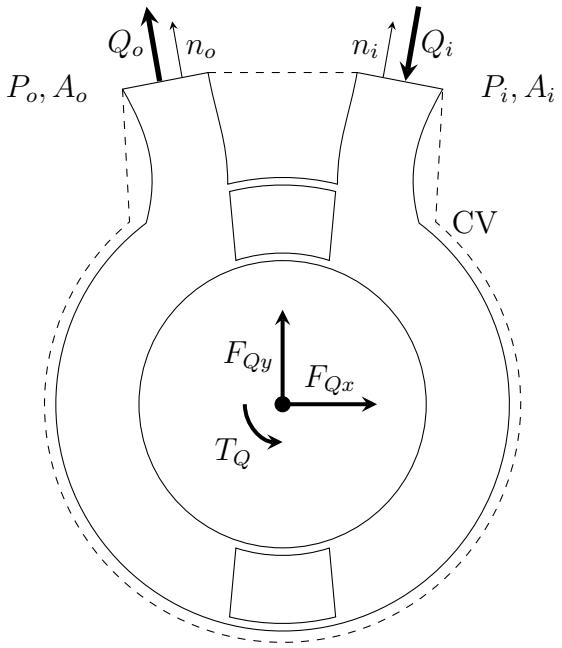

Figure A.3: 2PTP control volume analysis. Entrance flow Q_i with pressure P_i and area A_i and exit flow Q_o with pressure P_o and area A_o generate forces (F_{Qx} and F_{Qy}) and a torque T_Q on the pump.

The fluid momentum and pressure generates forces on the control volume:

$$F_{Qx} = P_i A_i n_{ix} + P_o A_o n_{ox} - \int_{CS} u_x \rho \mathbf{u} \cdot \hat{\mathbf{n}} dA - \frac{\partial}{\partial t} \int_{CV} u_x \mathbf{u} \rho dV \tag{A.1}$$

$$F_{Qy} = P_i A_i n_{iy} + P_o A_o n_{oy} - \int_{CS} u_y \rho \mathbf{u} \cdot \hat{\mathbf{n}} dA - \frac{\partial}{\partial t} \int_{CV} u_y \mathbf{u} \rho dV \tag{A.2}$$

In this case, the inflow and outflow area have the same area.

$$A_i = A_o = A$$

And for incompressible flow, the inflow and outflow have the same flow.

$$Q_i = Q_o = Q$$

The mean flow rate u can be found by,

$$u = \frac{Q}{A}$$

Letting θ_m be the angle of the entire pump mass with respect to the global coordinate system and θ_p the angle of the inflow and outflow ports with respect to the pump coordinate system, the inflow and outflow angles can be defined by,

$$\theta_i = \theta_m + \theta_p \quad \text{and} \quad \theta_o = \theta_m - \theta_p$$

And the normalized inflow and outflow vector components in the x and y direction are found by,

$$n_{ix} = -\sin(\theta_i)$$

$$n_{iy} = -\cos(\theta_i)$$

$$n_{ox} = -\sin(\theta_o)$$

$$n_{oy} = \cos(\theta_o)$$

For this analysis, the pressure effects from the dynamic flow inside the pump are small compared to the effects from the cannulas and cardiovascular system, so they are neglected.

$$\frac{\partial}{\partial t}\int_{CV} u = 0$$

The pressure at the inflow P_i and outflow P_o are functions of the cannula resistance and inertia as well as the external pressure on the system.

$$P_i = P_{LV} - I_i\dot{Q} - R_iQ \tag{A.3}$$

$$P_o = P_{ao} + I_o\dot{Q} + R_oQ \tag{A.4}$$

where P_{LV} is the left ventricular pressure, P_{ao} is the aortic arterial pressure, I is the fluid inertia in the inflow and outflow, and R is the viscous resistance of the inflow and outflow. Substituting

Leakage around the annular gap between the piston and torus is neglected and the motor and piston position are assumed to be identical (ideal magnetic coupling). Therefore, the flow can be expressed as a function of the two motors θ_1 and θ_2:

$$Q = \eta Ar\left(\dot{\theta}_1 - \dot{\theta}_2\right) \qquad \text{and} \qquad \dot{Q} = \eta Ar\left(\ddot{\theta}_1 - \ddot{\theta}_2\right)$$

$\eta = 1$ when θ_1 drive piston

$\eta = -1$ when θ_2 drive piston

$Ar =$ piston cross section area times mean piston radius

Finally, using the definitions and simplifications above, equations A.1 and A.2 can be integrated.

$$\begin{aligned} F_{Qx} = &- A\sin\theta_i\left[P_{LV} - \eta I_i Ar\left(\ddot{\theta}_1 - \ddot{\theta}_2\right) - \eta R_i Ar\left(\dot{\theta}_1 - \dot{\theta}_2\right)\right] \\ &- A\sin\theta_o\left[P_{ao} + \eta I_o Ar\left(\ddot{\theta}_1 - \ddot{\theta}_2\right) + \eta R_o Ar\left(\dot{\theta}_1 - \dot{\theta}_2\right)\right] \\ &- \frac{\rho\left(Ar\left(\dot{\theta}_1 - \dot{\theta}_2\right)\right)^2}{A}\left(\sin\theta_i + \sin\theta_o\right) \end{aligned}$$

$$\begin{aligned} F_{Qy} = &- A\cos\theta_i\left[P_{LV} - \eta I_i Ar\left(\ddot{\theta}_1 - \ddot{\theta}_2\right) - \eta R_i Ar\left(\dot{\theta}_1 - \dot{\theta}_2\right)\right] \\ &- A\cos\theta_o\left[P_{ao} + \eta I_o Ar\left(\ddot{\theta}_1 - \ddot{\theta}_2\right) + \eta R_o Ar\left(\dot{\theta}_1 - \dot{\theta}_2\right)\right] \\ &- \frac{\rho\left(Ar\left(\dot{\theta}_1 - \dot{\theta}_2\right)\right)^2}{A}\left(\cos\theta_i + \cos\theta_o\right) \end{aligned}$$

From the force in the x and y directions, the torque on the pump can be calculated by

$$T_{Qm} = \left(\frac{w_p}{2}A\sin\theta_p - h_p A\cos\theta_p\right)\left(RAr\left(\dot{\theta}_1 - \dot{\theta}_2\right) + \eta IAr\left(\ddot{\theta}_1 - \ddot{\theta}_2\right) + \Delta P\right)$$

where w_p is the distance between the ports and h_p is the relative height or distance of the ports with respect to the center of the pump.

The resistance and inertia of the cannulas also adds torque to the eccentric masses

$$T_{Q1} = -Ar\left[\eta RAr\left(\dot{\theta}_1 - \dot{\theta}_2\right) + \eta IAr\left(\ddot{\theta}_1 - \ddot{\theta}_2\right) + \eta\Delta P\right]$$

$$T_{Q2} = Ar\left[\eta RAr\left(\dot{\theta}_1 - \dot{\theta}_2\right) + \eta IAr\left(\ddot{\theta}_1 - \ddot{\theta}_2\right) + \eta\Delta P\right]$$

A.1.4 Model

State equations are needed to model the motion and forces generated by the device during pumping. The pump mass and eccentric masses can be treated as a multibody Lagrange subsystem to simplify the analysis. In this case, where a control volume is defined for hydraulic analysis, the Lagrange subsystem consists of those components within the control volume. Using a Lagrange subsystem approach allows for the formulation of state equations by analyzing the potential and kinetic energy of the system [95]. With vectorized bond graphs, the Lagrange subsystem approach is illustrated in Figure A.4.

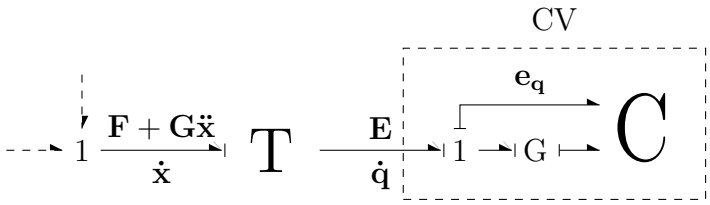

Figure A.4: Vectorized bond graph of a Lagrange subsystem

The bond graph incorporating the exogenous hydraulic effects and coupled inertia with the Lagrange subsystem can be seen in Figure A.5.

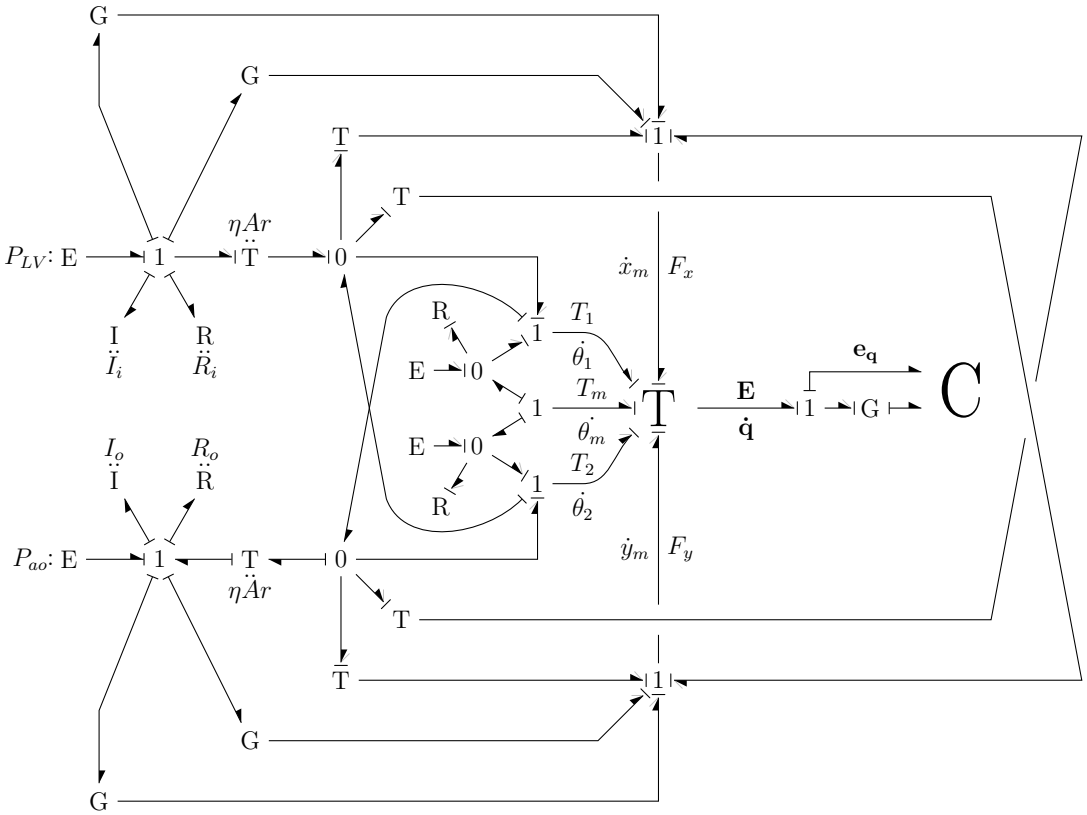

Figure A.5: Bond graph of the multibody Lagrange subsystem with exogenous hydraulic efforts and coupled inertia

The dependent variables are

$$\dot{\mathbf{x}} = \begin{bmatrix} \dot{x}_m & \dot{y}_m & \dot{\theta}_m & \dot{x}_1 & \dot{y}_1 & \dot{\theta}_1 & \dot{x}_2 & \dot{y}_2 & \dot{\theta}_2 \end{bmatrix}^T \tag{A.5}$$

which are the transnational (x and y) and rotational velocities for the pump mass m, piston and motor 1 eccentric mass (1), and piston and motor 2 eccentric mass (2). To obtain dynamic state equations, follow the 9 step procedure from Appendix B for Lagrange subsystems with conservative exogenous efforts.

For the multibody Lagrange system, the minimum set of flows are

$$\dot{\mathbf{q}} = \begin{bmatrix} \dot{x}_m & \dot{y}_m & \dot{\theta}_m & \dot{\theta}_1 & \dot{\theta}_2 \end{bmatrix}^T \tag{A.6}$$

1 - Define the transformation matrix T and take the time derivative $\dot{\mathbf{T}}$

From the geometry, the transformation matrix $\mathbf{T}$ can be found

$$\dot{\mathbf{x}} = \mathbf{T}\dot{\mathbf{q}}$$

$$\begin{bmatrix} \dot{x}_m \\ \dot{y}_m \\ \dot{\theta}_m \\ \dot{x}_1 \\ \dot{y}_1 \\ \dot{\theta}_1 \\ \dot{x}_2 \\ \dot{y}_2 \\ \dot{\theta}_2 \end{bmatrix} = \mathbf{T} \begin{bmatrix} \dot{x}_m \\ \dot{y}_m \\ \dot{\theta}_m \\ \dot{\theta}_1 \\ \dot{\theta}_2 \end{bmatrix} \qquad \mathbf{T} = \begin{bmatrix} 1 & 0 & 0 & 0 & 0 \\ 0 & 1 & 0 & 0 & 0 \\ 0 & 0 & 1 & 0 & 0 \\ 1 & 0 & 0 & r\cos(\theta_1) & 0 \\ 0 & 1 & 0 & -r\sin(\theta_1) & 0 \\ 0 & 0 & 0 & 1 & 0 \\ 1 & 0 & 0 & 0 & r\cos(\theta_2) \\ 0 & 1 & 0 & 0 & -r\sin(\theta_2) \\ 0 & 0 & 0 & 0 & 1 \end{bmatrix}$$

Then take the time derivative

$$\dot{\mathbf{T}} = \begin{bmatrix} 0 & 0 & 0 & 0 & 0 \\ 0 & 0 & 0 & 0 & 0 \\ 0 & 0 & 0 & 0 & 0 \\ 0 & 0 & 0 & -r\sin(\theta_1)\dot{\theta}_1 & 0 \\ 0 & 0 & 0 & -r\cos(\theta_1)\dot{\theta}_1 & 0 \\ 0 & 0 & 0 & 0 & 0 \\ 0 & 0 & 0 & 0 & -r\sin(\theta_2)\dot{\theta}_2 \\ 0 & 0 & 0 & 0 & -r\cos(\theta_2)\dot{\theta}_2 \\ 0 & 0 & 0 & 0 & 0 \end{bmatrix}$$

2 - Determine the mass matrix M for the kinetic energy, transform the mass matrix $\hat{\mathbf{M}} = \mathbf{T^T M T}$ and take the time derivative $\dot{\hat{\mathbf{M}}}$

The scalar kinetic energy function for the multibody Lagrnage subsystem is

$$K = \frac{1}{2}m\dot{x}_m^2 + \frac{1}{2}m\dot{y}_m^2 + \frac{1}{2}J\dot{\theta}_m^2 + \frac{1}{2}m_1\dot{x}_1^2 + \frac{1}{2}m_1\dot{y}_1^2 + \frac{1}{2}m_2\dot{x}_2^2 + \frac{1}{2}m_2\dot{y}_2^2$$

The mass matrix can be found by converting to matrix form

$$\mathbf{K} = \dot{\mathbf{x}}^\mathbf{T}\mathbf{M}\dot{\mathbf{x}} \quad \text{where } \mathbf{M} = \begin{bmatrix} m & 0 & 0 & 0 & 0 & 0 & 0 & 0 & 0 \\ 0 & m & 0 & 0 & 0 & 0 & 0 & 0 & 0 \\ 0 & 0 & J & 0 & 0 & 0 & 0 & 0 & 0 \\ 0 & 0 & 0 & m_1 & 0 & 0 & 0 & 0 & 0 \\ 0 & 0 & 0 & 0 & m_1 & 0 & 0 & 0 & 0 \\ 0 & 0 & 0 & 0 & 0 & J_1 & 0 & 0 & 0 \\ 0 & 0 & 0 & 0 & 0 & 0 & m_2 & 0 & 0 \\ 0 & 0 & 0 & 0 & 0 & 0 & 0 & m_2 & 0 \\ 0 & 0 & 0 & 0 & 0 & 0 & 0 & 0 & J_2 \end{bmatrix}$$

The mass matrix can be transformed by $\hat{\mathbf{M}} = \mathbf{T^T M T}$

$$\hat{\mathbf{M}} = \begin{bmatrix} m+m_1+m_2 & 0 & 0 & m_1 r\cos(\theta_1) & m_2 r\cos(\theta_2) \\ 0 & m+m_1+m_2 & 0 & -m_1 r\sin(\theta_1) & -m_2 r\sin(\theta_2) \\ 0 & 0 & J & 0 & 0 \\ m_1 r\cos(\theta_1) & -m_1 r\sin(\theta_1) & 0 & J_1+m_1 r^2 & 0 \\ m_2 r\cos(\theta_2) & -m_2 r\sin(\theta_2) & 0 & 0 & J_2+m_2 r^2 \end{bmatrix}$$

And the time derivative can be found, which will be used later in the exogenous effort equation

$$\dot{\hat{\mathbf{M}}} = \begin{bmatrix} 0 & 0 & 0 & -m_1 r\sin(\theta_1)\dot{\theta}_1 & -m_2 r\sin(\theta_2)\dot{\theta}_2 \\ 0 & 0 & 0 & -m_1 r\cos(\theta_1)\dot{\theta}_1 & -m_2 r\cos(\theta_2)\dot{\theta}_2 \\ 0 & 0 & 0 & 0 & 0 \\ -m_1 r\sin(\theta_1)\dot{\theta}_1 & -m_1 r\cos(\theta_1)\dot{\theta}_1 & 0 & 0 & 0 \\ -m_2 r\sin(\theta_2)\dot{\theta}_2 & -m_2 r\cos(\theta_2)\dot{\theta}_2 & 0 & 0 & 0 \end{bmatrix}$$

4 - Express the kinetic energy $\hat{\mathbf{K}}$ as a function of independent flows $\dot{\mathbf{q}}$ and displacements $\mathbf{q}$

$$\hat{\mathbf{K}} = \frac{\mathbf{1}}{\mathbf{2}}\dot{\mathbf{q}}^{\mathbf{T}}\hat{\mathbf{M}}\dot{\mathbf{q}} \tag{A.7}$$

5 - Express the potential energy $\hat{\mathbf{U}}$ as a function of independent displacements $\mathbf{q}$

First, the potential energy can be expressed in terms of the dependent variables $\mathbf{x}$

$$\begin{aligned}\mathbf{U}(\mathbf{x}) =& \frac{1}{2}k_x x_m^2 + \frac{1}{2}k_y y_m^2 + \frac{1}{2}k_\theta \theta_m^2 \\ &+ (m+m_1+m_2)gy_m + m_1 g\left(r+y_1\right)) + m_2 g\left(r+y_2\right)\end{aligned}$$

Which can each be converted to independent variables $\mathbf{q}$ so that the potential energy is expressed in terms of the independent variables of the Lagrange subsystem.

$$\begin{aligned}\hat{\mathbf{U}}(\mathbf{q}) =& \frac{1}{2}k_x x_m^2 + \frac{1}{2}k_y y_m^2 + \frac{1}{2}k_\theta \theta_m^2 \\ &+ (m+m_1+m_2)gy_m + m_1 gr\left(1+\cos(\theta_1)\right) + m_2 gr\left(1+\cos(\theta_2)\right)\end{aligned}$$

5 - Define the generalized conservative effort $\mathbf{e_q}$ of the Lagrange subsystem

$$\mathbf{e_q} = \nabla_{\mathbf{q}}(\mathbf{U}-\mathbf{K})$$

$$\mathbf{e_q} = \begin{bmatrix} e_{x_m} \\ e_{y_m} \\ e_{\theta_m} \\ e_{\theta_1} \\ e_{\theta_2} \end{bmatrix} = \begin{bmatrix} k_x x_m \\ k_x y_m + (m + m_1 + m_2)g \\ k_\theta \theta_m \\ m_1 r \left(\dot{\theta}_1 \dot{y}_m \cos\theta_1 + \dot{\theta}_1 \dot{x} \sin\theta_1 - g \sin\theta_1 \right) \\ m_2 r \left(\dot{\theta}_2 \dot{y}_m \cos\theta_2 + \dot{\theta}_2 \dot{x} \sin\theta_2 - g \sin\theta_2 \right) \end{bmatrix}$$

6 - Define the exogenous effort nonlinear $\hat{\mathbf{F}}(\mathbf{q}, \dot{\mathbf{q}})$ and exogenous mass matrix $\hat{\mathbf{G}}$

From the bond graph, the power flow from each bond into the Lagrange transformer can be found.

$$F_{x_m} = -b_x \dot{x}_m + F_{Qx}$$

$$F_{x_m} = -b_y \dot{y}_m + F_{Qy}$$

$$T_m = -b_\theta \dot{\theta}_m + b_r(\dot{\theta}_1 - \dot{\theta}_m) - T_1(t) + b_r(\dot{\theta}_2 - \dot{\theta}_m) - T_2(t) + T_{Qm}$$

$$F_{x_1} = 0$$

$$F_{x_1} = 0$$

$$T_1 = T_1(t) - b_r(\dot{\theta}_1 - \dot{\theta}_m) + T_{Q1}$$

$$T_2 = T_2(t) - b_r(\dot{\theta}_2 - \dot{\theta}_m) + T_{Q2}$$

From these, $\hat{\mathbf{F}}$ and $\hat{\mathbf{G}}$ can be found:

$$\hat{\mathbf{F}} = \begin{bmatrix} F_1 \\ F_2 \\ F_3 \\ 0 \\ 0 \\ T_1(t) - b_r(\dot{\theta}_1 - \dot{\theta}_m) - Ar \left[\eta R Ar \left(\dot{\theta}_1 - \dot{\theta}_2 \right) + \Delta P \right] \\ 0 \\ 0 \\ T_2(t) - b_r(\dot{\theta}_2 - \dot{\theta}_m) + Ar \left[\eta R Ar \left(\dot{\theta}_1 - \dot{\theta}_2 \right) + \Delta P \right] \end{bmatrix}$$

where

$$\begin{aligned} F_1 = & - b_x \dot{x}_m - \frac{\rho \left(Ar \left(\dot{\theta}_1 - \dot{\theta}_2 \right) \right)^2}{A} (\sin\theta_i + \sin\theta_o) \\ & - A \sin\theta_i \left[P_{LV} - \eta R_i Ar \left(\dot{\theta}_1 - \dot{\theta}_2 \right) \right] - A \sin\theta_o \left[P_{ao} + \eta R_o Ar \left(\dot{\theta}_1 - \dot{\theta}_2 \right) \right] \end{aligned}$$

$$F_2 = - b_y \dot{y}_m - \frac{\rho \left(Ar \left(\dot{\theta}_1 - \dot{\theta}_2 \right) \right)^2}{A} (\cos\theta_i + \cos\theta_o)$$
$$- A\cos\theta_i \left[P_{LV} - \eta R_i Ar \left(\dot{\theta}_1 - \dot{\theta}_2 \right) \right] - A\cos\theta_o \left[P_{ao} + \eta R_o Ar \left(\dot{\theta}_1 - \dot{\theta}_2 \right) \right]$$

$$F_3 = - b_\theta \dot{\theta}_m + b_r(\dot{\theta}_1 - \dot{\theta}_m) - T_1(t) + b_r(\dot{\theta}_2 - \dot{\theta}_m) - T_2(t)$$
$$+ (x_p A \sin\theta_p - y_p A \cos\theta_p) \left(\eta R Ar \left(\dot{\theta}_1 - \dot{\theta}_2 \right) + \Delta P \right)$$

and

$$\hat{\mathbf{G}} = \begin{bmatrix} 0 & 0 & 0 & 0 & 0 & \eta A^2 r \left(I_i \sin\theta_i - I_o \sin\theta_o \right) & 0 & 0 & \eta A^2 r \left(I_o \sin\theta_o - I_i \sin\theta_i \right) \\ 0 & 0 & 0 & 0 & 0 & \eta A^2 r \left(I_i \cos\theta_i - I_o \cos\theta_o \right) & 0 & 0 & \eta A^2 r \left(I_o \cos\theta_o - I_i \cos\theta_i \right) \\ 0 & 0 & 0 & 0 & 0 & \eta I Ar \left(x_p A \sin\theta_p - y_p A \cos\theta_p \right) & 0 & 0 & -\eta I Ar \left(x_p A \sin\theta_p - y_p A \cos\theta_p \right) \\ 0 & 0 & 0 & 0 & 0 & 0 & 0 & 0 & 0 \\ 0 & 0 & 0 & 0 & 0 & 0 & 0 & 0 & 0 \\ 0 & 0 & 0 & 0 & 0 & -A^2 r^2 I & 0 & 0 & A^2 r^2 I \\ 0 & 0 & 0 & 0 & 0 & 0 & 0 & 0 & 0 \\ 0 & 0 & 0 & 0 & 0 & 0 & 0 & 0 & 0 \\ 0 & 0 & 0 & 0 & 0 & A^2 r^2 I & 0 & 0 & -A^2 r^2 I \end{bmatrix}$$

7 - Obtain state equations

Finally, the state equations can be found

$$\dot{\mathbf{q}} = \hat{\mathbf{M}}^{-1}\mathbf{p} \tag{A.8}$$

$$\dot{\mathbf{p}} = \left(\mathbf{I} - \mathbf{T}^{\mathbf{T}} \hat{\mathbf{G}} \mathbf{T} \hat{\mathbf{M}}^{-1} \right)^{-1} \left[-\nabla_{\mathbf{q}} \left(\hat{\mathbf{U}} - \hat{\mathbf{K}} \right) + \mathbf{T}^{\mathbf{T}} \hat{\mathbf{F}} - \mathbf{T}^{\mathbf{T}} \hat{\mathbf{G}} \mathbf{T} \hat{\mathbf{M}}^{-1} \dot{\hat{\mathbf{M}}} \hat{\mathbf{M}}^{-1} \mathbf{p} + \mathbf{T}^{\mathbf{T}} \hat{\mathbf{G}} \dot{\mathbf{T}} \dot{\mathbf{q}} \right]$$

All matrices and scalar equations ($\mathbf{T}$, $\hat{\mathbf{G}}$, $\hat{\mathbf{M}}$, $\hat{\mathbf{U}}$, $\hat{\mathbf{K}}$, $\hat{\mathbf{F}}$) have been defined above.

8 - Solve the differential equations.

To model the system, the parameters are defined and Matlab is used to solve the differential equations. Some matrices are functions of states and need to be recomputed and inverted each time step.

Results

Preliminary results for three conditions are shown in the following figures: 5 L/min at zero pressure, no pump flow at physiological pressures, and synchronous support (2.7 L/min) at physiological pressures.

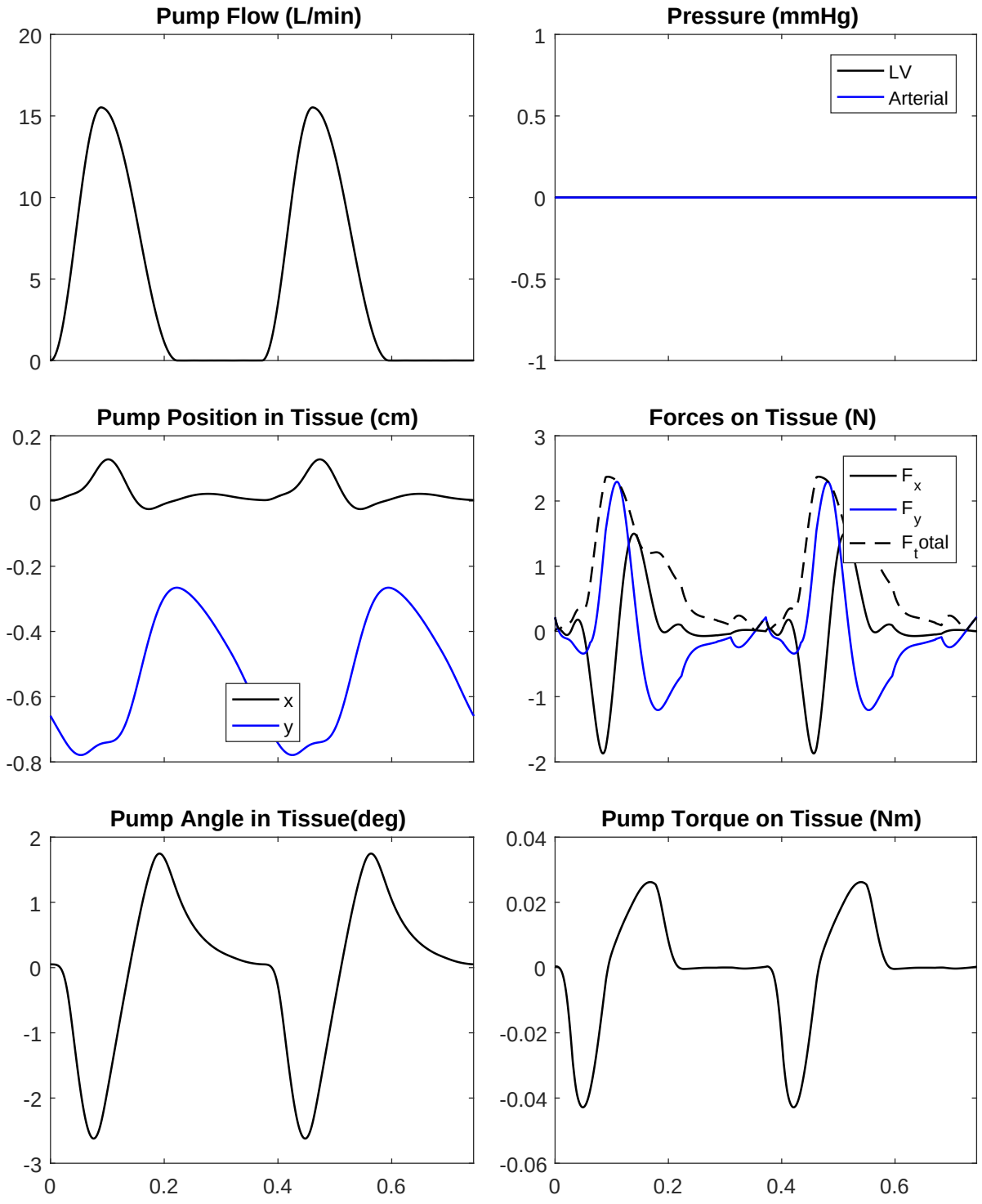

Figure A.6: Pump motion in and forces on surrounding tissue at 5 L/min pump flow rate

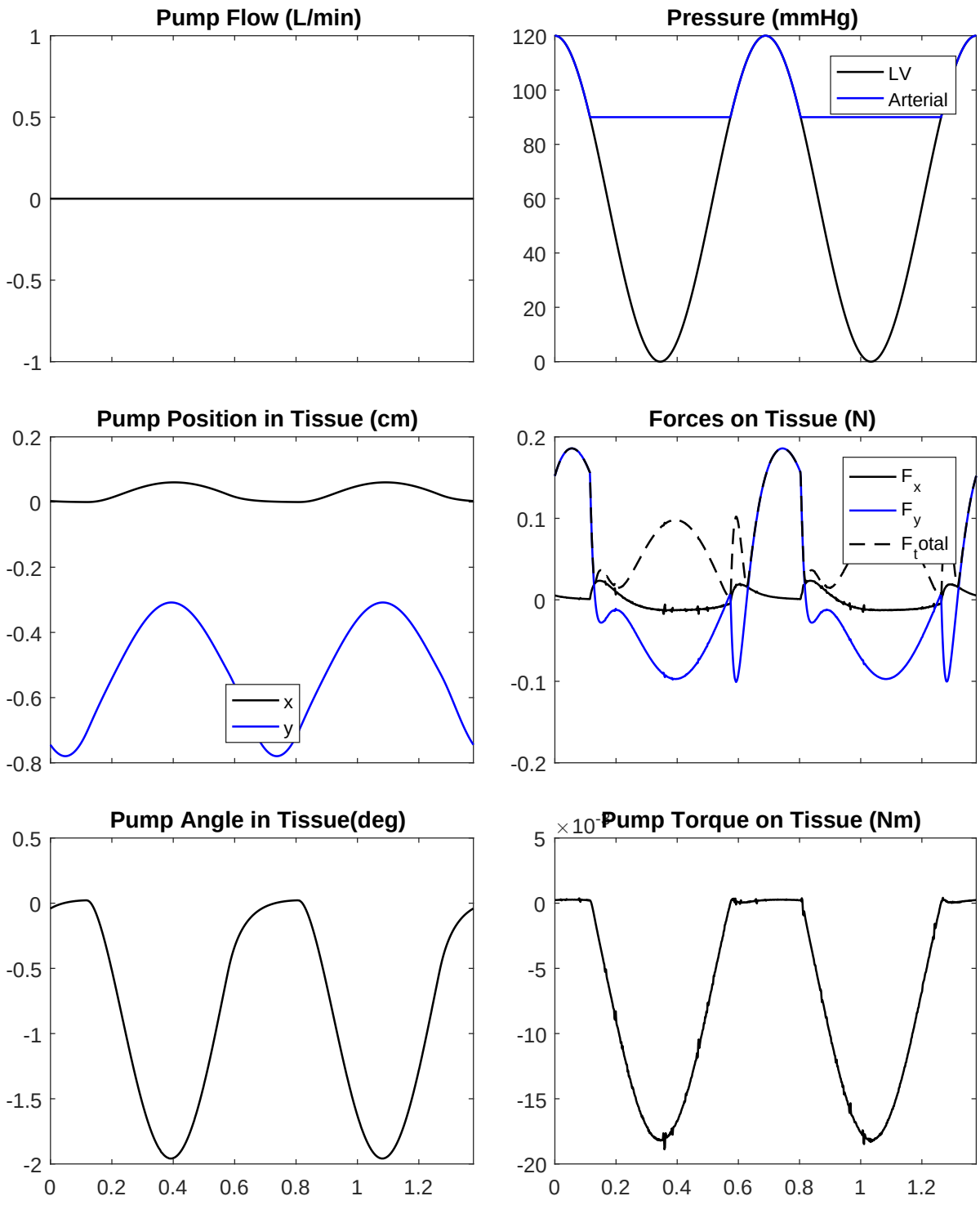

Figure A.7: Pump motion in and forces on surrounding tissue at 0 L/min pump flow rate with simulated beating heart pressure

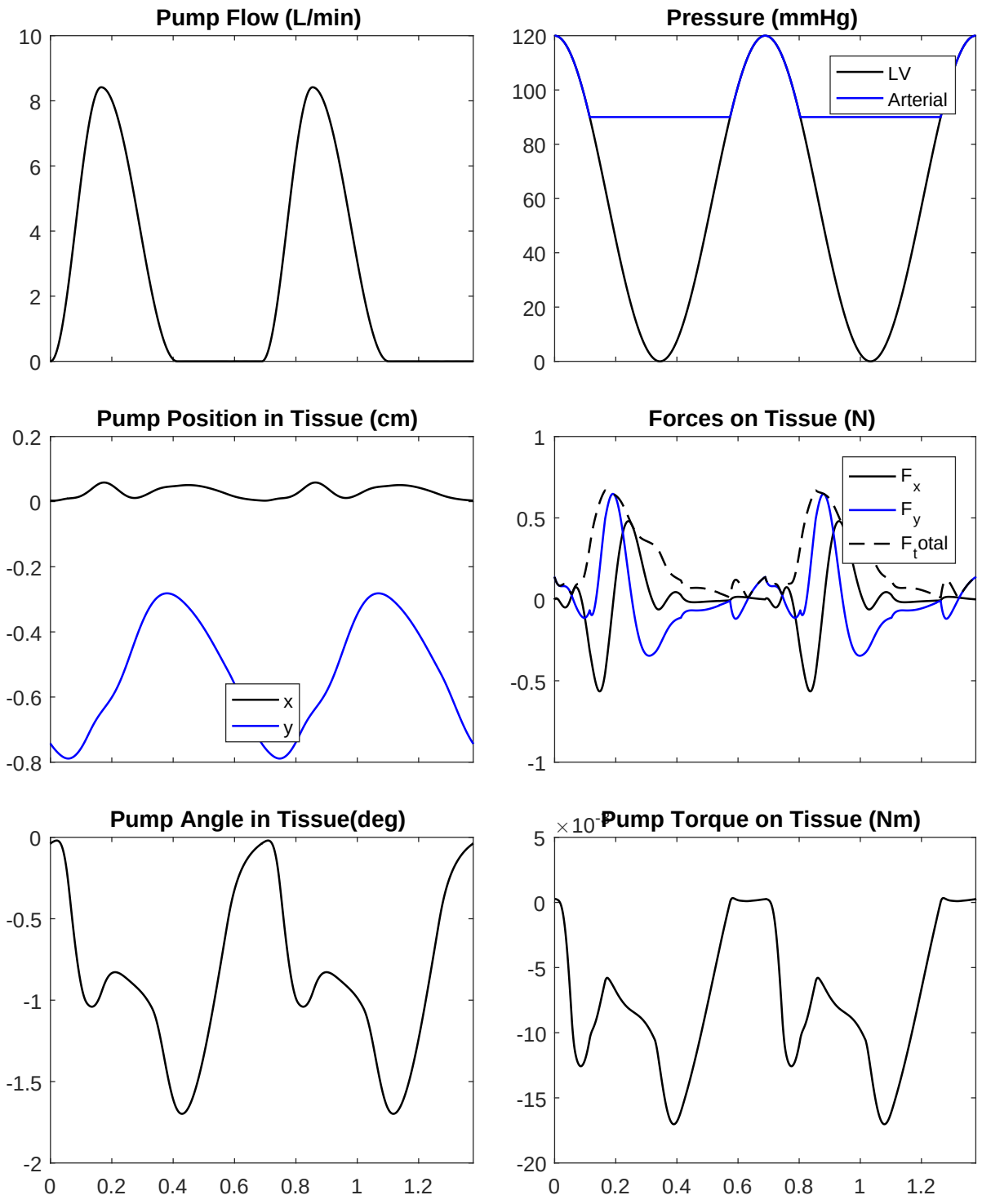

Figure A.8: Pump motion in and forces on surrounding tissue at 2.7 L/min counterpulse support

A.2 Future Direction

These are preliminary results and analysis that provide predictions of the forces that can be expected on the surrounding tissue from a 2PTP device. More work could be done to refine the tissue model. Problematic levels of force or motion should also be studied to assess whether the eccentric masses are a problem. Results should also be compared to other blood pumps such as continuous flow devices or first-generation sac-type pulsatile VADs.

Appendix B

General Solution for Lagrange Subsystem With Conservative Exogenous Efforts

Depending on where systems are reticulated or where control volumes are defined, some Lagrange subsystem problems may have exogenous efforts $\mathbf{E_e}$ that have non-conservative as well as conservative components. Of particular interest in this research is accounting for fluid pressure and momentum forces that exert forces on a control volume, which are functions not only of dependent displacements $\mathbf{x}$ and flow variables $\dot{\mathbf{x}}$, but also on coupled inertial terms that are functions of $\ddot{\mathbf{x}}$. For this analysis, exogenous forces that are functions of $\mathbf{x}$ or $\dot{\mathbf{x}}$ may be nonlinear as they are in the standard approach for Lagrange subsystem analysis, but the conditional will be made that the exogenous efforts $\mathbf{E_e}$ that are functions of $\ddot{\mathbf{x}}$ must be linear. The reason for this will become clear later.

$$\mathbf{E_e} = \mathbf{F}(\dot{\mathbf{x}}, \ddot{\mathbf{x}}) + \mathbf{G}\ddot{\mathbf{x}} \tag{B.1}$$

A bond graph in vectorized form for such a Lagrnage subsystem is shown below.

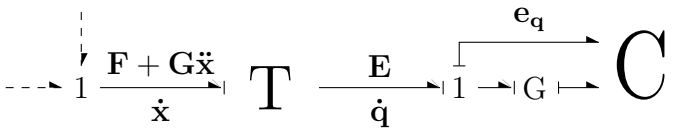

Figure B.1: Vectorized bond graph of a Lagrange subsystem

For such a system, the following analysis can be used.

Lagrange Transformer

First, the Lagrange transformer converts dependent flows $\dot{\mathbf{x}}$ $(n \times 1)$ to independent flows $\dot{\mathbf{q}}$ $(m \times 1)$ with the transformation matrix $\mathbf{T}(\mathbf{q})$

$$\dot{\mathbf{x}} = \mathbf{T}(\mathbf{q})\dot{\mathbf{q}} \tag{B.2}$$

where $\mathbf{T} = \mathbf{T}(\mathbf{q})$ is the transformation matrix with size $(n \times m)$.

Kinetic Energy

Next, the kinetic energy $\mathbf{K}$ of the Lagrange subsystem is a scalar function that can be expressed as a quadratic of $\dot{\mathbf{x}}$ using a mass matrix $\mathbf{M}$.

$$\mathbf{K} = \frac{1}{2}\dot{\mathbf{x}}^{\mathbf{T}}\mathbf{M}\dot{\mathbf{x}} \tag{B.3}$$

where $\mathbf{M} = \mathbf{M}(\mathbf{x})$ is the mass matrix with size $(n \times n)$.

Next, the relationship $\dot{\mathbf{x}} = \mathbf{T}\dot{\mathbf{q}}$ can be used to convert the kinetic energy to a quadratic of $\dot{\mathbf{q}}$.

$$\hat{\mathbf{K}} = \frac{1}{2}\dot{\mathbf{q}}^{\mathbf{T}}(\mathbf{T}^{\mathbf{T}}\mathbf{M}\mathbf{T})\dot{\mathbf{q}}$$

where $\hat{\mathbf{K}}$ is the transformed scalar function as a function of $\mathbf{q}$. The hat is used to specify a *transformed* vector or array. The expression is simplified by defining a transformed mass matrix.

$$\hat{\mathbf{K}} = \frac{1}{2}\dot{\mathbf{q}}^{\mathbf{T}}\hat{\mathbf{M}}\dot{\mathbf{q}} \tag{B.4}$$

where $\hat{\mathbf{M}} = \mathbf{T}^{\mathbf{T}}\mathbf{M}\mathbf{T}$ is the transformed mass matrix with size $(m \times m)$.

Generalized Momentum

The generalized momentum variables $\mathbf{p}$ of the Lagrange subsystem are found by taking the partial derivative of the transformed kinetic energy $\hat{\mathbf{K}}$ with respect to independent flows $\dot{\mathbf{q}}$.

$$\mathbf{p} = \frac{\partial \hat{\mathbf{K}}}{\partial \dot{\mathbf{q}}} \tag{B.5}$$

$$\mathbf{p} = \frac{\partial}{\partial \dot{\mathbf{q}}}\left(\frac{1}{2}\dot{\mathbf{q}}^{\mathbf{T}}\hat{\mathbf{M}}\dot{\mathbf{q}}\right)$$

$$\mathbf{p} = \hat{\mathbf{M}}\dot{\mathbf{q}} \tag{B.6}$$

when $\hat{\mathbf{M}}$ is symmetric and independent of $\dot{\mathbf{q}}$.

The generalized displacement state equations are found by inverting the transformed mass matrix $\hat{\mathbf{M}}$

$$\dot{\mathbf{q}} = \hat{\mathbf{M}}^{-\mathbf{1}}\mathbf{p} \tag{B.7}$$

Potential Energy

The potential energy $\mathbf{U}$ in the subsystem can be expressed as a scalar function of $\mathbf{x}$ and then converted to a function of $\mathbf{q}$

$$\mathbf{U} = \mathbf{U}(\mathbf{x}) \qquad \rightarrow \qquad \hat{\mathbf{U}} = \hat{\mathbf{U}}(\mathbf{q}) \tag{B.8}$$

where $\hat{\mathbf{U}}$ is the transformed scalar function of $\mathbf{q}$.

Conservative Efforts

Next, the generalized conservative efforts of the Lagrange subsystem can be found by taking the partial of the Hamiltonian with respect to each displacement variable q_i

$$e_{q_i} = \frac{\partial \hat{\mathbf{U}}}{\partial q_i} - \frac{\partial \hat{\mathbf{K}}}{\partial q_i}$$

This can also be expressed using the gradient of the scalar Hamiltonian with respect to the displacement vector $\mathbf{q}$

$$\mathbf{e_q} = \nabla_{\mathbf{q}} \left(\hat{\mathbf{U}} - \hat{\mathbf{K}} \right) \tag{B.9}$$

Exogenous Efforts

Exogenous efforts (which may be conservative and non-conservative in this case) - those from sources or coupled inertia external to the Lagrange subsystem - can be expressed in terms of the depdendent displacements, flows and accelerations ($\mathbf{x}$, $\dot{\mathbf{x}}$ and $\ddot{\mathbf{x}}$).

$$\dot{\mathbf{x}}^{\mathbf{T}} \mathbf{E_e} = \dot{\mathbf{q}}^{\mathbf{T}} \mathbf{E}$$

$$\dot{\mathbf{x}}^{\mathbf{T}} (\mathbf{F} + \mathbf{G}\ddot{\mathbf{x}}) = \dot{\mathbf{q}}^{\mathbf{T}} \mathbf{E} \tag{B.10}$$

where $\mathbf{F} = \mathbf{F}(\mathbf{x}, \dot{\mathbf{x}})$ and $\mathbf{G} = \mathbf{G}(\mathbf{x})$ can be transformed to $\hat{\mathbf{F}} = \hat{\mathbf{F}}(\mathbf{q}, \dot{\mathbf{q}})$ and $\hat{\mathbf{G}} = \hat{\mathbf{G}}(\mathbf{q})$

This formulation allows nonlinear function of $\mathbf{x}$ and $\dot{\mathbf{x}}$, but only linear formulations of the $\ddot{\mathbf{x}}$. The acceleration term $\ddot{\mathbf{x}}$ of the exogenous variables will need to be converted to the subsystem variables by taking the derivative of the generalized displacement state equations

$$\ddot{\mathbf{x}} = \frac{\partial}{\partial t}\dot{\mathbf{x}} = \frac{\partial}{\partial t}(\mathbf{T}\dot{\mathbf{q}}) = \mathbf{T}\ddot{\mathbf{q}} + \dot{\mathbf{T}}\dot{\mathbf{q}}$$

which is substituted into the power flow equation B.10,

$$\dot{\mathbf{q}}^{\mathbf{T}}\mathbf{T}^{\mathbf{T}}\left[\hat{\mathbf{F}}+\hat{\mathbf{G}}\left(\mathbf{T}\ddot{\mathbf{q}}+\dot{\mathbf{T}}\dot{\mathbf{q}}\right)\right]=\dot{\mathbf{q}}^{\mathbf{T}}\mathbf{E}$$

The transformed exogenous efforts $\mathbf{E}$ can then be expressed in terms of independent flow and acceleration

$$\mathbf{E}=\mathbf{T}^{\mathbf{T}}\left(\hat{\mathbf{F}}+\hat{\mathbf{G}}\mathbf{T}\ddot{\mathbf{q}}+\hat{\mathbf{G}}\dot{\mathbf{T}}\dot{\mathbf{q}}\right) \tag{B.11}$$

These terms ($\dot{\mathbf{q}}$ and $\ddot{\mathbf{q}}$) need to be expressed in terms of the generalized momenta state $\mathbf{p}$. From equation B.7, the expression for $\dot{\mathbf{q}}$ is known. To obtain $\ddot{\mathbf{q}}$, equation B.7 can be differentiated to get

$$\ddot{\mathbf{q}}=\frac{\partial}{\partial t}\dot{\mathbf{q}}=\frac{\partial}{\partial t}\left(\hat{\mathbf{M}}^{-\mathbf{1}}\mathbf{p}\right)=\hat{\mathbf{M}}^{-\mathbf{1}}\dot{\mathbf{p}}+\frac{\partial\hat{\mathbf{M}}^{-\mathbf{1}}}{\partial\mathbf{t}}\mathbf{p}=\hat{\mathbf{M}}^{-\mathbf{1}}\dot{\mathbf{p}}-\hat{\mathbf{M}}^{-\mathbf{1}}\dot{\hat{\mathbf{M}}}\hat{\mathbf{M}}^{-\mathbf{1}}\mathbf{p} \tag{B.12}$$

These are substituted into the transformed exogenous effort equation above to obtain the expression for the transformed exogenous effort as a function of the generalized momenta $\mathbf{p}$ and $\dot{\mathbf{p}}$.

$$\mathbf{E}=\mathbf{T}^{\mathbf{T}}\left[\hat{\mathbf{F}}+\hat{\mathbf{G}}\mathbf{T}\left(\hat{\mathbf{M}}^{-\mathbf{1}}\dot{\mathbf{p}}-\hat{\mathbf{M}}^{-\mathbf{1}}\dot{\hat{\mathbf{M}}}\hat{\mathbf{M}}^{-\mathbf{1}}\mathbf{p}\right)+\hat{\mathbf{G}}\dot{\mathbf{T}}\hat{\mathbf{M}}^{-\mathbf{1}}\mathbf{p}\right] \tag{B.13}$$

Generalized Momenta

The generalized momenta can be expressed as a function of the conservative subsystem efforts $\mathbf{e_q}$ and the transformed exogenous efforts $\mathbf{E}$

$$\dot{\mathbf{p}}=-\mathbf{e_q}+\mathbf{E} \tag{B.14}$$

Equations B.9 and B.13 can be substituted to obtain

$$\dot{\mathbf{p}}=-\nabla_{\mathbf{q}}\left(\hat{\mathbf{U}}-\hat{\mathbf{K}}\right)+\mathbf{T}^{\mathbf{T}}\left[\hat{\mathbf{F}}+\hat{\mathbf{G}}\mathbf{T}\left(\hat{\mathbf{M}}^{-\mathbf{1}}\dot{\mathbf{p}}-\hat{\mathbf{M}}^{-\mathbf{1}}\dot{\hat{\mathbf{M}}}\hat{\mathbf{M}}^{-\mathbf{1}}\mathbf{p}\right)+\hat{\mathbf{G}}\dot{\mathbf{T}}\hat{\mathbf{M}}^{-\mathbf{1}}\mathbf{p}\right] \tag{B.15}$$

The terms for the momenta derivatives are collected from both sides of the equation to get the state equations

$$\dot{\mathbf{p}}=\frac{\nabla_{\mathbf{q}}\left(\hat{\mathbf{U}}-\hat{\mathbf{K}}\right)+\mathbf{T}^{\mathbf{T}}\hat{\mathbf{F}}-\mathbf{T}^{\mathbf{T}}\hat{\mathbf{G}}\mathbf{T}\hat{\mathbf{M}}^{-\mathbf{1}}\dot{\hat{\mathbf{M}}}\hat{\mathbf{M}}^{-\mathbf{1}}\mathbf{p}+\mathbf{T}^{\mathbf{T}}\hat{\mathbf{G}}\dot{\mathbf{T}}\hat{\mathbf{M}}^{-\mathbf{1}}\mathbf{p}}{\mathbf{I}-\mathbf{T}^{\mathbf{T}}\hat{\mathbf{G}}\mathbf{T}\hat{\mathbf{M}}^{-\mathbf{1}}} \tag{B.16}$$

State Equations

In summary, the generalized displacement and momentum state equations are

$$\dot{\mathbf{q}} = \hat{\mathbf{M}}^{-1}\mathbf{p}$$

$$\dot{\mathbf{p}} = \frac{\nabla_{\mathbf{q}}\left(\hat{\mathbf{U}} - \hat{\mathbf{K}}\right) + \mathbf{T}^{\mathbf{T}}\hat{\mathbf{F}} - \mathbf{T}^{\mathbf{T}}\hat{\mathbf{G}}\mathbf{T}\hat{\mathbf{M}}^{-1}\dot{\hat{\mathbf{M}}}\hat{\mathbf{M}}^{-1}\mathbf{p} + \mathbf{T}^{\mathbf{T}}\hat{\mathbf{G}}\dot{\mathbf{T}}\hat{\mathbf{M}}^{-1}\mathbf{p}}{\mathbf{I} - \mathbf{T}^{\mathbf{T}}\hat{\mathbf{G}}\mathbf{T}\hat{\mathbf{M}}^{-1}}$$

Vectors and Matrix Definitions

$\dot{\mathbf{x}}$	$(n \times 1)$	Dependent flows
$\dot{\mathbf{q}}$	$(m \times 1)$	Independent flows
$\mathbf{T}$	$(n \times m)$	Transformation matrix ($\dot{\mathbf{x}} = \mathbf{T}\dot{\mathbf{q}}$)
$\dot{\mathbf{T}}$	$(n \times m)$	Transformation matrix time derivative
$\mathbf{T}$	$(n \times m)$	Transformation matrix ($\dot{\mathbf{x}} = \mathbf{T}\dot{\mathbf{q}}$)
$\mathbf{F}$	$(n \times 1)$	Exogenous efforts as a function of $\mathbf{x}$ and $\dot{\mathbf{x}}$
$\mathbf{E}$	$(m \times 1)$	Transformed exogenous efforts as a function of $\mathbf{q}$ and $\dot{\mathbf{q}}$
$\mathbf{e_q}$	$(m \times 1)$	Conservative subsystem efforts
$\hat{\mathbf{M}}$	$(m \times m)$	Transformed mass matrix ($\hat{\mathbf{M}} = \mathbf{T}^{\mathbf{T}}\mathbf{M}\mathbf{T}$)
$\dot{\hat{\mathbf{M}}}$	$(m \times m)$	Time derivative of the transformed mass matrix
$\mathbf{M}$	$(n \times n)$	Mass matrix
$\hat{\mathbf{K}}$	$(scalar)$	Kinetic energy scalar as a function of $\mathbf{q}$
$\hat{\mathbf{U}}$	$(scalar)$	Potential energy scalar as a function of $\mathbf{q}$
$\hat{\mathbf{F}}$	$(n \times 1)$	Non-conservative efforts as a function of $\mathbf{q}$ and $\dot{\mathbf{q}}$
$\hat{\mathbf{G}}$	$(n \times n)$	Non-conservative effort linear coefficients of $\ddot{\mathbf{q}}$

Solution Procedure

1. Define the transformation matrix $\mathbf{T}$ and take the time derivative $\dot{\mathbf{T}}$
2. Determine the mass matrix $\mathbf{M}$ for the kinetic energy, transform the mass matrix $\hat{\mathbf{M}} = \mathbf{T}^{\mathbf{T}}\mathbf{M}\mathbf{T}$ and take the time derivative $\dot{\hat{\mathbf{M}}}$
3. Express the kinetic energy $\hat{\mathbf{K}}$ as a function of independent variables $\dot{\mathbf{q}}$ and $\mathbf{q}$
4. Express the potential energy $\hat{\mathbf{U}}$ as a function of independent displacements $\mathbf{q}$
5. Define the generalized conservative effort $\mathbf{e_q}$ of the Lagrange subsystem
6. Define the exogenous effort nonlinear $\hat{\mathbf{F}}(\mathbf{q}, \dot{\mathbf{q}})$ and exogenous mass matrix $\hat{\mathbf{G}}$
7. Obtain state equations
8. Solve differential equations (most matrices will need to be recomputed each timestep).

Appendix C

Hybrid Model State Equations

This Appendix displays the bond graph for all 30 of the possible modes, and derives the state equations using the algorithmic procedure outlined in Section 7.5. In brief, the procedure is:

Determine if there are any coupled flows (A, B, C, or D), then for each flow:

1. Identify the first external bond in the counter-clockwise direction (for convenience, CC-bond) and the first external bond in the clockwise direction (CW-bond).
2. The differential equation for each flow will take the same form:

$$\dot{Q}_n = \left[\hat{p}\Delta P - R_n Q_n + R_{cc} Q_{cc} - R_{cw} Q_{cw}\right]/L_n \tag{C.1}$$

   where n is the flow (A, B, C, D, or S), $\hat{p}$ is either 1, -1, or 0 depending on the CC and CW bonds, R_n is the viscous torus resistance, L_n is the inertia in the torus, $R_{cc}Q_{cc}$ is the pressure from the inflow or outflow resistance at the CC-node, and $R_{cw}Q_{cw}$ is the pressure from the inflow or outflow resistance at the CW-node.
3. Determine $\hat{p}$
   3.1. $\hat{p} = 1$ if CC-node connects to outflow and CW-node connects to inflow.
   3.2. $\hat{p} = -1$ if CC-node connects to inflow and CW-node connects to outflow.
   3.3. $\hat{p} = 0$ if CC-node and CW-node connected to the same port.
4. Calculate the resistance R_n and inertance L_n, which are functions of the control volume for n plus any coupled control volume. For example, if A and B are coupled, then $R_A = R_B = R(V_A + V_B)$ and $L_A = L_B = L(V_A + V_B)$.
5. Identify the CC-node pressure from resistance $R_{cc}Q_{cc}$ and $R_{cw}Q_{cw}$. The resistances are functions of the partial occlusion leakage swept angle or port area of the inflow and outflow. And the flows are functions of state.

When there is no algebraic loop, the flows in and out of the pump are easily determined and can be expressed as a function of the state flow by summing the flows at the zero junctions.

$$
\begin{aligned}
Q_{i2} &= Q_C - Q_B & Q_{o2} &= Q_D - Q_A \\
Q_{i1} &= Q_A - Q_D & Q_{o1} &= Q_B - Q_C \\
Q_{iA} &= Q_B - Q_A & Q_{iB} &= Q_B - Q_A & Q_{iC} &= Q_D - Q_C & Q_{iD} &= Q_D - Q_C \\
Q_{oA} &= Q_A - Q_B & Q_{oB} &= Q_A - Q_B & Q_{oC} &= Q_C - Q_D & Q_{oD} &= Q_C - Q_D
\end{aligned}
$$

When the is an algebraic loop, the flows can still be analytically expressed as a function of the flow states because the leakage partial occlusion leakage resistance is linear.

$$
\begin{aligned}
\tilde{Q}_{iA} &= \frac{(1 - r_{iB})\, Ar\omega_{p1} - Q_A + r_{iB} Q_B}{(1 + R_{iA}/R_{\max})\,(1 - r_{iA} r_{iB})} & \tilde{Q}_{oA} &= -\frac{(1 - r_{oB})\, Ar\omega_{p1} - Q_A + r_{oB} Q_B}{(1 + R_{oA}/R_{\max})\,(1 - r_{oA} r_{oB})} \\
\tilde{Q}_{iB} &= \frac{(r_{iA} - 1)\, Ar\omega_{p1} + Q_B - r_{iA} Q_A}{(1 + R_{iB}/R_{\max})\,(1 - r_{iA} r_{iB})} & \tilde{Q}_{oB} &= -\frac{(r_{oA} - 1)\, Ar\omega_{p1} + Q_B - r_{oA} Q_A}{(1 + R_{oB}/R_{\max})\,(1 - r_{oA} r_{oB})} \\
\tilde{Q}_{iC} &= \frac{(1 - r_{iD})\, Ar\omega_{p2} - Q_C + r_{iD} Q_D}{(1 + R_{iC}/R_{\max})\,(1 - r_{iC} r_{iD})} & \tilde{Q}_{oC} &= -\frac{(1 - r_{oD})\, Ar\omega_{p2} - Q_C + r_{oD} Q_D}{(1 + R_{oC}/R_{\max})\,(1 - r_{oC} r_{oD})} \\
\tilde{Q}_{iD} &= \frac{(r_{iC} - 1)\, Ar\omega_{p2} + Q_D - r_{iC} Q_C}{(1 + R_{iD}/R_{\max})\,(1 - r_{iC} r_{iD})} & \tilde{Q}_{oD} &= -\frac{(r_{oC} - 1)\, Ar\omega_{p2} + Q_D - r_{oC} Q_C}{(1 + R_{oD}/R_{\max})\,(1 - r_{oC} r_{oD})}
\end{aligned}
$$

where r is the ratio below, which goes from 0 when the leakage resistance is zero (no piston overlap) to 1/2 at full occlusion.

$$r_{cc} = \frac{R_{cc}/R_{\max}}{1 + R_{cc}/R_{\max}}$$

for motor and piston 1:

$$\dot{\omega}_{m1} = \frac{1}{J_m}\left[\frac{V_{\text{in}} k_e - k_e^2 \omega_{m1}}{R} - b_m \omega_{m1} - T_{\max} \sin\left(2\pi \frac{\theta_{m1} - \theta_{p1}}{4 \cdot \theta_{\text{e}}}\right)\right] \tag{C.2}$$

$$\dot{\omega}_{p1} = \frac{1}{J_p}\left[T_{\max} \sin\left(2\pi \frac{\theta_{m1} - \theta_{p1}}{4 \cdot \theta_{\text{e}}}\right) - b_p \omega_{p1} - T_{p1}\right] \tag{C.3}$$

$$\dot{\theta}_{m1} = \omega_{m1} \tag{C.4}$$

$$\dot{\theta}_{p1} = \omega_{p1} \tag{C.5}$$

And motor and piston 2:

$$\dot{\omega}_{m2} = \frac{1}{J_m}\left[\frac{V_{2,\text{in}} k_e - k_e^2 \omega_{m1}}{R} - b_m \omega_{m2} - T_{\max} \sin\left(2\pi \frac{\theta_{m2} - \theta_{p2}}{4 \cdot \theta_{\text{e}}}\right)\right] \tag{C.6}$$

$$\dot{\omega}_{p2} = \frac{1}{J_p}\left[T_{\max}\sin\left(2\pi\frac{\theta_{m2}-\theta_{p2}}{4\cdot\theta_{\mathrm{e}}}\right) - b_p\omega_{p2} - T_{p2}\right] \tag{C.7}$$

$$\dot{\theta}_{m2} = \omega_{m2} \tag{C.8}$$

$$\dot{\theta}_{p2} = \omega_{p2} \tag{C.9}$$

The torques on the piston $Tp1$ and T_{p2} can be expressed as functions of the flow states, the expression of which depends on the piston location:

$$T_{p1} = \begin{cases} Ar\left(R_{iA}\tilde{Q}_{iA} - R_{iB}\tilde{Q}_{iB}\right) & \text{occluding inflow port} \\ Ar\left(R_{oB}\tilde{Q}_{oB} - R_{oA}\tilde{Q}_{oA}\right) & \text{occluding outflow port} \\ ArR_L\left(Ar\omega_{p1} - Q_B\right) & \text{for Piston 1} \quad \text{leading face in inflow or outflow port} \\ ArR_L\left(Ar\omega_{p1} - Q_A\right) & \text{trailing face in inflow or outflow port} \\ ArR_L\left(Ar\omega_{p1} - Q_{A=B}\right) & \text{in drive position} \end{cases}$$

$$T_{p2} = \begin{cases} Ar\left(R_{iC}\tilde{Q}_{iC} - R_{iD}\tilde{Q}_{iD}\right) & \text{occluding inflow port} \\ Ar\left(R_{oD}\tilde{Q}_{oD} - R_{oC}\tilde{Q}_{oC}\right) & \text{occluding outflow port} \\ ArR_L\left(Ar\omega_{p2} - Q_D\right) & \text{for Piston 2} \quad \text{leading face in inflow or outflow port} \\ ArR_L\left(Ar\omega_{p2} - Q_C\right) & \text{trailing face in inflow or outflow port} \\ ArR_L\left(Ar\omega_{p2} - Q_{C=D}\right) & \text{in drive position} \end{cases}$$

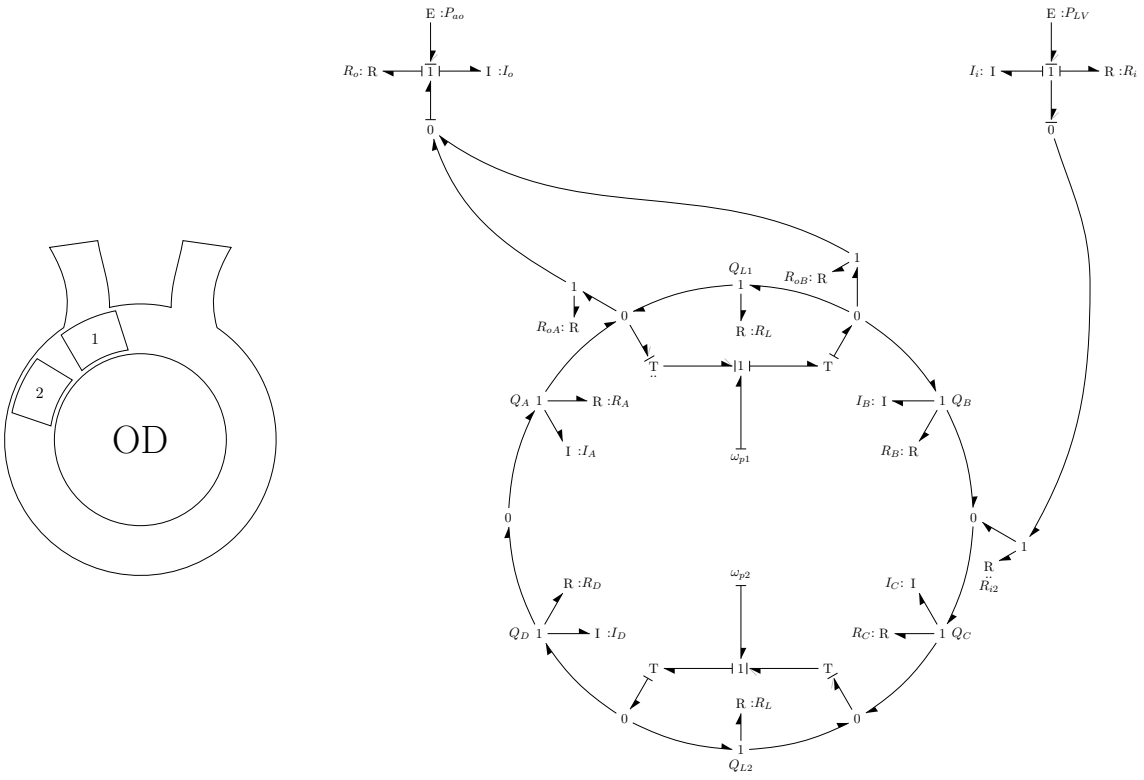

A-C-D coupled ($Q_A = Q_C = Q_D$)

$$\dot{Q}_A = \big[-\Delta P - (R_A + R_C + R_D)Q_A + R_L(Ar\omega_2 - Q_A) - R_{i2}Q_{i2}\,|Q_{i2}| - R_{oA}\tilde{Q}_{oA}\big]/(I_A + I_C + I_D)$$

$$\dot{Q}_B = \big[\Delta P - R_B Q_B + R_{oB}\tilde{Q}_{oB} + R_{i2}Q_{i2}\,|Q_{i2}|\,\big]/I_B$$

$$\dot{Q}_C = \big[-\Delta P - (R_A + R_C + R_D)Q_C + R_L(Ar\omega_2 - Q_C) - R_{i2}Q_{i2}\,|Q_{i2}| - R_{oA}\tilde{Q}_{oA}\big]/(I_A + I_C + I_D)$$

$$\dot{Q}_D = \big[-\Delta P - (R_A + R_C + R_D)Q_D + R_L(Ar\omega_2 - Q_D) - R_{i2}Q_{i2}\,|Q_{i2}| - R_{oA}\tilde{Q}_{oA}\big]/(I_A + I_C + I_D)$$

$$\dot{Q}_S = 0$$

$$\Delta P = P_{LV} - P_{ao} + I_{io}\left(\dot{Q}_{ACD} - \dot{Q}_B\right) + R_{io}\left(Q_{ACD} - Q_B\right)$$

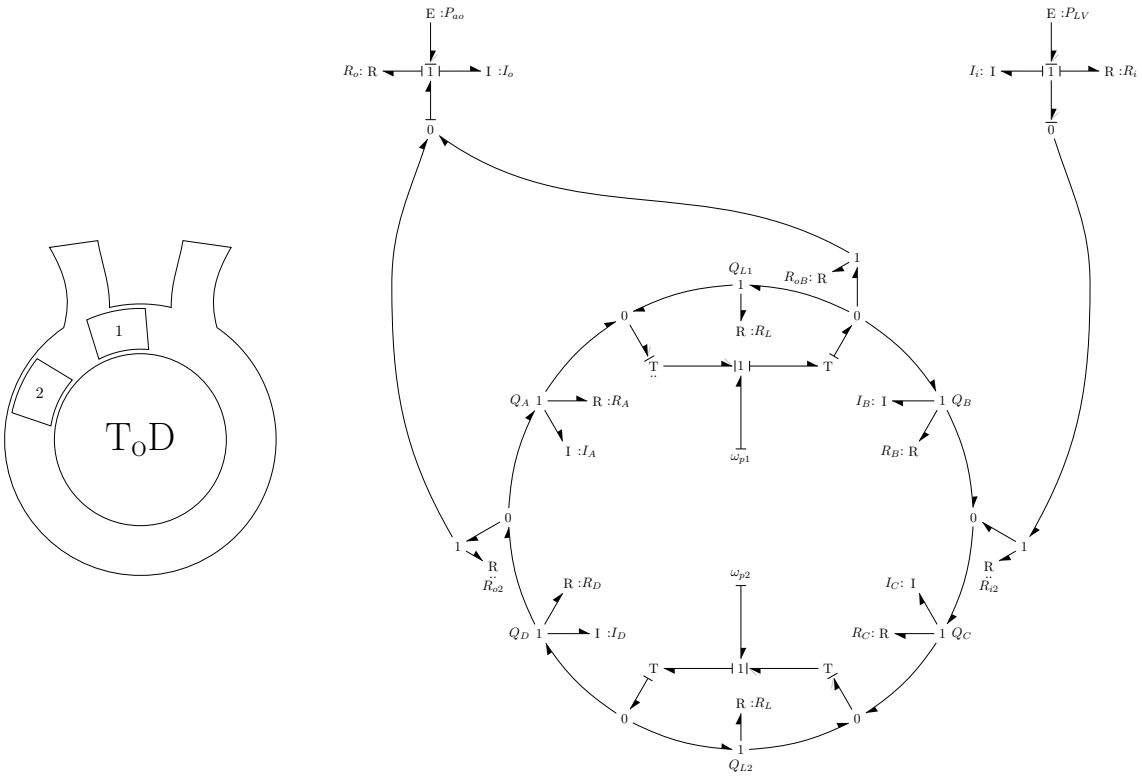

C-D coupled ($Q_C = Q_D$)

$$\dot{Q}_A = \big[- R_A Q_A + R_L(Ar\omega_1 - Q_A) + R_{o2} Q_{o2} \left| Q_{o2} \right| - R_{oB} Q_{oB} \big] / I_A$$

$$\dot{Q}_B = \big[\Delta P - R_B Q_B + R_{oB} Q_{oB} + R_{i2} Q_{i2} \left| Q_{i2} \right| \big] / I_B$$

$$\dot{Q}_C = \big[- \Delta P - (R_C + R_D) Q_C + R_L(Ar\omega_2 - Q_C) - R_{i2} Q_{i2} \left| Q_{i2} \right| - R_{o2} Q_{o2} \left| Q_{o2} \right| \big] / (I_C + I_D)$$

$$\dot{Q}_D = \big[- \Delta P - (R_C + R_D) Q_D + R_L(Ar\omega_2 - Q_D) - R_{i2} Q_{i2} \left| Q_{i2} \right| - R_{o2} Q_{o2} \left| Q_{o2} \right| \big] / (I_C + I_D)$$

$$\dot{Q}_S = 0$$

$$\Delta P = P_{LV} - P_{ao} + I_{io} \left(\dot{Q}_{CD} - \dot{Q}_B \right) + R_{io} \left(Q_{CD} - Q_B \right)$$

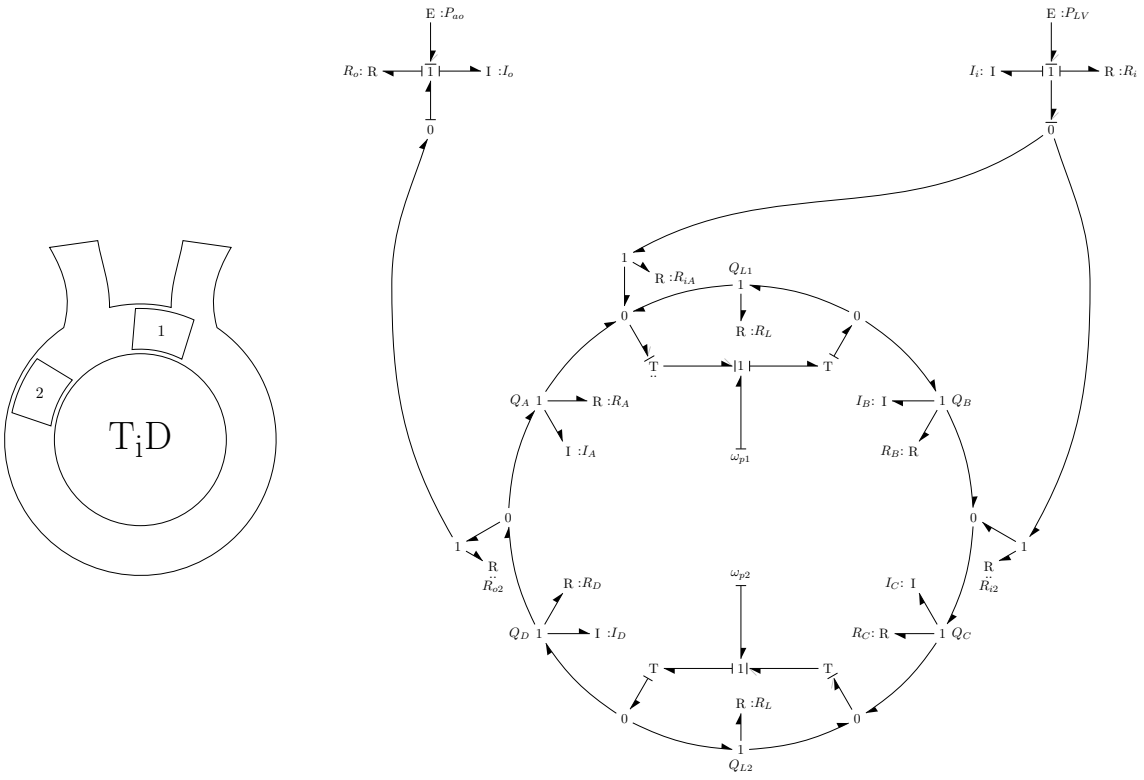

C-D coupled ($Q_C = Q_D$)

$$\dot{Q}_A = \left[\Delta P - R_A Q_A + R_{o2} Q_{o2} \left|Q_{o2}\right| + R_{iA} Q_{iA}\right] / I_A$$

$$\dot{Q}_B = \left[- R_B Q_B + R_L (Ar\omega_1 - Q_B) + R_{iA} Q_{iA} + R_{i2} Q_{i2} \left|Q_{i2}\right| \right] / I_B$$

$$\dot{Q}_C = \left[- \Delta P - (R_C + R_D) Q_C + R_L (Ar\omega_2 - Q_C) - R_{i2} Q_{i2} \left|Q_{i2}\right| - R_{o2} Q_{o2} \left|Q_{o2}\right| \right] / (I_C + I_D)$$

$$\dot{Q}_D = \left[- \Delta P - (R_C + R_D) Q_D + R_L (Ar\omega_2 - Q_D) - R_{i2} Q_{i2} \left|Q_{i2}\right| - R_{o2} Q_{o2} \left|Q_{o2}\right| \right] / (I_C + I_D)$$

$$\dot{Q}_S = 0$$

$$\Delta P = P_{LV} - P_{ao} + I_{io} \left(\dot{Q}_{CD} - \dot{Q}_A \right) + R_{io} \left(Q_{CD} - Q_A \right)$$

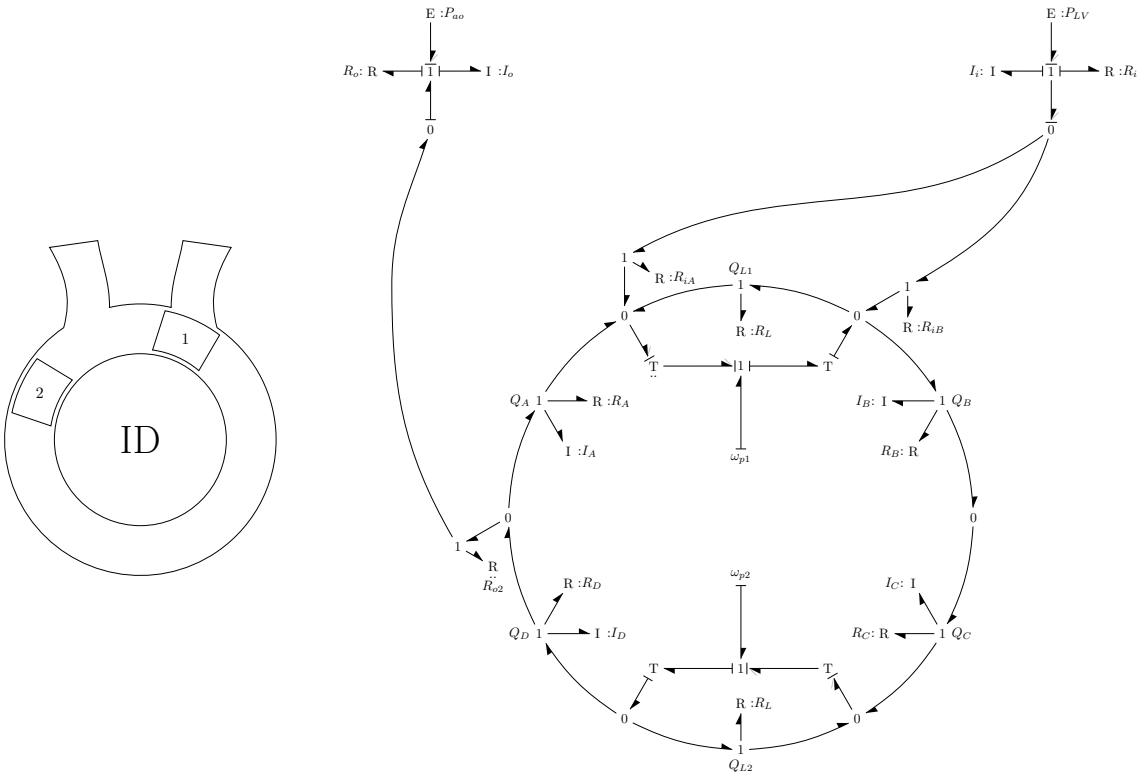

B-C-D coupled ($Q_B = Q_C = Q_D$)

$$\dot{Q}_A = \left[\Delta P - R_A Q_A + R_{o2} Q_{o2} \left|Q_{o2}\right| + R_{iA} \tilde{Q}_{iA}\right] / I_A$$

$$\dot{Q}_B = \left[- \Delta P - (R_B + R_C + R_D) Q_B + R_L (A r \omega_2 - Q_B) - R_{iB} \tilde{Q}_{iB} - R_{o2} Q_{o2} \left|Q_{o2}\right| \right] / (I_B + I_C + I_D)$$

$$\dot{Q}_C = \left[- \Delta P - (R_B + R_C + R_D) Q_C + R_L (A r \omega_2 - Q_C) - R_{iB} \tilde{Q}_{iB} - R_{o2} Q_{o2} \left|Q_{o2}\right| \right] / (I_B + I_C + I_D)$$

$$\dot{Q}_D = \left[- \Delta P - (R_B + R_C + R_D) Q_D + R_L (A r \omega_2 - Q_D) - R_{iB} \tilde{Q}_{iB} - R_{o2} Q_{o2} \left|Q_{o2}\right| \right] / (I_B + I_C + I_D)$$

$$\dot{Q}_S = 0$$

$$\Delta P = P_{LV} - P_{ao} + I_{io} \left(\dot{Q}_{BCD} - \dot{Q}_A \right) + R_{io} \left(Q_{BCD} - Q_A \right)$$

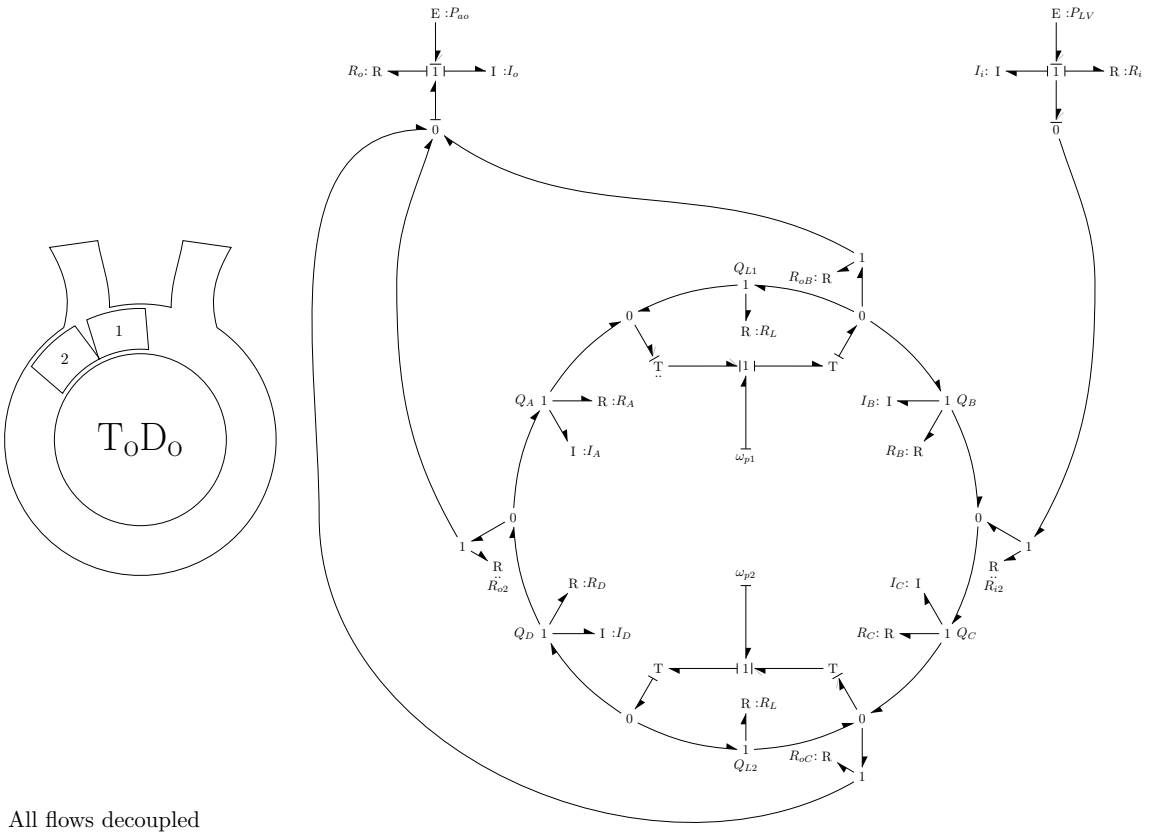

All flows decoupled

$$\dot{Q}_A = \big[- R_A Q_A + R_L(Ar\omega_1 - Q_A) + R_{o2} Q_{o2} \left| Q_{o2} \right| - R_{oB} Q_{oB} \big] / I_A$$

$$\dot{Q}_B = \big[\Delta P - R_B Q_B + R_{oB} Q_{oB} + R_{i2} Q_{i2} \left| Q_{i2} \right| \big] / I_B$$

$$\dot{Q}_C = \big[- \Delta P - R_C Q_C - R_{i2} Q_{i2} \left| Q_{i2} \right| - R_{oC} Q_{oC} \big] / I_C$$

$$\dot{Q}_D = \big[- R_D Q_D + R_L(Ar\omega_2 - Q_D) + R_{oC} Q_{oC} - R_{o2} Q_{o2} \left| Q_{o2} \right| \big] / I_D$$

$$\dot{Q}_S = 0$$

$$\Delta P = P_{LV} - P_{ao} + I_{io} \left(\dot{Q}_C - \dot{Q}_B \right) + R_{io} \left(Q_C - Q_B \right)$$

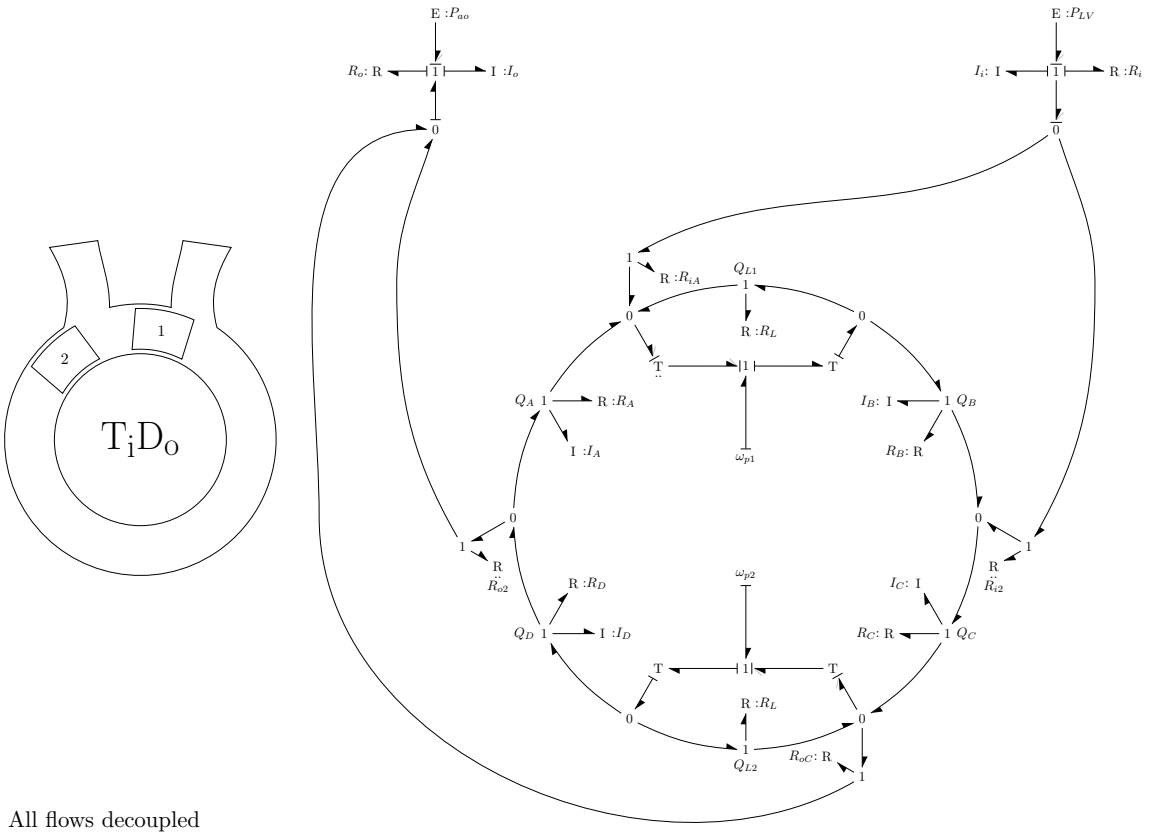

All flows decoupled

$$\dot{Q}_A = \left[\Delta P - R_A Q_A + R_{o2} Q_{o2} \left|Q_{o2}\right| + R_{iA} Q_{iA}\right] / I_A$$

$$\dot{Q}_B = \left[- R_B Q_B + R_L (Ar\omega_1 - Q_B) - R_{iA} Q_{iA} + R_{i2} Q_{i2} \left|Q_{i2}\right| \right] / I_B$$

$$\dot{Q}_C = \left[- \Delta P - R_C Q_C - R_{i2} Q_{i2} \left|Q_{i2}\right| - R_{oC} Q_{oC}\right] / I_C$$

$$\dot{Q}_D = \left[- R_D Q_D + R_L (Ar\omega_2 - Q_D) + R_{oC} Q_{oC} - R_{o2} Q_{o2} \left|Q_{o2}\right| \right] / I_D$$

$$\dot{Q}_S = 0$$

$$\Delta P = P_{LV} - P_{ao} + I_{io} \left(\dot{Q}_C - \dot{Q}_A\right) + R_{io} \left(Q_C - Q_A\right)$$

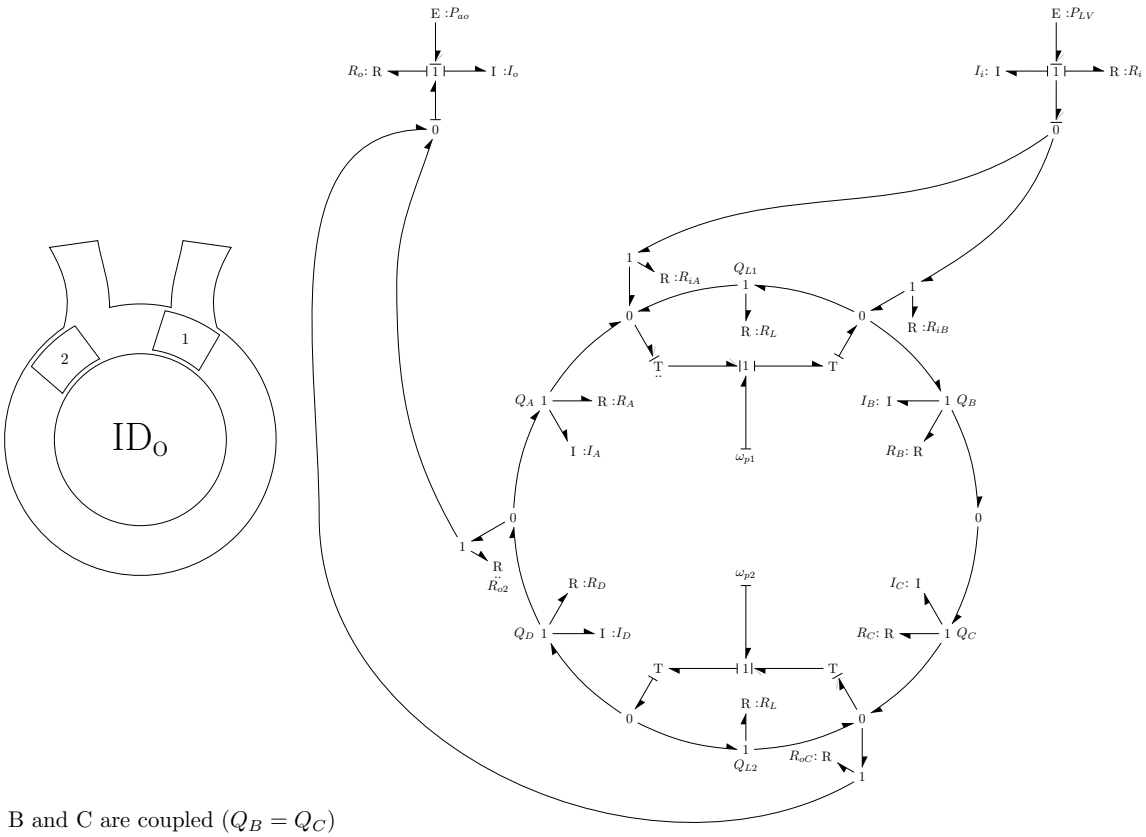

B and C are coupled ($Q_B = Q_C$)

$$\dot{Q}_A = \left[\Delta P - R_A Q_A + R_{o2} Q_{o2} \left|Q_{o2}\right| + R_{iA} \tilde{Q}_{iA}\right] / I_A$$

$$\dot{Q}_B = \left[- \Delta P - (R_B + R_C) Q_B - R_{iB} \tilde{Q}_{iB} - R_{oC} Q_{oC}\right] / (I_B + I_C)$$

$$\dot{Q}_C = \left[- \Delta P - (R_B + R_C) Q_C - R_{iB} \tilde{Q}_{iB} - R_{oC} Q_{oC}\right] / (I_B + I_C)$$

$$\dot{Q}_D = \left[- R_D Q_D + R_L (A r \omega_2 - Q_D) + R_{oC} Q_{oC} - R_{o2} Q_{o2} \left|Q_{o2}\right| \right] / I_D$$

$$\dot{Q}_S = 0$$

$$\Delta P = P_{LV} - P_{ao} + I_{io} \left(\dot{Q}_{BC} - \dot{Q}_A\right) + R_{io} \left(Q_{BC} - Q_A\right)$$

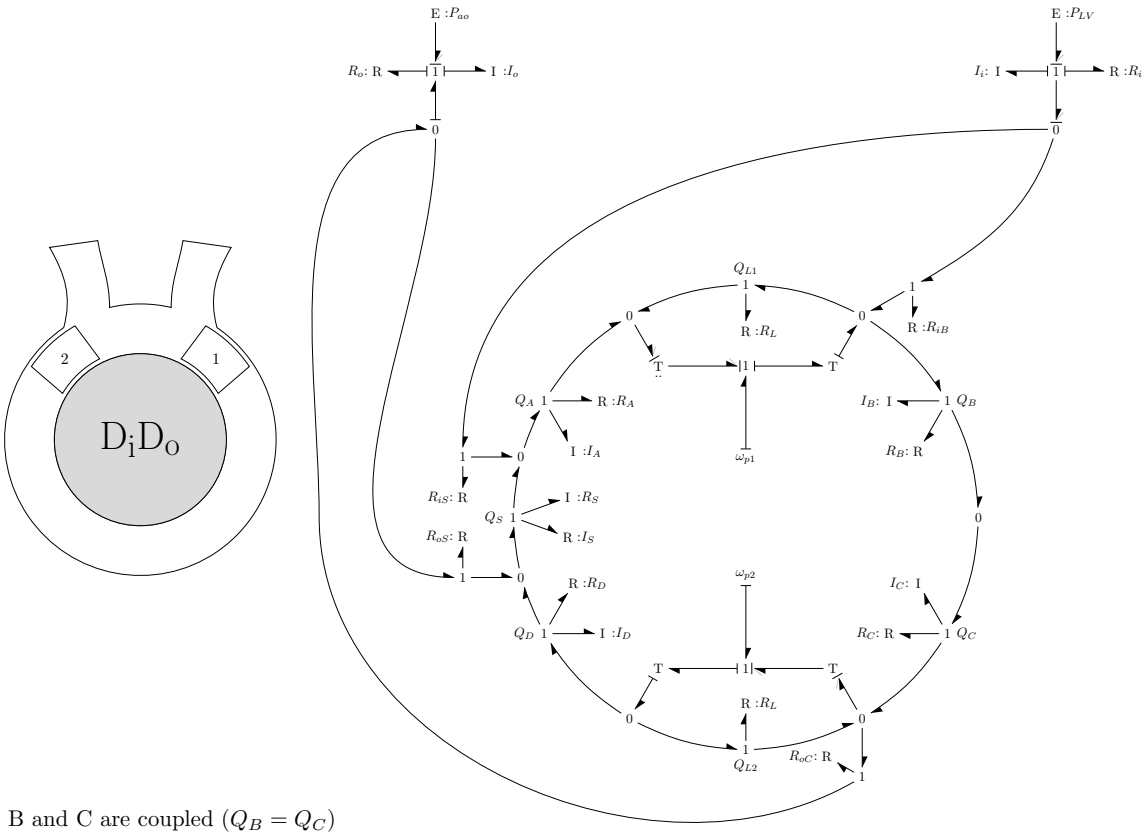

B and C are coupled ($Q_B = Q_C$)

$$\dot{Q}_A = \big[- R_A Q_A + R_L(Ar\omega_1 - Q_A) - R_{iS} Q_{iS} \left|Q_{iS}\right| + R_{iB} Q_{iB} \big] / I_A$$

$$\dot{Q}_B = \big[- \Delta P - (R_B + R_C) Q_B - R_{iB} Q_{iB} - R_{oC} Q_{oC} \big] / (I_B + I_C)$$

$$\dot{Q}_C = \big[- \Delta P - (R_B + R_C) Q_C + R_L(Ar\omega_2 - Q_C) - R_{iB} Q_{iB} - R_{oC} Q_{oC} \big] / (I_B + I_C)$$

$$\dot{Q}_D = \big[- R_D Q_D + R_{oC} Q_{oC} - R_{oS} Q_{oS} \left|Q_{oS}\right| \big] / I_D$$

$$\dot{Q}_S = \big[\Delta P - R_S Q_S + R_{oS} Q_{oS} \left|Q_{oS}\right| + R_{iS} Q_{iS} \left|Q_{iS}\right| \big] / I_S$$

$$\Delta P = P_{LV} - P_{ao} + I_{io} \left(\dot{Q}_{BC} - \dot{Q}_S \right) + R_{io} \left(Q_{BC} - Q_S \right)$$

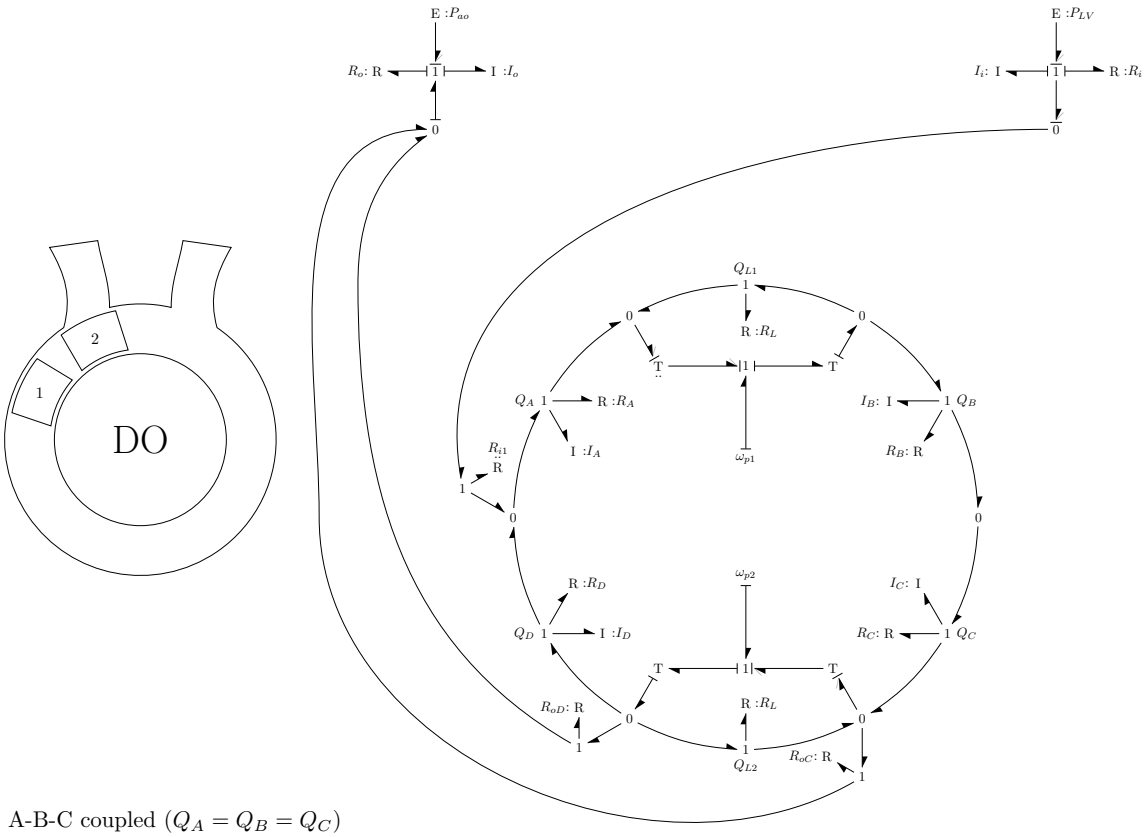

A-B-C coupled ($Q_A = Q_B = Q_C$)

$$\dot{Q}_A = \left[-\Delta P - (R_A + R_B + R_C)Q_A + R_L(Ar\omega_1 - Q_A) - R_{i1}Q_{i1}\left|Q_{i1}\right| - R_{oC}\tilde{Q}_{oC} \right] / (I_A + I_B + I_C)$$

$$\dot{Q}_B = \left[-\Delta P - (R_A + R_B + R_C)Q_B + R_L(Ar\omega_1 - Q_B) - R_{i1}Q_{i1}\left|Q_{i1}\right| - R_{oC}\tilde{Q}_{oC} \right] / (I_A + I_B + I_C)$$

$$\dot{Q}_C = \left[-\Delta P - (R_A + R_B + R_C)Q_C + R_L(Ar\omega_1 - Q_C) - R_{i1}Q_{i1}\left|Q_{i1}\right| - R_{oC}\tilde{Q}_{oC} \right] / (I_A + I_B + I_C)$$

$$\dot{Q}_D = \left[\Delta P - R_D Q_D + R_{oD}\tilde{Q}_{oD} + R_{i1}Q_{i1}\left|Q_{i1}\right| \right] / I_D$$

$$\dot{Q}_S = 0$$

$$\Delta P = P_{LV} - P_{ao} + I_{io}\left(\dot{Q}_{ABC} - \dot{Q}_D\right) + R_{io}\left(Q_{ABC} - Q_D\right)$$

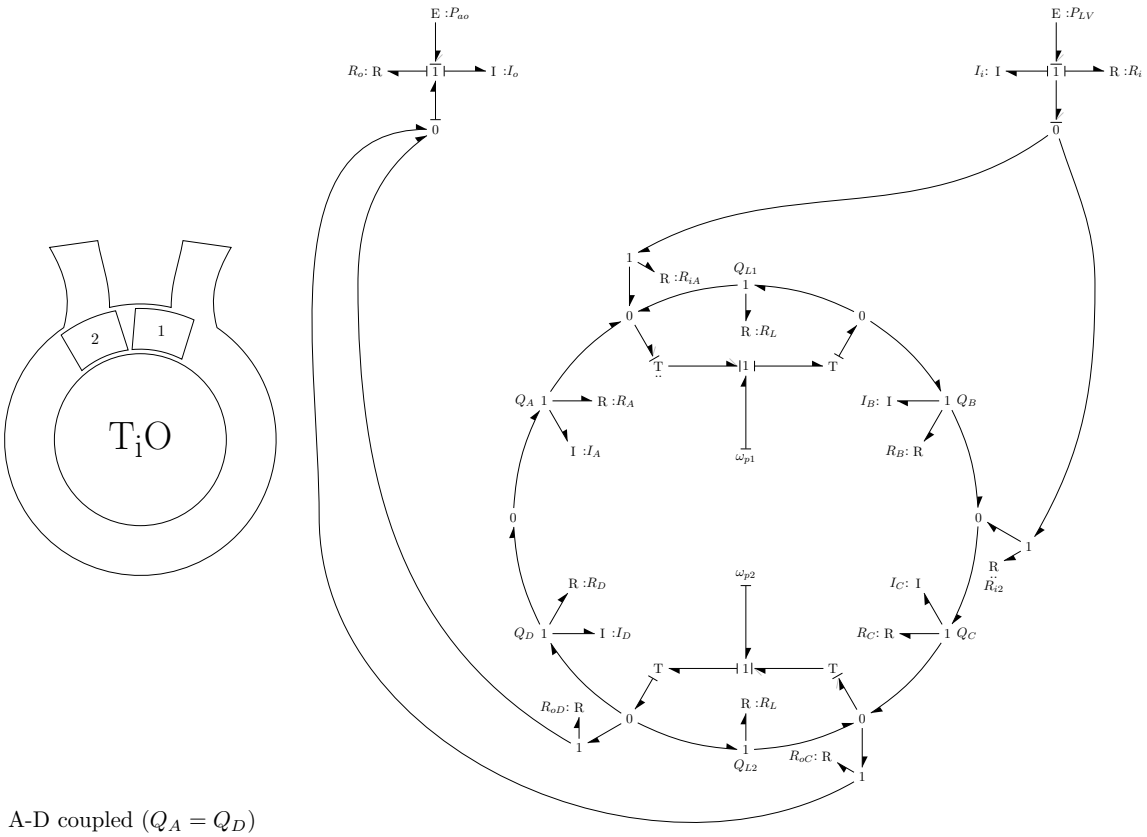

A-D coupled ($Q_A = Q_D$)

$$\dot{Q}_A = \big[\Delta P - (R_A + R_D)Q_A + R_{oD}\tilde{Q}_{oD} + R_{iA}Q_{iA}\big]/(I_A + I_D)$$

$$\dot{Q}_B = \big[- R_B Q_B + R_L(Ar\omega_1 - Q_B) - R_{iA}Q_{iA} + R_{i2}Q_{i2}\,|Q_{i2}|\,\big]/I_B$$

$$\dot{Q}_C = \big[- \Delta P - R_C Q_C + R_{i2}Q_{i2}\,|Q_{i2}| - R_{oC}\tilde{Q}_{oC}\big]/I_C$$

$$\dot{Q}_D = \big[\Delta P - (R_A + R_D)Q_D + R_{oD}\tilde{Q}_{oD} + R_{iA}Q_{iA}\big]/(I_A + I_D)$$

$$\dot{Q}_S = 0$$

$$\Delta P = P_{LV} - P_{ao} + I_{io}\left(\dot{Q}_C - \dot{Q}_{AD}\right) + R_{io}\left(Q_C - Q_{AD}\right)$$

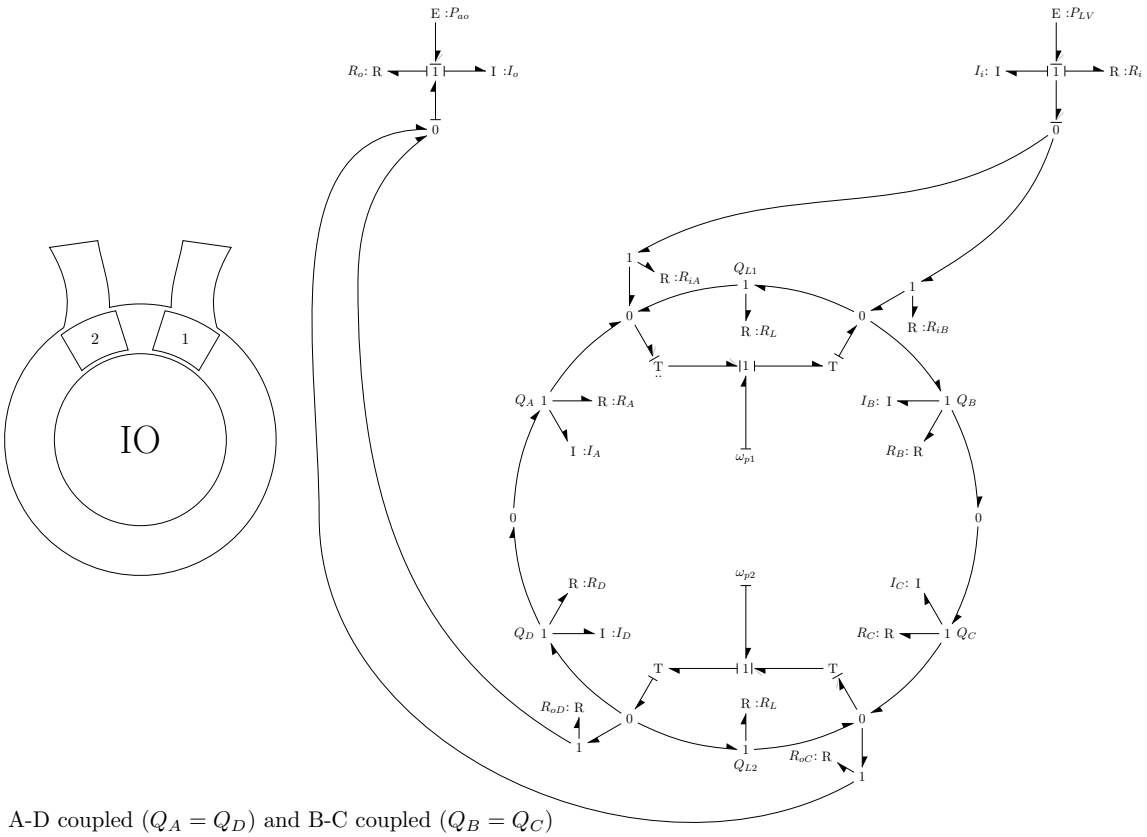

A-D coupled ($Q_A = Q_D$) and B-C coupled ($Q_B = Q_C$)

$$\dot{Q}_A = \left[\Delta P - (R_A + R_D)Q_A + R_{oD}\tilde{Q}_{oD} + R_{iA}\tilde{Q}_{iA}\right]/(I_A + I_D)$$

$$\dot{Q}_B = \left[-\Delta P - (R_B + R_C)Q_B - R_{iB}\tilde{Q}_{iB} - R_{oC}\tilde{Q}_{oC}\right]/(I_B + I_C)$$

$$\dot{Q}_C = \left[-\Delta P - (R_B + R_C)Q_C - R_{iB}\tilde{Q}_{iB} - R_{oC}\tilde{Q}_{oC}\right]/(I_B + I_C)$$

$$\dot{Q}_D = \left[\Delta P - (R_A + R_D)Q_D + R_{oD}\tilde{Q}_{oD} + R_{iA}\tilde{Q}_{iA}\right]/(I_A + I_D)$$

$$\dot{Q}_S = 0$$

$$\Delta P = P_{LV} - P_{ao} + I_{io}\left(\dot{Q}_{BC} - \dot{Q}_{AD}\right) + R_{io}\left(Q_{BC} - Q_{AD}\right)$$

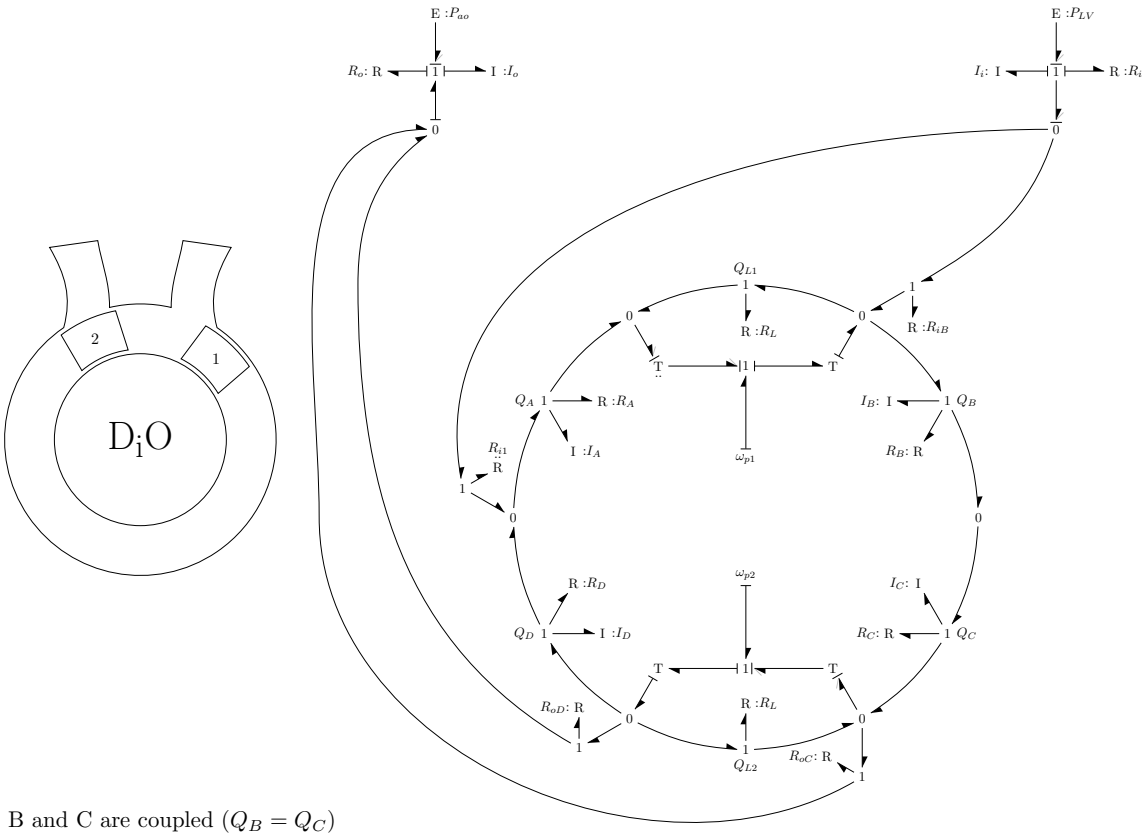

B and C are coupled ($Q_B = Q_C$)

$$\dot{Q}_A = \big[- R_A Q_A + R_L(Ar\omega_1 - Q_A) - R_{i1} Q_{i1} \left| Q_{i1} \right| + R_{iA} Q_{iA} \big] / I_A$$

$$\dot{Q}_B = \big[- \Delta P - (R_B + R_C) Q_B - R_{iA} Q_{iA} - R_{oC} \tilde{Q}_{oC} \big] / (I_B + I_C)$$

$$\dot{Q}_C = \big[- \Delta P - (R_B + R_C) Q_C - R_{iA} Q_{iA} - R_{oC} \tilde{Q}_{oC} \big] / (I_B + I_C)$$

$$\dot{Q}_D = \big[\Delta P - R_D Q_D + R_{oD} \tilde{Q}_{oD} + R_{i1} Q_{i1} \left| Q_{i1} \right| \big] / I_D$$

$$\dot{Q}_S = 0$$

$$\Delta P = P_{LV} - P_{ao} + I_{io} \left(\dot{Q}_{BC} - \dot{Q}_D \right) + R_{io} \left(Q_{BC} - Q_D \right)$$

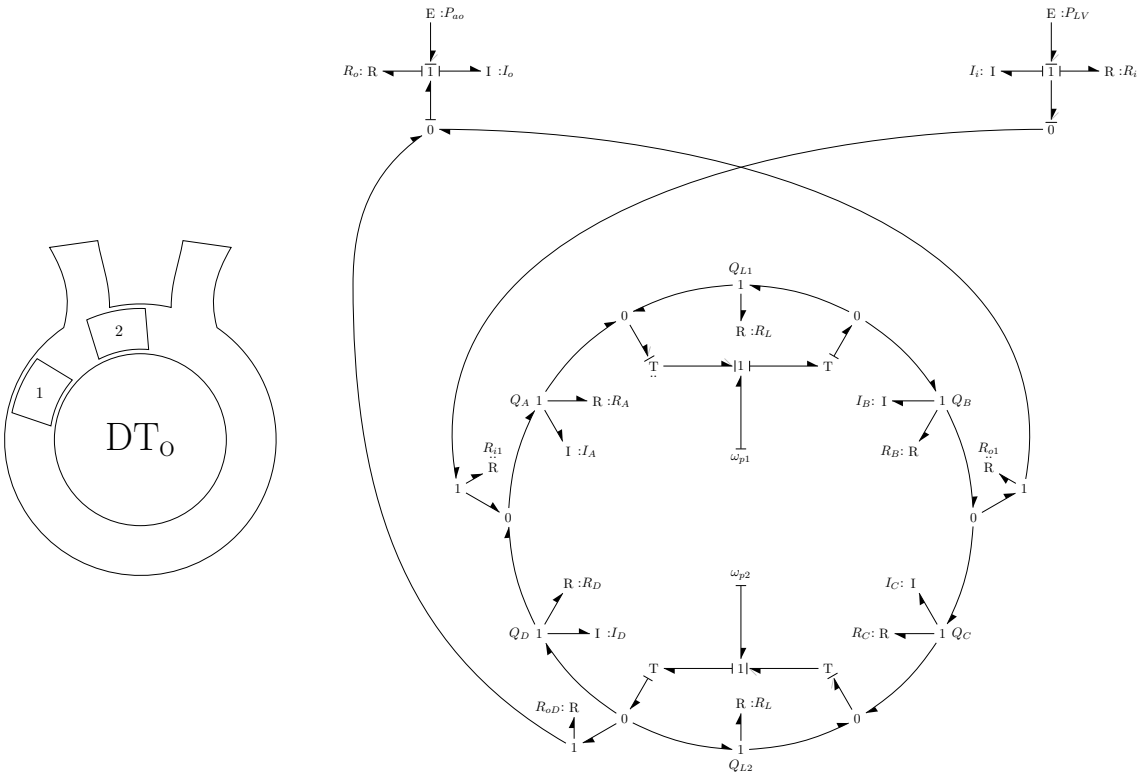

A-B coupled ($Q_A = Q_B$)

$$\dot{Q}_A = \big[-\Delta P - (R_A + R_B)Q_A + R_L(Ar\omega_1 - Q_A) - R_{i1}Q_{i1}\,|Q_{i1}| - R_{o1}Q_{o1}\,|Q_{o1}| \big]/(I_A + I_B)$$

$$\dot{Q}_B = \big[-\Delta P - (R_A + R_B)Q_B + R_L(Ar\omega_1 - Q_B) - R_{i1}Q_{i1}\,|Q_{i1}| - R_{o1}Q_{o1}\,|Q_{o1}| \big]/(I_A + I_B)$$

$$\dot{Q}_C = \big[-R_C Q_C + R_L(Ar\omega_2 - Q_C) + R_{o1}Q_{o1}\,|Q_{o1}| - R_{oD}Q_{oD} \big]/I_C$$

$$\dot{Q}_D = \big[\Delta P - R_D Q_D + R_{oD}Q_{oD} + R_{i1}Q_{i1}\,|Q_{i1}| \big]/I_D$$

$$\dot{Q}_S = 0$$

$$\Delta P = P_{LV} - P_{ao} + I_{io}\left(\dot{Q}_{AB} - \dot{Q}_D\right) + R_{io}\left(Q_{AB} - Q_D\right)$$

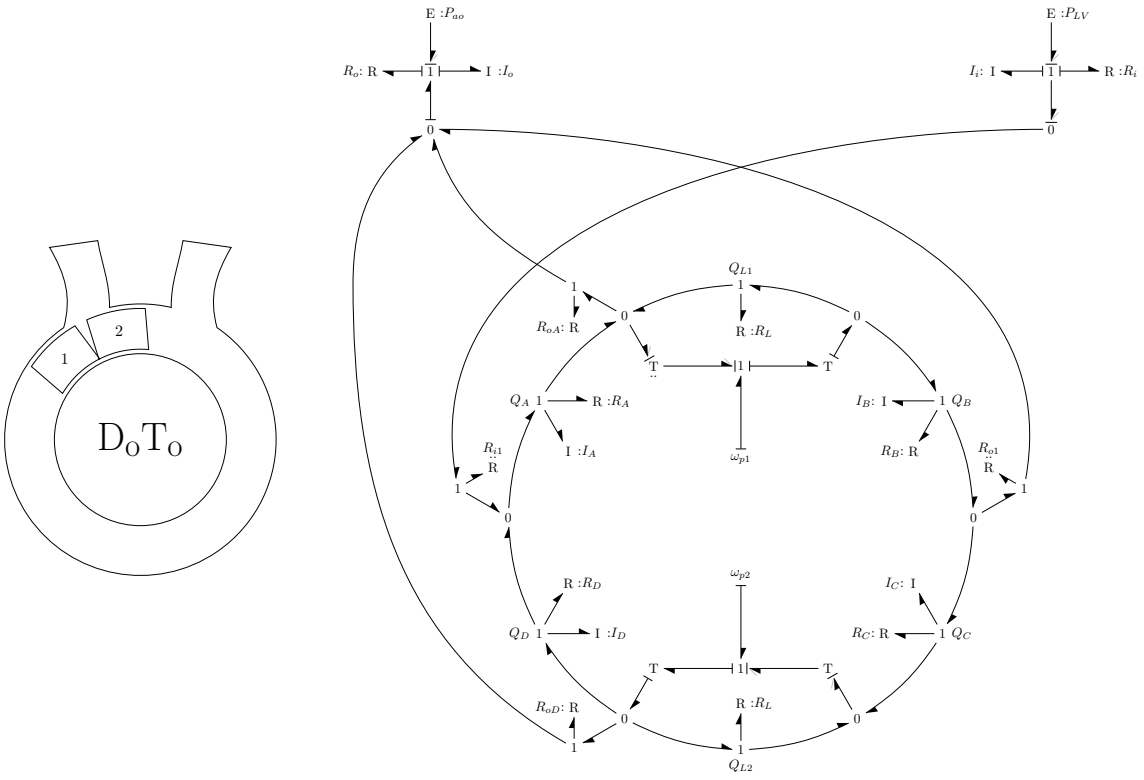

All flows decoupled

$$\dot{Q}_A = \big[-\Delta P - R_A Q_A - R_{i1} Q_{i1} \left| Q_{i1} \right| - R_{oA} Q_{oA} \big] / I_A$$

$$\dot{Q}_B = \big[-R_B Q_B + R_L (Ar\omega_1 - Q_B) + R_{oA} Q_{oA} - R_{o1} Q_{o1} \left| Q_{o1} \right| \big] / I_B$$

$$\dot{Q}_C = \big[-R_C Q_C + R_L (Ar\omega_2 - Q_C) + R_{o1} Q_{o1} \left| Q_{o1} \right| - R_{oD} Q_{oD} \big] / I_C$$

$$\dot{Q}_D = \big[\Delta P - R_D Q_D + R_{oD} Q_{oD} + R_{i1} Q_{i1} \left| Q_{i1} \right| \big] / I_D$$

$$\dot{Q}_S = 0$$

$$\Delta P = P_{LV} - P_{ao} + I_{io} \left(\dot{Q}_A - \dot{Q}_D \right) + R_{io} \left(Q_A - Q_D \right)$$

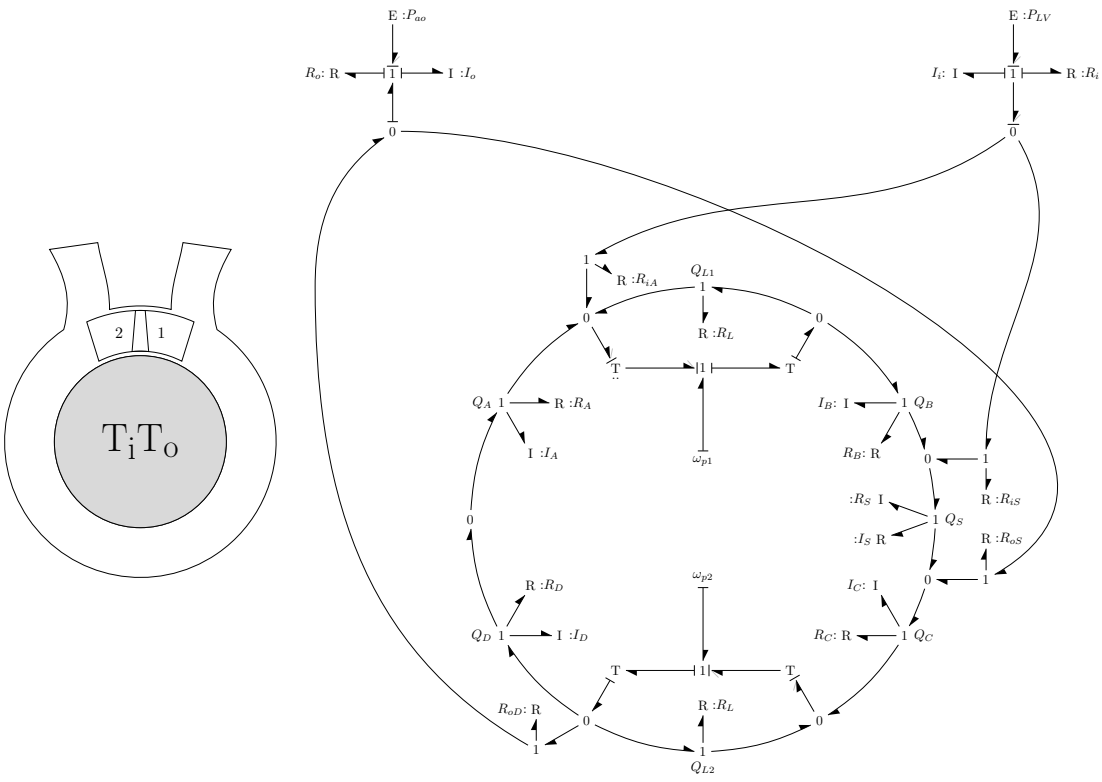

A-D coupled ($Q_A = Q_D$)

$$\dot{Q}_A = \big[\Delta P - (R_A + R_D)Q_A + R_{oD}Q_{oD} + R_{iA}Q_{iA}\big]/(I_A + I_D)$$

$$\dot{Q}_B = \big[- R_B Q_B + R_L(Ar\omega_1 - Q_B) - R_{iA}Q_{iA} + R_{iS}Q_{iS}\,|Q_{iS}|\,\big]/I_B$$

$$\dot{Q}_C = \big[- R_C Q_C + R_L(Ar\omega_2 - Q_C) + R_{oS}Q_{oS}\,|Q_{oS}| - R_{oD}Q_{oD}\big]/I_C$$

$$\dot{Q}_D = \big[\Delta P - (R_A + R_D)Q_D + R_{oD}Q_{oD} + R_{iA}Q_{iA}\big]/(I_A + I_D)$$

$$\dot{Q}_S = \big[- \Delta P - R_S Q_S - R_{oS}Q_{oS}\,|Q_{oS}| - R_{iS}Q_{iS}\,|Q_{iS}|\,\big]/I_S$$

$$\Delta P = P_{LV} - P_{ao} + I_{io}\left(\dot{Q}_S - \dot{Q}_{AD}\right) + R_{io}\,(Q_S - Q_{AD})$$

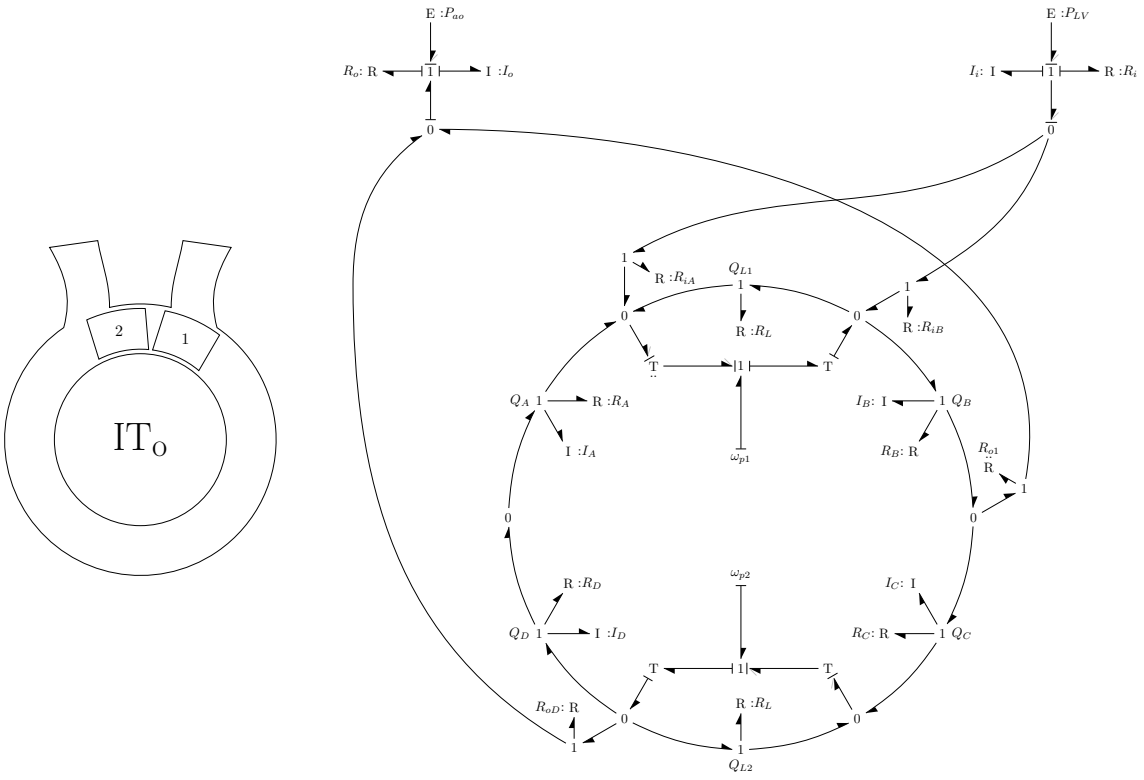

A-D coupled ($Q_A = Q_D$)

$$\dot{Q}_A = \left[\Delta P - (R_A + R_D)Q_A + R_{oD}Q_{oD} + R_{iA}\tilde{Q}_{iA}\right]/(I_A + I_D)$$

$$\dot{Q}_B = \left[- \Delta P - R_B Q_B - R_{iB}\tilde{Q}_{iB} - R_{o1}Q_{o1}\left|Q_{o1}\right|\right]/I_B$$

$$\dot{Q}_C = \left[- R_C Q_C + R_L(Ar\omega_2 - Q_C) + R_{o1}Q_{o1}\left|Q_{o1}\right| - R_{oD}Q_{oD}\right]/I_C$$

$$\dot{Q}_D = \left[\Delta P - (R_A + R_D)Q_D + R_{oD}Q_{oD} + R_{iA}\tilde{Q}_{iA}\right]/(I_A + I_D)$$

$$\dot{Q}_S = 0$$

$$\Delta P = P_{LV} - P_{ao} + I_{io}\left(\dot{Q}_B - \dot{Q}_{AD}\right) + R_{io}\left(Q_B - Q_{AD}\right)$$

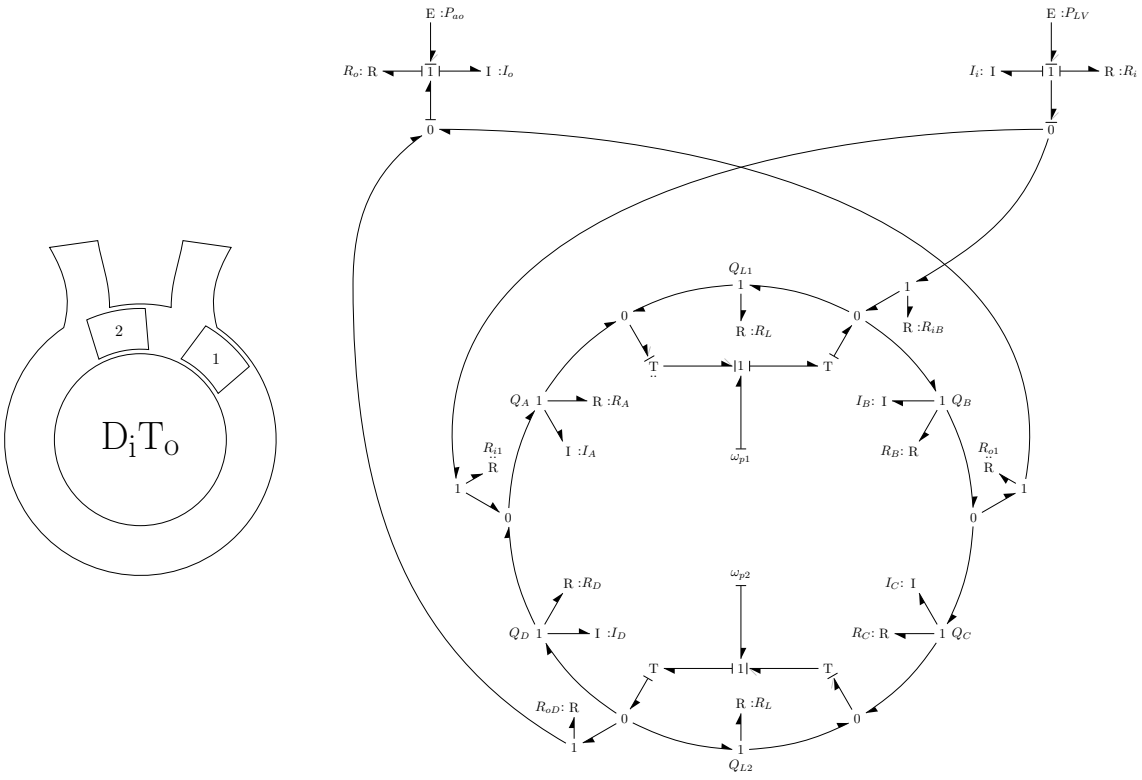

All flows decoupled

$$\dot{Q}_A = \big[- R_A Q_A + R_L(Ar\omega_1 - Q_A) - R_{i1} Q_{i1} \left| Q_{i1} \right| + R_{iB} Q_{iB} \big] / I_A$$

$$\dot{Q}_B = \big[- \Delta P - R_B Q_B - R_{iB} Q_{iB} - R_{o1} Q_{o1} \left| Q_{o1} \right| \big] / I_B$$

$$\dot{Q}_C = \big[- R_C Q_C + R_L(Ar\omega_2 - Q_C) + R_{o1} Q_{o1} \left| Q_{o1} \right| - R_{oD} Q_{oD} \big] / I_C$$

$$\dot{Q}_D = \big[\Delta P - R_D Q_D + R_{oD} Q_{oD} + R_{i1} Q_{i1} \left| Q_{i1} \right| \big] / I_D$$

$$\dot{Q}_S = 0$$

$$\Delta P = P_{LV} - P_{ao} + I_{io} \left(\dot{Q}_B - \dot{Q}_D \right) + R_{io} \left(Q_B - Q_D \right)$$

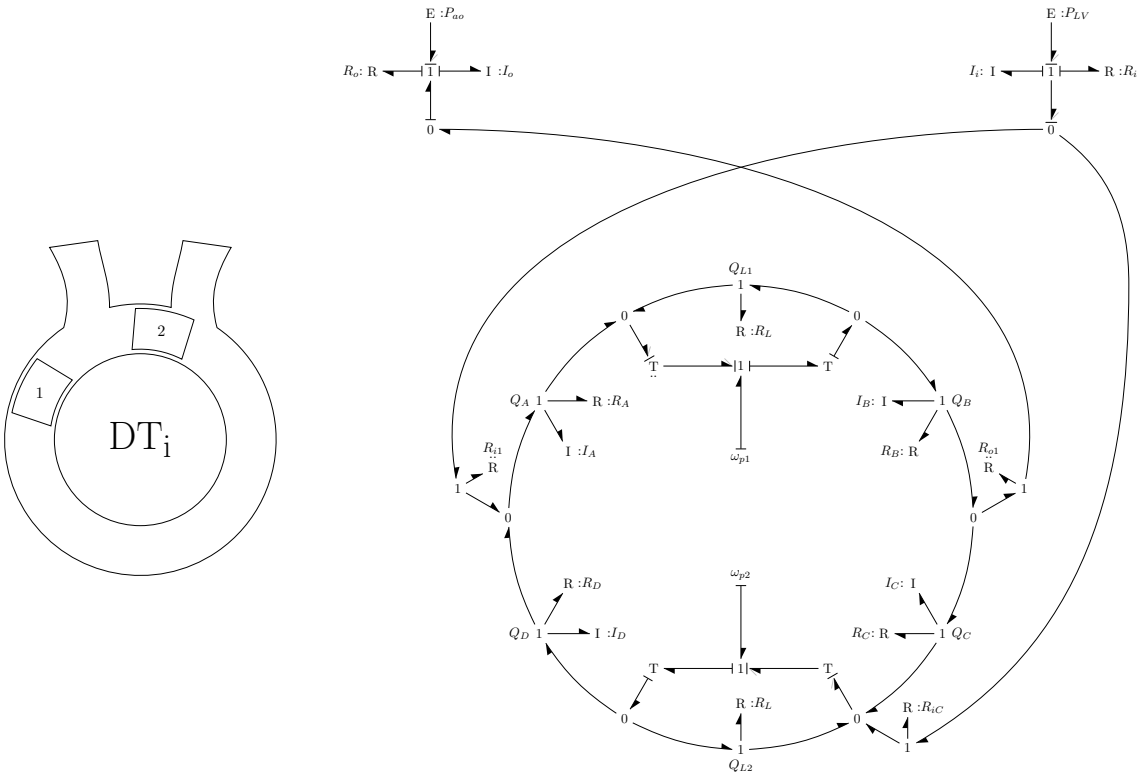

A-B coupled ($Q_A = Q_B$)

$$\dot{Q}_A = \big[-\Delta P - (R_A + R_B)Q_A + R_L(Ar\omega_1 - Q_A) - R_{i1}Q_{i1}\,|Q_{i1}| - R_{o1}Q_{o1}\,|Q_{o1}|\,\big]/(I_A + I_B)$$

$$\dot{Q}_B = \big[-\Delta P - (R_A + R_B)Q_B + R_L(Ar\omega_1 - Q_B) - R_{i1}Q_{i1}\,|Q_{i1}| - R_{o1}Q_{o1}\,|Q_{o1}|\,\big]/(I_A + I_B)$$

$$\dot{Q}_C = \big[-R_C Q_C + R_L(Ar\omega_2 - Q_C) + R_{o1}Q_{o1}\,|Q_{o1}| - R_{oD}Q_{oD}\big]/I_C$$

$$\dot{Q}_D = \big[\Delta P - R_D Q_D + R_{oD}Q_{oD} + R_{i1}Q_{i1}\,|Q_{i1}|\,\big]/I_D$$

$$\dot{Q}_S = 0$$

$$\Delta P = P_{LV} - P_{ao} + I_{io}\left(\dot{Q}_{AB} - \dot{Q}_C\right) + R_{io}\,(Q_{AB} - Q_C)$$

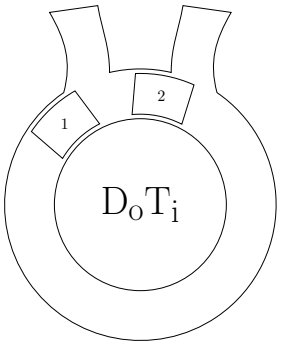

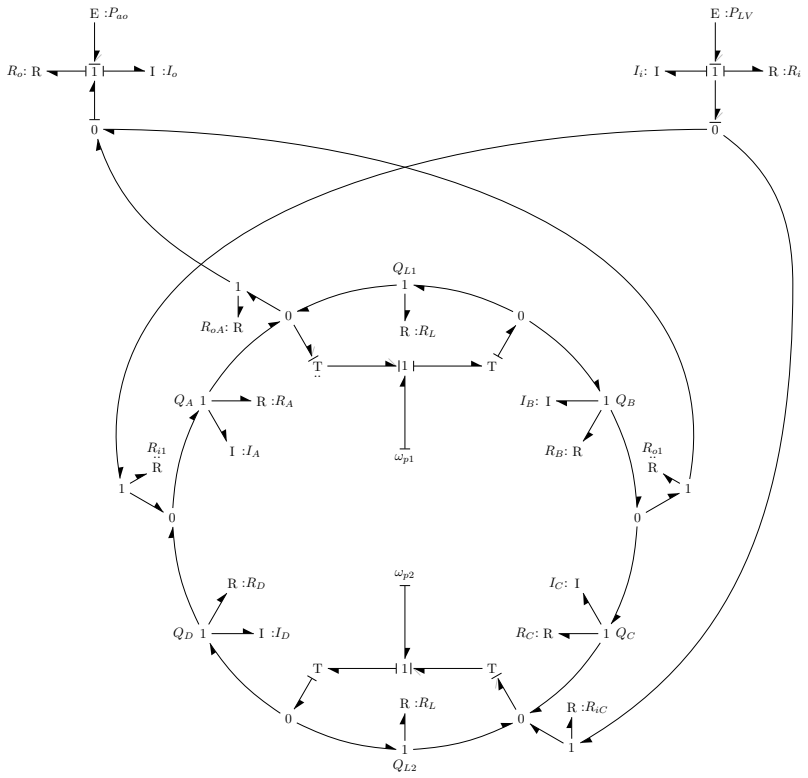

All flows decoupled

$$\dot{Q}_A = \big[-\Delta P - R_A Q_A - R_{i1} Q_{i1} \left|Q_{i1}\right| - R_{oA} Q_{oA} \big] / I_A$$

$$\dot{Q}_B = \big[-R_B Q_B + R_L (Ar\omega_1 - Q_B) + R_{oA} Q_{oA} - R_{o1} Q_{o1} \left|Q_{o1}\right| \big] / I_B$$

$$\dot{Q}_C = \big[\Delta P - R_C Q_C + R_{o1} Q_{o1} \left|Q_{o1}\right| + R_{iC} Q_{iC} \big] / I_C$$

$$\dot{Q}_D = \big[-R_D Q_D + R_L (Ar\omega_2 - Q_D) - R_{iC} Q_{iC} + R_{i1} Q_{i1} \left|Q_{i1}\right| \big] / I_D$$

$$\dot{Q}_S = 0$$

$$\Delta P = P_{LV} - P_{ao} + I_{io} \left(\dot{Q}_A - \dot{Q}_C \right) + R_{io} \left(Q_A - Q_C \right)$$

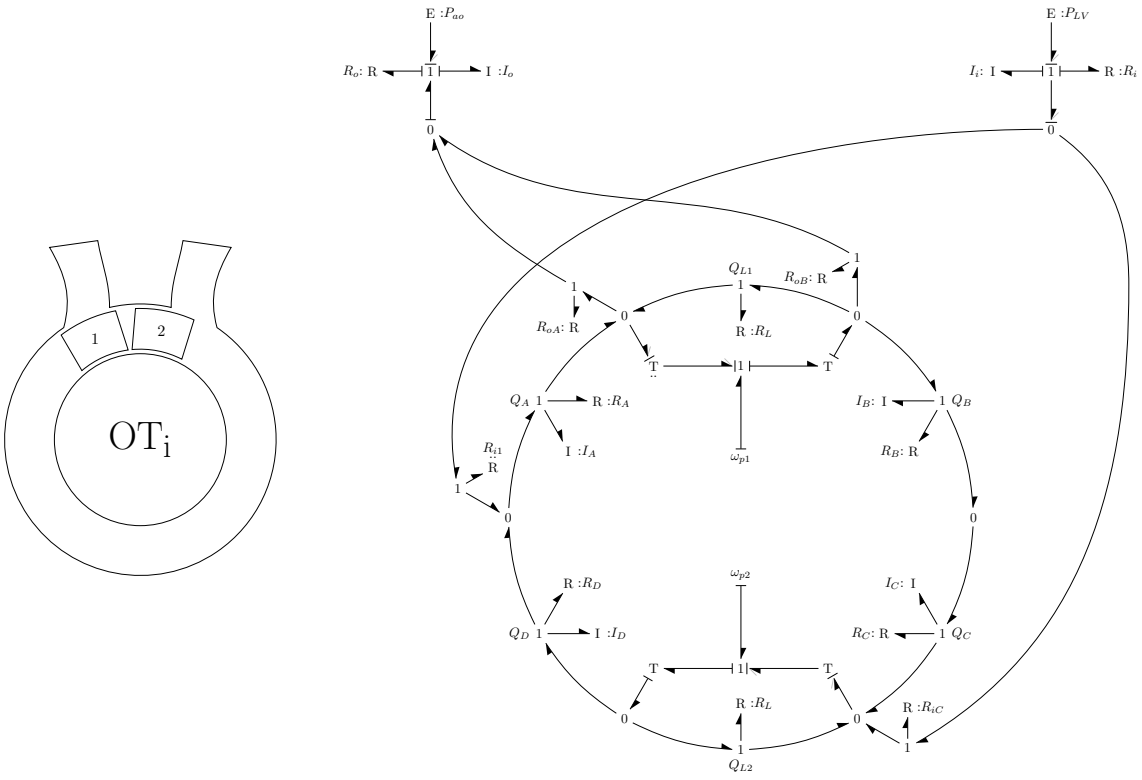

B and C are coupled ($Q_B = Q_C$)

$$\dot{Q}_A = \big[-\Delta P - R_A Q_A - R_{i1} Q_{i1} \left|Q_{i1}\right| - R_{oA} \tilde{Q}_{oA} \big] / I_A$$

$$\dot{Q}_B = \big[\Delta P - (R_B + R_C) Q_B + R_{oB} \tilde{Q}_{oB} + R_{iC} Q_{iC} \big] / (I_B + I_C)$$

$$\dot{Q}_C = \big[\Delta P - (R_B + R_C) Q_C + R_{oB} \tilde{Q}_{oB} + R_{iC} Q_{iC} \big] / (I_B + I_C)$$

$$\dot{Q}_D = \big[-R_D Q_D + R_L (A r \omega_2 - Q_D) - R_{iC} Q_{iC} - R_{i1} Q_{i1} \left|Q_{i1}\right| \big] / I_D$$

$$\dot{Q}_S = 0$$

$$\Delta P = P_{LV} - P_{ao} + I_{io} \left(\dot{Q}_A - \dot{Q}_{BC} \right) + R_{io} \left(Q_A - Q_{BC} \right)$$

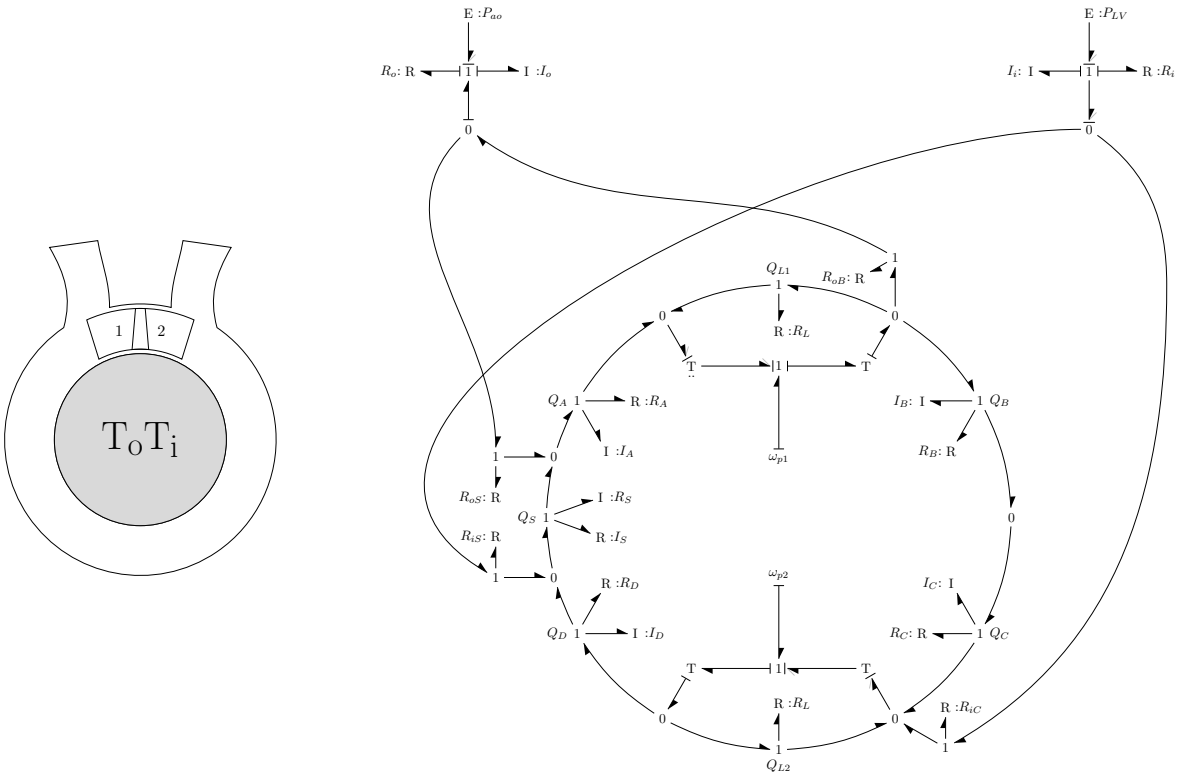

B and C are coupled ($Q_B = Q_C$)

$$\dot{Q}_A = \big[- R_A Q_A + R_L(Ar\omega_1 - Q_A) + R_{oS} Q_{oS} \left| Q_{oS} \right| - R_{oA} \tilde{Q}_{oA} \big] / I_A$$

$$\dot{Q}_B = \big[\Delta P - (R_B + R_C) Q_B + R_{oB} Q_{oB} + R_{iC} Q_{iC} \big] / (I_B + I_C)$$

$$\dot{Q}_C = \big[\Delta P - (R_B + R_C) Q_C + R_{oB} Q_{oB} + R_{iC} Q_{iC} \big] / (I_B + I_C)$$

$$\dot{Q}_D = \big[- R_D Q_D + R_L(Ar\omega_2 - Q_D) - R_{iC} Q_{iC} + R_{iS} Q_{iS} \left| Q_{iS} \right| \big] / I_D$$

$$\dot{Q}_S = \big[- \Delta P - R_S Q_S - R_{oS} Q_{oS} \left| Q_{oS} \right| - R_{iS} Q_{iS} \left| Q_{iS} \right| \big] / I_S$$

$$\Delta P = P_{LV} - P_{ao} + I_{io} \left(\dot{Q}_S - \dot{Q}_{BC} \right) + R_{io} \left(Q_S - Q_{BC} \right)$$

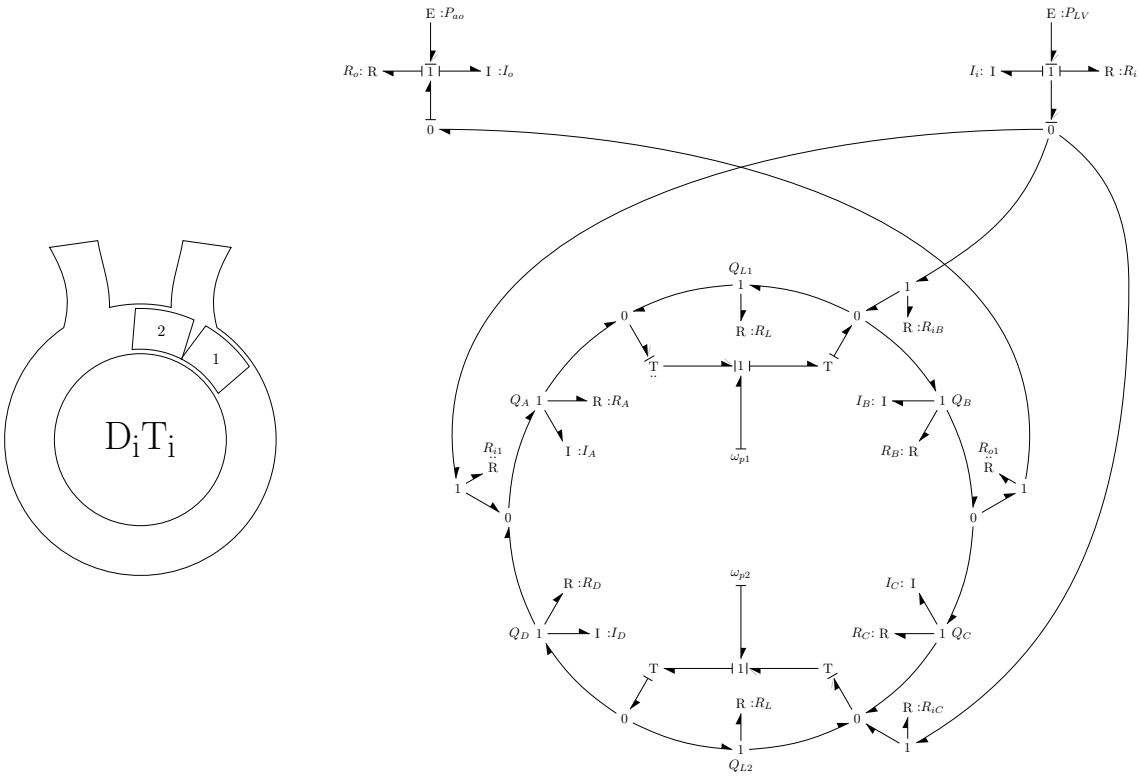

B and C are coupled ($Q_B = Q_C$)

$$\dot{Q}_A = \big[- R_A Q_A + R_L(Ar\omega_1 - Q_A) - R_{i1} Q_{i1} \left| Q_{i1} \right| + R_{iB} Q_{iB} \big] / I_A$$

$$\dot{Q}_B = \big[- \Delta P - (R_B + R_C) Q_B - R_{iB} Q_{iB} - R_{o1} Q_{o1} \left| Q_{o1} \right| \big] / (I_B + I_C)$$

$$\dot{Q}_C = \big[\Delta P - (R_B + R_C) Q_C + R_{o1} Q_{o1} \left| Q_{o1} \right| + R_{iC} Q_{iC} \big] / (I_B + I_C)$$

$$\dot{Q}_D = \big[- R_D Q_D + R_L(Ar\omega_2 - Q_D) - R_{iC} Q_{iC} + R_{i1} Q_{i1} \left| Q_{i1} \right| \big] / I_D$$

$$\dot{Q}_S = 0$$

$$\Delta P = P_{LV} - P_{ao} + I_{io} \left(\dot{Q}_B - \dot{Q}_C \right) + R_{io} \left(Q_B - Q_C \right)$$

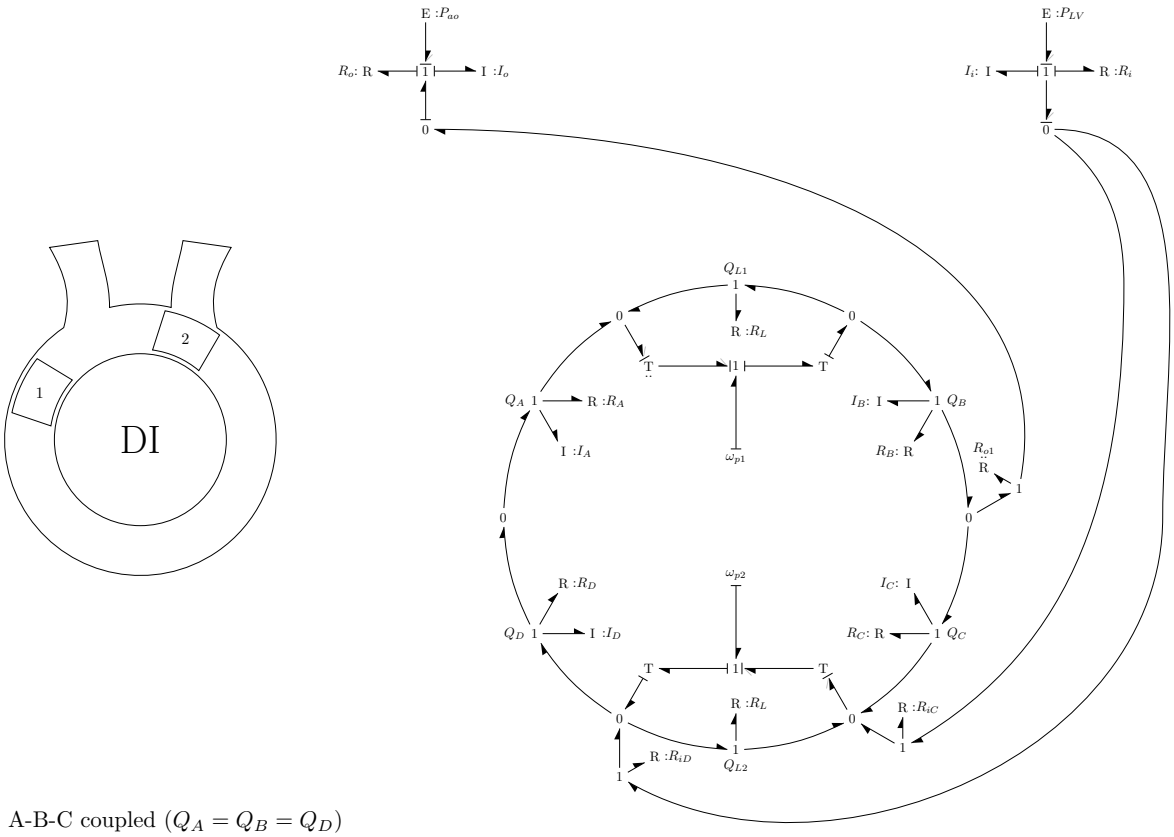

A-B-C coupled ($Q_A = Q_B = Q_D$)

$$\dot{Q}_A = \big[-\Delta P - (R_A + R_B + R_D)Q_A + R_L(Ar\omega_1 - Q_A) - R_{iD}\tilde{Q}_{iD} - R_{oA}Q_{oA}\big]/(I_A + I_B + I_D)$$

$$\dot{Q}_B = \big[-\Delta P - (R_A + R_B + R_D)Q_B + R_L(Ar\omega_1 - Q_B) - R_{iD}\tilde{Q}_{iD} - R_{oA}Q_{oA}\big]/(I_A + I_B + I_D)$$

$$\dot{Q}_C = \big[-R_C Q_C + R_{o1}Q_{o1}\,|Q_{o1}| + R_{iC}\tilde{Q}_{iC}\big]/I_C$$

$$\dot{Q}_D = \big[-\Delta P - (R_A + R_B + R_D)Q_D + R_L(Ar\omega_1 - Q_D) - R_{iD}\tilde{Q}_{iD} - R_{oA}Q_{oA}\big]/(I_A + I_B + I_D)$$

$$\dot{Q}_S = 0$$

$$\Delta P = P_{LV} - P_{ao} + I_{io}\left(\dot{Q}_{ABD} - \dot{Q}_C\right) + R_{io}\left(Q_{ABD} - Q_C\right)$$

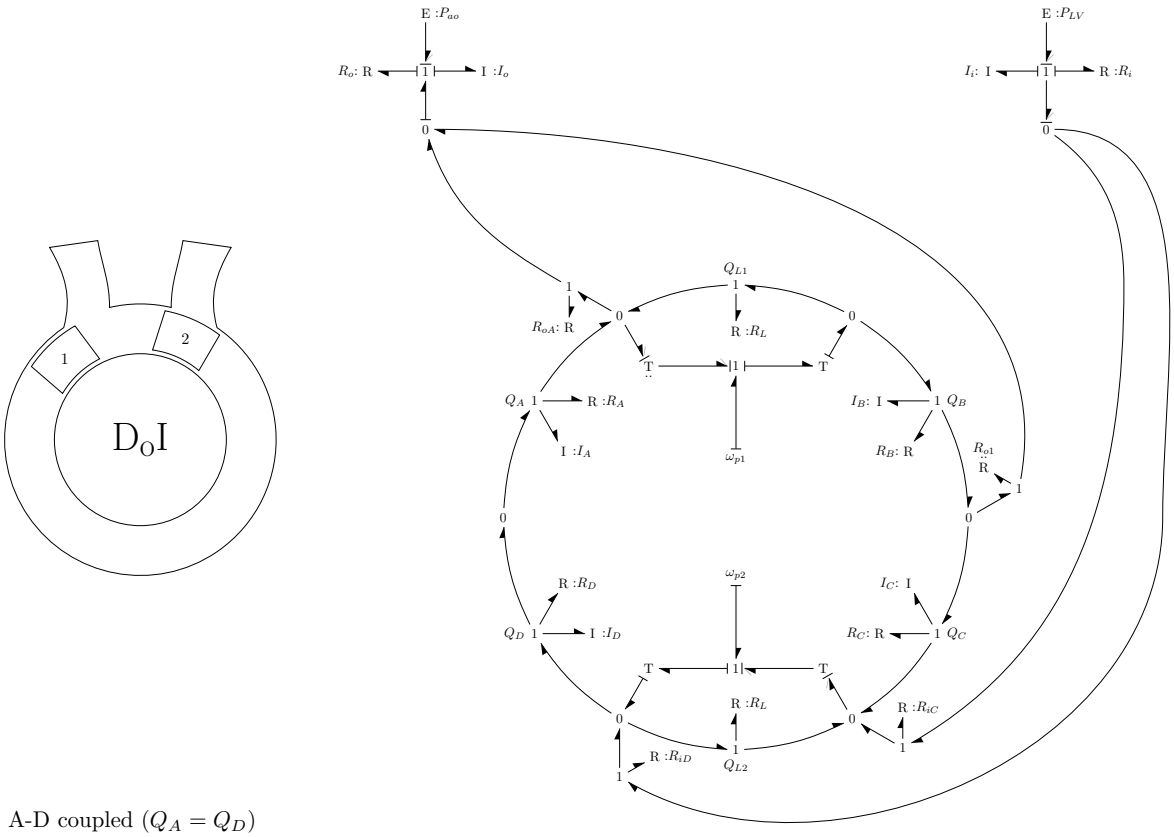

A-D coupled ($Q_A = Q_D$)

$$\dot{Q}_A = \big[-\Delta P - (R_A + R_D)Q_A - R_{iD}\tilde{Q}_{iD} - R_{oA}Q_{oA} \big] / (I_A + I_D)$$

$$\dot{Q}_B = \big[-R_B Q_B + R_L(Ar\omega_1 - Q_B) + R_{oA}Q_{oA} - R_{o1}Q_{o1}\,|Q_{o1}| \big] / I_B$$

$$\dot{Q}_C = \big[-R_C Q_C + R_{o1}Q_{o1}\,|Q_{o1}| + R_{iC}\tilde{Q}_{iC} \big] / I_C$$

$$\dot{Q}_D = \big[-\Delta P - (R_A + R_D)Q_D - R_{iD}\tilde{Q}_{iD} - R_{oA}Q_{oA} \big] / (I_A + I_D)$$

$$\dot{Q}_S = 0$$

$$\Delta P = P_{LV} - P_{ao} + I_{io}\left(\dot{Q}_{AD} - \dot{Q}_C\right) + R_{io}\left(Q_{AD} - Q_C\right)$$

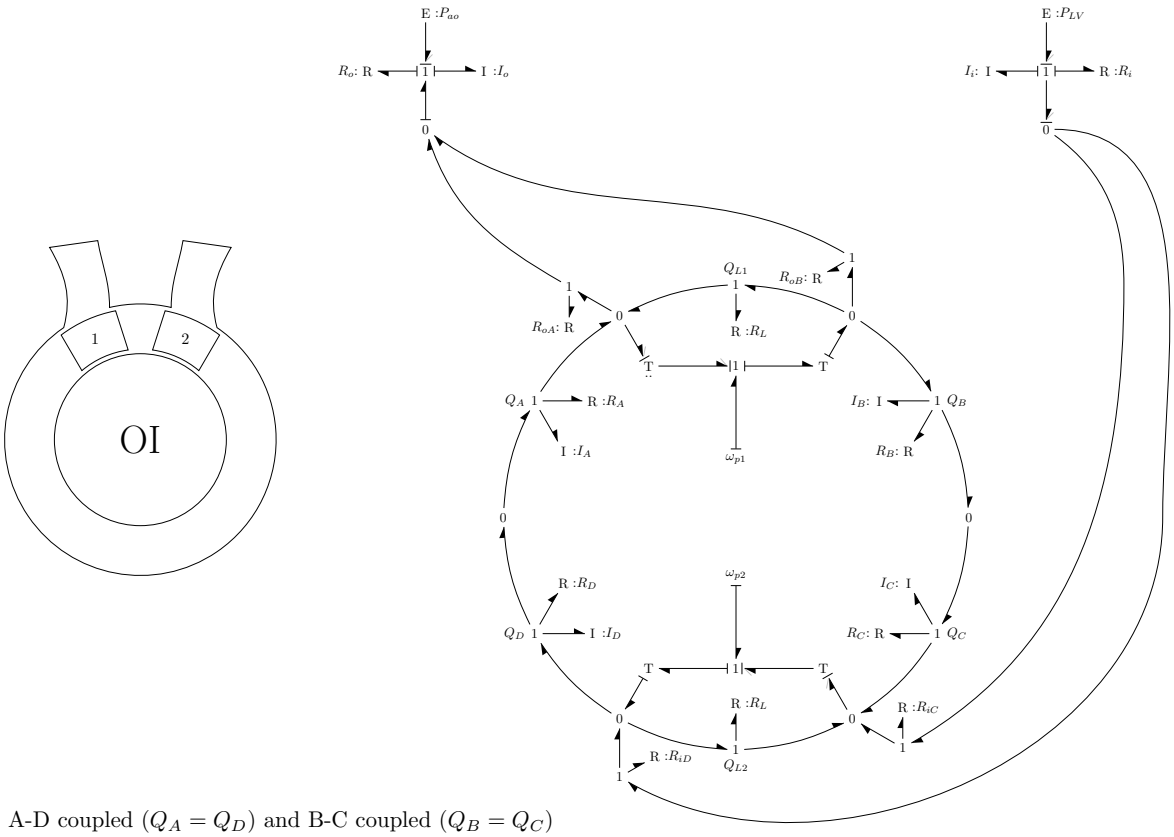

A-D coupled ($Q_A = Q_D$) and B-C coupled ($Q_B = Q_C$)

$$\dot{Q}_A = \big[-\Delta P - (R_A + R_D)Q_A - R_{iD}\tilde{Q}_{iD} - R_{oA}\tilde{Q}_{oA}\big]/(I_A + I_D)$$

$$\dot{Q}_B = \big[\Delta P - (R_B + R_C)Q_B + R_{oB}\tilde{Q}_{oB} + R_{iC}\tilde{Q}_{iC}\big]/(I_B + I_C)$$

$$\dot{Q}_C = \big[\Delta P - (R_B + R_C)Q_C + R_{oB}\tilde{Q}_{oB} + R_{iC}\tilde{Q}_{iC}\big]/(I_B + I_C)$$

$$\dot{Q}_D = \big[-\Delta P - (R_A + R_D)Q_D - R_{iD}\tilde{Q}_{iD} - R_{oA}\tilde{Q}_{oA}\big]/(I_A + I_D)$$

$$\dot{Q}_S = 0$$

$$\Delta P = P_{LV} - P_{ao} + I_{io}\left(\dot{Q}_{AD} - \dot{Q}_{BC}\right) + R_{io}\left(Q_A - Q_D\right)$$

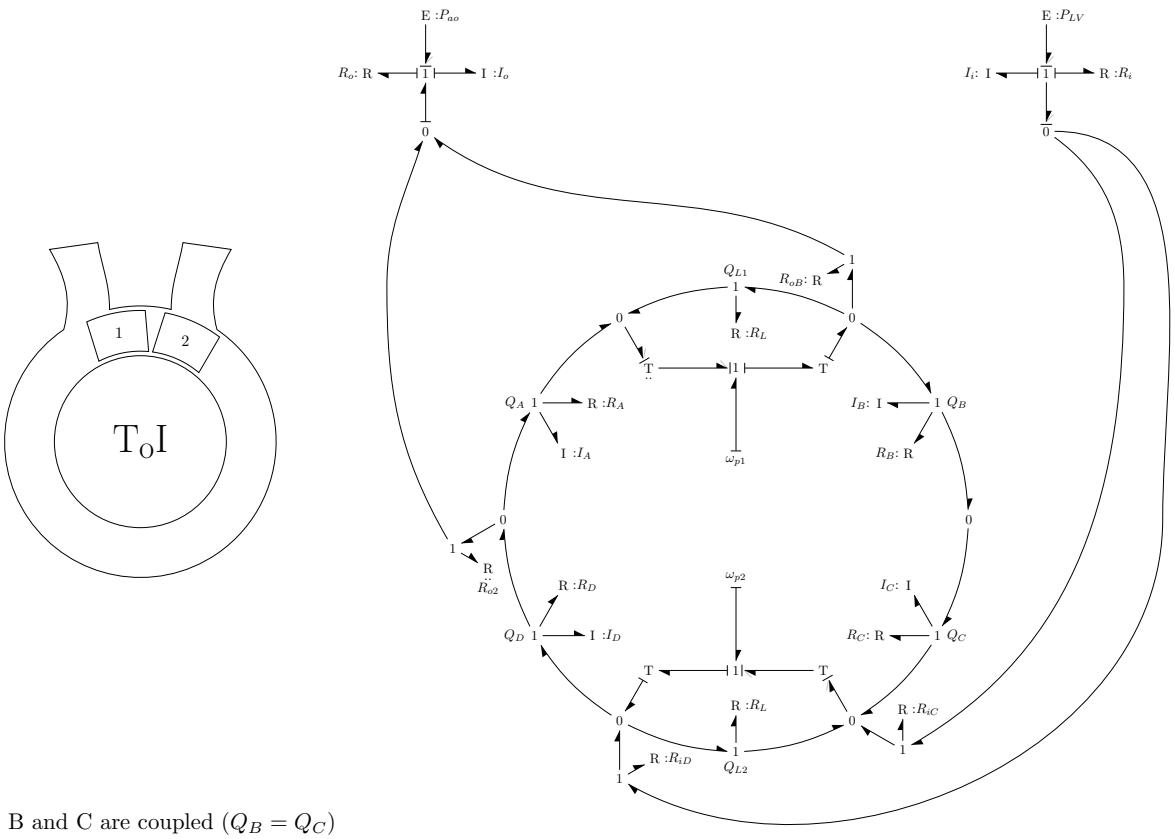

B and C are coupled ($Q_B = Q_C$)

$$\dot{Q}_A = \left[-R_A Q_A + R_L(Ar\omega_1 - Q_A) + R_{o2}Q_{o2}\left|Q_{o2}\right| - R_{oB}Q_{oB}\right]/I_A$$

$$\dot{Q}_B = \left[\Delta P - (R_B + R_C)Q_B + R_{oB}Q_{oB} + R_{iC}\tilde{Q}_{iC}\right]/(I_B + I_C)$$

$$\dot{Q}_C = \left[\Delta P - (R_B + R_C)Q_C + R_{oB}Q_{oB} + R_{iC}\tilde{Q}_{iC}\right]/(I_B + I_C)$$

$$\dot{Q}_D = \left[-\Delta P - R_D Q_D - R_{iD}\tilde{Q}_{iD} - R_{o2}Q_{o2}\left|Q_{o2}\right|\right]/I_D$$

$$\dot{Q}_S = 0$$

$$\Delta P = P_{LV} - P_{ao} + I_{io}\left(\dot{Q}_D - \dot{Q}_{BC}\right) + R_{io}\left(Q_D - Q_{BC}\right)$$

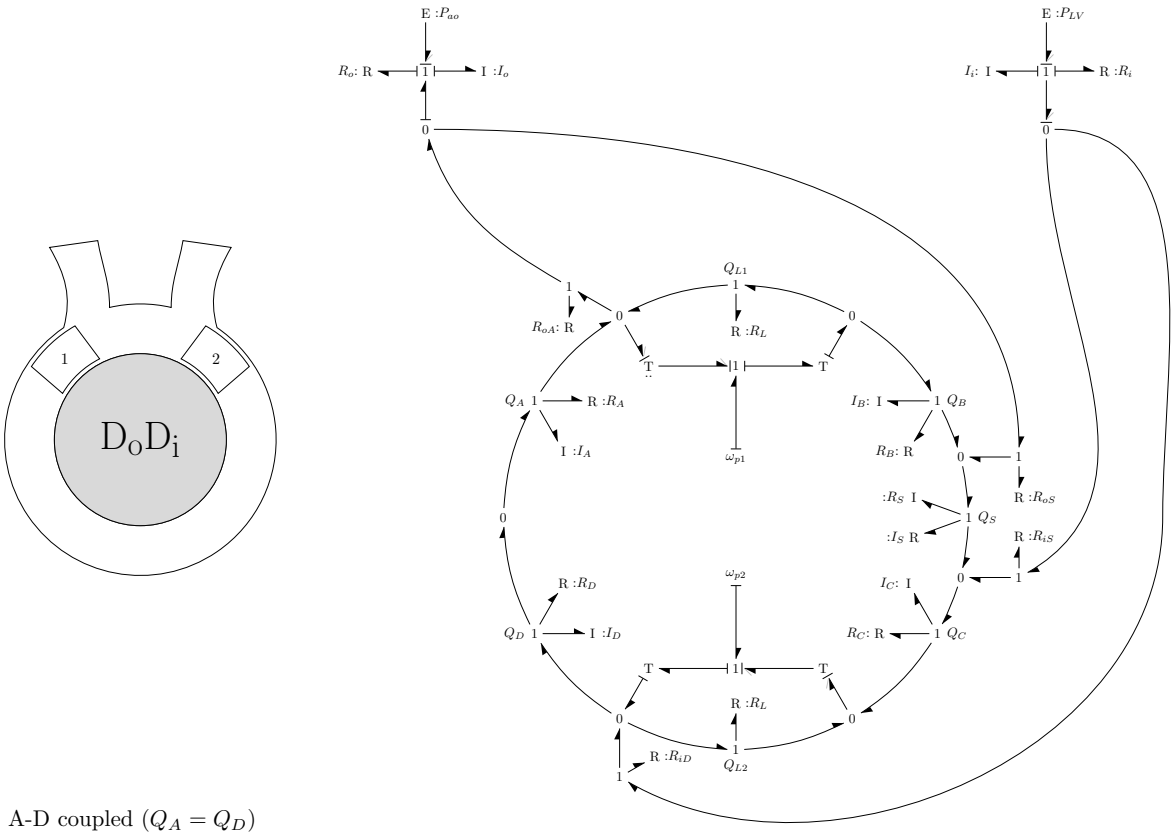

A-D coupled ($Q_A = Q_D$)

$$\dot{Q}_A = \big[-\Delta P - (R_A + R_D)Q_A - R_{iD}Q_{iD} - R_{oA}Q_{oA} \big] / (I_A + I_D)$$

$$\dot{Q}_B = \big[\Delta P - R_B Q_B + R_L(Ar\omega_1 - Q_B) + R_{oA}Q_{oA} - R_{oS}Q_{oS}\,|Q_{oS}| \big] / I_B$$

$$\dot{Q}_C = \big[-R_C Q_C + R_L(Ar\omega_2 - Q_C) - R_{iS}Q_{iS}\,|Q_{iS}| + R_{iD}Q_{iD} \big] / I_C$$

$$\dot{Q}_D = \big[-\Delta P - (R_A + R_D)Q_D - R_{iD}Q_{iD} - R_{oA}Q_{oA} \big] / (I_A + I_D)$$

$$\dot{Q}_S = \big[\Delta P - R_S Q_S + R_{oS}Q_{oS}\,|Q_{oS}| + R_{iS}Q_{iS}\,|Q_{iS}| \big] / I_S$$

$$\Delta P = P_{LV} - P_{ao} + I_{io}\left(\dot{Q}_{AD} - \dot{Q}_S\right) + R_{io}\left(Q_{AD} - Q_S\right)$$

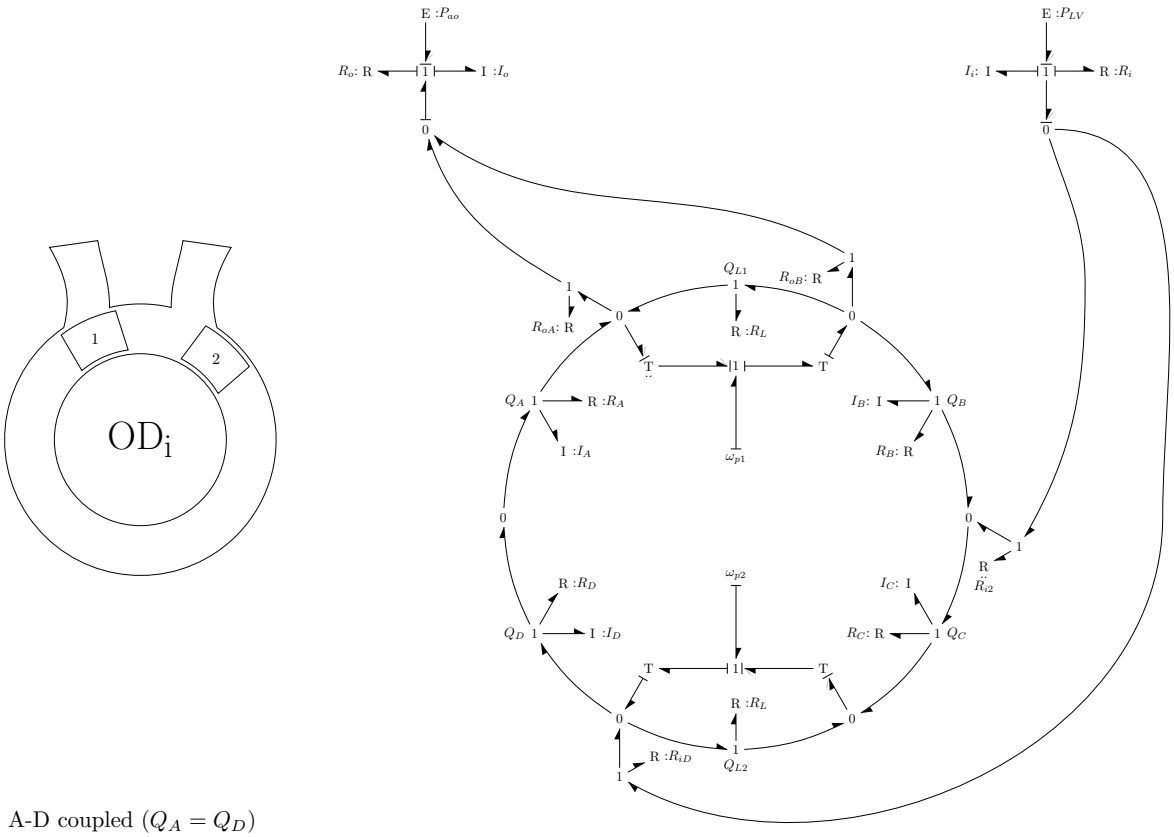

A-D coupled ($Q_A = Q_D$)

$$\dot{Q}_A = \big[-\Delta P - (R_A + R_D)Q_A - R_{iD}Q_{iD} - R_{oA}\tilde{Q}_{oA}\big]/(I_A + I_D)$$

$$\dot{Q}_B = \big[\Delta P - R_B Q_B + R_{oB}\tilde{Q}_{oB} + R_{i2}Q_{i2}\,|Q_{i2}|\,\big]/I_B$$

$$\dot{Q}_C = \big[-R_C Q_C + R_L(Ar\omega_2 - Q_C) - R_{i2}Q_{i2}\,|Q_{i2}| + R_{iD}Q_{iD}\big]/I_C$$

$$\dot{Q}_D = \big[-\Delta P - (R_A + R_D)Q_D - R_{iD}Q_{iD} - R_{oA}\tilde{Q}_{oA}\big]/(I_A + I_D)$$

$$\dot{Q}_S = 0$$

$$\Delta P = P_{LV} - P_{ao} + I_{io}\left(\dot{Q}_{AD} - \dot{Q}_B\right) + R_{io}\left(Q_{AD} - Q_B\right)$$

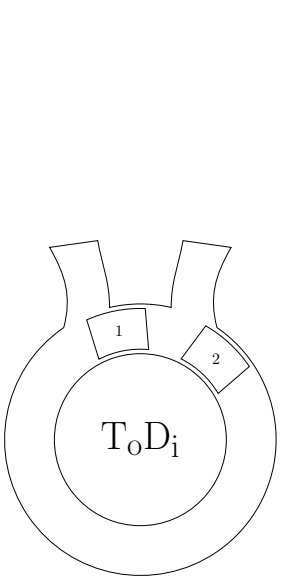

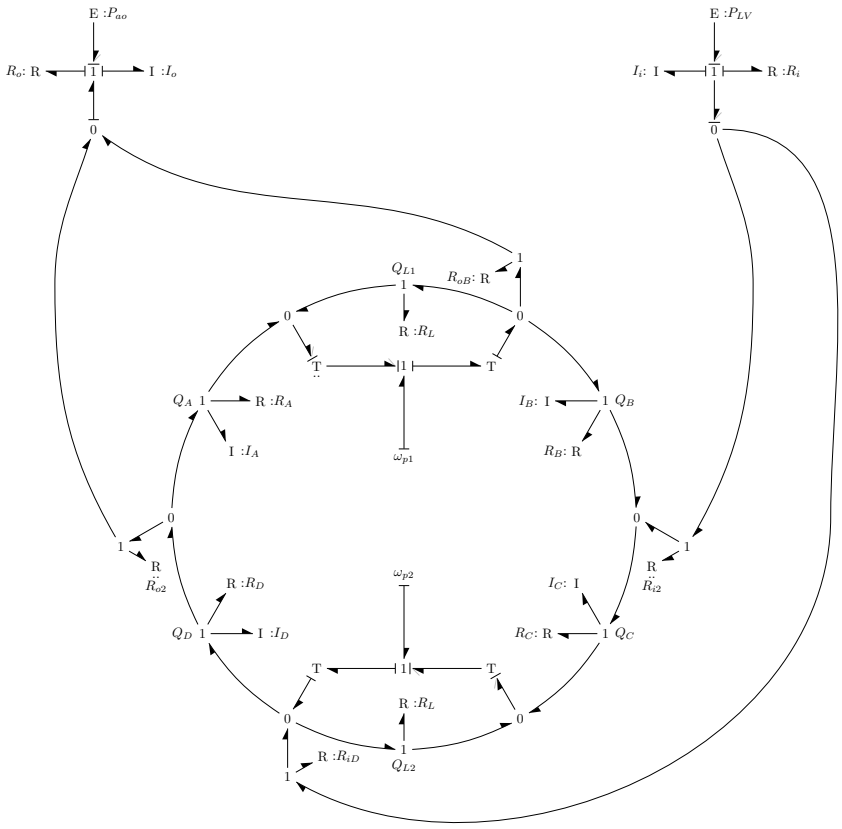

All flows decoupled

$$\dot{Q}_A = \big[- R_A Q_A + R_L(Ar\omega_1 - Q_A) + R_{o2} Q_{o2} \left| Q_{o2} \right| - R_{oB} Q_{oB} \big] / I_A$$

$$\dot{Q}_B = \big[\Delta P - R_B Q_B + R_{oB} Q_{oB} + R_{i2} Q_{i2} \left| Q_{i2} \right| \big] / I_B$$

$$\dot{Q}_C = \big[- R_C Q_C + R_L(Ar\omega_2 - Q_C) - R_{i2} Q_{i2} \left| Q_{i2} \right| + R_{iD} Q_{iD} \big] / I_C$$

$$\dot{Q}_D = \big[- \Delta P - R_D Q_D - R_{iD} Q_{iD} - R_{o2} Q_{o2} \left| Q_{o2} \right| \big] / I_D$$

$$\dot{Q}_S = 0$$

$$\Delta P = P_{LV} - P_{ao} + I_{io} \left(\dot{Q}_D - \dot{Q}_B \right) + R_{io} \left(Q_D - Q_B \right)$$

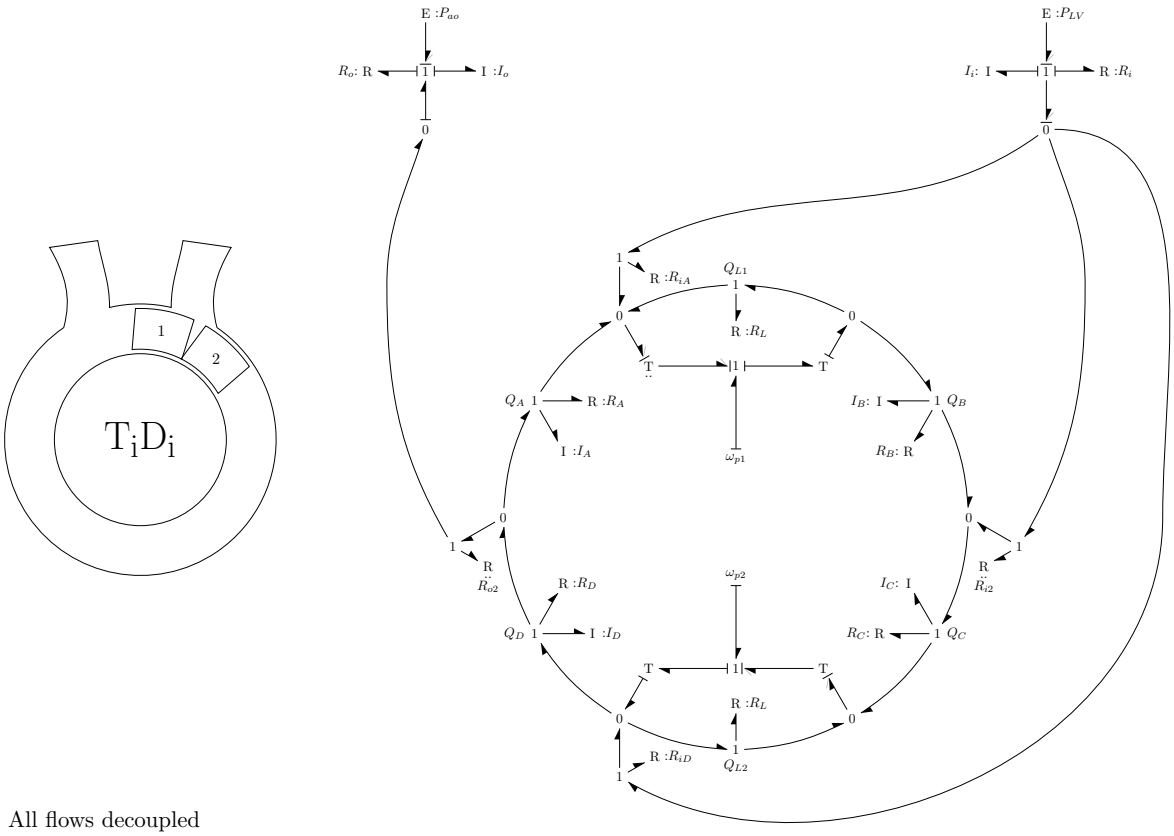

All flows decoupled

$$\dot{Q}_A = \left[\Delta P - R_A Q_A + R_{o2} Q_{o2} \left|Q_{o2}\right| + R_{iA} Q_{iA}\right] / I_A$$

$$\dot{Q}_B = \left[- R_B Q_B + R_L (Ar\omega_1 - Q_B) - R_{iA} Q_{iA} + R_{i2} Q_{i2} \left|Q_{i2}\right| \right] / I_B$$

$$\dot{Q}_C = \left[- R_C Q_C + R_L (Ar\omega_2 - Q_C) - R_{i2} Q_{i2} \left|Q_{i2}\right| + R_{iD} Q_{iD}\right] / I_C$$

$$\dot{Q}_D = \left[- \Delta P - R_D Q_D - R_{iD} Q_{iD} - R_{o2} Q_{o2} \left|Q_{o2}\right| \right] / I_D$$

$$\dot{Q}_S = 0$$

$$\Delta P = P_{LV} - P_{ao} + I_{io} \left(\dot{Q}_D - \dot{Q}_A\right) + R_{io} \left(Q_D - Q_A\right)$$

Appendix D

Coupled Fluid Inertia in Flow Junctions

Flow in the 2PTP has an analog in flow junction, where one branch is the drive piston flow, one is the the hold piston flow, and the other is the cannula flow. Understanding and quantifying the coupling between these flows is important flow control.

This chapter derives the dynamic equations for a general flow junction and quantifies the coupling effect that results.

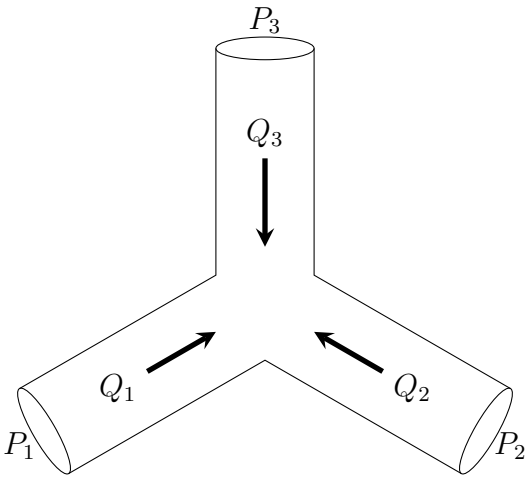

Figure D.1: Schematic of an inertially coupled flow junction

D.1 Generalized Model for Inertial Coupling at a Flow Junction

This section will derive the dynamic equations for inertial flow at a junction. While we're primarily concerned with fluid flow, these equations are generalized to account for any domain (electrical, fluid, mechanical, etc) by using generalized flow (f), effort (e), resistance (R), and inertia (I).

One key assumption that is made is that inertial energy dominates and that any capacitance

is negligible.

$$I\dot{f} \gg C\dot{e} \tag{D.1}$$

This would be the case in hydraulic fluid network systems with rigid tubes that have significant acceleration and deceleration of flow and where the fluid is 'stiff' or incompressible. With this assumption, conservation of mass at the junction dictates that the sum of the flows is zero.

$$f_1 + f_2 + f_3 = 0 \tag{D.2}$$

The energy flow at the flow junction can be determined using the bond graph seen in Figure D.2.

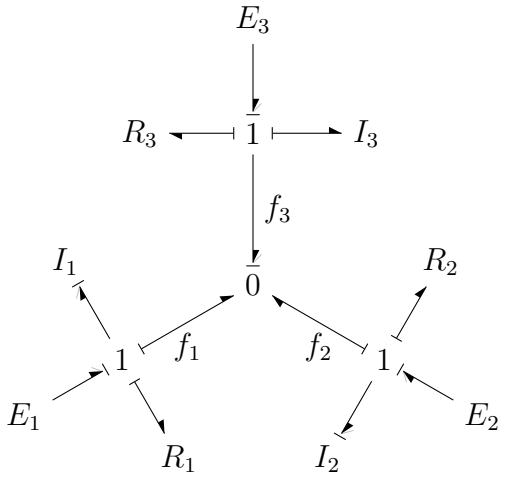

Figure D.2: Causal bond graph of a flow junction

To derive the dynamic equations for the intertially coupled system, an arbitrary assigment must be made on the bond graph. Two of the three inertial elements are given integral causality, which makes the third dependent. Any two could have been chosen. For this analysis, flows 1 and 2 are the independent variables, which makes 3 dependent. Now the bond graph can be used to derive the dynamic equations for the independent flows (f_1 and f_2).

$$I_1\dot{f_1} = E_1 - R_1f_1 - E_3 + I_3\dot{f_3} + R_3f_3 \tag{D.3}$$

$$I_2\dot{f_2} = E_2 - R_2f_2 - E_3 + I_3\dot{f_3} + R_3f_3 \tag{D.4}$$

To eliminate the dependent flow variable f_3 and it's derivative $\dot{f}_3$ from the equations above, the conservation of flow relationship at the zero junction is used.

$$f_3 = -f_1 - f_2 \tag{D.5}$$

The derivative of both sides can also be taken to get to get the relationship between flow accelerations.

$$\dot{f}_3 = -\dot{f}_1 - \dot{f}_2 \tag{D.6}$$

These can be substituted into the equations D.3 and D.4 to get

$$I_1\dot{f}_1 = E_1 - R_1 f_1 - E_3 - I_3\left(\dot{f}_1 + \dot{f}_2\right) - R_3\left(f_1 + f_2\right) \tag{D.7}$$

$$I_2\dot{f}_2 = E_2 - R_2 f_2 - E_3 - I_3\left(\dot{f}_1 + \dot{f}_2\right) - R_3\left(f_1 + f_2\right) \tag{D.8}$$

These are implicit equations, which can be put into matrix form for a linear system.

$$\begin{bmatrix} I_1 + I_3 & I_3 \\ I_3 & I_2 + I_3 \end{bmatrix} \begin{bmatrix} \dot{f}_1 \\ \dot{f}_2 \end{bmatrix} = - \begin{bmatrix} R_1 + R_3 & R_3 \\ R_3 & R_2 + R_3 \end{bmatrix} \begin{bmatrix} f_1 \\ f_2 \end{bmatrix} - \begin{bmatrix} 1 \\ 1 \end{bmatrix} E_3 \tag{D.9}$$

The inertial matrix on the left hand side can be inverted to find the differential equations

$$\begin{bmatrix} \dot{f}_1 \\ \dot{f}_2 \end{bmatrix} = \begin{bmatrix} I_1 + I_3 & I_3 \\ I_3 & I_2 + I_3 \end{bmatrix}^{-1} \left(- \begin{bmatrix} R_1 + R_3 & R_3 \\ R_3 & R_2 + R_3 \end{bmatrix} \begin{bmatrix} f_1 \\ f_2 \end{bmatrix} - \begin{bmatrix} 1 & 0 & -1 \\ 0 & 1 & -1 \end{bmatrix} \begin{bmatrix} e_1 \\ e_2 \\ e_3 \end{bmatrix} \right) \tag{D.10}$$

In simplified form, the system can be expressed as follows:

$$\dot{\mathbf{x}} = \hat{\mathbf{I}}^{-1}\left(-\mathbf{R}\mathbf{x} + \mathbf{B}\mathbf{u}\right) \tag{D.11}$$

where $\mathbf{x}$ is the column vector of flow states f_1 and f_2, $\hat{\mathbf{I}}^{-1}$ is the inverted inertial matrix (defined below), $\mathbf{R}$ is the linear resistance matrix, and $\mathbf{Bu}$ make up the effort inputs at the boundaries of the coupled system.

$$\hat{\mathbf{I}}^{-1} = \begin{bmatrix} \dfrac{1}{\hat{I}_1} & -\dfrac{1}{\hat{I}_C} \\ -\dfrac{1}{\hat{I}_C} & \dfrac{1}{\hat{I}_2} \end{bmatrix} \begin{bmatrix} I_1 + I_3 & I_3 \\ I_3 & I_2 + I_3 \end{bmatrix}^{-1} \tag{D.12}$$

To determine the effective inertial terms $\hat{I}_1$ and $\hat{I}_2$ for flows 1 and 2 and the off-diagnoal coupled effective inertial term $\hat{I}_C$, the inertial matrix is inverted

$$\begin{bmatrix} \frac{1}{\hat{I}_1} & -\frac{1}{\hat{I}_C} \\ -\frac{1}{\hat{I}_C} & \frac{1}{\hat{I}_2} \end{bmatrix} = \frac{1}{I_1 I_2 + I_1 I_3 + I_2 I_3} \begin{bmatrix} I_2 + I_3 & -I_3 \\ -I_3 & I_1 + I_3 \end{bmatrix}^{-1} \tag{D.13}$$

Then each term can be isolated and simplified.

$$\hat{I}_1 = I_1 + I_3 \left(1 - \frac{I_3}{I_2 + I_3}\right) \tag{D.14}$$

$$\hat{I}_2 = I_2 + I_3 \left(1 - \frac{I_3}{I_1 + I_3}\right) \tag{D.15}$$

$$\hat{I}_C = I_1 + I_2 + \frac{I_1}{I_3}\frac{I_2}{I_3} I_3 \tag{D.16}$$

Putting it in this form allows the effects of the inverted coupling matrix to be examined and quantify the degree of coupling between the controlled flow f_1 and f_2. To understand this relationship, it's instructive to look at two extreme cases, when the outflow is either very short (case 1) or very long (case 2).

D.1.1 Case 1: Decoupled Inertance ($I_3 \ll I_1 \& I_2$)

When the system inertance (3) is much smaller than the inertance of 1 and 2, then the flows 1 and 2 inertially decoupled.

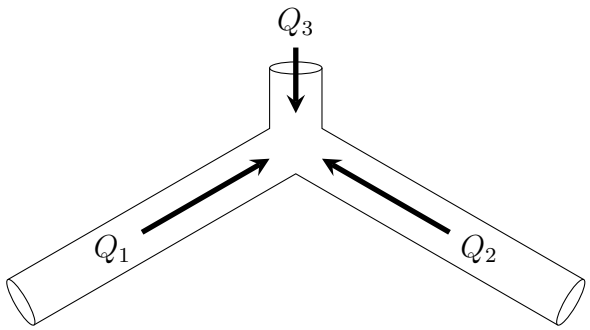

Figure D.3: Coupled flow through T-junction with small system inertance ($I_3 \ll I_1 \& I_2$). In this case, the flows 1 and 2 become inertially decoupled.

The effect of small system inertance on the dynamic equations can be understood by examining the effective inertance terms, which simply to:

$$\hat{I}_1 = I_1 + I_3\left(1 - \frac{I_3}{I_2 + I_3}\right) \to I_1 \tag{D.17}$$

$$\hat{I}_2 = I_2 + I_3\left(1 - \frac{I_3}{I_1 + I_3}\right) \to I_2 \tag{D.18}$$

$$\hat{I}_C = I_1 + I_2 + \frac{I_1}{I_3}\frac{I_2}{I_3}I_3 \to \infty \tag{D.19}$$

The inverted inertia matrix the system becomes

$$\begin{bmatrix} \frac{1}{\hat{I}_1} & -\frac{1}{\hat{I}_C} \\ -\frac{1}{\hat{I}_C} & \frac{1}{\hat{I}_2} \end{bmatrix} \to \begin{bmatrix} 1/I_1 & 0 \\ 0 & 1/I_2 \end{bmatrix} \tag{D.20}$$

The off-diagonal terms have become zero, which decouples flows 1 and 2. In this case, each branch could be treated individually.

D.1.2 Case 2: Strongly Coupled ($I_3 \gg I_1 \& I_2$)

When the system inertance (3) is much larger than the inertance of 1 and 2, then the flows 1 and 2 inertially couple.

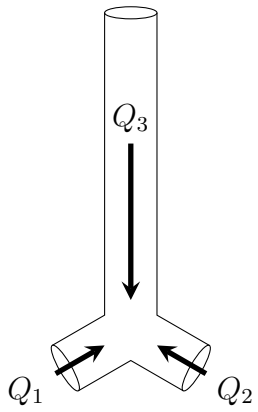

Figure D.4: Coupled flow at a junction with large system inertance ($I_3 \gg I_1 \& I_2$). In this case, the flows 1 and 2 become strongly coupled.

If the system inertia is very large, much larger than 1 and 2, then the flows 1 and 2 strongly couple. Again, this can be shown by simplifying the effective inertial terms:

$$\hat{I}_1 = I_1 + I_3\left(1 - \frac{I_3}{I_2 + I_3}\right) \rightarrow I_1 + I_2 \tag{D.21}$$

$$\hat{I}_2 = I_2 + I_3\left(1 - \frac{I_3}{I_1 + I_3}\right) \rightarrow I_2 + I_1 \tag{D.22}$$

$$\hat{I}_C = I_1 + I_2 + \frac{I_1}{I_3}\frac{I_2}{I_3}I_3 \rightarrow I_1 + I_2 \tag{D.23}$$

The inverted impedance matrix then becomes

$$\begin{bmatrix} \frac{1}{\hat{I}_1} & -\frac{1}{\hat{I}_C} \\ -\frac{1}{\hat{I}_C} & \frac{1}{\hat{I}_2} \end{bmatrix} = \frac{1}{I_1 + I_2}\begin{bmatrix} 1 & -1 \\ -1 & 1 \end{bmatrix} \tag{D.24}$$

Interestingly, the inertance term I_3 falls out entirely. It's as if the system flow becomes a rigid wall, directly coupling flows 1 and 2.

D.1.3 Case 3: Coupled ($I_1 = I_2 = I_3$)

When the system inertance (3) is equal to the inertance of 1 and 2, then the flows partially couple.

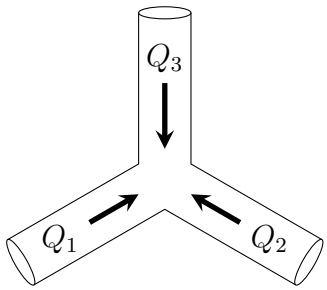

Figure D.5: Coupled flow at a junction with large system inertance ($I_3 \gg I_1 \& I_2$). In this case, the flows 1 and 2 become strongly coupled.

This can be shown by simplifying the effective inertial terms:

$$\hat{I}_1 = I_1 + I_3\left(1 - \frac{I_3}{I_2 + I_3}\right) \rightarrow 1.5I \tag{D.25}$$

$$\hat{I}_2 = I_2 + I_3\left(1 - \frac{I_3}{I_1 + I_3}\right) \rightarrow 1.5I \tag{D.26}$$

$$\hat{I}_C = I_1 + I_2 + \frac{I_1}{I_3}\frac{I_2}{I_3}I_3 \rightarrow 3I \tag{D.27}$$

The inverted impedance matrix then becomes

$$\begin{bmatrix} \frac{1}{\hat{I}_1} & -\frac{1}{\hat{I}_C} \\ -\frac{1}{\hat{I}_C} & \frac{1}{\hat{I}_2} \end{bmatrix} = \frac{1}{1.5I}\begin{bmatrix} 1 & -\frac{1}{2} \\ -\frac{1}{2} & 1 \end{bmatrix} \tag{D.28}$$

This has the effect of increasing the

Bibliography

[1] A. S. Go, D. Mozaffarian, V. L. Roger, E. J. Benjamin, J. D. Berry, W. B. Borden, D. M. Bravata, S. Dai, E. S. Ford, C. S. Fox, S. Franco, H. J. Fullerton, C. Gillespie, S. M. Hailpern, J. A. Heit, V. J. Howard, M. D. Huffman, B. M. Kissela, S. J. Kittner, D. T. Lackland, J. H. Lichtman, L. D. Lisabeth, D. Magid, G. M. Marcus, A. Marelli, D. B. Matchar, D. K. McGuire, E. R. Mohler, C. S. Moy, M. E. Mussolino, G. Nichol, N. P. Paynter, P. J. Schreiner, P. D. Sorlie, J. Stein, T. N. Turan, S. S. Virani, N. D. Wong, D. Woo, and M. B. Turner, "Heart disease and stroke statistics-2013 update: A Report from the American Heart Association," *Circulation*, vol. 127, no. 1, 2013.

[2] P. A. Heidenreich, J. G. Trogdon, O. A. Khavjou, J. Butler, K. Dracup, M. D. Ezekowitz, E. A. Finkelstein, Y. Hong, S. C. Johnston, A. Khera, D. M. Lloyd-Jones, S. A. Nelson, G. Nichol, D. Orenstein, P. W. F. Wilson, and Y. J. Woo, "Forecasting the future of cardiovascular disease in the United States: A policy statement from the American Heart Association," *Circulation*, vol. 123, no. 8, pp. 933–944, 2011.

[3] M. Colvin-Adams, J. M. Smith, B. M. Heubner, M. A. Skeans, L. B. Edwards, C. D. Waller, E. R. Callahan, J. J. Snyder, A. K. Israni, and B. L. Kasiske, "OPTN/SRTR 2013 Annual Data Report: heart," *American journal of transplantation : official journal of the American Society of Transplantation and the American Society of Transplant Surgeons*, vol. 15, pp. 1–28, 2015.

[4] T. Thom, N. Haase, W. Rosamond, V. J. Howard, J. Rumsfeld, T. Manolio, Z. J. Zheng, K. Flegal, C. O'Donnell, S. Kittner, D. Lloyd-Jones, D. C. Goff Jr., Y. Hong, R. Adams, G. Friday, K. Furie, P. Gorelick, B. Kissela, J. Marler, J. Meigs, V. Roger, S. Sidney, P. Sorlie, J. Steinberger, S. Wasserthiel-Smoller, M. Wilson, and P. Wolf, "Heart disease and stroke statistics–2006 update: a report from the American Heart Association Statistics Committee and Stroke Statistics Subcommittee," *Circulation*, vol. 113, no. 6, pp. e85–151, 2006.

[5] E. A. Rose, A. J. Moskowitz, M. Packer, J. A. Sollano, D. L. Williams, A. R. Tierney, D. F. Heitjan, P. Meier, D. D. Ascheim, R. G. Levitan, A. D. Weinberg, L. W. Stevenson, P. A. Shapiro, R. M. Lazar, J. T. Watson, D. J. Goldstein, and A. C. Gelijns, "The REMATCH trial: rationale, design, and end points. Randomized Evaluation of Mechanical Assistance for the Treatment of Congestive Heart Failure.," *The Annals of Thoracic Surgery*, vol. 67, no. 3, pp. 723–730, 1999.

[6] J. G. Rogers, J. Butler, S. L. Lansman, A. Gass, P. M. Portner, M. K. Pasque, and R. N. Pierson, "Chronic Mechanical Circulatory Support for Inotrope-Dependent Heart Failure Patients Who Are Not Transplant Candidates. Results of the INTrEPID Trial," *Journal of the American College of Cardiology*, vol. 50, no. 8, pp. 741–747, 2007.

[7] H. R. Mallidi, J. Anand, and W. E. Cohn, "State of the art of mechanical circulatory support.," *Texas Heart Institute journal / from the Texas Heart Institute of St. Luke's Episcopal Hospital, Texas Children's Hospital*, vol. 41, no. 2, pp. 115–20, 2014.

[8] C. A. Milano and A. A. Simeone, "Mechanical circulatory support: Devices, outcomes and complications," *Heart Failure Reviews*, vol. 18, no. 1, pp. 35–53, 2013.

[9] A. H. Healy, S. H. McKellar, S. G. Drakos, A. Koliopoulou, J. Stehlik, and C. H. Selzman, "Physiologic effects of continuous-flow left ventricular assist devices," *Journal of Surgical Research*, vol. 202, no. 2, pp. 363–371, 2016.

[10] J. G. Rogers, F. D. Pagani, A. J. Tatooles, G. Bhat, M. S. Slaughter, E. J. Birks, S. W. Boyce, S. S. Najjar, V. Jeevanandam, A. S. Anderson, I. D. Gregoric, H. Mallidi, K. Leadley, K. D. Aaronson, O. Frazier, and C. A. Milano, "Intrapericardial Left Ventricular Assist Device for Advanced Heart Failure," *New England Journal of Medicine*, vol. 376, no. 5, pp. 451–460, 2017.

[11] J. Wappenschmidt, S. J. Sonntag, M. Buesen, S. Gross-Hardt, T. Kaufmann, T. Schmitz-Rode, R. Autschbach, and A. Goetzenich, "Fluid Dynamics in Rotary Piston Blood Pumps," *Annals of Biomedical Engineering*, 2016.

[12] I. A. Ulert and M. Lang, "Circular Artificial Heart," 2003.

[13] S. M. Patel, P. E. Allaire, H. G. Wood, A. L. Throckmorton, C. G. Tribble, and D. B. Olsen, "Methods of failure and reliability assessment for mechanical heart pumps," *Artif Organs*, vol. 29, no. 1, pp. 15–25, 2005.

[14] J. R. Gohean, M. J. George, K.-W. Chang, E. R. Larson, T. D. Pate, M. Kurusz, R. G. Longoria, and R. W. Smalling, "Preservation Of Native Aortic Valve Flow And Full Hemodynamic Support With The TORVAD Using A Computational Model Of The Cardiovascular System.," *ASAIO journal (American Society for Artificial Internal Organs : 1992)*, pp. 259–265, 2014.

[15] K. Klute, U. Tasch, and D. B. Geselowitz, "An Optimal ContKpller for an Electric Ventricular- Assist DeviEe : Theory , Implementation , and Testing," vol. 39, no. 4, 1992.

[16] U. Tsach, D. B. Geselowitz, A. Sinha, J. Tirinato, H. K. Hsu, G. Rosenberg, and W. S. Pierce, "Minimum Power Consumption of the Electric Ventricular Assist Device through the Design of an Optimal Output Controller," $\{ASAIO\}$ $\{J\}$, vol. 33, no. 3, p. 714, 1987.

[17] A.-H. H. AlOmari, A. V. Savkin, M. Stevens, D. G. Mason, D. L. Timms, R. F. Salamonsen, and N. H. Lovell, "Developments in control systems for rotary left ventricular assist devices for heart failure patients: a review.," *Physiological measurement*, vol. 34, no. 1, pp. R1–27, 2013.

[18] S. M. Parnis, J. L. Conger, J. M. Fuqua Jr., R. K. Jarvik, R. W. Inman, D. Tamez, M. P. Macris, S. Moore, G. Jacobs, M. J. Sweeney, and O. H. Frazier, "Progress in the development of a transcutaneously powered axial flow blood pump ventricular assist system," *ASAIO J*, vol. 43, no. 5, pp. M576–80, 1997.

[19] G. A. Giridharan and M. Skliar, "Control strategy for maintaining physiological perfusion with rotary blood pumps," *Artificial Organs*, vol. 27, no. 7, pp. 639–648, 2003.

[20] T. Waters, P. Allaire, G. Tao, M. Adams, G. Bearnson, N. Wei, E. Hilton, M. Baloh, D. Olsen, and P. Khanwilkar, "Motor feedback physiological control for a continuous flow ventricular assist device," *Artificial Organs*, vol. 23, no. 6, pp. 480–486, 1999.

[21] Y. Wu, P. Allaire, G. Tao, H. Wood, D. Olsen, and C. Tribble, "An Advanced Physiological Controller Design for a Left Ventricular Assist Device to Prevent Left Ventricular Collapse," *Artificial Organs*, vol. 27, no. 10, pp. 926–930, 2003.

[22] M. Yoshizawa, "Assessing Cardiovascular Dynamics During Ventricular Assistance," *IEEE Engineering in Medicine and Biology*, 1994.

[23] R. Kaufmann, C. Nix, M. Klein, H. Reul, and G. Rau, "The implantable fuzzy controlled Helmholtz-left ventricular assist device: first in vitro testing," *Artif Organs*, vol. 21, no. 2, pp. 131–137, 1997.

[24] A. Ferreira, J. R. Boston, and J. F. Antaki, "A control system for rotary blood pumps based on suction detection," *IEEE Transactions on Biomedical Engineering*, vol. 56, no. 3, pp. 656–665, 2009.

[25] L. Baloa, J. Boston, M. Simaan, and J. Antaki, "Control of rotary heart assist devices," *Proceedings of the 2000 American Control Conference. ACC (IEEE Cat. No.00CH36334)*, vol. 5, no. June, pp. 2982–2986, 2000.

[26] M. A. Bakouri, R. F. Salamonsen, A. V. Savkin, A. H. H. Alomari, E. Lim, and N. H. Lovell, "A Sliding Mode-Based Starling-Like Controller for Implantable Rotary Blood Pumps," *Artificial Organs*, vol. 38, no. 7, pp. 587–593, 2014.

[27] Y. Chang, B. Gao, and K. Gu, "A model-free adaptive control to a blood pump based on heart rate.," *ASAIO journal (American Society for Artificial Internal Organs : 1992)*, vol. 57, no. 4, pp. 262–7, 2011.

[28] S. Bozkurt, F. N. van de Vosse, and M. C. M. Rutten, "Improving arterial pulsatility by feedback control of a continuous flow left ventricular assist device via in silico modeling," *International Journal of Artificial Organs*, vol. 37, no. 10, pp. 773–785, 2014.

[29] S. Bozkurt, F. N. V. D. Vosse, and M. C. M. Rutten, "Enhancement of Arterial Pressure Pulsatility by Controlling Continuous-Flow Left Ventricular Assist Device Flow Rate in Mock Circulatory System," *Journal of Medical and Biological Engineering*, vol. 36, no. 3, pp. 308–315, 2016.

[30] R. Amacher, J. Asprion, G. Ochsner, H. Tevaearai, M. J. Wilhelm, A. Plass, A. Amstutz, S. Vandenberghe, and M. S. Daners, "Numerical Optimal Control of Turbo Dynamic Ventricular Assist Devices," *Bioengineering*, vol. 1, pp. 22–46, 2014.

[31] V. Naveen Kumar, A. Syed, D. Kuruganti, A. Egoor, and S. Vemuri, "Measurement of position (angle) information of BLDC motor for commutation used for e-bike," *Proceedings of the 2013 International Conference on Advanced Electronic Systems, ICAES 2013*, pp. 316–318, 2013.

[32] A. C. Guyton, *Circulatory physiology: Cardiac output and its regulation*. W.B. Saunders Company, 1st ed., 1963.

[33] D. A. Berlin and J. Bakker, "Starling curves and central venous pressure," *Critical Care*, vol. 19, no. 1, 2014.

[34] S. W. Patterson and E. H. Starling, "On the mechanical factors which determine the output of the ventricles.," *J Physiol*, vol. 48, no. 5, pp. 357–379, 1914.

[35] R. F. Salamonsen, D. G. Mason, and P. J. Ayre, "Response of Rotary Blood Pumps to Changes in Preload and Afterload at a Fixed Speed Setting Are Unphysiological When Compared With the Natural Heart," *Artificial Organs*, vol. 35, no. 3, 2011.

[36] D. Doshi and D. Burkhoff, "Cardiovascular Simulation of Heart Failure Pathophysiology and Therapeutics," *Journal of Cardiac Failure*, vol. 22, no. 4, pp. 303–311, 2016.

[37] B. A. Houston, R. J. Kalathiya, S. Hsu, R. Loungani, M. E. Davis, S. T. Coffin, N. Haglund, S. Maltais, M. E. Keebler, P. J. Leary, D. P. Judge, G. R. Stevens, J. Rickard, C. M. Sciortino, G. J. Whitman, A. S. Shah, S. D. Russell, and R. J. Tedford, "Right ventricular afterload sensitivity dramatically increases after left ventricular assist device implantation: A multi-center hemodynamic analysis," *Journal of Heart and Lung Transplantation*, vol. 35, no. 7, pp. 868–876, 2016.

[38] N. R. Gaddum, M. Stevens, E. Lim, J. Fraser, N. Lovell, D. Mason, D. Timms, and R. Salamonsen, "Starling-like flow control of a left ventricular assist device: In vitro validation," *Artificial Organs*, vol. 38, no. 3, 2014.

[39] M. Horn, W. Hooper, B. Brach, W. Ashburn, and K. Moser, "Postural Changes in Pulmonary Blood Flow in Pulmonary Hypertension: A Noninvasive Technique Using Ventilation-Perfusion Scans," *Circulation*, vol. 66, no. 3, pp. 621–627, 1982.

[40] J. P. Pauls, M. C. Stevens, N. Bartnikowski, J. F. Fraser, S. D. Gregory, and G. Tansley, "Evaluation of Physiological Control Systems for Rotary Left Ventricular Assist Devices: An In-Vitro Study," *Annals of Biomedical Engineering*, pp. 1–11, 2016.

[41] J. P. Pauls, M. C. Stevens, N. Bartnikowski, J. F. Fraser, S. D. Gregory, and G. Tansley, "Evaluation of Physiological Control Systems for Rotary Left Ventricular Assist Devices: An In-Vitro Study," *Annals of Biomedical Engineering*, vol. 44, no. 8, pp. 1–11, 2016.

[42] M. C. Stevens, S. Wilson, A. Bradley, J. Fraser, and D. Timms, "Physiological control of dual rotary pumps as a biventricular assist device using a master/slave approach," *Artificial Organs*, vol. 38, no. 9, pp. 766–774, 2014.

[43] J. R. Gohean, M. J. George, T. D. Pate, M. Kurusz, R. G. Longoria, and R. W. Smalling, "Verification of a Computational Cardiovascular System Model Comparing the Hemodynamics of a Continuous Flow to a Synchronous Valveless Pulsatile Flow Left Ventricular Assist Device," *Asaio Journal*, vol. 59, no. 2, pp. 107–116, 2013.

[44] H. Watanabe, S. Sugiura, H. Kafuku, and T. Hisada, "Multiphysics Simulation of Left Ventricular Filling Dynamics Using Fluid-Structure Interaction Finite Element Method," *Biophysical Journal*, vol. 87, no. 3, pp. 2074–2085, 2004.

[45] A. Pironet, T. Desaive, S. Kosta, A. Lucas, S. Paeme, A. Collet, C. G. Pretty, P. Kolh, and P. C. Dauby, "A multi-scale cardiovascular system model can account for the load-dependence of the end-systolic pressure-volume relationship," *BioMedical Engineering Online*, vol. 12, no. 1, 2013.

[46] H. SUGA and K. SAGAWA, "Instantaneous Pressure-Volume Relationships and Their Ratio in the Excised, Supported Canine Left Ventricle," *Circulation Research*, vol. 35, no. 1, pp. 117–126, 1974.

[47] L. Zhong, D. N. Ghista, E. Y. Ng, and S. T. Lim, "Passive and active ventricular elastances of the left ventricle," *BioMedical Engineering Online*, vol. 4, pp. 1–13, 2005.

[48] D. Burkhoff, "Assessment of systolic and diastolic ventricular properties via pressure-volume analysis: a guide for clinical, translational, and basic researchers," *AJP: Heart and Circulatory Physiology*, vol. 289, no. 2, pp. H501–H512, 2005.

[49] D. Morley, K. Litwak, P. Ferber, P. Spence, R. Dowling, B. Meyns, B. Griffith, and D. Burkhoff, "Hemodynamic effects of partial ventricular support in chronic heart failure: Results of simulation validated with in vivo data," *Journal of Thoracic and Cardiovascular Surgery*, vol. 133, no. 1, 2007.

[50] K. R. Walley, "Left ventricular function : time-varying elastance and left ventricular aortic coupling," *Critical Care*, pp. 1–11, 2016.

[51] K. R. Walley and D. J. Cooper, "Diastolic stiffness impairs left ventricular function during hypovolemic shock in pigs.," *The American journal of physiology*, vol. 260, no. 3 Pt 2, pp. H702–H712, 1991.

[52] S. Nikolić, E. L. Yellin, K. Tamura, H. Vetter, T. Tamura, J. S. Meisner, and R. W. Frater, "Passive Properties of Canine Left Ventricle: Diastolic Stiffness and Restoring Forces," *Circ. Res.*, vol. 62, no. 6, pp. 1210–1222, 1988.

[53] H. Abe, T. Nakamura, M. Motomiya, K. Konno, and S. Arai, "Stresses in left ventricular wall and biaxial stress-strain relation of the cardiac muscle fiber for the potassium-arrested heart," *J Biomech Eng*, vol. 100, no. August 1978, pp. 116–121, 1978.

[54] H. H. Hardy and R. E. Collins, "On the pressure-volume relationship in circulatory elements," *Medical & Biological Engineering & Computing*, vol. 20, no. 5, pp. 565–570, 1982.

[55] T. Nakamura, H. Abe, S. Arai, T. Kimura, H. Kushibiki, M. Motomiya, K. Konno, and N. Suzuki, "The Stress-Strain Relationship of the Diastolic Cardiac Muscle and Left Ventricular Compliance in the Pressure-Overloaded Canine Heart," *Japanese Circulation Journal*, vol. 46, pp. 76–83, 1982.

[56] J. P. Holt, E. A. Rhode, and H. Kines, "Pericardial and Ventricular Pressure," *Circulation Research*, vol. 8, no. 6, pp. 1171–1181, 1960.

[57] S. a. Glantz, G. a. Misbach, W. Y. Moores, D. G. Mathey, J. Lekven, D. F. Stowe, W. W. Parmley, and J. V. Tyberg, "The pericardium substantially affects the left ventricular diastolic pressure-volume relationship in the dog.," *Circulation research*, vol. 42, no. 3, pp. 433–441, 1978.

[58] F. M. Colacino, F. Moscato, F. Piedimonte, M. Arabia, and G. A. Danieli, "Left ventricle load impedance control by apical VAD can help heart recovery and patient perfusion: A numerical study," *ASAIO Journal*, vol. 53, no. 3, pp. 263–277, 2007.

[59] T. Conover, A. M. Hlavacek, F. Migliavacca, E. Kung, A. Dorfman, R. S. Figliola, and T. Y. Hsia, "An interactive simulation tool for patient-specific clinical decision support in single-ventricle physiology," *Journal of Thoracic and Cardiovascular Surgery*, no. February, 2017.

[60] S. Klotz, I. Hay, M. L. Dickstein, G.-H. Yi, J. Wang, M. S. Maurer, D. A. Kass, and D. Burkhoff, "Single-beat estimation of end-diastolic pressure-volume relationship: a novel method with potential for noninvasive application," *American Journal of Physiology-Heart and Circulatory Physiology*, vol. 291, no. 1, pp. H403–H412, 2006.

[61] R. E. Newcomb, "Fluid Pump," 1919.

[62] F. Wankel, *Rotary Piston Machines: Classificaiton of Design Principles for Engines, Pumps, and Compressors*. London: Iliffe Books Ltd, 1965.

[63] J. P. Norbye, "Rivals to the Wankel: A Roundup of Rotary Engines," *Popular Science*, pp. 86–91, jan 1967.

[64] A. D. DeVore, R. J. Mentz, and C. B. Patel, "Medical management of patients with continuous-flow left ventricular assist devices," *Curr Treat Options Cardiovasc Med*, vol. 16, no. 2, p. 283, 2014.

[65] M. S. Slaughter, F. D. Pagani, J. G. Rogers, L. W. Miller, B. Sun, S. D. Russell, R. C. Starling, L. Chen, A. J. Boyle, S. Chillcott, R. M. Adamson, M. S. Blood, M. T. Camacho, K. A. Idrissi, M. Petty, M. Sobieski, S. Wright, T. J. Myers, and D. J. Farrar, "Clinical management of continuous-flow left ventricular assist devices in advanced heart failure," *Journal of Heart and Lung Transplantation*, vol. 29, no. 4 SUPPL., pp. S1–S39, 2010.

[66] J. K. Kirklin, F. D. Pagani, R. L. Kormos, L. W. Stevenson, E. D. Blume, S. L. Myers, M. A. Miller, J. T. Baldwin, J. B. Young, and D. C. Naftel, "Eighth annual INTERMACS report: Special focus on framing the impact of adverse events," *Journal of Heart and Lung Transplantation*, vol. 36, no. 10, pp. 1080–1086, 2017.

[67] K. Fukamachi, A. Shiose, A. Massiello, D. J. Horvath, L. A. R. Golding, S. Lee, and R. C. Starling, "Preload sensitivity in cardiac assist devices," *Annals of Thoracic Surgery*, vol. 95, no. 1, pp. 373–380, 2013.

[68] H. S. Lim, N. Howell, and A. Ranasinghe, "The Physiology of Continuous-Flow Left Ventricular Assist Devices," *Journal of Cardiac Failure*, vol. 23, no. 2, pp. 169–180, 2017.

[69] J. C. Cleveland, D. C. Naftel, T. B. Reece, M. Murray, J. Antaki, F. D. Pagani, and J. K. Kirklin, "Survival after biventricular assist device implantation: An analysis of the Interagency registry for mechanically assisted circulatory support database," *Journal of Heart and Lung Transplantation*, vol. 30, no. 8, pp. 863–869, 2011.

[70] N. C. Dang, V. K. Topkara, M. Mercando, J. Kay, K. H. Kruger, M. S. Aboodi, M. C. Oz, and Y. Naka, "Right heart failure after left ventricular assist device implantation in patients with chronic congestive heart failure," *Journal of Heart and Lung Transplantation*, vol. 25, no. 1, pp. 1–6, 2006.

[71] J. Baumwol, P. S. MacDonald, A. M. Keogh, E. Kotlyar, P. Spratt, P. Jansz, and C. S. Hayward, "Right heart failure and "failure to thrive" after left ventricular assist device: Clinical predictors and outcomes," *Journal of Heart and Lung Transplantation*, vol. 30, no. 8, pp. 888–895, 2011.

[72] D. G. Mason, A. K. Hilton, and R. F. Salamonsen, "Reliable suction detection for patients with rotary blood pumps," *ASAIO Journal*, vol. 54, no. 4, pp. 359–366, 2008.

[73] V. Tchantchaleishvili, J. G. Luc, C. M. Cohan, K. Phan, L. Hübbert, S. W. Day, and H. T. Massey, "Clinical implications of physiological flow adjustment in continuous-flow left ventricular assist devices," *ASAIO Journal*, p. 1, 2016.

[74] J. R. Gohean, M. J. George, K. W. Chang, E. R. Larson, T. D. Pate, M. Kurusz, R. G. Longoria, and R. W. Smalling, "Preservation of native aortic valve flow and full hemodynamic support with the TORVAD using a computational model of the cardiovascular system," *ASAIO J*, vol. 61, no. 3, pp. 259–265, 2015.

[75] M. S. Slaughter, F. D. Pagani, J. G. Rogers, L. W. Miller, B. Sun, S. D. Russell, R. C. Starling, L. Chen, A. J. Boyle, S. Chillcott, R. M. Adamson, M. S. Blood, M. T. Camacho, K. A. Idrissi, M. Petty, M. Sobieski, S. Wright, T. J. Myers, and D. J. Farrar, "Clinical management of continuous-flow left ventricular assist devices in advanced heart failure," *J Heart Lung Transplant*, vol. 29, no. 4 Suppl, pp. S1–39, 2010.

[76] K. May-Newman, Y. K. Wong, R. Adamson, P. Hoagland, V. Vu, and W. Dembitsky, "Thromboembolism is linked to intraventricular flow stasis in a patient supported with a left ventricle assist device," *Asaio Journal*, vol. 59, no. 4, pp. 452–455, 2013.

[77] J. Fried, A. R. Garan, S. Shames, A. Masoumi, M. Yuzefpolskaya, K. Takeda, H. Takayama, N. Uriel, Y. Naka, P. C. Colombo, *et al.*, "Aortic root thrombosis in patients supported with continuous-flow left ventricular assist devices," *The Journal of Heart and Lung Transplantation*, vol. 37, no. 12, pp. 1425–1432, 2018.

[78] M. C. Stevens, N. R. Gaddum, M. Pearcy, R. F. Salamonsen, D. L. Timms, D. G. Mason, and J. F. Fraser, "Frank-starling control of a left ventricular assist device," *2011 Annual International Conference of the IEEE Engineering in Medicine and Biology Society*, pp. 1335–1338, 2011.

[79] R. F. Salamonsen, E. Lim, N. Gaddum, A. H. H. Alomari, S. D. Gregory, M. Stevens, D. G. Mason, J. F. Fraser, D. Timms, M. K. Karunanithi, and N. H. Lovell, "Theoretical

Foundations of a Starling-Like Controller for Rotary Blood Pumps," *Artificial Organs*, vol. 36, no. 9, pp. 787–796, 2012.

[80] R. F. Salamonsen, D. G. Mason, and P. J. Ayre, "Response of rotary blood pumps to changes in preload and afterload at a fixed speed setting are unphysiological when compared with the natural heart," *Artif Organs*, vol. 35, no. 3, pp. E47–53, 2011.

[81] J. Fan, C. Myant, R. Underwood, and P. Cann, "Synovial fluid lubrication of artificial joints: protein film formation and composition," *Faraday Discuss*, vol. 156, pp. 69–103, 2012.

[82] J. Fan, C. W. Myant, R. Underwood, P. M. Cann, and A. Hart, "Inlet protein aggregation: a new mechanism for lubricating film formation with model synovial fluids," *Proc Inst Mech Eng H*, vol. 225, no. 7, pp. 696–709, 2011.

[83] C. Myant and P. Cann, "In contact observation of model synovial fluid lubricating mechanisms," *Tribology International*, vol. 63, no. 0, pp. 97–104, 2013.

[84] I. C. Burgess, E. Jones, S. C. Scholes, and A. Unsworth, "Compliant layer bearings in artificial joints. Part 1: the effects of different manufacturing techniques on the interface strength between an elastomeric layer and a rigid substrate," *Proc Inst Mech Eng H*, vol. 222, no. 6, pp. 853–864, 2008.

[85] B. Armstrong-Hélouvry, P. Dupont, and C. C. D. Wit, "A Survey of Models , Analysis Tools and Compensation Methods for the Control of Machines with Friction," *Automatica*, vol. 30, no. 7, pp. 1083–1138, 1994.

[86] M. Ruderman and M. Iwasaki, "Observer of nonlinear friction dynamics for motion control," *IEEE Transactions on Industrial Electronics*, vol. 62, no. 9, pp. 5941–5949, 2015.

[87] S. Zhao, Y. Chen, and Y. Mao, "Adaptive load observer-based feed- forward control in PMSM drive system," *Transactions of the Institute of Measurement & Control*, vol. 37, no. 38, pp. 414–424, 2015.

[88] M. Ruderman, "Tracking control of motor drives using feedforward friction observer," *IEEE Transactions on Industrial Electronics*, vol. 61, no. 7, pp. 3727–3735, 2014.

[89] J. R. Gohean, E. R. Larson, B. H. Hsi, M. Kurusz, R. W. Smalling, and R. G. Longoria, "Scaling the low-shear pulsatile torvad for pediatric heart failure," *ASAIO journal (American Society for Artificial Internal Organs: 1992)*, vol. 63, no. 2, p. 198, 2017.

[90] T. A. S. Corporation and A. Gelb, *Applied Optimal Estimation*. The MIT Press, 1974.

[91] D. Liberzon, *Switching in Systems and Control*. Systems & Control: Foundations & Applications, Birkhäuser Boston, 2003.

[92] B. Friedland, *Control System Design: An Introduction to State-Space Methods (Dover Books on Engineering)*. New York, NY, USA: Dover Publications, Inc., 2005.

[93] E. Chapman, J. Parameshwar, D. Jenkins, S. Large, and S. Tsui, "Psychosocial issues for patients with ventricular assist devices: a qualitative pilot study.," *American Journal of Critical Care*, vol. 16, no. 1, 2007.

[94] N. Özkaya, D. Leger, M. Nordin, and D. Goldsheyde, "Mechanical Properties of Biological Tissues," in *Fundamentals of Biomechanics*, pp. 221–236, 2012.

[95] R. G. Longoria, "Modeling of Mechanical Systems for Mechatronic Applications," in *Mechatronic Systems, Sesnors, and Actuators: Fundamentals of Modeling*, pp. 9–1 – 9–54, 2007.